AD-A108 255 RESEARCH INST FOR GEODETIC SCIENCES FORT BELVOIR VA F/G 20/12
GAS-SURFACE INTERACTIONS IN CRYOGENIC WHOLE AIR SAMPLING,(U)
MAY 81 J M CALO, R J FEZZA, E J DINEEN F19628-77-C-0071
UNCLASSIFIED AFGL-TR-81-0162 NL

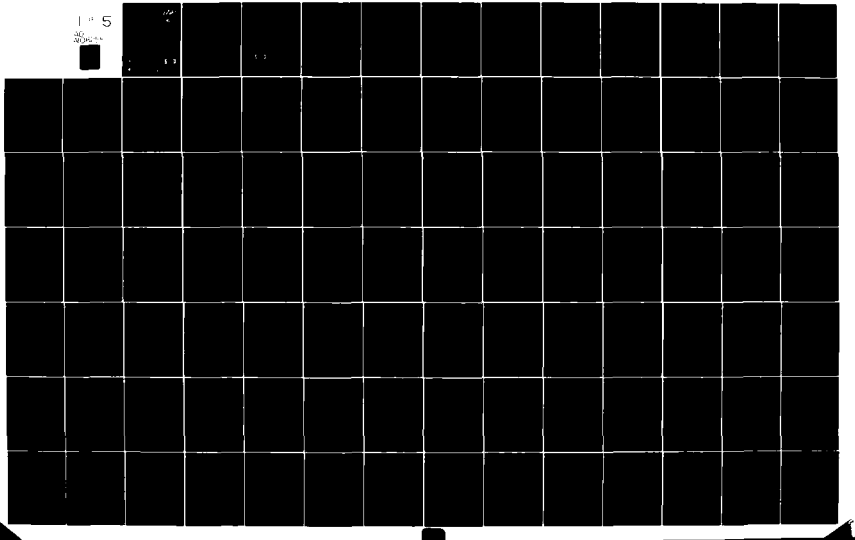

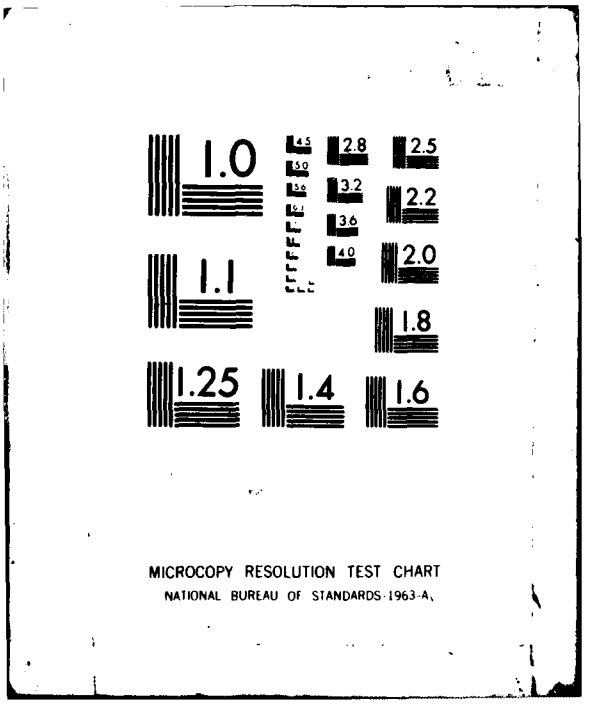
1.0
1.1
1.25
1.4
1.6
1.8
2.0
2.2
2.5
2.8
3.2
3.6
4.0
4.5
5.0
5.6
MICROCOPY RESOLUTION TEST CHART
NATIONAL BUREAU OF STANDARDS-1963-A

AD A108255

AFGL-TR-81-0182

GAS-SURFACE INTERACTIONS IN CRYOGENIC WHOLE AIR SAMPLING

J. M. Calo
R. J. Fezza
E. J. Dineen

Department of Chemical Engineering
Princeton University
Princeton, New Jersey 08544

Final Report
1 November 1976 - 31 March 1980

May 1981

Approved for public release; distribution unlimited

AIR FORCE GEOPHYSICS LABORATORY
AIR FORCE SYSTEMS COMMAND
HANSCOM AFB, MASSACHUSETTS 01731

Unclassified

SECURITY CLASSIFICATION OF THIS PAGE (When Data Entered)

REPORT DOCUMENTATION PAGE	READ INSTRUCTIONS BEFORE COMPLETING FORM
1. REPORT NUMBER: AFGL-TR-81-0162	2. GOVT ACCESSION NO.: AD A108255
3. RECIPIENT'S CATALOG NUMBER:	
4. TITLE (and Subtitle): GAS-SURFACE INTERACTIONS IN CRYOGENIC WHOLE AIR SAMPLING	5. TYPE OF REPORT & PERIOD COVERED: Final Report for Period 1 Nov. 1976-31 March 1980
	6. PERFORMING ORG. REPORT NUMBER:
7. AUTHOR(s): J. M. Calo, R. J. Fezza, and E. J. Dineen	8. CONTRACT OR GRANT NUMBER(s): F19628-77-C-0071
9. PERFORMING ORGANIZATION NAME AND ADDRESS: Department of Chemical Engineering Princeton University Princeton, New Jersey 08544	10. PROGRAM ELEMENT, PROJECT, TASK AREA & WORK UNIT NUMBERS: 62101F 668703AB
11. CONTROLLING OFFICE NAME AND ADDRESS: Air Force Geophysics Laboratory Hanscom AFB Massachusetts 01731 Monitor/Charles C. Gallagher/LKD	12. REPORT DATE: May 1981
	13. NUMBER OF PAGES: 418
14. MONITORING AGENCY NAME & ADDRESS (if different from Controlling Office): Office of Naval Research Resident Representative 715 Broadway (5th Floor) New York, New York 10003	15. SECURITY CLASS. (of this report): UNCLAS
	15a. DECLASSIFICATION/DOWNGRADING SCHEDULE:

16. DISTRIBUTION STATEMENT (of this Report)

"Approved for public release; distribution unlimited."

17. DISTRIBUTION STATEMENT (of the abstract entered in Block 20, if different from Report)

18. SUPPLEMENTARY NOTES

The basis of this report is the doctoral dissertation of Mr. R. J. Fezza submitted to the faculty of Princeton University in partial fulfillment of the requirements for the degree of Doctor of Philosophy.

19. KEY WORDS (Continue on reverse side if necessary and identify by block number)

Cryogenic sampling of atmospheric gases; condensation; stratospheric species; chemical reactions in cryofrosts

20. ABSTRACT (Continue on reverse side if necessary and identify by block number)

Physico-chemical phenomena associated with in-situ cryogenic whole air sampling of stratospheric species (i.e., CF_2Cl_2, $CFCl_3$, N_2, O_2, O_3, NO, NO_2, N_2O, and CO_2) are examined. Condensation phenomena on disks of various materials, (e.g., electropolished, gold-flashed, and hexamethyldisilazane-coated stainless steel), cooled by a mechanical, helium cycle refrigerator, and subsequent thermal desorption behavior were studied using quadrupole mass spectrometry and NO_x chemiluminescence.

DD FORM 1 JAN 73 1473 EDITION OF 1 NOV 65 IS OBSOLETE
S/N 0102-LF-014-6601

SECURITY CLASSIFICATION OF THIS PAGE (When Data Entered)

401537

20 (continued)

Strong, spurious "first" condensations in the 200-250 K temperature range were observed for most of the species studied. This phenomenon is attributed to water vapor contamination of the surface, which affects both the temperature and mechanism of the subsequent "true" thermodynamic condensation, resulting in supersaturation and condensate growth initiation by surface nucleation.

Desorption spectra of binary cryofrosts and of the pure components revealed significant levels of interaction between species in the cryofrost. These results preclude chromatographic cryo-fractionation as a reliable technique for whole air sample analysis.

Reactions which occur during cryofrost regeneration were studied via temperature programmed and flash desorption. Surprisingly persistent disproportionation of NO (i.e., $4NO \longrightarrow N_2 + 2NO_2$) occurred with conversions of nearly 50% upon desorption of NO- containing cryofrosts. Rapid ozone recombination and oxidation of NO to NO_2 by ozone are also reported.

Table of Contents

Table of Contents (Cont'd)

Appendices

List of Figures

List of Figures (Continued)

List of Figures (Continued)

List of Figures (Continued)

List of Tables

SUMMARY

Physico-chemical phenomena associated with in situ cryogenic whole air sampling of stratospheric species are examined. Species of interest include CF_2Cl_2, $CFCl_3$, N_2, O_2, O_3, NO, N_2O, and CO_2, condensing on various cryosurface materials including electropolished, gold-flashed, or hexamethyldisilazane coated stainless steel disks. A high vacuum apparatus was devised to deposit the species of interest in a beam-like fashion on cryosurfaces cooled by a mechanical helium-cycle refrigerator. Condensation behavior and subsequent thermal desorption of these species were monitored with quadrupole mass spectrometry and NO_x chemiluminescence.

Condensation studies revealed a strong, spurious, "first" condensation in the 200-250K temperature range for N_2O, CO_2, NO, CF_2Cl_2, and $CFCl_3$, with weaker effects for N_2 and O_2. This phenomenon is believed due to water vapor contamination of the cryosurface, possibly forming a clathrate-like structure with the beam and background species. The growth of this structure is kinetically controlled, with condensation temperature being a complex function of beam intensity, energy, and water vapor availability. A modulated detection system shows the beam dynamics in front of the cryosurface to be complex, and reveals details of the "first" condensation. The occurrence of this spurious condensation affects the temperature and mechanism of the "true" thermodynamic condensation, resulting in supersaturation, as judged from vapor pressure data. This effect, similar to Stranski-

Krastonov growth, is explained by a kinetic model which assumes nucleation as the growth-initiating step.

Controlled thermal desorption was examined as a fractionation technique by studying desorption spectra for the binary systems CF_2Cl_2/N_2, CF_2Cl_2/O_2, $CFCl_3/N_2$, and $CFCl_3/O_2$, as well as those for the pure components. Carry over of the chlorofluoromethanes at low concentrations by N_2 and O_2 desorption was observed to occur. Conversely, small amounts of N_2 and O_2 were held over to relatively high temperatures (80-130K) by large deposits of chlorofluoromethanes. This is probably due to aggregation of binary component clusters due to van der Waals interactions. Ar/N_2 and CO_2/N_2 systems exhibited similar effects, eliminating dipole-induced dipole forces as those primarily responsible.

Studies of possible reactions occurring during cryo-frost regeneration were also performed employing temperature programmed and flash desorption techniques. Results included a surprising, persistent disproportionation of NO to NO_2 (i.e., $4NO \quad N_2 + 2NO_2$) during desorption of NO-containing condensates at levels near 50%. A self-catalytic mechanism is hypothesized. Ozone was found to recombine during desorption, exhibiting a threshold concentration effect, and conversion related to absolute quantities of deposits. A marked aging effect of the cryosurface was noted, with catalytic activity towards ozone recombination increasing steadily with time, possibly due to metal oxide formation on small areas of exposed steel. A significant oxidation of NO to NO_2 by ozone was also observed over and above that produced by nitric oxide disproportionation.

These results encompass several specific phenomena which have direct bearing on the qualitative and quantitative accuracy of cryogenic whole air sampling techniques, as well as condensation and kinetic phenomena occurring on cold surfaces in general.

1 INTRODUCTION

The effects of anthropogenic modification of the chemical composition of the stratosphere, particularly the ozone concentration, are topics of considerable current concern. More specifically, the role of trace stratospheric concentrations of the chlorofluoromethanes (Freons)^{R}, and the oxides of nitrogen (NO_x) in catalytic cycles which reduce the ozone concentration have become the target of much scientific investigation and debate (see Appendix A), due to the role of the ozone layer in shielding the earth's surface from damaging ultraviolet radiation (DUV).

Much of the current effort in this area is being directed towards atmospheric modeling, in attempts to enhance the understanding of the complex physical and chemical phenomena which control stratospheric composition. However, experimental verification of model predictions are also of critical importance if such models are to be accepted as accurate, and therefore, useful.

There are several techniques that can be used to determine stratospheric composition experimentally. Three such are balloon-borne instrumental analysis, ambient air grab-sampling, and cryogenic whole air sampling. Balloon-borne in situ instrumental analysis, a common technique, is difficult to perform accurately, due to the exceedingly low concentrations (ppmv to pptv) of the species of interest, and technical difficulties in keeping such sensitive instruments calibrated under field conditions. They are also inherently specific to a narrow range of species and

concentrations. Ambient air grab-sampling (i.e., filling an evacuated container with a stratospheric sample at ambient temperature and pressure) allows ground-based analysis, which is an advantage, but produces a small sample, and provides time and possibly catalytic sites (i.e., the container walls) for decomposition of the sample. In this regard, the cryogenic whole air sampler seems to be an improvement over the grab-sampling technique. The cryogenic whole air sampler, simply put, is a vacuum chamber containing a surface at cryogenic (typically 4K) temperature (Gallagher and Pieri, 1976). Samples are collected by allowing stratospheric gas to condense onto this cryosurface, and are then retrieved and analyzed under laboratory conditions. The two major advantages of this technique are comparatively large sample size, and low chemical reactivity of the sample due to the low temperature.

One of the original proposals for such a technique was given by Snelson (1972), who proposed cryogenic whole air sampling, followed by laboratory analysis using electron paramagnetic resonance (EPR) for the cryofrost in the solid phase, and gas chromatography for samples desorbed to the gas phase. A similar technique, at least as regards the sampling phase, is currently used by the Air Force Geophysics Laboratory to determine stratospheric composition (Gallagher, and Pieri, 1976, Gallagher, Pieri, and Goldan, 1977).

Figure (1-1) illustrates the sampling apparatus employed by the Air Force. A metal cylinder, with a specially treated surface (e.g., gold-flashed stainless steel)

is surrounded by a bath of liquid He (∿4K) surrounded by a guard volume of liquid N_2 (∿77K). Three of these samplers share the same cryogen bath and are arranged into a flight package similar to that shown in Figure (1-2). Samples are taken, one per sampler, at various stratospheric altitudes (typically 12-30km). Experiments of this type have been performed at various locations in order to ascertain latitudinal variations. Once sampling is completed, the sample parachutes to the ground, where it is kept at cryogenic temperature and transported to the ground-based laboratory. It is then subjected to various manipulations and analytical techniques; e.g. cryogenic-fraction (used on occasion), and/or controlled vaporization, followed by analysis using NO_x chemiluminescence, gas chromatography, and mass spectrometry.

Many phenomena associated with this technique are not well understood. Physico-chemical effects associated with condensation of atmospheric species onto metal surfaces, cryogenic fractional distillation, and subsequent manipulations during analysis are all important factors which affect both the qualitative and quantitative overall results of this technique. Questions such as:

A) What is (are) the condensation mechanism(s)?

B) Can species such as ozone and the oxides of nitrogen react in the cryofrost matrix, or during desorption and/or sample manipulation?

C) Is cryogenic fractional distillation an acceptable technique for accurate quantitative analysis of samples?

are all of extreme importance in understanding the results of the technique, and its accuracy. It is to these questions, and others regarding physico-chemical phenomena associated with cryogenic whole air sampling, that this thesis is devoted.

In the text that follows, Chapter 2 deals with the experimental apparatus employed to simulate the cryofrosts formed in the cryogenic whole air sampler, as well as the analytical instruments used to analyze the results. Chapter 3 deals with the condensation process, and proposes a kinetic model which explains the experimental results. Chapter 4 examines thermal desorption of cryofrosts in relation to possible effects on quantitative accuracy. Chapter 5 deals with experimentally observed chemical reactions during desorption, which have obvious effects on both qualitative and quantitative accuracy.

As noted, this area of research is relatively uncharted. Therefore, the current work, in addition to identifying the various important phenomena, has generated a significant amount of information which warrants further research.

REFERENCES

Gallagher, C.C., Pieri, R.V., AFGL-TR-76-0161, July, 1976.

Gallagher, C.C., Pieri, R.V., Goldan, P.D., J. Atm. Sci. 34, 1481-2, 1977.

Snelson, A., "The Chemical Composition of The Atmosphere at 40,000-65,000 Feet Using a Modified Matrix Isolation Technique", Project Suggestion #IITRI-72-107CX, IIT Research Institute, Ill., 1972.

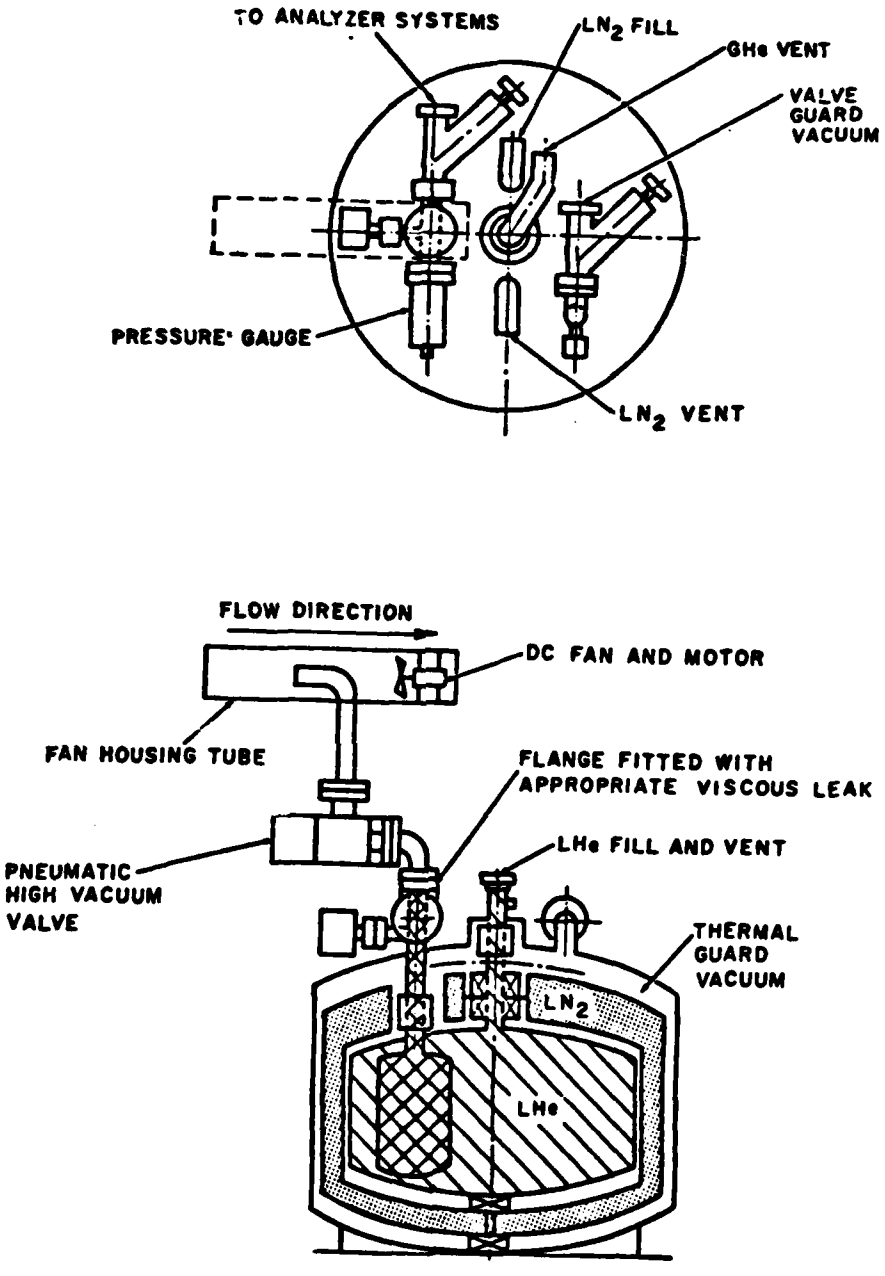

Figure (1-1)
Sampler and Air Intake System (Gallagher et al., 1976)

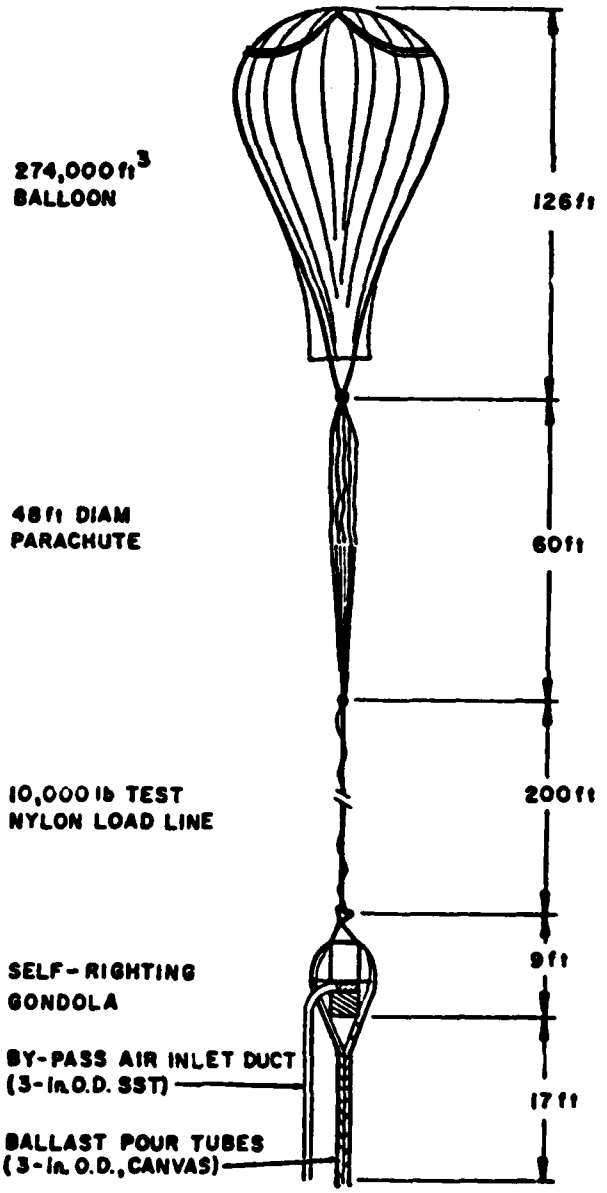

Figure (1-2)
Flight Package
(Gallagher et al., 1976)

2 EXPERIMENTAL APPARATUS

2.1 Introduction

The apparatus employed in the current study was constructed in a diffusion pumped vacuum system. The original configuration of the apparatus and additional details can be found in the thesis by Dineen (1977). Although various modifications were made to the system during the course of the work, the arrangement described herein is fairly typical of that used for the majority of the experiments performed. Pertinent modifications are discussed where appropriate in subsequent chapters.

The primary functions of the experimental system are to allow the controlled deposition and subsequent desorption of various gases and vapors of interest onto and from a cryogenic surface while monitoring gas phase compositions with appropriate analytical techniques. The apparatus can be divided into three major categories:

A) Vacuum and sample production, including introduction of the gaseous feeds.

B) Refrigeration, temperature measurement, and control.

C) Instrumental analysis.

The current chapter deals with the description of the apparatus organized in this manner, as well as cryosurface materials, gases and vapors of interest, and calibration techniques.

2.2 The System

An overall schematic of the vacuum system is given in Figure (2.2-1). The vacuum chamber is basically a stainless

steel cylinder with an inner radius of 7.6 cm and a length of approximately 32 cm, the interior surface of which has been electropolished to reduce surface roughness. This chamber was fitted with two 8 inch, copper-gasketed vacuum flanges, and with four 2.75 inch flanged ports, and two 4 inch flanged ports. In the configuration of Figure (2.2-1), with all internal apparatus in place and sealed off from the pumping system, the internal volume was determined to be approximately 8.9 liters.

As shown in Figure (2.2-1), the chamber was pumped through a 6.6 cm I.D. port (2.75 inch flange), and a right angle, 2.75 inch flanged bellows valve, through a liquid nitrogen (LN_2) trapped, 4 inch NRC-VHS4 diffusion pump, backed by a Sargent-Welch 1402 mechanical pump. This diffusion pump is rated at 1200 l/s for air at the mouth, and 550 l/s with a cryogenic trap. It will be shown in the following section that the pumping speed is conductance-limited with a much lower effective pumping speed. The typical, zero-load background pressure of the chamber, employing only the diffusion pump system, was $1x10^{-6}$ torr.

In several experiments, additional pumping capacity was provided by a cryogenic surface consisting of a 1 foot length of 3/8 inch I.D., flexible, ribbed stainless steel tubing. The tubing was connected to a liquid nitrogen feed-through mounted on a 2.75 inch flanged port on the bottom of the vacuum chamber (not visible in Figure (2.2-1)), and was kept filled with LN_2 from a constant-head reservoir

located above the chamber with a temperature sensor and an automatic solenoid valve. With cryopumping, the typical chamber background pressure was reduced to the 10^{-8} torr range.

Gas samples are introduced via a Granville-Phillips, series 203 variable leak valve (300-10^{-10} torr-l/s) through a 1/4 inch stainless steel tubing feedthrough mounted on one of the 2.75 inch flanged ports. The feed tubulation inside the chamber terminates in a 1 mm I.D. tube, 3.175 cm in length, positioned 5 mm from the cryosurface in a manner such that the centerline of the resultant molecular beam is normal to the cryosurface and impinges at its center (cf. Figure (2.2-1)). As shown below, the flow from the tip of this narrow tube is effusive in nature. Mass flow rates of the feed gas were determined from the pumping speed of the system, ionization gauge correction factors for each gas, and the steady-state pressure in the chamber. This technique relies on the constant pumping speed provided by the conductance limitation of the pump-out port.

Since the vacuum system is discussed here, for the sake of completeness, it is noted that the Thermo Electron Model 10AR Chemiluminescent NO/NO_x analyzer has a self-contained vacuum system, as shown in the instrument schematic, Figure (2.2-2). The reaction chamber of this instrument is maintained at -29 in. Hg by a model 1399 Welch Duo-Seal vacuum pump equipped with special metal vanes and pump oil resistant to NO, NO_2, and O_3. The instrument is also equipped

with a sample bypass system maintained at -5 in. Hg by a Metal Bellows MB-41 vacuum pump.

Gases were introduced to the vacuum chamber manifold system by an evacuated teflon tubing network. Most sample gases were introduced directly from gas cylinders, with the exception of ozone, which was available as an ozone-oxygen mixture produced by a model T-408 Welsbach high voltage discharge laboratory ozonator. This ozone generator is capable of producing a maximum of 2.25% ozone in oxygen (molar percentage), and is calibration is discussed in Chapter 5.

Refrigeration of the cryosurface was accomplished by an Air Products Displex CS202 closed cycle cryogenic refrigerator, which employs helium as the working fluid. This refrigerator is comprised of two basic sections - an expander which was mounted on one of the eight inch vacuum chamber ports, and an air-cooled helium compressor connected to the expander by two flexible hoses and an electrical cable. The expander is also referred to as the cryogenic probe in the current work, and operates by, as the name implies, expanding compressed helium in two stages, to cool the tip of the probe, nominally rated at 10K at zero refrigeration load in a vacuum. In the present system, a temperature minimum of 14K was routinely achieved, primarily due to the lack of radiation shielding. A two inch diameter circular plate of the surface material of interest is mounted on the tip and serves as the cryosurface. The probe

tip was modified to accept these plates, which are secured by four screws and gasketed to the probe tip by a layer of gold foil to insure good thermal contact.

The principal temperature measurement device consists of a silicon diode temperature sensor, and a model DRC-7C digital thermometer-controller, manufactured by Lake Shore Cryotronics. This instrument is capable of temperature measurement in the 1-400K range with an accuracy of $\pm$1K. The sensor was calibrated at the factory with LN_2 and liquid He, and a laboratory test with LN_2 and ice substantiated its accuracy. The expander probe was also equipped with two chromel-constantan thermocouples, (cf. Figure (2.2-2)) (which Dineen (1977) showed were inaccurate in the temperature range of interest), and a hydrogen vapor bulb thermometer (cf. Figure (2.2-2)) useful for temperature measurement in the 10-25K range. As shown in Figure (2.2-3), a capsule heater in a brass casing was attached to the back of the brass expander tip. The heating element was wired to the temperature controller, and could be set to dissipate 0-50 W. The on-off controller set point is adjustable over the entire 1-400K range. The controller also provided an analog voltage proportional to the temperature which was used to generate the time-temperature profile on a strip chart recorder. Typical cooldown and warmup curves are presented in the following chapters, where appropriate.

Pressure measurement instrumentation consisted of two types. The roughing pump line to the diffusion pump contained a thermocouple gauge operated by a Veeco thermocouple

gauge controller. This gauge was used to provide a measure of chamber pressure when evacuated by the mechanical pump. With the diffusion pump in operation, pressure was measured by a Veeco RG series ionization gauge with a thoriated iridium filament operated by a Granville-Phillips model 271 ionization gauge controller (cf. Figure (2.2-1)), which allows pressure measurement in the 10^{-4} to 10^{-10} torr range.

Total pressure in the chamber could also be determined with the UTI model 100C quadrupole mass spectrometer. As shown in Figure (2.2-1), the mass spectrometer consists of a probe, DC-RF generator, and a control unit. However, the primary function of this instrument is to provide mass discrimination in the 2 to 400 m/e range. The signal from this instrument was observed with a Heathkit model 10-4540 5MHz oscilloscope, and/or recorded on a Varian 9176 dual pen strip chart recorder (cf. Figure (2.2-1)).

In Chapter 3, experiments are described in which it became necessary to distinguish between the mass spectrometer signal as a result of molecules directly reflected from the cryosurface and those present in the background. The Bulova 200 Hz optical chopper, indicated in Figure (2.2-1) was used to accomplish this. Essentially, this chopper utilizes a set of vibrating vanes which open and close a window. The chopper was positioned on the centerline in between the mass spectrometer probe and cryosurface, and allowed the mass spectrometer probe to record the signal from both background and reflected species with the vanes open, but only background species with the vanes closed. A Princeton Applied

Research model 8H lock-in amplifier was used to determine the modulated AC signal arising from the reflected species only. This information was of considerable value in ascertaining condensation behavior in Chapter 3.

The mass spectrometer was not useful for experiments involving NO_2 and O_3 due to the complete fragmentation of these species upon electron impact into NO and O_2, which were also present as pure species in these experiments. In order to circumvent this problem, a Thermo Electron model 10AR chemiluminescence analyzer, shown schematically in Figure (2.2-2), was employed. In standard operation, it measures the photon flux associated with the chemiluminescent reaction sequence

$$NO + O_3 \longrightarrow NO_2^* + O_2 \qquad (2.2\text{-}1)$$

$$NO_2^* \longrightarrow NO_2 + h\nu \qquad (2.2\text{-}2)$$

occurring in the reaction chamber. This instrument can also be used to measure NO_2 by first reducing it to NO at 650°C on stainless steel, and then subjecting the resultant NO to the same reaction scheme. Under normal operating conditions a gas dilute in NO and/or NO_2 is fed to the analyzer as the sample stream, and the ozone is produced internally from a separate pure oxygen feed stream. The analyzer was modified by adding a manifold with two-valved feed ports on the oxygen-ozone input line to the reactor, which enabled the use of either the internally generated ozone, or a feed stream of externally produced ozone. A standard 5% NO in N_2 mixture, in lieu of the conventional sample, could then be used to measure the ozone content of

an external stream. This technique is discussed in more detail in Chapter 5. In the normal mode, the analyzer gives direct linear readout of NO/NO_2 concentrations over eight ranges ranging from (0-2.5 ppm to 0-10000 ppm) with an accuracy of $\pm 1\%$ of full scale in each range. The analyzer was calibrated with a 5.6 ppm NO in N_2 Matheson primary standard in the low concentration range, and a 5000 ppm NO in N_2 Matheson primary standard in the high range. The modifications had no effect on the calibration, which proved quite stable over time.

The gases employed in the following work (i.e., Ar, N_2, O_2, NO, N_2O, NO_2, CO_2) were rated at least at 99.5% purity, and were analyzed mass spectrometrically and found to contain no detectable impurities. Relevant species were also checked with the chemiluminescence analyzer for purity (see Chapter 5) and again, no detectable levels of impurities were found. The only exceptions to these purities were Freons 11 and 12, which were of commercial grade. Freon 12 was determined as pure mass spectrometrically, but the Freon 11 was prepressurized with N_2. The N_2 was released, and the Freon 11 was subsequently vacuum stripped of N_2, leaving it of acceptable purity (i.e., no N_2 by mass spectrometry).

The three cryosurface disks used in this study were all supplied by the Air Force Geophysics Laboratory, Hanscom Air Force Base, Massachusetts. All were stainless steel-based and polished to various finishes, the finest with 600 grit aluminum oxide paste. One was electropolished

by Dineen (1977) and was used in the initial thermal desorption experiments (see Chapter 4). Another was gold-flashed in vacuo, using a technique much like electron microscope slide preparation, while yet another was coated with purified hexamethyldisilazane ($(CH_3)_3SiNHSi(CH_3)_3$), a polymer used in the whole air sampler due to its particularly low capacity for the Freons in comparison to stainless steel.

The preceding has described the basic apparatus, including the instrumental techniques employed for analysis. The following section deals with the calibration of the system pumping speed, ionization gauge, and analysis of the flow regime of the molecular beam generated. All of this information is necessary for the data analysis.

2.3 Calibration Techniques

Pumping Speed

The conductance-limited pumping speed was determined for the vacuum system, without cryopumping, by two separate methods. The first is a technique proposed by Dushman (1949), in which the vacuum chamber is raised to an elevated pressure by the addition of a leak stream, which is then instantaneously shut off. The pressure of the chamber is then followed as it returns to its base pressure. Application of continuity, i.e.,

$$\mathring{V}/V_s = -dP/Pdt \qquad (2.3\text{-}1)$$

where

$\dot{V}$ = system pumping speed (ℓ/s)

V_s = system volume (ℓ)

P = system pressure (torr)

t = time (s)

yields the instantaneous pumping speed of the system. Table (2.3-1) presents data for three such experiments, performed on three separate occasions. Since conductance-limited pumping should occur at constant speed, and noting that V_s = 8.9 liters, averaging the V/V_s values and multiplying by V_s, yields V = 17.0 ℓ/s with a standard deviation of $\pm$1.15 ℓ/s.

The second technique employed a calibrated glass nozzle positioned in a feedthrough to the vacuum chamber, the foreline pressure of which was monitored with a Baratron diaphragm-type pressure transducer. The nozzle orifice was first calibrated on a roughing pump line with one side of the nozzle at atmospheric pressure and the other under vacuum. Since these conditions assured sonic flow (Liepmann and Roshke, 1957):

$$\dot{V} = \left(1 + \frac{1}{2} M^2 (\gamma-1)\right)^{-\left(\frac{1}{\gamma-1}\right)} M\left(\frac{R\gamma T_o}{MW}\right)^{1/2} \left(1 + M^2 \frac{\gamma-1}{2}\right)^{-1/2} \quad (2.3\text{-}2)$$

where

M = Mach number of flow at nozzle throat = 1

$\gamma = C_p/C_v$ for species of interest

R = gas constant

MW = molecular weight

A = cross sectional area of the orifice

In this manner it was found that the nozzle had a diameter of 0.01245 cm. This nozzle was then installed, as described, on the high vacuum chamber. Systematic variation of the pressure applied to the nozzle yielded the data contained in Table (2.3-2). The pumping speed of the chamber was then calculated employing both the sonic flow equation (2.3-2) ($\mathring{V}_{sonic}$) and that for effusive flow ($\mathring{V}_{effusive}$), i.e.,

$$N = \frac{\pi}{4} d^2 n \frac{1}{4} \left(\frac{8kT}{\pi MW}\right)^{1/2} \qquad (2.3\text{-}3)$$

where

N = molecular flow (molecules/s)

n = upstream number density

d = orifice diameter

as given in Davidson (1962). This approach was necessitated by the fact that the ratio of the mean free path of the gas to the diameter of the nozzle (L_a/D, Table (2.3-2)) was close to one, which raises the possibility that the flow might not be sonic. Figure (2.3-1) presents the results of the pumping speeds determined using both assumptions versus L_a/D for the nozzle. Note that for $L_a/D>0.3$, the pumping speed remains relatively constant at approximately 17.6 ℓ/s, whereas below this value, it drops off sharply. This behavior is interpreted as indicating that the nozzle flow is effusive for $L_a/D>0.3$. The calculated sonic pumping speed approaches the effusive pumping speed at values for $L_a/D<0.3$. Thus, the conduction-limited pumping speed of the system was assumed to be 17.6 ℓ/s, which agrees quite well with the value determined with the alternate technique.

Ionization Gauge Correction Factors

The ionization gauge signal is species-dependent due to differences in ionization cross sections. In order to correct for this effect, experiments were performed to determine a correction factor for each of the species of interest. This was accomplished with the experimental configuration of Figure (2.3-2). A roughing pump line was connected to the vacuum side of the variable leak valve and to a tee connected to both N_2 and the species of interest. N_2 was then allowed to flow into the system, by opening the leak valve, and the steady-state pressure was recorded. The N_2 was then shut off at the source, with the leak valve setting unchanged, and all the lines were evacuated. Then the second gas was allowed into the system at the same leak valve setting. Knowing the pumping speed characteristics of the system and the foreline pressures and molecular weights of the particular gas, and insuring that the flow across the variable leak valve is sonic, it is a simple matter to determine ionization gauge correction factors employing the ideal gas relationship. These resultant correction factors are presented in Table (2.3-3) along with those obtained from the ion gauge manufacturer (Veeco). The fact that two reported values (for O_2 and CO_2) correspond closely to the experimental values implies that the technique is valid and accurate. It is noted that Freon 12 has a very low correction factor; i.e., its ionization efficienty is high in comparison to the other species. This fact will become important in subsequent calculations concerning condensation coefficients.

Flow Regime of Feed System Delivery Tube

For the condensation experiments, it is important to know the flow regime of the gas emanating from the 3.175 cm long, 1 mm I.D. tubing used to direct the gas molecules onto the cryosurface. Whether sonic or effusive, the resultant beam would have a different intensity distribution. Assuming, for the moment, that the flow is effusive, Dushman's (1949) work on conductance in ultra-high vacuum leads, with appropriate substitutions, to the estimate that the conductance in this tube is 3.9×10^{-3} ℓ/s for air. Using this value, and assuming that the chamber pressure for a given leak rate is 4.75×10^{-5} torr, the average pressure in the tube should be 0.212 torr. An experiment was performed in which the chamber was raised to this pressure, and the pressure upstream of this tubing section was measured to be 0.441 torr with a Baratron pressure gauge. If one assumes that the calculated average pressure in the tube, 0.212, torr is an average of the foreline pressure, 0.441 torr and the chamber pressure, 4.75×10^{-5} torr, it is clearly evident that the flow through the narrow tubing must be effusive. Therefore the flow emanating from this narrow tube should have a cosine intensity distribution. This result will be of use in Chapter 3.

2.4 Summary

In summary, an experimental apparatus was devised to freeze out gases and/or vapors onto cryogenically-cooled surfaces in a controlled fashion under vacuum. These samples can be retained on the surface indefinitely or could be

desorbed and monitored via ionization gauge, mass spectrometer and chemiluminescence analyzer. The pumping speed of the system (without cryopumping), the species-dependent ionization gauge correction, and the flow regime of the molecular beam were determined.

In the following chapters, this apparatus was applied to the study of condensation phenomena, desorption phenomena, and cryofrost reactions. Future modifications of the apparatus might include a supersonic molecular beam apparatus, as well as an in situ spectroscopic technique, such as infrared spectrophotometry. The reasons for such future improvements will become evident in the work which follows.

REFERENCES

Davidson, N., Statistical Mechanics, McGraw-Hill, N.Y., 1962.

Dineen, E.J., "Cryofrost Deposition and Desorption As Related To Cryogenic Whole Air Sampling in the Stratosphere", Masters Thesis, Princeton University, 1977.

Dushman, S., Scientific Foundations of Vacuum Technique, Wiley, N.Y., 1949.

Liepmann, H.W., Rochke, A., Elements of Gasdynamics, Wiley, N.Y., 1957.

TABLE (2.3-1)

PUMPING SPEED DATA; FIRST TECHNIQUE

Pressure (torr)	Time(s)	$\dot{V}/V_s$ (s^{-1})
Experiment 1		
5.9×10^{-6}	0	
4.6×10^{-6}	0.3	1.16
2.7×10^{-6}	0.6	1.85
1.6×10^{-6}	0.9	1.82
0.95×10^{-6}	1.2	1.84
0.55×10^{-6}	1.5	1.61
0.42×10^{-6}	1.8	0.58
0.41×10^{-6}	2.1	
Experiment 2		
4.7×10^{-5}	0	
2.3×10^{-5}	0.3	2.57
1.2×10^{-5}	0.6	2.54
0.55×10^{-5}	0.9	2.58
0.30×10^{-5}	1.2	2.33
0.13×10^{-5}	1.5	3.08
0.06×10^{-5}	1.8	2.67
0.034×10^{-5}	2.1	1.37
0.032×10^{-5}	2.4	
Experiment 3		
7.7×10^{-6}	0	
5.5×10^{-6}	0.3	1.39
3.1×10^{-6}	0.6	2.04
1.7×10^{-6}	0.9	2.06
1.0×10^{-6}	1.2	2.000
0.5×10^{-6}	1.5	2.200
0.34×10^{-6}	1.8	.86
0.33×10^{-6}	2.1	

TABLE (2.3-2)

PUMPING SPEED DATA; SECOND TECHNIQUE

P_o (torr)	P (torr)	$\dot{V}_{sonic}$ (ℓ/s)	$V_{effusive}$ (ℓ/s)	L_a/d
0.340	2.95×10^{-5}	27.63	16.25	1.20
0.609	4.85×10^{-5}	29.85	17.56	0.68
0.719	5.75×10^{-5}	29.97	17.62	0.57
0.925	7.40×10^{-5}	29.96	17.62	0.44
1.216	1.0×10^{-4}	29.15	17.14	0.34
1.358	1.13×10^{-4}	28.81	16.94	0.30
1.629	1.6×10^{-4}	24.40	14.35	0.25
1.897	1.85×10^{-4}	24.58	14.45	0.22
2.2	2.2×10^{-4}	23.97	14.09	0.19
2.54	2.55×10^{-4}	23.88	14.04	0.16
3.06	3.15×10^{-4}	23.28	13.68	0.13
3.91	4.2×10^{-4}	22.31	13.11	0.10
4.39	4.8×10^{-4}	21.92	12.89	0.09
5.08	5.9×10^{-4}	20.64	12.13	0.08

TABLE (2.3-3)

IONIZATION GAUGE CORRECTION FACTORS

	Experimental	Veeco*
F11	0.30	-
F12	0.016	-
N_2O	0.92	-
O_2	1.21	1.20
CO_2	0.70	0.73
NO	0.67	-

*Ref. Veeco Product Catalog,
Plainview, N.Y., 1977

Figure (2.2-1) Experimental Apparatus

KEY

(1) Mass spectrometer controller

(2) Phase lock amplifier

(3) Oscilliscope

(4) Strip chart recorder

(5) RF/DC generator

(6) NO_x chemiluminescence analyzer

(7) Ozone generator

(8) Ion gauge controller

(9) Digital thermometer/controller

(10) He compressor

(11) Constant head LN_2 reservoir

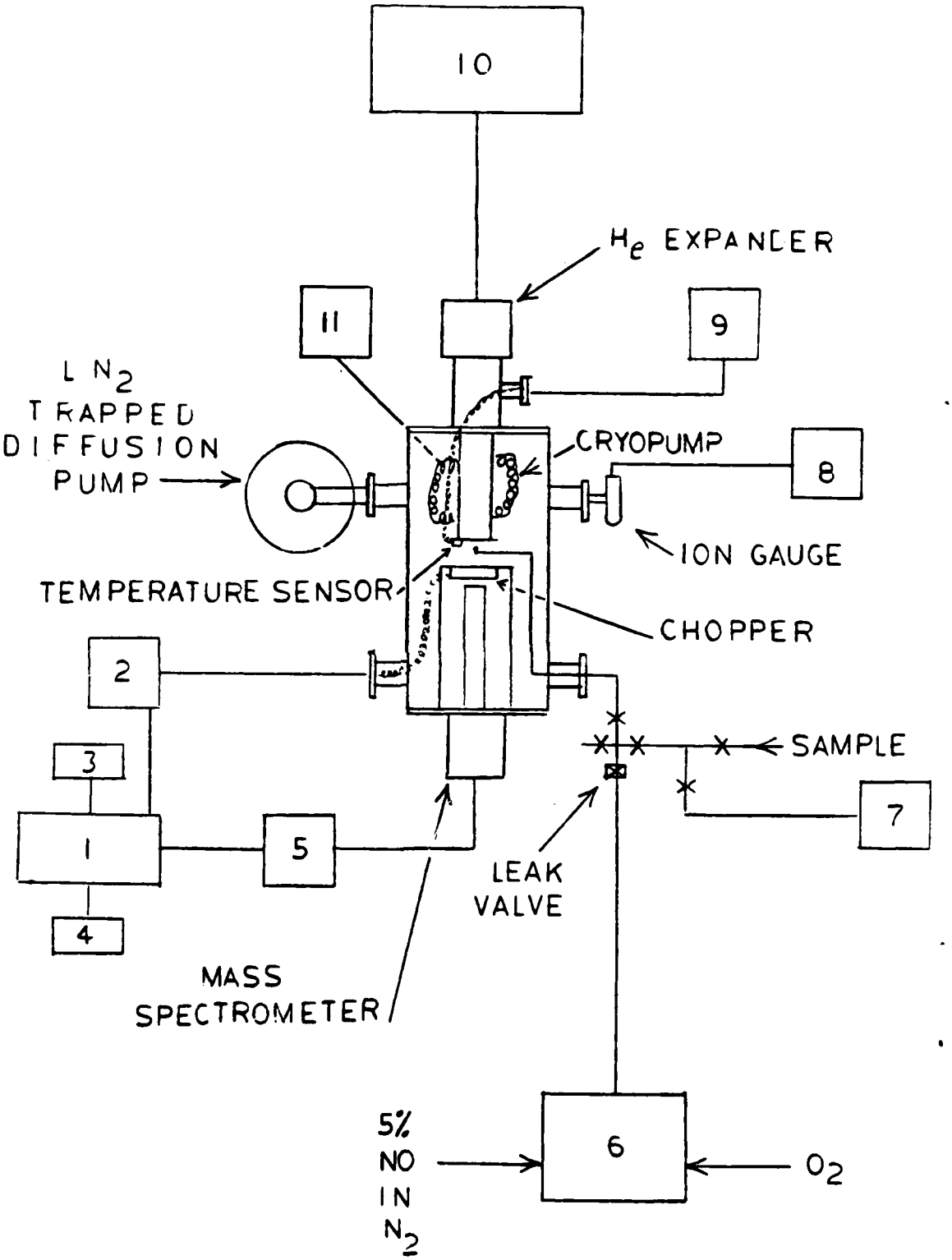
10
He EXPANDER
11
9
L N2
TRAPPED
DIFFUSION
PUMP
CRYOPUMP
8
ION GAUGE
TEMPERATURE SENSOR
CHOPPER
2
SAMPLE
3
7
1
5
LEAK
VALVE
4
MASS
SPECTROMETER
5%
NO
IN
N2
6
O2

Figure (2.2-1)

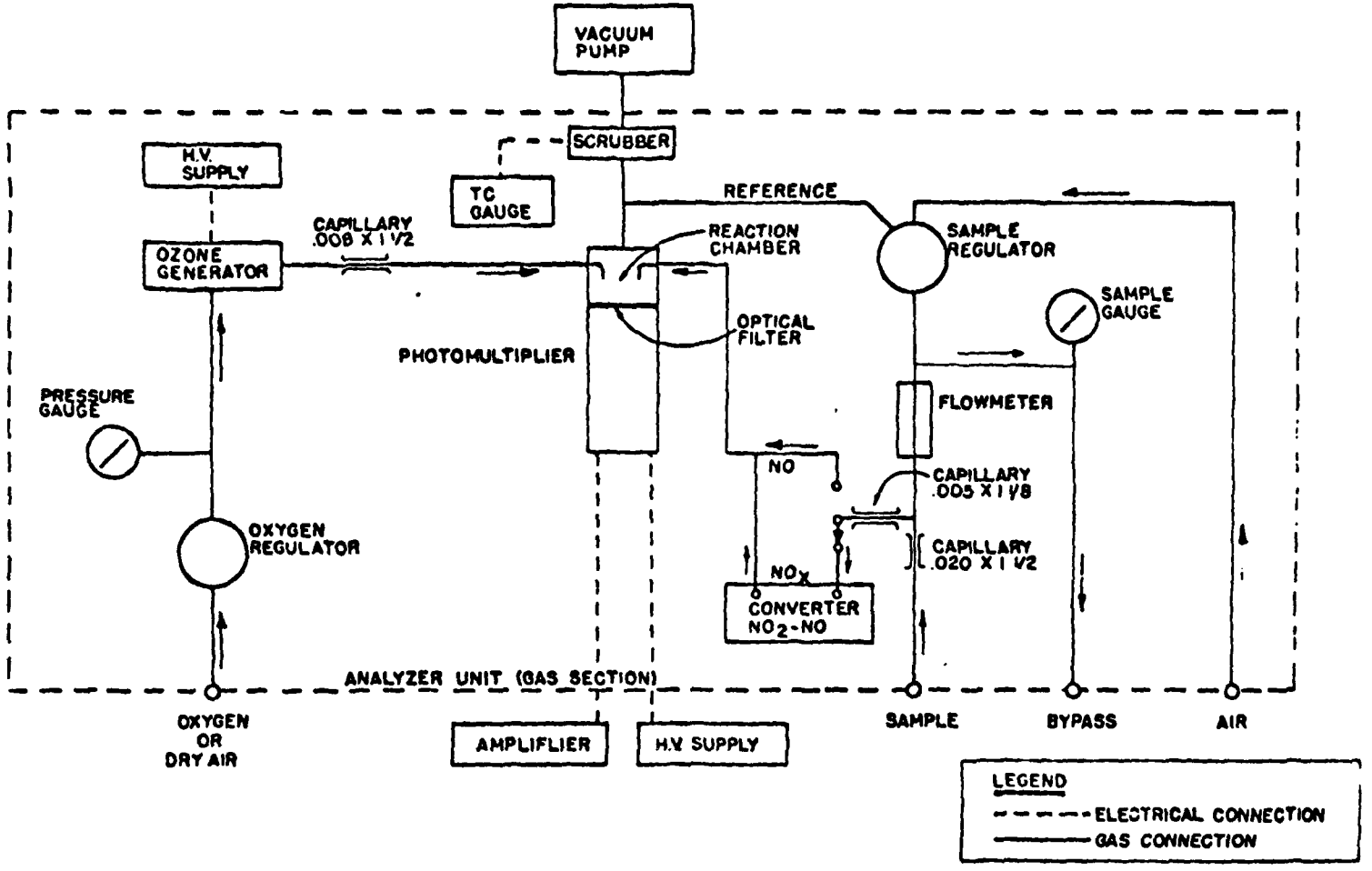

Figure (2.2-2) NO_x Chemiluminescence Analyzer Flow Diagram
(Reference: Model 10AR Instruction Manual, Thermo Electron Corp., Mass.)

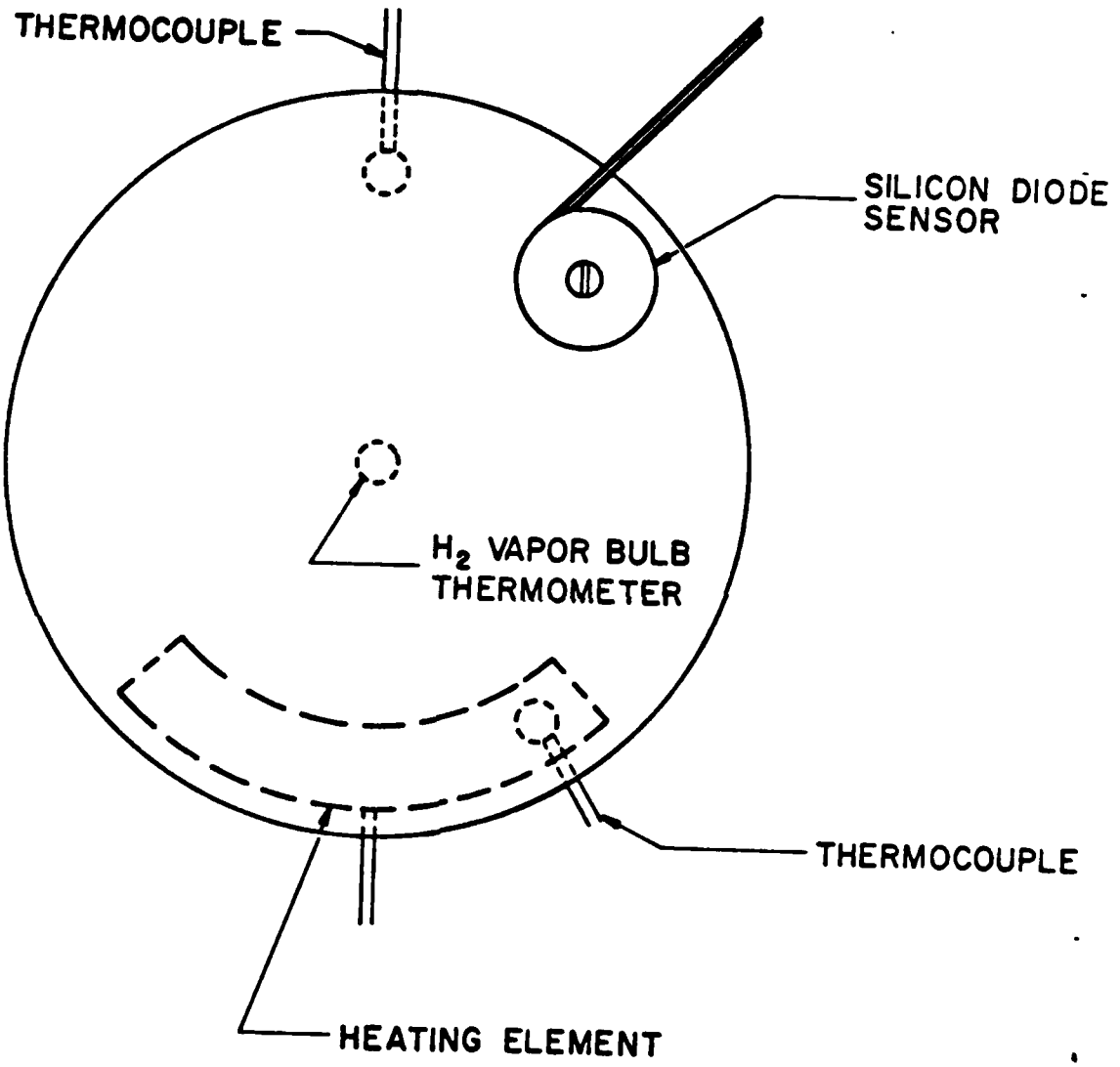

Figure (2.2-3)
The Cryosurface

Figure (2.3-1)
Pumping Speed Vs Mean Free Path

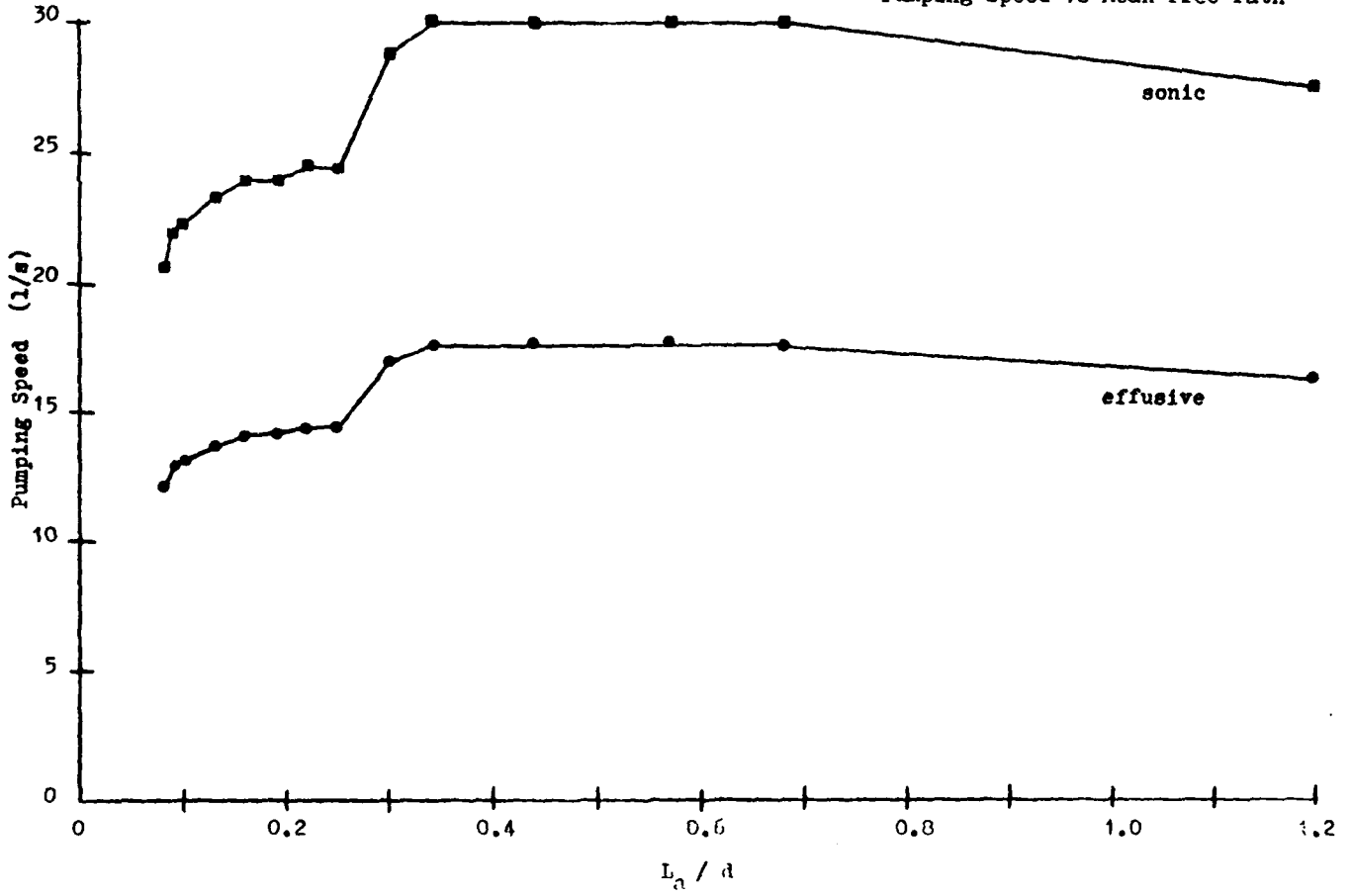

Figure (2.3-2)

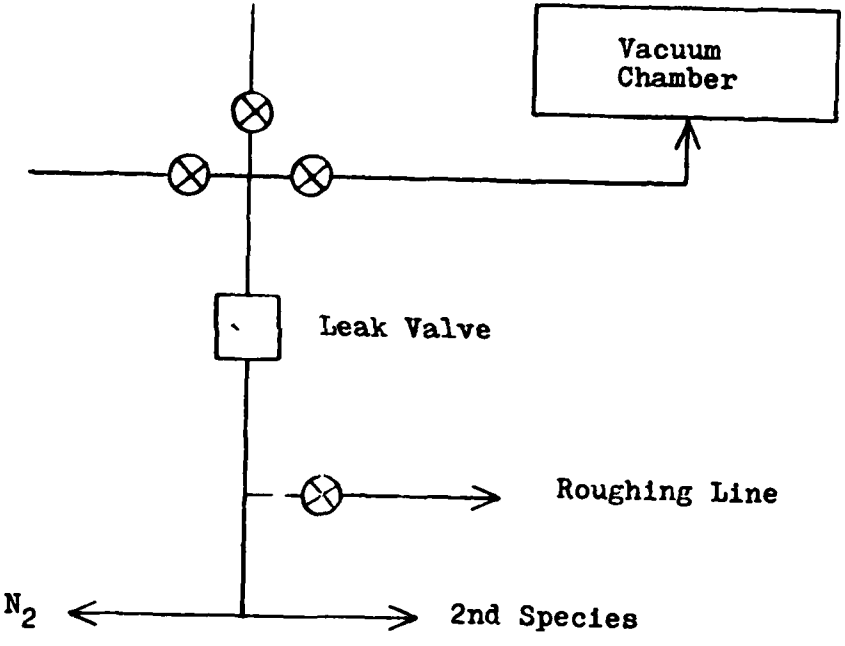

Apparatus Configuration Used To Determine Ionization Gauge Correction Factors

3. CONDENSATION PHENOMENA

3.1 CONDENSATION AND NUCLEATION LITERATURE

This section deals with the extant literature concerning condensation of atmospheric gases onto cryogenic surfaces. A review is given of developments in technique, as well as in the understanding of the physical chemistry involved. The interaction between a condensed gas and a solid surface cooled to cryogenic temperatures is a complex one dependent on many parameters, such as surface and gas contamination, energy and flux of the incident molecules, and interaction between different species in the frost. This complex and multiparametric nature leads to a spectrum of condensation mechanisms, some of which are explored in greater detail in the following section on nucleation kinetics.

Early interest in this area was engendered by the space program, primarily due to the need to simulate vacuum conditions approaching that of outer space. It was found that the pumping speeds necessary to test rocket engines in simulated space environments necessitated configurations of conventional mechanical and diffusion pumps that were both cumbersome, expensive, and limited with respect to ultimate vacuum. Thus the prospect of cryopumping gases, i.e., trapping them by heterogeneous condensation on a cold surface, received considerable attention. It is therefore understandable that government agencies such as the United States Air Force and NASA sponsored much of the early work.

As the quantity and depth of research in this area has grown, so has the level of understanding, as well as the realization of the many complexities involved; e.g., interactions

in the cryofrost, the morphology of the frost, deposition and growth mechanisms, and surface effects including even the possibility of catalytic reactions. The variety and multiplicity of these phenomena forces the worker in this field to draw from many disciplines. The disparate nature of the relevant literature necessitates a survey with an emphasis on specific phenomena related to the current work in order to present the analysis in a coherent fashion.

Early Condensation Studies

Early work in this field is typified by that of: Wang, Collins and Haygood (1961, 1962), dealing with CO_2, N_2, and H_2O; Dawson, Haygood, and Collins (1964), who examined the condensation of CO_2, N_2, and Ar; Brown (1964), on N_2O condensation; and Brown and Wang (1965) and Dawson and Haygood (1965), dealing with NH_3, H_2O, CH_3OH, CO_2, N_2O, C_2H_5OH, CH_3Cl, CH_3COCH_3, SO_2, CH_2Cl_2, $CHCl_3$, CCl_2F_2, and CCl_4.

The procedure involved in these early studies usually consisted of cooling a metal sphere, located in a vacuum chamber, with cryogens, and then admitting gas into the vacuum system via a calibrated leak. The gas involved was not preferentially directed towards the surface and therefore kinetic theory was used to calculate the collision rate of gas molecules with the cold surface. The system pressure was usually recorded with an ionization gauge or mass spectrometer as a function of time and cryosurface temperature, and the capture coefficient (i.e., the ratio of molecules captured by the surface divided by the number of molecules which collide with the surface) was reported. Results were often conflicting in nature, due to

inadequate control over experimental parameters, including surface temperature, gas leak rates, calibration of pumping speeds, and surface irregularities and contamination levels.

Subsequent work, typified by Brown and Heald (1967) and Heald and Brown (1968), involved the use of directed molecular beams, with well characterized energy and intensity distributions. Measurement of the reflected beam was accomplished by modulation and detection with a mass spectrometer probe, capable of determining reflected beam intensity at variable angles from the surface normal, as well as differentiating between direct reflective and evaporative flux. The sensitivity of this technique enabled the study of condensation in its earliest stages, thereby allowing discrimination between initiation and bulk condensation phenomena.

In particular, this approach led to the elucidation of the "bare surface" effect. In the early experimental efforts, it was generally found that a "bare" surface, when cooled from ambient to cryogenic temperatures, exhibited a lower pumping speed than one that had been pre-coated with the condensable species of interest. This "bare surface" effect, as it was named, was noted by Wang, Collins, and Haygood (1962) for CO_2 and H_2O frosts, by Brown (1964) for N_2O, and by Dawson, Haygood, and Collins (1964) for CO_2, N_2, and Ar. In these papers, the effect was generally explained in terms of the preferential adsorption sites provided by the pre-deposited frost for its own species, thereby allowing the impinging gas to condense with a greater accommodation efficiency than on the bare metal surface.

Employing the molecular beam technique, Brown and Heald (1967) reported a bare surface effect for CO_2 on a gold-flashed cryosurface. By careful control of the deposition rate, it was determined that a cryofrost thickness of approximately 10μm eliminated the variation in pumping speed. It was theorized that upon initiation of the experiment, during reduction of the surface temperature from ambient, background gases (consisting mainly of water and organics arising from the thermal cracking of diffusion pump oil), adsorb onto the surface preferentially on fault and grain boundary sites (i.e., the sites with the largest energies of adsorption). Thus, the contaminant layer reduces the average adsorption energy of the surface, resulting in less efficient trapping of subsequent impinging molecules. On the other hand, pre-coating of the target surface (usually with a molecular beam of higher intensity than employed in the experiment, e.g., pre-coating at $4.5 \times 10^{20}/m^2 s$ as opposed to an intensity of $4.5 \times 10^{19}/m^2 s$ in a typical run), would tend to create new defect sites on the resultant cryosurface, thereby increasing the average energy of adsorption. Direct evidence that high intensities ($1.5 \times 10^{20}/m^2 s$) can induce polycrystalline, faulted cryofrost structures is given by the electron microscope studies of Venables and Ball (1971) for rare gases, which are discussed later in more detail. Thus at lower beam intensities these sites act as growth centers, and result in faster cryopumping speeds. In short, surface morphology and surface contamination were theorized to be major contributing factors to subsequent condensation behavior.

In a later work by the same authors (Heald and Brown, 1968) examination of the intensity distribution in the molecular beam revealed that the lower intensities at the outer perimeter of the beam (i.e., the penumbra) allow condensation at lower temperatures than for the central part of the beam (the umbra). This relationship between beam intensity and condensation temperature (explored at length subsequently), caused them to question their previous conclusions regarding the "bare surface" effect, since condensation in the penumbra could also account for observed changes in pumping speed. In subsequent experiments, these authors found that complete condensation occurred at lower temperatures at constant beam intensities with no noticeable low pumping speed induction time. Thus it was shown that beam intensity profiles are important in analyzing condensation phenomena, and that if a bare surface effect does indeed exist, that it would be difficult to differentiate from intensity profile effects.

The work of Brown and Heald (1967) and Heald and Brown (1968) made many more contributions to this field. These authors developed a method of determining the capture coefficient directly from mass spectrometric measurement of the reflected signal intensity. C, the capture coefficient, was shown (Brown and Heald, 1967) to be equal to

$$C = 1 - \frac{S_c - S_{ec}}{S_{rw}} , \qquad (3.1\text{-}1)$$

where S_c, and S_{ec} are the reflected beam and evaporative flux intensity at the surface temperature, respectively, and S_{rw} is

the reflected beam intensity at an elevated temperature (i.e., room temperature) where condensation is not a factor. Using this technique, direct determination of capture coefficients can be made without many of the inaccuracies involved with previous methods.

These same workers also conducted investigations into many experimental effects arising from beam dynamics. They found that a molecular beam impinging on a polycrystalline metal surface is reflected as a cosine distribution, unlike that from single crystal surfaces. It was also found that a pre-deposit of a gas on the surface did not alter this effect; i.e., the deposit does not reflect as a single crystal, but also as a cosine distribution. Evaporation of a pre-deposited "spot" also exhibited a cosine intensity distribution. Thus, the intensity distribution of the reflected beam cannot be used to determine information about how the beam interacts with the surface; i.e., it remains a cosine distribution in all cases. This conclusion is drawn upon in the analysis of the current experimental data.

Polarization Effects

Brown and Wang (1965) attempted to correlate experimental, constant temperature capture coefficients with the physical properties of the gaseous species studied. They found good correlation with molecular weight and heat of condensation. Perhaps of even more significance, however, they attempted to relate condensation to the polarizability of the gas. The polarizability, P, is given by the Debye equation (Barrow, 1973):

$$P = \frac{1}{3} N_{av} \left(\alpha + \frac{\mu^2}{3\varepsilon_o kT}\right) = \frac{\varepsilon/\varepsilon_o - 1}{\varepsilon/\varepsilon_o + 2} \frac{M}{\rho} \qquad (3.1\text{-}2)$$

where N_{av} is Avogadro's number, α is the molar polarizability, μ is the dipole moment, ε_o is the permittivity of free space, and $\varepsilon/\varepsilon_o$ is the dielectric constant. The polarizabilities of the gases of interest in the current work are given in Table (3.1-1). Brown and Wang (1965) were unsuccessful in correlating their data with polarizabilities.

The relevance of polarizability, and electrostatic aspects in general, to physical adsorption are discussed by Benson and King (1965). It is noted that the attractive potential between a permanent dipole and an ion is given by

$$\phi_p = \frac{-C_{A+}\ \mu_P}{r^2} \qquad (3.1\text{-}3)$$

where C_{A+} is the charge on the cation, μ_p is the dipole moment, and r is the separation. For nonpolar molecules

$$\phi_{NP} = \frac{-\alpha\ C_{A+}}{2r^4} \qquad (3.1\text{-}4)$$

As a rough estimate of the magnitude of electrostatic forces in comparison to thermal energies, at 240K the ratio of the potential of a dipole of 0.51D at a separation of 5Å from a species with a single electronic charge to the thermal energy of a 240K molecule is approximately 25. Under these circumstances the potential is over an order of magnitude greater than thermal energies, illustrating that electrostatics may indeed be a factor in adsorption phenomena influenced by thermal effects.

The potential effects of polarizability on adsorption are also discussed by de Boer (1953), who adds an important observation. It is generally believed that adsorbed species which erect themselves (i.e., assume a mutual parallel orientation), are more stable than other types of adsorbates. It is also noted, however, that polar molecules which attempt to orient themselves in this manner are less stable, due to the mutual repulsion exerted by the oriented dipoles. One interpretation of these observations is that in order for an adsorbed species of a polar nature to be able to enhance condensation, the dipoles must, most probably, orient themselves in alternating directions. This effect is discussed again in connection with water clathrates in what follows.

As experimental evidence of polarizability effects, Benson and King (1965) note that ortho and para hydrogen can be separated on aluminum oxide as well as Linde molecular sieve 5A and 13A. The 0.8 kcal/mole necessary for hindered rotation to achieve such a separation is too high for van der Waals attraction, and thus only electrostatic forces can account for such a barrier. These authors also note that separation of light gases on molecular sieves is a monotonic function of polarizability, and that separation of N_2 and O_2 cannot be explained by cage size, because their molecular dimensions are well below those of minimum cage sizes.

Adamson (1967) has also suggested that surface polarizability effects are important, and cites the work of Pritchard (1962), who found changes in surface potential of Cu, Ni, Au,

and Pt surfaces upon adsorption of Xe at -183°C. Adamson attributed these results to induced surface dipoles.

Lewis and Anderson (1978) have noted that adsorption on ionic crystals is affected by permanent and induced dipoles, and that the electrostatic field at the surface is difficult to determine theoretically. As will be seen in the analysis of the present experimental data, polarizability can play an important role in the current work also.

Trapping and Adsorption Onto Sublayers

During the early studies of condensation, gas phase species contamination was a problem, due to the fact that the experimental observation indicative of condensation was the decrease in total system pressure, and thus any noncondensable contaminant species such as carbon monoxide, would tend to falsify the relationship between total system pressure and actual condensation, and thereby result in erroneously low capture coefficients. Wang, Collins, and Haygood (1961, 1962) did discover, however, that some species which are not normally condensable at high surface temperatures were effectively trapped during the condensation of another gas species. For example, nitrogen was found to be effectively trapped by CO_2 at 77K, a temperature at which it should still exist in the gaseous state under vacuum. More significantly with respect to the current work, nitrogen was also found to be effectively trapped by condensing water vapor, leading Wang et al. (1961) to speculate that a water clathrate-like structure was responsible. These authors also noted the ability of condensed water to pump nitrogen onto its surface at 77K. Dawson and Haygood (1965) speculated that

the ability of condensed water vapor to pump nitrogen would be an effective way of cutting pumping costs. These authors also noted that if H_2 and He were effectively pumped by H_2O and CO_2 at, say, 10K, a very real savings could be achieved in cryo-pumping systems.

In the same vein, Becker et al. (1972, 1972(A)) investigated the pumping speed of hydrogen onto frozen substrates of Ar, C_2H_6, NH_3, and CO_2. Their results included the conclusions that: (a) each gas substrate exhibited an optimum temperature for the adsorption of H_2; (b) CO_2 was by far the best substrate material (in the optimal temperature range of 10-22K, CO_2 was found to have a capacity of 0.2 moles of H_2 per mole of CO_2 deposited); and (c) at the optimal temperature, layer thickness and base layer deposition rates had little effect, whereas at higher and lower temperatures, H_2 adsorption capacity decreased with increasing substrate layer thickness, thereby indicating that substrate porosity is of some importance. It is interesting to note that these cryofrosts are comparable to zeolites in their ability to adsorb gases.

In a study of H_2 adsorption onto CO_2 substrates at 20K, Bewilogua and Jackel (1974) found that the thickness of the condensed substrate was not critical until it attained approximately 30μm, at which point increasing layer thickness caused pumping capacity to decrease dramatically. This precipitous change, while attributed primarily to diffusional limitations, may also involve morphological alterations in sublayers which render them less permeable to hydrogen. In the same study it was also noted that once the pumping capacity of a CO_2 substrate

layer was exhausted, it could be regenerated to near maximum capacity by depositing a fresh layer of CO_2 over the previously saturated sample. This implies that the trapped H_2 gas is stable in its configuration with CO_2, for if it were not, it would surely diffuse into the fresh layer along the concentration gradient, reducing its sorption capacity for hydrogen by filling adsorption sites close to the surface.

In a more recent work, Abe and Schultz (1979) studied H_2 adsorption onto rare gas (Xe, Kr, and Ar) matrices. These authors found a maximum adsorption capacity of 0.2 moles H_2 per mole of Xe at 13K, a ratio which is quite similar to that for H_2 on CO_2 (Becker et al., 1972, 1972(A)). It was also found that the amount of H_2 condensed was a strong function of matrix porosity; the substrate density (and therefore porosity) was a function of the substrate deposition temperature (i.e., the temperature at which the substrate was formed); and density begins to decrease from its bulk value at a characteristic temperature, about 0.25 of the triple point temperature of the substrate species. The substrate density passes through a plateau which begins at approximately 0.15 of the triple point temperature, extends for several degrees, depending on the gas species, and then continues to decline. Some interesting conclusions derived from these observations are that: (a) very thin films at high temperatures should exhibit the maximum sorption capacity, but that experimentally they do not (probably due to an annealing effect); and (b) adsorption capacity attains a maximum at an intermediate temperature, although as the temperature is lowered, the density decreases. This is explained by

the hypothesis that the pore size distribution is skewed towards smaller pore sizes at lower temperatures.

In summary, it has been shown that: (a) condensable species can readily trap non-condensable species at specific surface temperatures; (b) sorption onto substrates is dependent on morphology of the solid layers; (c) theoretically thin layers at high temperatures can be effective adsorbents, if counter-effects produced by annealing can be prevented; and (d) in certain cases, electrostatic fields associated with ionic crystals can enhance adsorption. All of these observations will be drawn upon in the analysis of experimental results.

Nucleation As A Growth Initiator

In their comprehensive work, Heald and Brown (1968) noted that if the vapor pressures of CO_2, N_2, and Ar were converted to intensities a la,

$$P_{sat} = R_{sat} \sqrt{2\pi mkT} \qquad (3.1\text{-}5)$$

(where R_{sat} is the intensity corresponding to P_{sat}), condensation could not occur until the surface temperature was such that $R_{beam} > R_{sat}$; i.e., supersaturation. Of the three gases studied, CO_2 required the most extreme supersaturation; i.e., surface temperatures of 7K, on the average, below that predicted from equilibrium considerations (Figure 3.1-1). From an early work of Frenkel (1955),

$$R_{sat} = (4\sigma_o\tau_o)^{-1} \exp(-H_v/k\,T_s) \qquad (3.1\text{-}6)$$

where σ_o is the atomic cross section, τ_o the period of oscillation of an adatom, T_s the saturation temperature, and H_v the heat of vaporization. Thus a plot of ln R_c vs. 1/T should yield a straight

line. It will be shown that this is also the case when nucleation is the rate controlling step in bulk condensation. In fact, Heald and Brown (1968) realized that nucleation was a possibility, but found the classical nucleation approach developed at that time to have too many unknown parameters to enable meaningful correlation of experimental data.

In a review article on thin films of condensable gases by Venables and English (1971) it was noted that Kohin (1960) theoretically found the principal forces which determine the structure of condensed N_2 and CO are primarily due to three contributions: (1) the interaction of molecular quadrupoles; (2) the effect of anisotropic molecular polarizability; and (3) short range repulsive forces. These factors were sufficient to explain the crystalline structure, as well as the phase transitions, in a satisfactory manner. Again, this emphasizes the importance of molecular polarizability in condensed frosts.

Venables and English (1971) also cite evidence that nucleation may be the precursor to bulk deposition in the gas films from the work of Venables and Ball (1971). In this latter work, in situ electron microscope technique was applied to a study of the growth of Ar, Kr, and Xe condensates on graphite and amorphous carbon substrates at cryogenic temperatures. Small, distinct crystals were observed on the substrate, showing that deposition is indeed initiated by nucleation for these gases under the experimental conditions employed. In addition, their number density could also be predicted by nucleation theory. This particular system was chosen by the authors because values of the parameters for the nucleation model were already known

from a previous work (Ross and Olivier, 1964). However, for the case of graphite, the adsorption energy (E_a) was known to be high, which, as will be evident from later sections of this thesis, does not lead to growth by nucleation. Venables and Ball (1971) also found that the crystal size was approximately 0.2μm and that the structure was highly faulted.

In later work which examined more carefully problems concerned with the purity of the graphite surface, Price and Venables (1975) and Venables and Price (1975) obtained different results. With a two-stage heat treatment of the surface (900°C for 2 minutes, 1500°C for a few seconds), they found Xe to deposit by layered growth, and not nucleation, on the graphite substrate. This same result was found for condensation temperatures between 9 and 55K. Yet island growth (i.e., nucleation) was still observed to be the growth mechanism for Xe on an amorphous carbon substrate. This would be expected from the theory, since the values of the nucleation parameters for the two carbon substrates are quite different, with graphite having a higher adsorption energy, which would be consistent with a layered growth mode (see the following nucleation kinetics section).

Thus this series of studies supports the nucleation theory (see section 3.2), which predicts that for high values of E_a, deposition should occur via layered growth, and not by nucleation. It also illustrates the ability of surface contamination to alter the deposition mechanism, as well as providing a "visual" verification of the nucleation phenomenon and associated data concerning the morphology of such systems.

A study of the caputre coefficient of CO_2 on a film or solid H_2O was conducted by Cazcarra, Bryson, and Levenson (1973). Employing a molecular beam source and a unique cryogenic microbalance detection system, doubly distilled water was deposited on a copper target at 100K, and then annealed to 150K to obtain a reproducible surface. The vacuum system had a base pressure of 10^{-9} torr, and for an intensity of 6.65×10^{13} $cm^{-2}s^{-1}$ it was found that CO_2 condensation was initiated on this H_2O surface at temperatures between 74.46 and 76.4K. More significantly, it was found that a strongly-bound base layer was first adsorbed prior to condensation, and that the calculated energy of activation for diffusion of CO_2 across this H_2O surface was 12.6 kcal/mole -- an extremely high value for a cryogenic system. Recalling the literature on adsorption onto polarized substrates, this high value may be due to the inability of CO_2, a polarizable molecule (P=7.35 cm^3/mole, Table 3.1-1), to diffuse across H_2O, which forms an ionic crystalline lattice.

In a subsequent work, Bryson and Levenson (1974) repeated the CO_2 condensation on H_2O films, but this time employed a gold-plated copper surface as the base substrate. It was found that at a CO_2 intensity of $R = 7.7 \times 10^{13}/cm^2s$ the condensation temperature shifted from the previous range to 72.2 to 74.4K. These authors point out the fact that the gold surface probably has a specific surface area of 2.8 (i.e., that the actual surface area is 2.8 times the apparent surface area) and that the specific surface area of the water film is unknown. A variation in this value may account for differences in condensation temperature at nearly equal intensities. Employing a nucleation

analysis similar to that presented in section 3.2, a value of E_a = 4.4 kcal/mole was found. This value, together with an interaction energy calculated from the Lennard-Jones parameters for CO_2, resulted in a critical cluster size of four.

Thus this group of studies illustrates that: (a) CO_2 nucleation occurs after an initial amount of CO_2 is first bound to the H_2O surface; (b) the system can be characterized using an atomistic model of the nucleation phenomena; and (c) the activation energy for diffusion is quite high, possibly indicating a diffusional barrier due to electrostatic hindrance.

Bently and Hands (1974) repeated the work of Heald and Brown (1968), on the condensation of CO_2 and Ar on a gold-flashed copper surface. The novel feature of the Bently and Hands apparatus, however, was the ability to study the effect of partially condensed beams (i.e., homogeneous nucleation in the beam prior to impact with the cryosurface). For the uncondensed beam, it was found that the supersaturation ratio for CO_2 (intensity of the beam at condensation divided by the equilibrium intensity at the cryofrost temperature) varied from 14 to 42, in essential agreement with the data of Heald and Brown (1968). Argon, however, did not exhibit a strong supersaturation behavior, and the authors concluded that Heald and Brown's surface was most probably contaminated. Studies with pre-condensed beams produced data with a very different slope (i.e., on an intensity vs. temperature plot), which intersected the vapor pressure curve at $1.2 \times 10^{16}/cm^2 s$ -- an effect which can be attributed to the existence of stable nucleation sites in the beam prior to when they would be expected to form on the surface.

In a later paper, Bently and Hands (1978) showed that N_2, as well as Ar, does not undergo a statistically significant supersaturation prior to condensation, while CO_2 does. Using a simplified nucleation model, the authors predicted a critical cluster size of nine for CO_2, and E_a = 9.4 kJ/mole (2.25 kcal/mole). In this analysis, bond energies were calculated using the heat of sublimation for CO_2. These authors concluded that with such a low value of E_a, nucleation must have occurred either on a strongly bound layer of CO_2 or a contaminant hydrocarbon deposit.

Thus in summary, the literature supports nucleation as a probable mechanism for deposition of atmospheric gases under certain cryogenic conditions. Many different effects arise, however, due to the deposition of contaminant or base gas layers prior to or during the deposition of the primary gas. All these effects will be drawn upon in the analysis of the experimental data.

TABLE 3.1-1

	μ(D)	P(cm^3/mole) 25°C
Brown and Wang (1965)		
N_2O	0.14	8.25
CO_2	0	7.35
H_2O	1.85	73.36
Watson et al (1934)		
NO	0.16	4.83
NO_2	0.17	8.33
Fuoss (1938)		
CF_2Cl_2	0.55	26.2
$CFCl_2$	0.53	30.7
Handbook of Physics and Chemistry (1974)		
N_2	0	4.67*
O_2	0	4.22*

*From dielectric constant data

3.2 NUCLEATION KINETICS

Introduction to Heterogeneous Nucleation

In the previous section, heterogeneous nucleation was introduced as one of the controlling factors in the process of deposition of atmospheric gases on metal surfaces. In this section, the literature concerning the modeling of heterogeneous nucleation will be examined, with an eye towards developing rate expressions to relate microscopic surface phenomena to experimentally observable macroscopic changes in variables such as reflected beam intensity. Most of the extant literature has been developed to explain the heterogeneous nucleation of metal atom clusters on single crystal surfaces, so that care must be taken in applying these models to condensing atmospheric gases on polycrystalline and coated surfaces. Yet with judicious estimation of parameters, resultant rate expressions can aid in developing an understanding of the physical processes which occur during condensation.

The first consideration that arises when describing how gases deposit on surfaces, concerns the difference between nucleation-induced and true thermodynamic condensation (i.e., that condensation which occurs when the pressure experienced by the surface equals the sublimation vapor pressure at the surface temperature). Bently and Hands (1978) have considered the physical parameters which control nucleation under these conditions. The following parameter designations from this work will be used in the ensuing discussion: E_2 is the energy of attraction between two adsorbed molecules (related to the sublimation energy, i.e., E_2 generally increases with increasing

sublimation energy); E_a is the energy of adsorption onto the base substrate; and E_a' is the energy of adsorption of a molecule onto a layer of its own species, a quantity which is also dependent on E_2, the deposit layer thickness, and the type of adsorption site. Three condensation regimes arise from this formulation (Bently and Hands, 1978):

I. $E_a' \leq E$ - In this case bulk deposition proceeds via true thermodynamic condensation (Venables and Price, 1975, Voorhoeve, 1976). Here the adsorption energy is dominant, and the adatoms favor growth by first forming a stable monolayer, followed by successive layering on top of the base layer. It is noted that the crystalline structure can assume different morphologies, depending on the nature of the particular species and deposition conditions. It is even possible for the morphology to change with increasing film thickness, depending on the relative magnitude of interaction between species in the deposit, and the change in the value of E_a' with the addition of subsequent layers (Bently and Hands, 1978).

II. $E_a' > E_a$, or the stronger condition $E_2 > E_a$ - In this case, the interaction between adsorbed species is dominant, and the solid is formed by nucleation and growth (Venables, 1973). Deposition no longer occurs at the sublimation pressure, but at supersaturated values; i.e., when the pressure is significantly greater than the sublimation pressure of the species at the temperature of the surface. In this regime, adatoms adsorb and desorb from the surface, diffuse across it, and eventually form supercritical and stable clusters (Figure 3.2-1). Clusters larger than a given critical size are stable, because it is

energetically more favorable for them to grow than to dissociate. Growth can occur by adatom diffusion, or by direct impingement from the vapor phase. Cluster growth in this manner is strongly temperature dependent, and much of the following focuses on the development of rate expressions to describe this phenomenon.

III. The third regime of deposition is sometimes called the Stranski-Krastonov growth mode (Voorhoeve, 1976, Bauer and Poppa, 1972) in which the initial deposition is type I (i.e., thermodynamic), but if, as the deposit grows, the value of E_a' decreases below that for an infinite crystal, after a finite number of layers, the process then changes to nucleation on top of the strongly bound layers. Voorhoeve (1976) explains that this is often the case when the potential wells associated with E_a and E_a' are of approximately the same depth, while the lattice parameter of the substrate is quite different from that of the condensed phase. When this occurs, strong adsorption sites exist on the surface (called traps), which act as a barrier to surface diffusion and nucleation until they are filled. Once filled, nucleation controls. This author also notes that there is the possibility of competition between nuclei formation and adlayer growth, which adds to the complexity of the system. This type of growth has been experimentally observed for silver and gold on a Si(111) surface, and for alkali metals deposited on tungsten (Bauer and Poppa, 1972). In a nucleation study of CO_2 on an ice (H_2O) substrate, Cazcarra et al. (1973) found the capture coefficient to exhibit a minimum with increasing CO_2 coverage, which indicates a type III growth mode. Venables and Ball (1971)

found this effect for Xe, Kr, and Ar on amorphous carbon as well as graphite; i.e., nucleation did not occur until a strongly bound sublayer was formed. It was later conceded, however, (Venables and Price, 1975, Price and Venables, 1975) that for the case of graphite, type III nucleation was probably due to surface contamination. Thus nucleation and growth may occur on a strongly bound layer of adsorbate rather than initially on the metal surface itself.

There are basically two theories of heterogeneous nucleation. In the classical theory, nuclei are considered as small droplets, and the focus of the development is on the relationship between bulk and surface free energy. This method is usually applied to nuclei of 100 molecules or more, assumes a critical supersaturation below which nucleation does not occur, and also assumes growth via the creation of stable nuclei.

In the atomistic approach, attention is focused primarily on the detailed microscopic kinetics (i.e., the rates of adsorption, desorption, and surface diffusion), and the bond energies involved in forming stable clusters. The formation of stable nuclei and their subsequent growth are considered as the initiation steps for bulk deposition.

In an early atomistic analysis, Walton (1962) pointed out one of the primary problems associated with classical analysis; viz., that in many cases the critical cluster size can be as small as one to ten molecules, for which the use of bulk values for surface energy is quite questionable. For example, for cluster sizes less than six, all the molecules are located essentially at the surface of the cluster, and the difference

between "bulk" and "surface" becomes ambiguous, at best. It is also obvious that with the addition of each subsequent molecule in the cluster, significant changes in structure and physical properties can occur. Evidence is presented by Taylor et al. (1974) that photoionization appearance potentials for methanol clusters irradiated by ultraviolet light are dependent on cluster size. In similar work on photoionization of alkali metal atoms, Foster et al. (1969) note that the most striking feature of their measurements was the large reduction of the ionization potential of three and four atom clusters relative to the monomer, and the trend of the potential to approach the work function of the metal at larger cluster sizes. Briant and Burton (1975), modeling homogeneous nucleation of argon atoms noted that surface energies of microclusters are strong functions of cluster size, and that argon clusters of size 7, 13, 55, and 100 undergo a process similar to a first order transition upon melting, whereas clusters of other sizes do not. Thus the problem then becomes one of judging exactly when bulk properties are applicable.

A theoretical treatment of the effect of cluster size on the free energies of microclusters in the 2 to 100 atom range is given by Griffin and Andres (1979). Their treatment suggests that an improved estimate of cluster free energies can be obtained by a microscopic capillarity approximation in which the free energy of the trimer is used as the base estimate, with correction terms added for the bulk contribution of the other (i-3) atoms, as well as for the increased surface energy due to the increased area of the i atom cluster. It must be noted, however, that

this treatment is for the homogeneously nucleated cluster, and does not apply to heterogeneous systems which are the focus of the present work.

With the advent of electron microscope studies of rare gas nucleation (Venables and Ball, 1971), data on saturated cluster density has confirmed the advantages of atomistically-oriented analyses for heterogeneous nucleation. The technique of using mass spectrometric monitoring of reflected molecular beam intensities during the initial stages of nucleation, where the physical situation is still relatively simple, has also been applied to this problem. Using an atomistic approach, Bently and Hands (1978) determined that stable cluster growth is the dominant adatom capture mechanism for carbon dioxide nucleation on a gold-flashed, stainless steel surface. Thus it was proven that the classical approach, which stresses critical nuclei formation as the primary sink for adatoms, does not adequately represent the actual physical situation.

Heterogeneous Nucleation Rate Model

Approximations

Several assumptions must be made in order to develop a workable heterogeneous nucleation rate model. Following the example of Routledge and Stowell (1970), an early modeling study, we assume the following:

(1) Only adatoms are mobile on the surface. Cluster mobility is negligible in comparison.

(2) Cluster growth and decay occurs by capture and loss of single molecules, and growth by coalescence occurs only when the immobile clusters attain overlapping boundaries.

(3) Only single molecules desorb from the substrate.

(4) There are no preferential sites; all sites are equivalent for adsorption. (A treatment of adsorption on preferred sites is given by Stowell and Hutchinson, 1971 (a)).

(5) The concentration of subcritical clusters exists at steady state.

(6) Cluster islands are hemispherical in structure.

(7) Distributions of stable cluster sizes are not considered (i.e., once the cluster size exceeds the critical, an average size is used).

(8) Critical cluster configurations are assumed (discussed subsequently in this section).

As previously described, condensation experiments are carried out while varying the surface temperature in a controlled fashion. The wide variation in surface temperature allows for two regimes of condensation. The first, incomplete condensation, occurs at relatively high temperatures, where the adatom population is controlled by the rates of adsorption and desorption as described by

$$\tau = \upsilon_o^{-1} \exp\ (E_a/kT) \qquad (3.2\text{-}1)$$

where τ is the average adatom residence time on the surface, υ_o is the vibrational frequency of the adatom on an adsorption site, and E_a is the adsorption energy. If we set R equal to the beam intensity (molecules area^{-1} time^{-1}), then for incomplete condensation,

$$n_1 = \tau R \qquad (3.2\text{-}2)$$

where n is the adatom concentration on the surface (molecules area^{-1}). Note that this implies that all molecules which impinge on the surface are accommodated and adsorbed for some average period of time. It has been experimentally shown (Bently and Hands, 1978) that the nucleation process proceeds independently of the beam energy and angle of incidence for properly normalized beam intensities. Thus an adsorbed molecule accommodates rapidly enough to render its previous vapor phase history unimportant, and intensity becomes the primary beam parameter.

When τ is large in comparison to the time scale associated with diffusion and incorporation into a stable cluster, complete condensation occurs. This usually takes place at relatively low temperatures, where most of the incident adatoms are captured and complete condensation of the incident beam is achieved.

In order to apply the atomistic approach, the equilibrium critical cluster density on the surface must be related to the binding energy and to surface parameters. Walton (1962) approached this problem by considering the partition function for the arrangement of n atoms into n_1 single atoms, n_2 pairs, etc. Setting C_i equal to the number of orientations of a cluster of size i on a single adsorption site, and ε_i equal to the potential energy of a cluster of size i, it was determined that

$$Q = A\sum_{n_i i}\pi \; (1/n_i!) \; (C_i N_o \exp(\varepsilon_i/kT)) \qquad (3.2\text{-}3)$$

where Q is the partition function, N_o is the adsorption sites per unit area, and A is a constant. With the following assumptions:

(a) The most probable distribution is that with the largest term in the summation.

(b) $C_i = 1$ (i.e., that one orientation of the cluster on the surface is preferred).

(c) The concentration of adatoms is much greater than that of clusters on the surface (i.e., n) equation (3.2-3) simplifies to

$$(n_i/N_o) = (n_1/N_o)^i \exp (E_i/kT) \qquad (3.2\text{-}4)$$

where E_i is the net increase in potential energy upon formation of an i-sized cluster. In this manner, the equilibrium concentration of clusters of size i can be related to: temperature, T; the number of adsorption sites on the substrate per unit area, N_o; and parameters associated with cluster size and configuration.

As mentioned previously, stable clusters are efficient sinks for the surrounding adatom population. Thus a nucleation rate model must account for depletion of adatoms about the stable cluster, as well as their diffusion and capture rate on the surface. If n_1 (r,t) is defined as the adatom concentration surrounding a stable cluster, where r is radial distance and t is time, its value may be calculated by solving the diffusion equation with the appropriate boundary conditions:

$$D\nabla^2 n_1 - (1/\tau)n_1 + R = \partial n_1/\partial t \qquad (3.2\text{-}5)$$

If a capture number, σ_k, is defined such that diffusion to, and capture by a k-sized cluster is denoted by $\sigma_k n_1 D$, then this can

be related to the adatom distribution about the cluster via

$$\sigma_k n_1 D = 2\pi r_k D (\partial n_1/\partial r)_{r=r_k} \qquad (3.2\text{-}6)$$

where r_k is the radius of a cluster of size k. Therefore, the capture number, σ_k, is given by

$$\sigma_k = (2\pi r_k/n_1)\ (\partial n_1/\partial r)_{r=r_k} \qquad (3.2\text{-}7)$$

Thus if $n_1(r,t)$ is known, a convenient form for expressing cluster growth by adatom capture is available.

For the simplified boundary conditions:

$$n_1(r_k)=0, \text{ (at the cluster boundary)} \qquad (3.2\text{-}8)$$

$$n_1(r_\infty)=R, \text{ (at large distances from the boundary)}$$

Venables (1973) presents the following steady state solution to the diffusion equation:

$$n_1(r) = R\tau\ (1-K_o\ ((r^2/D\tau))^{.5}/K_o(r_k^2/D\tau)^{.5}) \qquad (3.2\text{-}9)$$

from which

$$\sigma_k = (2\pi r_k/(D\tau)^{.5}) K_1((r_k^2/D\tau)^{.5})/K_o((r_k^2/D\tau)^{.5}) \qquad (3.2\text{-}10)$$

where K_o and K_1 are Bessel functions of the second kind of orders zero and one, respectively. Actually, however, σ_i and σ_k, for critical and stable clusters, respectively, are required when n_1 is not equal to $R\tau$ at large distances, and the exact location and size of stable clusters on the surface is not known.

In considering this problem, Stowell (1972) used a lattice approximation with which an approximate solution is found by placing clusters in a contrived set of lattice positions on the metal surface. It was found that σ_x is a function of the coverage,

Z ($=n_x a_x$, where a_x is the average cross sectional area of a stable cluster); viz.,

$$\sigma_x=4\ \pi(1-Z)/(\ln(1/Z)-(3-Z)(1-Z)/2), \qquad (3.2\text{-}11)$$

and, in the complete condensation limit (Routledge and Stowell, 1970)

$$\sigma_k=4\pi(1-Z_k)(L_k^2/L^2)/(\ln(1/Z)-(3-Z)(1-Z)/2), \qquad (3.2\text{-}12)$$

where L_k is determined implicitly from

$$(L_k/L)^2(\ln(L_k/r_k)^2-(1-(r_k/L_k)^2))=\ln(1/Z)-(1-Z), \qquad (3.2\text{-}13)$$

and $L^2 n_x=1$, $Z_k=\pi n_x r_k^2$, n_x is the number of average size clusters (x) per unit area, and r_k is the radius of a cluster of size k. Thus the diffusion problem about the cluster is treated by defining the capture number in terms of the adatom concentration gradient, and solving the diffusion equation numerically.

Development of the Rate Equations

Development of the generalized heterogeneous nucleation rate equations are described by Venables (1973) in a comprehensive manner. If n_1 is defined as the adatom population on the surface (molecules area^{-1}), n_x as the stable cluster surface population, i as the number of adatoms in a stable cluster, and U_1, U_j, and U_x as the rate, at which single atoms join pairs, j+1, and stable clusters, respectively, then the time rates of change of n_1, n_j, and n_x are given by:

$$\dot{n}_1=R-n_1/\tau-2U_1-\sum_{j>1}^{i} U_j-U_x, \qquad (3.2\text{-}14)$$

$$\dot{n}_j=U_{j-1}-U_j, \quad (1\leq j\leq i), \qquad (3.2\text{-}15)$$

$$\dot{n}_x = U_j - U_c, \text{ (for } j=i) = U_i - U_c, \tag{3.2-16}$$

where U_c is the rate of coalescence. As stated previously, an equilibrium concentration of subcritical clusters is assumed, and thus $\dot{n}_j = 0$. If it is also assumed that U_1 and U_j are small in comparison to the rate of formation and growth of stable clusters, (i.e., U_x is the rate of growth of all stable clusters, not one multimer species only) then

$$\dot{n}_1 = R - n_1/\tau - U_x \tag{3.2-17}$$

$$\dot{n}_x = U_i - U_c \tag{3.2-18}$$

In order to develop an expression for U_x, consider a stable cluster of size k, with radius r_k, covering substrate area a_k. A specific number of beam molecules will impinge directly on a cluster from the gas phase and be captured by it, rather than by unimolecular adsorption on the surface. Thus the expression, $Rn_k a_k$, represents the number of molecules impinging on the surface per unit area, multiplied by the percentage of the surface area covered by k-sized clusters. The diffusion of adatoms to the clusters can be described by $\sigma_k D n_1 n_k$, or the rate of adatom capture per cluster multiplied by the number of k-sized clusters. Thus, for <u>all</u> stable clusters

$$U_x = \Sigma_k (\sigma_k D n_1 n_k + a_k R n_k) \tag{3.2-19}$$

Selecting σ_x and a_x as suitable averages,

$$U_x = \sigma_x D n_1 n_x + R a_x n_x \tag{3.2-20}$$

By similar reasoning,

$$U_i=\sigma_i D n_1 n_x+\Sigma_k\Sigma_\ell \sigma_{k\ell} n_k n_i (D_k+D_\ell) \quad (3.2\text{-}21)$$

where ℓ and k vary between 1 and i, and $\ell+k>i$. Since it has been assumed that D_k and D_ℓ are << D (i.e., the clusters have negligible mobility) the second term of equation (3.2-21) is small in comparison to the first, and thus

$$U_i \tilde{=} \sigma_i D n_1 n_i \quad (3.2\text{-}22)$$

Employing Walton's (1962) expression for the equilibrium critical cluster density (i.e., eq. (3.2-4)), eq. (3.2-22) becomes:

$$U_i=\sigma_i N_o^{1-i} D n_1^{i+1} \exp(\beta E_i) = D n_1^{i+1} \quad (3.2\text{-}23)$$

where $\beta=1/kT$.

The next step in the development is the formulation of an expression for the rate of cluster coalescence, or equivalently, the rate at which cluster boundaries intersect. For a spherical cluster, it can be shown (Venables, 1973) that for clusters of radii r_k and r_ℓ,

$$U_c=1/2\Sigma_k\Sigma_\ell n_k n_\ell (d/dt)(\pi(r_k+r_\ell)^2), \quad (3.2\text{-}24)$$

i.e., the coalescence rate is proportional to the time rate of change of a circle the radius of which is defined as the sum of the radii of the two clusters. If the simplification,

$$\pi(r_k+r_\ell)^2=4\pi r_x^2=4a_x \quad (3.2\text{-}25)$$

is included, then eq. (3.2-24) becomes

$$U_c=n_x^2 (d/dt)(2a_x) \quad (3.2\text{-}26)$$

Vincent (1971), using a more sophisticated analysis, found that

$$U_c=2n_x(dZ/dt) \tag{3.2-27}$$

Since $Z=n_x a_x$, eq. (3.2-27) is equivalent to eq. (3.2-26) if $\dot{n}_x=0$, or if $2n_x\dot{Z}>>Z\dot{n}_x$, which is generally true in the regime where coalescence is important. Thus

$$\dot{n}_1=R-(n_1/\tau)-(\sigma_x Dn_1+Ra_x)n_x \tag{3.2-28}$$

and

$$\dot{n}_x=(1-Z)^{-i}\ \gamma_i Dn_1^{\,i+1}-2n_x Z \tag{3.2-29}$$

where $D=.25\nu_o N_o^{-1}\exp(-\beta E_d)$.

In order to solve the resultant model, a method must be found to calculate Z, the surface coverage. If w_x is defined as the mean number of atoms in a stable cluster, then $d(n_x w_x)/dt$ is the time rate of loss of single adatoms, which has already been defined by eq. (3.2-28) for $\dot{n}_1$, as

$$d(n_x w_x)/dt=(\sigma_x Dn_1+Ra_x)n_x \tag{3.2-30}$$

If the cluster is hemispherical and composed of molecules with atomic volume Ω, then

$$w_x=2\pi r_x^{\,3}/(3\Omega) \tag{3.2-31}$$

and since $a_x=\pi r_x^{\,2}$,

$$a_x=w_x^{\,2/3} \tag{3.2-32}$$

Thus, eq. (3.2-30) becomes

$$(2/3\sqrt{\pi\Omega})d/dt(Z^{1.5}/n_x^{.5})=(\sigma_x Dn_1+Ra_x)n_x, \tag{3.2-33}$$

and therefore,

$$(dZ/dt)(1-(1/3)(d\ \ln\ n_x/d\ \ln\ Z)=\Omega(\pi n_x/Z)^{.5}(\sigma_x Dn_1 n_x+RZ) \tag{3.2-34}$$

Since the time scale for the capture coefficient experiments is much greater than the value of τ, $\dot{n}_1=0$ (for $t>>\tau$) and

$$n_1=R\tau(1-Z) \tag{3.2-35}$$

$$\dot{n}_x=(1-Z)\gamma_i D(R\tau)^{i+1}-2n_x\dot{Z} \tag{3.2-36}$$

$$\dot{Z}=(\pi\Omega R)^{.5}(n_x/Z)^{.5}(\sigma_x Dn_x\tau(1-Z)+Z)/(1-m/3), \tag{3.2-37}$$

where $m=d(\ln n_x)/d(\ln Z)$. Equations (3.2-35) to (3.2-37) are the final expressions which must be solved simultaneously, with appropriate initial conditions to yield n_x and Z as a function of time and temperature.

Venables (1973) found that integration along Z rather than t was the more efficient way to solve these equations. In dimensionless form equations (3.2-36) and (3.2-37) become

$$\overset{*}{N}=((1-Z)\sigma_i B_i(A/(1+\sigma_x AN))^{i+1}\overset{*}{T}-2N, \tag{3.2-38}$$

and

$$\overset{*}{T}=(1-ZN/\overset{*}{N})/((\pi\Omega^2 N_o^3)^{.5})(Z/N)^{.5}((1+\sigma_x AN)/(Z+\sigma_x AN)), \tag{3.2-39}$$

respectively, where

$$n=n_x/N_o,$$

$$T=Rt/N_o,$$

$$A=D\tau N_o$$

$$B_i=(R/N_o^2 D)^i \exp(\beta E_i),$$

$\overset{*}{N}=dN/dZ$, and $\overset{*}{T}=dT/dZ$

If R_s is the fraction of the incident flux which is permanently captured, then

$$R_s=R-n_1/\tau \tag{3.2-40}$$

represents continuity between what impinges on the surface and what is captured. Substituting eq. (3.2-28) for n_1 while assuming a psuedo-steady-state of monomer (i.e., $\dot{n}_1=0$)

$$R_s=R(1-(1-Z)/(1+\sigma_x Dn_x \tau)) \qquad (3.2-41)$$

or in terms of the percentage decrease in the reflected flux (an observable experimental quantity),

$$1-(R_s/R)=(1-Z)/(1+\sigma_x AN) \qquad (3.2-42)$$

Equation (3.2-42) relates N and Z calculated from the kinetic rate expressions to an experimentally observable quantity. Thus the application of this model, with reasonable estimates of N_o, ν, E_a, E_d, and E_i can be used to examine, correlate, and explain observed condensation phenomena.

One problem which arises in solving the model is in estimating the initial conditions. Recalling that the actual experiment involves the cooling of a surface in a controlled fashion while a molecular beam impinges on it at constant intensity, an appropriate initial condition involves deposition in the higher temperature, incomplete condensation regime. Stowell and Hutchinson (1971), and later Stowell (1972), have considered this problem. For nucleation at relatively high temperature, adatom depletion by stable clusters is negligible, and thus three-dimensional cluster growth is almost entirely due to impingement from the vapor phase. Under these conditions,

$$n_x=\eta(Z)F^{2/3} \qquad (3.2-43)$$

where

$$F=N_o^{1-i}(\sigma_i \exp(E_i/kT))DR^i\tau^{i+1}/(\Omega\sqrt{\pi}) \qquad (3.2\text{-}44)$$

and

$$\eta(Z)=(\sqrt{3}/6)(7(\exp(-3Z)\int_o^{\sqrt{32}} \exp q^2\, dg)-(3Z)^{.5})^{2/3} \qquad (3.2\text{-}45)$$

which is known as Dawson's integral. Solving for the maximum in n_x, which is the saturation cluster density N_{xs}, it is found that

$$N_{xs}=0.61(\sigma_i N_o^{2.5-i} R^i D\tau^{i+1} \exp(E_i/kT))^{2/3} \qquad (3.2\text{-}46)$$

At the temperatures under consideration, this saturation density is very low and occurs during a much shorter time span than that resolvable in the experiment (i.e., on the order of seconds). Thus it can be used to calculate an initial value of n_x at temperatures higher than those of interest, and then the full equations can be integrated down in temperature, in the region where this equation does not apply. The initial coverage value may be calculated by assuming that at these high temperatures, most stable nuclei are just above critical size, which gives $Z_o=n_{xo}a_{xo}$.

Bently and Hands (1978) developed a simplified atomistic nucleation model, which is particularly relevant to the current work. Their development centered on the derivation of an expression for U_i, the rate of growth of critical sized clusters, by assuming this growth is limited to accretion via surface diffusion of monomer only, and then solving the diffusion problem, presented earlier in this section, by assuming the monomer gradient is given by n_1/a to the first approximation, where a is a diffusional "jump" distance. By defining a critical temperature, T_c, at which it was claimed that nucleation, and thus formation

of critical and stable clusters, becomes important, and by ignoring cluster coalescence, the expression for U_i was integrated backwards in time, (recalling, as in eq. (3.2-18), that $\dot{n}_x=U_i$ when $U_c=0$). This corresponds to integrating upward in temperature to an upper limit (which the authors estimated as T_c + 5K), where U_i is negligible, to obtain n_{xc}, the stable cluster concentration at the critical temperature.

It must be noted here, however, that as discussed in Venables (1973) and Stowell and Hutchinson (1971), increasing the temperature not only reduces the concentration of critical clusters, but also changes the regime of condensation. The assumptions of Bently and Hands (1978) place their value of T_c at the onset of the regime of complete condensation. Thus, when the temperature is increased, the regime changes to incomplete condensation, and then to extremely incomplete condensation, where depletion of adatoms about the growing clusters by diffusion is not the major growth mechanism. In these two higher temperature regimes, growth by direct beam impingement becomes an increasingly important mechanism for formation of both stable and critical clusters. This mechanism was ignored in the development of Bently and Hands (1978). The present work circumvents this problem by initializing the numerical integration of a more complete model (equations (3.2-38) and (3.2-39)) at elevated temperatures with an approximate solution which is valid in the incomplete condensation regime (equation (3.2-46)), and then the full model to simulate entry into the complete condensation regime. By failing to take this into account, the development of Bently and Hands (1978) introduces some inaccuracy

in the formulation of n_{xc}. Also, once n_{xc} was found, U_{xc} was calculated, again ignoring growth by impingement, and also oversimplifying the diffusion problem by assuming a constant value for the capture coefficient, σ_x. These authors prove that $U_x >> U_i$, as originally assumed in Venables (1973) and develop a simplified expression relating the beam intensity to the critical temperature, T_c; viz.,

$$\ln R_c = \frac{\ln G + i \ln(N_o \nu)}{i+1} - \frac{E^* - E_d}{k(i+1)} \frac{1}{T_c} \qquad (3.2\text{-}47)$$

where

$G = N_o i E^* C / \omega_o k T_c$

ω_o = diffusion frequency factor, $\tilde{=} \nu$

C = surface cooling rate K_s^{-1}

α = % change in detector signal/second at the onset of condensation (T_c)

and $E^* = E_i + (i+1) E_a - E_d$

Equation (3.2-47) is convenient for fitting to data using a slope-intercept technique, if, as was found, $\ln G << i \ln(N_o \nu)$. Consequently, i can be obtained from the intercept of a linear plot of $\ln R_c$ vs. $1/T_c$, and E_a from the slope, if values for both E_i and E_d are assumed.

The entire approach, however, is deficient in several respects. As mentioned, the procedure for calculating n_{xc} ignores the transitions in the condensation regimes. The diffusion problem is oversimplified, and the expression for U_i is, according to Bently and Hands, admittedly "very approximate".

The concept of a critical temperature forces one to extrapolate the data to the very instant of deviation from the baseline, which is often difficult to do. Also, the authors never show a direct comparison of their resultant approximation to a numerical solution of the full model. The present development, on the other hand, allows simulation of the initial transition to nucleation - initiated condensation. The model of Bently and Hands is compared to the current work in the section on the "true" condensation, and will be seen to yield somewhat different predictions than the more complete model used here.

In this section, it has been shown that using reasonable assumptions, heterogeneous nucleation can be approximately modeled to relate microscopic variables to experimentally observable effects. Thus applying this model to heterogeneous nucleation of atmospheric gases, with attention to parameter estimation, can aid in developing insight into the condensation process. Results of such calculations are discussed in subsequent sections.

Figure (3.2-1)

Heterogeneous Nucleation

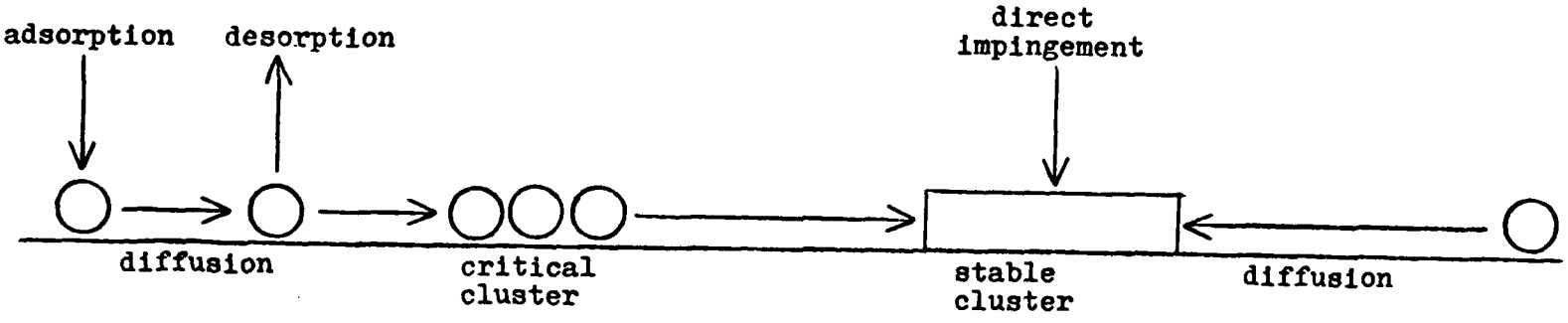

3.3 THE "FIRST CONDENSATION"

Early Experiments

The original technique applied to studies of cryogenic deposition, or "cryopumping", processes involved the addition of the species of interest to the gas phase of a vacuum chamber in a non-directed fashion with respect to the cryogenic surfaces, while monitoring the partial pressure of the species with a mass spectrometer or ionization gauge (in the case of a single species). The frequency of collisions with the cryogenic surfaces was determined from kinetic theory considerations. The decrease in gas phase partial pressure upon condensation was assumed indicative of, and used to characterize the attendant phenomena.

During some of these experiments an unexpected or spurious condensation was often observed; i.e., a very strong adsorption in the 260-210K temperature range condensing approximately 90% of the gas phase. This phenomenon was also observed in the present work for CO_2, N_2O, NO, Freon 11, and Freon 12, on both 304 stainless steel and gold-flashed, stainless steel surfaces. The current section deals with the analysis of this phenomenon.

Data typical of this condensation phenomenon are presented in Table (3.3-1), which lists calculated collision intensities (R) and temperatures at which spurious condensation begins to occur for N_2O on a gold-flashed, stainless steel surface. Figure (3.3-1) is a plot of N_2O partial pressure in the vacuum chamber (mass peak 44) as a function of surface temperature between 300 to 60K, for three different intensities: low (run 130), moderate (run 131), and high (run 135). It should be

noted that in all three experiments the initial slope is negative. The low intensity data (run 130) exhibit a sharp break in residual partial pressure as the surface temperature decreases to 250K, and then drops more than an order of magnitude over a 15K temperature range. The medium intensity run (131), however, exhibits a slight peak before it decreases, which, as will be discussed in the nucleation kinetics section concerned with the Stranski-Krastonov growth mode, could be indicative of a transition in the surface capture mechanism; i.e., a strongly bound layer adsorbing first, and then saturating, at which point a second capture mechanism, in this case a more powerful one, controls. The high intensity case (run 135), exhibits the same saturation peak, followed by a second peak towards the end of the condensation (247K), possibly due to phase change or cryofrost matrix rearrangement. This case also exhibited slight oscillations between 220 and 200K, soon after the onset of the strong adsorption. Note that for all three runs, a second condensation occurs in the 75-85K range, where true thermodynamic condensation normally would be expected.

Figure (3.3-2) presents the temperature at which the spurious condensation begins as a function of the background intensity. The trend observed is clearly that this temperature decreases as the intensity increases. Since the intensity at condensation is proportional to the vapor pressure of the species on the substrate, this implies that the vapor pressure increases with decreasing temperature, contrary to thermodynamics. Thus this spurious first condensation seems to be more complex than the more conventional thermodynamic process, and occurs at a

temperature and pressure at which N_2O would not normally condense. In what follows, this phenomenon will be referred to as the "first condensation", for obvious reasons. The second condensation, however, occurs at approximately the expected temperature range based on vapor pressure. Thus the second condensation will be called the "true condensation".

In this chapter, analysis of results pertaining to condensation experiments is divided into two subsections. The first presents experimental observations, analysis, and relevant literature citations directed at understanding and explaining the "first condensation" adsorption process. The second part examines the "true condensation" in terms of rates, mechanisms, and values of surface and cryofrost parameters. It is emphasized that the "true condensation" often occurs on top of a "first condensation" sublayer. The effects of this sublayer on the "true condensation" mechanism are also explored.

Experimental Configurations

Based upon the previously described experiments, it was decided that a directed molecular beam source would facilitate the analysis, since a beam with known characteristics (e.g., velocity and intensity distributions, etc.) would be more amenable to a systematic study of the first condensation phenomenon. Such a system also allows differentiation between reflected and background sources of the same species. Thus a 1 mm I.D. tube was installed 5 mm from the cryosurface, as previously described in Chapter 2. As also previously indicated, this source was found to be effusive (i.e., a constant intensity profile on the surface of a hemisphere centered at the source, with a thermal velocity distribution).

In order to reduce the background pressure below that routinely attainable with the diffusion pump, a stainless steel, ribbed, flexible hose was installed, as noted in the apparatus description. This tube served as a cryogenic pumping surface, when filled with liquid nitrogen from an overhead reservoir, for species condensable at temperatures greater than 77K at the chamber pressure (e.g., CO_2, N_2O, F11, F12, and unidentified condensable contaminant species). In use, it usually decreased the background pressure during a condensable gas experiment by approximately one order of magnitude. This cryopumping system will be referred to as the LN_2 cryopump.

The quadrupole mass spectrometer electron impact ionizer head was located 0.94 inches from the cryosurface, the closest possible spacing consistent with apparatus constraints. Thus with a directed beam of known intensity distribution, additional pumping capacity supplied by the LN_2 cryopump, and an ionizer head located close to the surface, background effects could be assessed more readily.

Experimental Results

Since the thermodynamic properties of CO_2 and N_2O are quite similar (e.g., heat of vaporization and vapor pressure), they are discussed together first. Tables (3.3-2) and (3.3-3) give values of beam intensity, R, first condensation temperature, T (i.e., the temperature at which the mass spectrometer first deviates significantly from steady-state values), and percent reduction in mass spectrometer signal calculated at the bottom of the steep decline caused by the first condensation, and the fractional intensity captured, R_s, as a function of both the gold-

flashed and hexamethyldisilazane (HMDS)-coated surface, for experiments run with LN_2 cryopumping, for CO_2 and N_2O, respectively. It can be seen that for these data the condensation temperature no longer decreases with increasing intensity, but seems to be scattered in the range of 241 to 224K for both species. This implies that the first condensation temperature is a function of several parameters, beam intensity being only one, and that cryopumping seems to affect more than one. It will be subsequently observed that variation of the background pressures of CO_2 or N_2O, along with cryopumping of residual water vapor, are pertinent to these results.

Figures (3.3-3) and (3.3-4), for CO_2 and N_2O, respectively, present the logarithm of the fractional intensity of the beam which condenses when the first condensation is at its steady-state level (e.g., percent reduction in mass spectrometer signal multiplied by the incident beam intensity) versus the logarithm of the incident beam intensity. Thus the 45° line represents 100% condensation of the incident beam during the first condensation. For both species, data for the gold-flashed surface lie significantly below that for the HMDS-coated surface. Also, as the beam intensity increases, the efficiency of the first condensation in trapping gas molecules begins to decline (i.e., the data moves away from the 45° line). These data also imply that for both gases on the HMDS-coated surface, the fractional intensity which condenses approaches an asymptote, indicating that there may be a limit to the adsorption capacity of the first condensation as a function of increasing beam intensity; i.e., an absolute limit to the accommodation rate of the first condensation.

In fact, data obtained with both LN_2 cryopumping and the HMDS-coated surface show that an absolute saturation of the first condensation is possible. Figure (3.3-5), a plot of mass spectrometer signal (peak 44) versus surface temperature for CO_2 (run 195), is typical of these observations. Here the first condensation occurs at 241K and the mass spectrometer signal returns to its original value at 116K; i.e., at 116K the first condensation appears to have saturated. Another significant feature is that between 88 and 70K, a second drop occurs followed by a break point at 70K where the signal drops precipitously. It is believed that the second decline (88-70K), after saturation of the first condensation, is due to a process similar to the first condensation, and that the break at 70K is due to the onset of the true condensation. These features (i.e., saturation of the first condensation followed by a two stage drop in signal) occur for both CO_2 and N_2O on the HMDS-coated surface with LN_2 cryopumping.

Tables (3.3-4) and (3.3-5) pertain to the saturation effect on the HMDS-coated surface for CO_2 and N_2O, respectively. In these two tables are listed the beam intensity and amount captured between the onset of the first condensation and either the saturation of this effect or the onset of the true condensation. For both CO_2 and N_2O, saturation occurs at high intensity, while low intensity runs do not saturate. While there is no sharp demarcation between absolute amounts of deposit that will and will not cause saturation, the range for the transition is relatively narrow between 0.93×10^{19} to 1.1×10^{19} molecules for CO_2 (runs 197 and 194) and 6.7×10^{18} to 7.2×10^{18} molecules (run 200 and

201) for N_2O. Thus for the HMDS-coated surface, saturation of the first condensation can occur - - an effect which will be discussed further subsequently.

The behavior of nitric oxide (NO) is examined next. Table (3.3-6) gives results for NO on both gold-flashed and HMDS-coated surfaces, in terms of fractional intensity captured in the first condensation as a function of beam intensity, R_s, as well as the surface temperature, T, at the onset of the first condensation. From these data, the first condensation temperature appears to be an increasing function of intensity in the 216 to 230K range. Figure (3.3-6) is a plot of fractional intensity captured as a function of beam intensity. The fact that all the points are close to the 45° line, signifies that the first condensation capacity is quite high for NO. Also, unlike CO_2 and N_2O, there is no apparent difference between the gold-flashed and HMDS-coated surface for NO, and deviation of the data from the 45° line, apparent at the higher beam intensities for CO_2 and N_2O, is practically nonexistent for NO.

It is natural at this point to examine the properties of NO, in comparison to CO_2 and N_2O, which could account for these observed differences. At the vacuum chamber operating pressure (approximately 10^{-5} torr), NO does not condense at 77K on the LN_2-filled tubing, while CO_2 and N_2O do. Thus one possibility is that background species have higher capture coefficients than beam species. Thus by limiting the background in the case of CO_2 and N_2O, the resultant data reflects directed molecules only, whereas for NO, the data reflect the accommodation of both

directed and a relatively large fraction of background species. Again, this point will be developed more fully in what follows.

Freon 11, which readily condenses on the LN_2 surfaces, exhibited a weak, difficult to distinguish first condensation on the gold-flashed surface. On the HMDS-coated surface, the mass spectrometer signal decreased slowly from 300K to the true condensation temperature. This is illustrated in Table (3.3-7), which lists beam intensity, the percentage decrease in mass spectrometer signal due to the slow decline, and the fractional intensity captured. These data again exhibit the superiority of the HMDS-coated surface in stabilizing the first condensation , in comparison to the gold-flashed surface. It can also be discerned from the data (Table (3.3-7)) that the highest beam intensity run condensed the lowest percentage of the beam for Freon 11, and also for CO_2 and N_2O -- all of which readily condense on the LN_2 cryopump.

Freon 12 condensation experiments represent a special case which must be carefully considered. Due to the high ionization cross section of F12 in the ionization gauge (determined experimentally as discussed in Chapter 2), only low intensities (10^{17} to 10^{18} $m^{-2}s^{-1}$) could be accurately investigated. Since beam intensity is an important parameter affecting the first condensation process, comparison of Freon 12 behavior with that of other species at higher beam intensities is not directly possible. Yet, it was found that with LN_2 cryopumping, which effectively condenses F12 background, no detectable first condensation was observed. Thus the reduction

of F12 in the background, as well as low beam intensity, effectively eliminate the effect. This observation too will be drawn upon in the following development.

Investigations of the condensation behavior of O_2 and N_2 provided an interesting contrast to the behavior of the species discussed thus far. As an example, Figure (3.3-7) presents the mass spectrometer signal versus surface temperature for O_2, with no LN_2 cooling (run 131). A strong first condensation was not observed in the temperature range 260-200K, but, at 217K, the mass spectrometer signal began to oscillate, and continued to do so until the precipitous decrease in signal at 48K. The amplitude of these oscillations was as much as 50% of the mean value. The frequency was 144 $min.^{-1}$ -- the exact frequency of the helium expander which cools the cryosurface. The oscillatory behavior is also observable in the total pressure, as measured by the ionization gauge. These oscillations probably arise as a result of a limited first condensation which occurs on the cold expansion stroke of the refrigerator, followed by condensate evaporation during the compression stroke. The observed evaporation is perhaps due to heat transfer limitations which arise as a result of the transient thermal gradient which develops during the compression stroke. Eventually, however, as shown in Figure (3.3-7), a 'first condensation of sorts does occur at 48K, which is quite close to the true condensation temperature. A signal plateau separates the first condensation from the second, true condensation.

To examine this effect further, LN_2 cryopumping was not used in some O_2 and N_2 experiments. The early oscillation, late

first condensation pattern was typical of O_2 and N_2 on the gold-flashed surface under these conditions, as illustrated in Tables (3.3-8) and (3.3-9), respectively. $T_{osc.}$, (the temperature at which the oscillations begin) does not correlate simply with beam intensity for either gas, nor does the first condensation temperature, T_{fc}, for oxygen on the gold-flashed surface. For nitrogen, however, a plot of the logarithm of the beam intensity versus T_{fc} (Figure (3.3-8)) does suggest a linear relationship with a negative slope, as does the non-LN_2 cryopumped N_2O data. This behavior is contrary to that expected from thermodynamic considerations only. Data were not obtained for O_2 and N_2 on the HMDS-coated surface, because the increased surface emissivity did not allow the cryosurface to attain temperatures below 30K with the mass spectrometer ion source on.

Experiments were performed to determine whether or not the radiation heat load from the mass spectrometer ion source affected the first condensation phenomenon. Runs 170 and 171, (Table (3.3-9)) are data taken with the ionization gauge only, without use of the mass spectrometer. These data were compared with runs employing similar intensities (165 and 167, respectively) but with the mass spectrometer. The results of these comparisons were that the mass spectrometer ionizer did indeed increase the effective heat load on the cryosurface, which affected the cool down curve, (i.e., temperature versus time), but did not significantly affect the first condensation parameters, i.e., T_{fc} and true condensation temperature as a function of beam intensity.

In order to assess the possible effects of LN_2 cryopumping on N_2 condensation, runs 173 and 174 were performed with LN_2 cryopumping, and compared to runs 167 and 165, respectively, of similar beam intensities. From these comparisons it was concluded that LN_2 cryopumping had no significant effect on the N_2 first condensation.

Due to the relatively low pumping speed of the vacuum system (discussed in Chapter 2), along with an inability to bake the cryosurface at high temperatures (imposed by the temperature sensitivity of the silicon diode sensor located on the cryosurface), water vapor was never fully eliminated from the background at zero gas load. It was noted during the course of one experiment that the water vapor background peak was substantially reduced as the cryosurface was cooled, especially at temperatures below 260K. Thus, there is a possibility that background water vapor plays a part in the first condensation process. It must be emphasized that this water vapor contamination is not introduced with the test gas species employed, but rather is residual water arising from thermal cracking of the diffusion pump oil, and is common to all oil diffusion-pumped vacuum systems.

In order to test the hypothesis that water vapor plays a role in the first condensation process, another experiment was devised. For both CO_2 and N_2O, experiments were conducted until immediately prior to, and then just after the onset of the first condensation event (i.e., two experiments for each gas). When these points were attained, the molecular beam and the refrigerator were shut off, and the thermal desorption of CO_2 or N_2O (both monitored as m/e=44), and H_2O (m/e=18) were recorded.

Since the maximum effect was desired, LN_2 cryopumping was not employed.

The first of these experiments involved N_2O on the HMDS-coated surface. The beam and refrigerator were shut off at 245K, immediately after the onset of the "first condensation". The areas under the desorption peaks of N_2O and H_2O, when corrected for ionization efficiency (e.g., see Flaim and Ownby, 1971) and secondary electron multiplier gain (UTi 100C operating manual), yielded a molar ratio of water vapor to N_2O desorbed of $\sim$0.6. When the same experiment was conducted for CO_2, the desorption peak areas, corrected in a similar fashion, resulted in a molar ratio of water vapor to CO_2 desorbed of $\sim$2.74.

In the second phase of these experiments, the refrigerator and beam were halted just prior to the first condensation event, as estimated by the behavior observed during two previous experiments. In run 206 for CO_2, upon thermal desorption, both H_2O and CO_2 were generated, with relative desorption areas as shown in Figure (3.3-9) (the time axes are offset such that the maxima coincide). When the areas under the desorption peaks were calculated, it was found that the water vapor to CO_2 molar ratio was 6.05. A second experiment for N_2O (run 207), conducted in the same manner, revealed that prior to the first condensation, the molar ratio of H_2O to N_2O was 6.61, as illustrated in Figure (3.3-10).

The fact that the molar ratios of water vapor-to-CO_2 and water vapor to N_2O just prior to the first condensation are very similar implies a stoichiometric process. The fact that both values are similar (i.e., ca. 6) suggests that CO_2 and N_2O

AD-A108 255 RESEARCH INST FOR GEODETIC SCIENCES FORT BELVOIR VA F/G 20/12
GAS-SURFACE INTERACTIONS IN CRYOGENIC WHOLE AIR SAMPLING.(U)
MAY 81 J M CALO, R J FEZZA, E J DINEEN F19628-77-C-0071
UNCLASSIFIED AFGL-TR-81-0162 NL

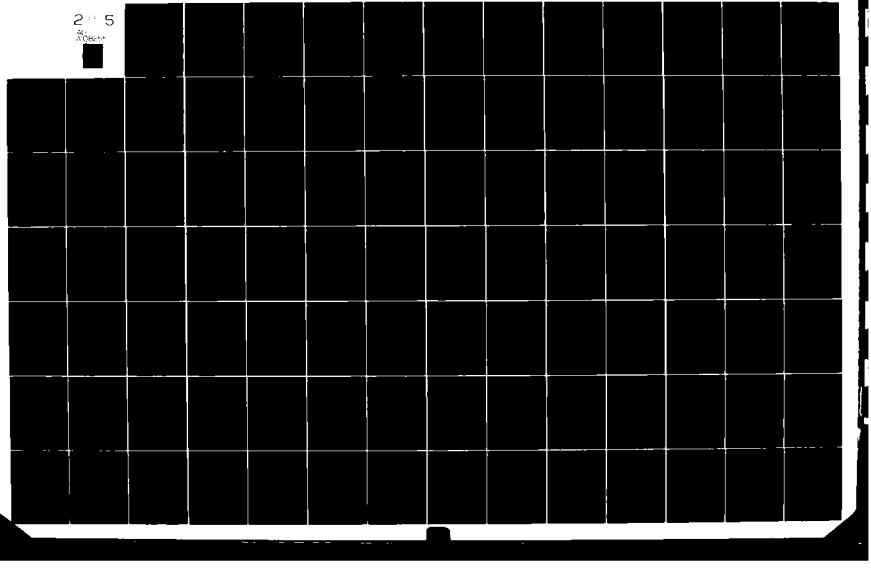

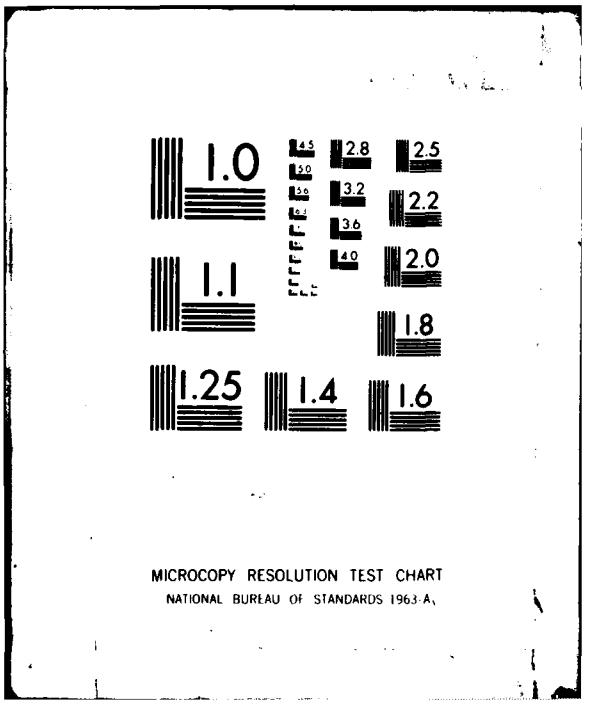
1.0
1.1
1.25
1.4
1.6
1.8
2.0
2.2
2.5
2.8
3.2
3.6
4.0
4.5
5.0
5.6
MICROCOPY RESOLUTION TEST CHART
NATIONAL BUREAU OF STANDARDS 1963-A

may be complexing with water -- perhaps preferentially forming ordered water clathrate structures (Davidson, 1973, Miller, 1973, Siksna, 1973). Immediately after the onset of the first condensation the molar ratio decreases precipitously, implying strong adsorption of CO_2, or N_2O, onto the previously formed sublayer. In order to develop the relationship between the first condensation phenomenon and water further, a closer examination of the theory and properties of water complex clathrates follows.

Clathrate Hydrates

Clathrate hydrates are solid phase structures of water molecules. The simplest form, as described by Siksna (1972), consists of 20 water molecules, arranged in 12 pentagons, forming a dodecahedron with a water molecule at each of the 20 vertices. Included inside of the cage structure is a guest molecule, which stabilizes the structure, as illustrated in Figure (3.3-11). As shown, the water molecules at the vertices of the cage are arranged such that hydrogen bonding is possible between them, linking the cage structure together. This orientation also gives the outer surface of the clathrate an excess charge structure (Siksna, 1973).

From this basic structure, two types of unit cells are possible (Miller, 1973). In structure I, 46 molecules form 2 pentagonal dodecahedra and 6 tetrakaidecahedra (a fourteen-sided polyhedron). In structure II, 136 H_2O molecules form 16 pentagonal dodecahedra and 8 hexakaidecahedra (a sixteen-sided polyhedron). Structures such as these are examined in more detail by Davidson (1973), and Jeffrey and McMullan (1967).

The particular structure formed (i.e., either I or II) is largely determined by the size and properties of the guest species. Davidson (1973) shows that the choice of structure correlates well with van der Waals radii, with the larger guest molecules favoring a type II unit cell. As noted by Jeffrey and McMullan (1967), properties of the guest molecule are also a factor. Of the species of interest in the current work which have been observed in clathrate structures (i.e., N_2, O_2, N_2O, CO_2, Fll, and Fl2) all but CO_2 are hydrophobic guests. For the hydrophobic guests, clathration gives rise to solubility in the solid phase that is not present in the liquid phase, and is often many orders of magnitude greater. For water-soluble CO_2, clathration competes with other possible processes, such as hydrolytic reaction leading to ion formation, when formed in the bulk aqueous phase. Davidson (1973) reports that N_2, O_2, N_2O, and CO_2 are known to form structure I hydrates, due to their size relative to the size of the structure I guest cages. Fll ($CFCl_3$) and Fl2 (CF_2Cl_2) form a structure II hydrate. Although no published evidence was found, it is suspected that NO clathrates also occur, which, according to their size, would probably form a type I structure.

The unit cell structures of clathrates I and II are comprised of various types of polyhedra, thus they include various cavity sizes. It is often the case that clathrate structures hosting guest molecules that do not fit in the smaller cage sizes can be stabilized by inclusion of a "help" molecule of a second species such as CO_2, N_2, O_2, H_2S, and H_2Se. As noted by Davidson (1973), Siksna (1973), and Jeffrey and McMullan (1967),

these "mixed" clathrates are often more stable than clathrates of the principal constituents alone.

The ideal stoichiometry of structure I clathrates is a water-to-guest molar ratio of 5.75. For structure II, the ideal water-to-guest molar ratio is 17. Miller and Smythe (1970) have noted, however, that the actual molar ratio for CO_2 is six (i.e., $CO_2 \cdot 6H_2O$), due to the fact that all the cages in the structure are not filled. Miller (1969) found similar results for N_2 and O_2 (i.e., $(N_2;O_2) \cdot 6H_2O$), and for F11 and F12, Wittstruck et al. (1961) found the molar ratios to be 16.6 and 15.6, respectively (i.e., $F11 \cdot 16.6H_2O$, $F12 \cdot 15.6H_2O$). The Freon case is interesting in that the molar ratios are below those theoretically predicted; i.e., more Freon is included than predicted. This could be due in part to additional surface adsorption. Thus some clathrates are classified as nonstoichiometric compounds (Siksna, 1973, Davidson, 1973).

Jeffrey and McMullan (1967) describe the laboratory preparation of clathrates. Liquid H_2O is introduced into a vessel, pressurized to the vapor pressure of the clathrate at a specified temperature along with a gas of the guest species, and agitated. Crystallization takes place at the phase boundaries; i.e., clathration occurs in the froth surrounding bubbles of the guest species. This may be indicative of transport limitations of the gas species in the liquid phase. Davidson (1973) notes that for hydrophobic guest species, guest absorption into the liquid phase is indeed the rate-limiting step. He also notes that pure ice crystals serve as nucleation sites for clathrate formation, and promote their production -- a fact which

may be relevant in the current system.

Siksna (1973) considered the possibility of water clathrates as atmospheric aerosols. The importance of low temperature in the formation of the clathrate structure was emphasized; i.e., guest molecules with high thermal energy tend to destabilize the cage structure. It was also noted that the effect of pressure is less well understood. Siksna cites the early work of Nikitin (1936, 1939), who produced Rn guest clathrates of water, and found that "mixed" clathrates formed with SO_2 or H_2S as the second guest, could be formed at a Rn partial pressure as low as 10^{-10} torr. Siksna (1973) estimated that the pressure necessary at 0°C (the experimental temperature) for the formation of pure Rn clathrates is approximately 0.16 atm. Thus it was concluded (Siksna, 1973) that "(1) a limiting upper temperature depending on the included substance may be accepted, but (2) a limiting upper pressure may be lowered considerably when mixed clathrates are formed".

This leads to one of the problems associated with hypothesizing the formation of clathrate hydrates during formation of the initial sublayer in the current work. Vapor pressure data for pure clathrates of the species of interest here are reported by Miller (1969) for N_2 and O_2, by Wittstruck et al. (1961) for F11 and F12, by Miller and Smythe (1970) for CO_2, and by Miller (1973) for N_2O. Table (3.3-10) presents the vapor pressures necessary for clathrate formation for the various species considered here, extrapolated from the literature values cited above to the temperature range of the first condensation, and, in the case of N_2 and O_2, the temperature at which

oscillation begins. As shown, the vapor pressures required for clathrate formation are greater than atmospheric for N_2O and CO_2, approximately 10 torr for the Freons; and 35.5 and 26 atm. for N_2 and O_2 at their oscillation temperatures, respectively. Also, the vapor pressures at which N_2 and O_2 undergo their "first condensation" are very low; i.e., 2×10^{-10} and 4×10^{-8} torr, respectively. Thus if water clathrates are responsible for the initial sublayer formation in the present work, the question arises as to how they can be stable at vacuum chamber pressures of approximately 10^{-5} torr. Several possibilities exist. First of all, there are secondary "help" gases in the background, including CO and various other unidentified species. Siksna (1973) has reported that these "help" gases can lower the clathrate vapor pressure significantly (i.e., by many orders of magnitude). Secondly, the initial sublayer is only of the order of several monolayers in thickness. The molecules involved in its formation are readily supplied to the surface by the beam and by collisions of the background gas. More importantly, however, the film is formed on a metal surface, or more probably, a metal surface coated with water frost. It has been shown (Davidson, 1973) that clathrates form much more readily on solid ice, possibly due to strong adsorption energies for the guest species on the ice surface. Thus, the guest species of interest are probably pre-adsorbed on an ice surface, and clathration occurs subsequently as water vapor continues to deposit over the strongly adsorbed guest species and water in an alternating "trapping" type mechanism, as previously discussed in section 3.1.

As indicated previously, the first condensation is not stable; i.e., rapid desorption occurs when the refrigeration is

turned off, without any noticeable rise in surface temperature. Thus the clathrate layer probably exists in a metastable adsorbed state on top of a mostly water sublayer. These observations, when added to the stoichiometry data and the fact that stabilization of mixed clathrates is not too difficult, lends credence to the theory that a mixed water clathrate structure is probably formed on the "dirty" metal surface. Indeed, there is a steadily increasing body of evidence which suggests that clathrate formation is a factor in a variety of physical systems. Daee et al. (1972), in a theoretical study of water cluster formation during homogeneous phase expansion of water vapor, calculated the free energies of various sized water clusters. It was found that the Helmholtz free energy of the clusters was not a smooth function of cluster size, but that definite minima were exhibited corresponding to closed clathrate cage structures.

Barrer (1978), in reviewing water sorption into zeolites, predicted that H_2O molecules absorbed into zeolite A are arranged in the form of a pentagonal dodecahedron, a cage structure identified as a clathrate.

Holland and Castleman (1980) examined the possibility that clathrate formation, occurring in both thermal ion cluster formation and neutral beam expansion type experiments, account for abnormalities observed for $H^+(H_2O)_n$ ion distributions. A model was also developed which predicts a charged clathrate structure in which the movement of "excess" protons in water stabilize the cage structure. In a supersonic beam study, Kay et al. (1979) report work on water clustering about neutral HNO_3. Also, in a survey work considering molecular nucleation,

Castleman (1979) alludes to ongoing work in which the photo-ionization of neutral clusters produces a clathrate-like structure.

Thus, current interest in clathrates formed in the gas phase is indeed quite high. Yet, our case may be unique in that clathration is observed as an unintentional byproduct of the condensation process, caused primarily by high background water vapor pressures. That clathrate surface properties explain the first condensation phenomenon quite readily, is shown in the succeeding section.

Clathrate Surface Properties

Siksna (1973) presents water molecules (in the simple clathrate dodecahedron) with the oxygen in the center and the two hydrogen atoms and two lone pairs of oxygen electrons arranged in a tetrahedral configuration about it. In this model of the clathrate structure, twenty oxygen atoms are located at the vertices of the cage, and so thirty hydrogen atoms lie along the edges of the dodecahedron to form hydrogen bonds with thirty of the lone electron pairs. This leaves ten hydrogens and ten electron pairs on the water surface of the clathrate, which gives it a unique surface excess charge structure, as illustrated in Figure (3.3-12). Siksna (1973) contends that it is even possible for a quadrupole to exist, as shown in Figure (3.3-13). This excess charge structure may play an important role in the first condensation , because, as described in detail in a previous section on polarization effects, an alternating polar surface is ideal for adsorption of a polarizable molecule. All of the species of interest here possess significant polarizability.

Adamson (1967) examined multilayer adsorption of polarizable species onto a polar surface. The interaction energy between the multilayer structure and a surface molecule was derived as

$$\varepsilon(x) = \varepsilon_o e^{-ax} \qquad (3.3\text{-}1)$$

where

$$a = 1/d_o \ln(\alpha/d^3)^2,$$

d_o is the atomic diameter, d is an effective diameter ($d \leq d_o$), x is the distance (thickness) of the film and α is the polarizability of the molecule. Thus, the interaction potential falls off in a negative exponential fashion with layer thickness. It follows, therefore, that molecules with permanent dipoles will experience interaction energies that are weaker powers of layer thickness; i.e., that the permanent dipole will have a high interaction potential for a greater layer thickness. Thus, the clathrate structure can contribute to a strong "first condensation", and is consistent with multilayering which is possible for polarizable molecules.

Indeed, Siksna (1973) reports that calculations of the fugacity of water vapor above the clathrate lattice is smaller than that above the surface of ice or liquid water, lending additional support to the stabilizing effect of the clathrate surface. In this regard, Siksna (1973) also questions the mechanism regarding CO_2 as a seeding agent for nucleation of water in supercooled clouds. Previous explanations included only the effects of the CO_2 "seed" temperature, while Siksna speculates that enclathration of the CO_2 guest may indeed be the initiation

mechanism, and that the clathrate surface may act as a preferential nucleation center for the larger drop formation.

Thus it is shown that clathrate formation is reasonable in our experimental system, and that clathrate surface properties can contribute to a strong first condensation effect, due to the interaction of the excess charge distribution with dipole-induced dipole and dipole-dipole forces which lead to multilayer adsorption, as discussed in Chapter 3.1. The remainder of this chapter emplores in greater detail how clathration can account for the experimental observations of the "first condensation" phenomenon.

Enclathration and the First Condensation

The mechanism assumed for clathrate formation in the present system begins with the realization that background water vapor is readily available to the cryosurface. Initially, water vapor adsorbs onto the cryosurface when the temperature energetically favors chemisorption. The distribution of this initial water film is probably heterogeneous, and dependent on surface characteristics. Thus the gold-flashed and HMDS-coated surfaces may have different coverages at the same temperature. During this time, guest molecules (e.g., CO_2) impinge on the surface, where some are adsorbed and trapped in the manner described by Wang, Collins, and Haygood (1962); i.e., they are covered by condensing water molecules. Once surrounded by water, clathration may occur in a manner similar to Siksna's (1973) cage development mechanism. Once the surface density of clathrate cages becomes high enough, and the surface temperature becomes low enough, the clathrate surface, due to its surface properties, induces gross adsorption of beam (guest) species onto its surface. As in

the work of Abe and Schultz (1979), a thin (possibly monolayer) film of clathrate structure, bound in a specific orientation by strong inter-clathrate hydrogen bonds and thus prevented from rearranging (i.e., annealing), becomes a powerful adsorbent. As guest species deposition continues, the adsorbent surface is continually renewed by constant deposition of water, a la Bewilogua and Jackel (1974). The renewed clathrate structure continues to pump guest species molecules as sublayers become saturated.

With a mechanism such as this, the use of LN_2 cryopumping complicates the analysis, because it affects not only one, but many of the relevant parameters. For example:

(1) The water vapor background level is significantly reduced by the cryopump, but not to zero.

(2) Depending on the properties of the guest species in the beam, the background level of this species (i.e., CO_2) may be decreased by the cryopump.

(3) Guest adsorption stability on the surface is a function of the beam pressure, and therefore its intensity and related beam dynamics, also (see below).

(4) Anderson (1974) (also referred to in the section on phase-locked studies), has shown that beam dynamics may be critical in situations like our own. A directed beam tends to pump background species away from its centerline. Thus, increasing the beam intensity of "guest" species decreases the availability of water vapor to the surface. Since the time-dependent temp rature - ofile during cooldown is almost

invariant, increasing the beam intensity will create a longer induction period prior to the first condensation , which may then occur at lower temperatures.

(5) The LN_2 cryopump tends to lower the average temperature of the background species.

(6) The emissivity of the surface increases by approximately an order of magnitude when water deposits, thereby changing the rate of radiative heat transfer, a process which is also affected by lowering the temperature of the surfaces "seen" by the cryosurface.

The problem then becomes, which of these factors controls the first condensation process? If stability of the guest species on the surface controls, then as intensity increases, the first condensation temperature will increase, in accordance with thermodynamic considerations. On the other hand, if water vapor availability is the rate controlling factor, due to the beam pumping it away from the surface, then increasing intensity should cause the first condensation to occur at increased times after cool down initiation, or lower temperatures. This effect is the exact opposite of the intensity-temperature behavior that is expected thermodynamically. As a rough measure of the ability of the beam to pump away background species, a comparison was made of the intensity reduction due to a Beer's law type attenuation of the beam by background gases with the effusive flux per unit area of background species. In a system with a background of 1×10^{-6} torr and a molecular cross section for total interaction of 500 $\mathring{A}^2$ (discussed in a later section), a 10^{19} $m^{-2}s^{-1}$ beam has a scattered intensity-to-background intensity

ratio of 0.34%, while a $10^{21} m^{-2} s^{-1}$ beam has a ratio of 34%. Although this does not specifically correlate with background reduction, it does illustrate that in the beam intensity range of interest, beam attenuation does in fact approach the order of the background flux, illustrating that interaction between the two can be significant.

In the case of N_2O, condensation experiments on the gold-flashed surface with no LN_2 cryopumping resulted in a T_{fc} range of 248-257K and a functional dependence of decreasing T_{fc} with increasing beam intensity, as illustrated in Figure (3.3-1). Thus the first condensation was probably controlled by water vapor deposition. When LN_2 cryopumping was employed, the T_{fc} range decreased to 224-240K on both gold-flashed and HMDS-coated surfaces, as might be expected from the decrease in background water vapor. More interestingly, however, the functional dependence of T_{fc} on beam intensity became unclear. The same general effects were observed for CO_2.

In the case of the Freons, the low beam intensity problem (mentioned previously) controlled. For Freon 12, low beam intensity, coupled with low water vapor background levels, served to eliminate the first condensation effect entirely; i.e., the intensity was probably too low to promote guest stability on the surface. In the case of Freon 11, the first condensation effect was barely discernible.

For NO, as indicated in Table (3.3-6), with LN_2 cryopumping it seems that guest stability is the controlling factor (i.e., T_{fc} increases with increasing beam intensity). Also, the low

temperature range (216-230K) is probably due to decreased water vapor availability. In addition, since background NO is not pumped by the LN_2 cryopump, the attendant beam attenuation decreases the effect of beam intensity on background exclusion.

It was found that for CO_2 (Figure (3.3-3), N_2O (Figure (3.3-4)), and NO (Figure 3.3-6)), reduction of the background of the guest species had a considerable effect on the rate at which the first condensation adsorbs guest species. In the case of NO, no guest species background is pumped, and the first condensation results in 90-95% reflected beam reduction. In the case of N_2O and CO_2, LN_2 cryopumping reduced the background pressure by an order of magnitude, and, as shown in Figures (3.3-3) and (3.3-4), discernible differences in condensation rates were found between the gold-flashed and HMDS-coated surfaces -- the HMDS-coated surface was slightly more efficient for condensation. Also, the total capacity of the first condensation appears to approach an asymptotic value at high beam intensities; i.e., it saturates.

For the Freons, comparison of relative surface efficiencies is obfuscated by the low intensity problem. The "first condensation" capacity was zero for Freon 12, and near-zero for Freon 11.

As indicated previously, and illustrated in Figure (3.3-7), O_2 and N_2 condensation experiments yield data which oscillate about a mean value, under certain conditions. The oscillations in Figure (3.3-7) begin at 217K and extend to 48K, with no first condensation apparent until 48K. These oscillations occurred at the exact frequency of the helium refrigerator expander. From Table (3.3-10), it is evident that N_2 and O_2

clathrates are the least stable in the 220K temperature range. This can be interpreted to mean that clathrates of N_2 and O_2 are not stable at the experimental conditions employed. The oscillations are probably due to the beam species (N_2 or O_2) adsorbing onto a water film or possibly a clathrate structure in which the guest species is a background contaminant molecule, such as CO. During the cold expansion stroke of the refrigerator, the thermal gradient across the sublayer is large enough to condense the beam species (N_2 or O_2). When this transient gradient diminishes during the compression stroke, the surface becomes supersaturated with the adsorbed beam species, and it evaporates. This condensation/evaporation behavior results in the observed oscillatory behavior.

As indicated previously, CO_2 and N_2O exhibit saturation of the first condensation on the HMDS-coated surface; i.e., after an initial decrease, the mass spectrometer signal slowly rises back to its original level, indicating that the ability of the surface to adsorb additional beam molecules gradually diminishes. This is illustrated in Tables (3.3-4) for CO_2 and (3.3-5) for N_2O, and in Figure (3.3-5) for CO_2. Note that in Figure (3.3-5), a second condensation appears at approximately 86K. Employing an explanation based on clathration, it appears that water vapor availability, with LN_2 cryopumping, becomes low enough that the clathrate surface cannot regenerate itself at a rate fast enough to maintain continuous adsorption. After the occurrence of saturation, the clathrate surface does slowly begin to regenerate, and as the surface temperature continues to decrease, the stabilizing effect of the guest species on the

clathrate surface continues to increase. Thus, as in Figure (3.3-5), 86K is the temperature at which the "first condensation" reoccurs, and continues until 70K, where the sharp break signifies the true condensation. This second, first condensation becomes evident only after saturation occurs. One experiment was run in which CO_2 was directed at the gold-flashed cryosurface without LN_2 cryopumping. The surface temperature was lowered until the "first condensation" occurred, and then was held constant in the 210-211K temperature range. At this temperature, the "first condensation" showed no sign of saturation in 1.5 hours. This illustrates that, without LN_2 cryopumping to limit background water vapor contamination, continuous surface renewal prevents saturation.

As mentioned in the literature review, Wang, Collins, and Haygood (1962), report a study of cryopumping CO_2 onto an H_2O surface at 77K, in which similar saturation effects were observed. These authors calculated a cryopumping speed on the H_2O surface of $2.06\ell\ cm^{-2}s^{-1}$ at 2.7×10^{-5} torr for 5.5 minutes prior to saturation. At saturation, therefore, the CO_2 surface density would be $5.9 \times 10^{17}\ cm^{-2}$ at a pumping speed of $1.79 \times 10^{15}\ cm^{-2}s^{-1}$. In Table (3.3-11), pumping speeds and saturation densities for CO_2 on the HMDS-coated surface are reported for the current work.

Our observed pumping speed is approximately an order of magnitude less than that found by Wang et al. (1962). This is presumably due to the fact that the average cryosurface temperature is much higher in our condensation experiment, than in that of Wang et al. (1962). More significantly, however, the saturation

densities of the present experiment are very similar to the 5.9×10^{17} cm^{-2} calculated from the data of Wang et al. (1962), indicating that the controlling mechanism in both experiments was similar; e.g., clathration of CO_2 with surface water molecules providing a surface for adsorption of the beam.

In the study of CO_2 adsorption on H_2O by Cazcarra, Bryson, and Levenson (1973), clathrate formation on the H_2O surface is also a strong possibility. These authors observed a strong period of adsorption, followed by a transition preceding the bulk deposition of CO_2 onto the water surface. The induction period can be caused by the rate of formation of clathrates, followed by a transition when their surface density reaches the required level to pump CO_2. This type of behavior was noted in Figure (3.3-2) for N_2O without LN_2 cryopumping on the gold-flashed surface, and is consistent with the clathration mechanism. The high diffusion energy for CO_2 across the water surface found by these authors is also indirect supporting evidence for the clathration mechanism, in that the alternating polar surface structure tends to hinder surface diffusion of polarizable species.

In summary, it has been shown that:

(A) Clathration of beam species is consistent with all the available data and can in fact account for the first condensation phenomenon.

(B) That the available literature on this subject also supports this contention.

(C) That the parameters controlling the first condensation and clathrate formation are numerous, and that under different conditions, different steps of the mechanism may control.

(D) That in certain respects, surface parameters are important; e.g., CO_2 and N_2O exhibit different behavior on the two different surfaces, and the saturation effect seems to occur only on the HMDS-coated surface. This will be explored further in the discussion of the true condensation .

(E) That molecular accommodation between background and surface seems to be more efficient than between beam molecules and the surface (more evidence follows below).

The formation and stabilization of a mixed water clathrate layer as a contaminant sublayer at relatively high temperatures, which can strongly adsorb beam species and is capable of continuous renewal under certain conditions of water vapor availability, is consistent with all our experimental data and the pertinent extant literature. However, since we have no direct morphological confirmation of their existence in our system, this contention is in no way meant to exclude any other plausible mechanism consistent with all the observations.

One further avenue was explored in order to clarify the first condensation mechanism. Modulation of the reflected beam was performed with an optical chopper, and a lock-in amplifier was employed to differentiate between the reflected beam and the background signal. The next section deals with the information provided by this technique and how it complements the preceding observations.

Modulation of the Reflected Beam with Lock-In Amplification

As described in Chapter 2, modulation of the reflected beam was accomplished with a 200Hz Bulova tuning fork chopper placed between the mass spectrometer and the surface. The

reference signal from the chopper was fed into a lock-in amplifier along with the mass spectrometer signal. The lock-in amplifier allows measurement of the modulated reflected species only.

Since the objective of these experiments was to study the "first condensation" phenomenon, the strongest "first condensation" effect attainable was desired. Therefore, no LN_2 cryocooling was employed. As will be shown, modulation of the reflected beam yields more information concerning the nature of the first condensation process, as well as underscoring the fact that the physics involved with molecular beam reflection and scattering must be considered in order to achieve a more complete understanding of the entire process. Experiments were performed in this manner for CO_2, N_2O, Fll, F12, and NO, which are the species of major interest for the first condensation process.

In what follows, the term "total signal" refers to the gross signal (background plus reflected), while the term "lock-in signal" refers to the signal from the lock-in amplifier.

Figure (3.3-14), for the gold-flashed surface, and Figure (3.3-15), for the HMDS-coated surface, present both the total and lock-in response as a function of surface temperature for CO_2 as the beam species. In Figure (3.3-14), as cooldown begins, the total signal rises slightly, while the lock-in signal decreases. This is indicative of early sublayer formation at the more intense center of the beam, which is also the section which has the greatest input to the lock-in signal. Upon initiation of the "first condensation", the lock-in signal jumps up in

response, while the total signal dramatically decreases simultaneously. This effect, which at first seems strange, was observed in many of these experiments, and will be explained with the help of a simple model. After the onset of the first condensation , the lock-in and total signals parallel each other quite closely until the true condensation temperature range is reached. Upon initiation of the true condensation , both the lock-in and total signals drop dramatically. It should be noted, however, that the lock-in signal drops much more sharply than does the total signal. This is because the mass spectrometer records the full range of reflected intensities while the lock-in only "sees" the central portion of the reflected beam, and therefore a more limited intensity profile. This result is quite similar to the previously mentioned observations of Heald and Brown (1968) (see Chapter 3.1).

For CO_2 on the HMDS-coated surface, the data are similar in most respects, except that the lock-in signal continues to rise between the onset of the first condensation and the onset of the true condensation . This is probably due to the slow onset of saturation of the first condensation taking place in the central portion of the beam. It should also be noted that the HMDS-coated surface is the one that previously exhibited saturation with CO_2.

The behavior of N_2O is illustrated in Figure (3.3-16) for the gold-flashed surface, and Figure (3.3-17) for the HMDS-coated surface. Figure (3.3-16) shows erratic lock-in signal behavior prior to the onset of the first condensation . Since the formation of the clathrate sublayer is dependent on many

parameters, this type of behavior is not totally unreasonable. Yet, in general, the behavior is generally a decreasing signal with decreasing temperature prior to the first condensation. Again, the lock-in signal jumps up while the total signal simultaneously jumps down during the first condensation , as in the case of CO_2. An upward trend in the lock-in signal then ensues between the onset of the first condensation and the true condensation , at which a rapid lock-in signal decrease occurs. This final decrease corresponds to the point on the total signal curve where a rapid decrease occurs, not where the gradual decline begins. This slower decline in total signal is believed to correspond to a first condensation effect, which illustrates that care must be taken in interpreting the total signal in order to ascertain the true condensation event.

In Figure (3.3-17) for N_2O on the HMDS-coated surface, the lock-in signal increases prior to the first condensation, possibly due to rapid clathrate formation at the beam center. These data exhibit the same precipitous increase upon the onset of the first condensation , as did the previous N_2O data, and in this case, a gradual rise in both the total and lock-in data is observed between the first and the true condensation . This probably indicates the onset of saturation over the entire surface. Again it should be noted that prior to the first condensation , the total signal decreases slowly.

For Freon 12 on the gold-flashed surface (Figure (3.3-18)) the lock-in signal is initially erratic, and a definite upward trend is evident in both signals. This is interpreted as a strong initial adsorption-saturation effect of the surface for

Freon 12. Both the lock-in and total signals decrease upon the onset of the first condensation , but the latter does so in a much broader fashion. This implies that, again, there is a difference between the accommodation of background Freon 12 as indicated by the total signal, in comparison to the reflected beam molecules, as indicated by the lock-in signal. Both signals continue to drop after the first condensation event, indicating the absence of saturation. This is consistent with the observations that: (1) the low beam intensity for Freon 12 provides less of a load on the surface; (2) that the low intensity beam does not effectively remove background water from the centerline; and (3) that the Freon 12 clathrate is relatively stable (i.e., low vapor pressure). Figure (3.3-19) for Freon 12 on the HMDS-coated surface is quite similar, except that the lock-in signal does begin to rise between the onset of the first condensation and the true condensation . This onset of saturation, again, is typical of the HMDS-coated surface, a surface which was chosen because of its relatively poor Freon adsorption characteristics.

The Freon 11 data are represented by Figure (3.3-20) for the gold-flashed surface, and Figure (3.3-21) for the HMDS-coated surface. In Figure (3.3-20) it can be seen that both the total and lock-in data begin with an initial increase in intensity, perhaps due to the beam system adsorption phenomena mentioned earlier. Again, as in the case of Freon 12, the total signal drops dramatically while the lock-in signal decreases more gradually, due to superior accommodation of background molecules. Between the onset of the first condensation and the onset of the true

condensation , complete saturation of the lock-in signal occurs (i.e., the lock-in signal returns to its pre-first condensation value), whereas the total signal does not. This behavior implies that the cryosurface center is saturating while the outer perimeter is not. This may be due to several reasons, two of which are maximum mass load and minimum water background availability at the center. At the true condensation , both signals drop simultaneously.

Figure (3.3-21), representing Freon 11 on the HMDS-coated surface, is quite similar except for two aspects. Between the first and true condensations , the lock-in signal increases while the mass spectrometer signal decreases. This signifies that the directed beam molecules, measured by the lock-in signal, begin to saturate the central cryosurface target, while the overall adsorptive capacity of the first condensation increases, as measured by the total signal. This again suggests that background molecules have a superior ability to sorb onto the cryosurface during the first condensation . The second difference is that both the total and lock-in data for the true condensation exhibit a definite shoulder. This implies that the true condensation mechanism is more complex, possibly involving sites with different adsorption energies.

Data concerning the adsorption of NO on the gold-flashed and HMDS-coated surfaces are presented in Figures (3.3-22) and (3.3-23), respectively. In Figure (3.3-22), both the lock-in and total signals decrease slowly prior to the first condensation event, possibly due to clathrate formation on the surface. Upon the onset of the first condensation , the lock-in signal increases

as the total signal decreases, as in the case of N_2O and CO_2. The onset of the true condensation causes a near simultaneous drop in both lock-in and total signals, with the lock-in signal shifted slightly to lower temperatures.

Figure (3.3-23) for NO on the HMDS-coated surface is quite similar, except for two observations. First, the pre-first condensation lock-in signal is erratic, possibly due to complex behavior during clathrate formation. Secondly, at the true condensation , the total signal exhibits a two-stage drop, while the lock-in signal exhibits only a single-stage drop, corresponding to the second stage of the more complex total signal behavior. The first stage is actually a manifestation of the first condensation effect, similar to that found for CO_2 and N_2O with LN_2 cooling; i.e., the saturation effect competes with increased adsorbate stability on the clathrate surface.

In summary, by employing lock-in detection, it has been shown that: (1) erratic behavior usually exists prior to the first condensation event, which may be due to random clathrate formation; (2) as in the previous section, significant differences between how background and beam molecules accommodate to the surface during the first condensation process were observed; (3) a trend towards saturation is evident in the lock-in signal data between the first and true condensation events, even though in many cases, the total signal continues to decrease; (4) often, the true condensation is immediately preceded by first condensation effects; and (5) a seemingly anomalous increase in lock-in signal accompanies the drop in the total signal coincident with the first condensation event for CO_2, N_2O, and NO.

One additional interesting effect is noted. Table (3.3-12) summarizes condensation temperature data as a function of beam intensity for CO_2, N_2O, NO, Fl1, and Fl2 lock-in experiments, along with data for N_2 and O_2 oscillation temperatures from non-LN_2 cryopumped experiments, for beam intensities of the same order of magnitude to allow direct comparison. In Figure (3.3-24), the first condensation temperatures (and the oscillation temperatures for N_2 and O_2) are plotted as a function of the total polarizabilities. The resultant figure shows that for the case of no LN_2 cryopumping, the first condensation temperature is an increasing function of the total polarizability of the beam molecules, as would be expected if water clathrates are the predominant species in determining the first condensation .

Analysis of the Increase In Lock-in Signal Upon the "First" Condensation

Many possibilities were explored in attempting to explain why the lock-in signal increased dramatically, while the total signal decreased during the onset of the first condensation . The first possibility considered was that the surface created by the first condensation significantly affected the scattering reflectivity; i.e., that the first condensation changed the distribution of the reflected beam intensity such that the lock-in signal increases. This explanation is contrary to the conclusions of Heald and Brown (1968) (e.g., see section 3.1).

In order to further test this hypothesis, a first condensation was induced on the gold-flashed surface with CO_2 as the beam species. The CO_2 beam was then discontinued, with the refrigerator running, and a nitrogen beam was substituted in

its place. Since nitrogen does not exhibit a significant first condensation , the beam would just reflect off the CO_2 deposited sublayer. Thus, upon thermal desorption of the CO_2 sublayer, the nitrogen lock-in signal would change if there was a difference in surface reflectivity. The results of these experiments were definitive. The nitrogen lock-in signal did not change at all upon thermal desorption of the CO_2 sublayer. Thus, in agreement with Heald and Brown (1968), the CO_2 first condensation layer does not change the reflectivity of the surface. The actual amounts of CO_2 adsorbed during the first condensation and then desorbed were measured. It was found that the adsorbed to desorbed ratios for two separate experiments were 1.06 and 0.94, both within 6% of the expected result (1.00), and well within the range of experimental error. This experiment provides direct evidence that the first condensation , in fact, quantitatively pumps the beam species.

A second alternative explanation which was explored involved employing the molecular beam as a density probe. From Anderson (1974) it is known that an effusive source entering a low density chamber can experience scattering due to collisions with background molecules. Represented in terms of a Beer's law-type attenuation:

$$R = R_o \exp(-n_b \sigma_c x) \qquad (3.3\text{-}3)$$

where R_o is the incident beam intensity, n_b is the background density, σ_c is the collision cross section, and x is the distance traveled through the background. If the beam was to be left on during the thermal desorption of a first condensation layer,

the resultant lock-in signal would act as a density probe; i.e., the degree of scattering would indicate the density of the gas layer immediately above the surface during thermal desorption.

The experiments were conducted as follows: CO_2 was directed at the gold-flashed surface and the refrigerator was started. Lock-in and total signals were simultaneously recorded as a function of surface temperature as the temperature decreased and the first condensation occurred. Then the refrigerator was shut off, and the mass spectrometer and lock-in signals were followed as desorption occurred.

The results are illustrated in Figure (3.3-25), which give the mass spectrometer lock-in signals as a function of time measured from the point at which the refrigerator was shut off. Several points are evident from the data:

(1) At t=0, the lock-in signal is greater than its pre- first condensation value; i.e., it has already "jumped up".

(2) The adsorbed CO_2 sublayer does not begin to desorb for approximately 5 minutes, which is considerably longer than when the beam is turned off. Thus, the sublayer experiences increased stability due to the continuous supply of gas from the beam.

(3) Initially, as desorption occurs and the total signal begins to rise, the lock-in signal begins to drop, indicating that the desorbed gas attenuates the initial and reflected beam.

(4) However, as the desorption rate of the first condensation material begins to accelerate (i.e., when its slope is

highest), the lock-in signal increases dramatically, and passes through a maximum. According to Heald and Brown (1968), condensed material desorbing from a surface exhibits a cosine intensity distribution -- the same distribution expected from a beam reflected off a polycrystalline surface. Thus, as the first condensation begins to desorb strongly, it looks exactly like a strong reflected beam to the lock-in signal.

(5) As the total signal passes through its maximum, the lock-in signal falls to zero. Thus at this point, both the reflected beam and the desorbing material are fully attenuated by the background.

(6) Once the first condensation desorption is over, the lock-in and total signals return to their pre- first condensation values.

From these experiments it is concluded that beam dynamics must be taken into account if the lock-in amplified data are to be fully understood. Thus the physical situation was examined in greater detail, and a model was devised to account for attenuation due to collisions.

A Scattering Model

It was decided that modeling the gas density distribution in front of the cryosurface would elucidate the mechanism responsible for the lock-in signal behavior during the first condensation . A unit cell model was devised, in which the volume between the nozzle and the cryosurface was modeled as a cylinder divided along its length into twenty unit cells of equal dimensions. A constant intensity, parallel beam was assumed to

enter one end of the cylinder (a relatively good assumption at the beam centerline). This approach avoids following individual molecular paths before and after collisions, as in Monte Carlo techniques (e.g., see Vogenitz et al., 1968). A time constant was chosen on the order of the unit cell length divided by the velocity of the beam molecules, in order to insure that each molecule would pass through only one unit cell during a given time interval. It was next assumed that all molecules possess the mean thermal velocity, in order to make the problem more tractable while retaining the significant features of the physical processes involved. It is noted that an error is introduced by assuming the reflected beam velocity is the same as that of the initial beam, since it must at least partially accommodate to the colder surface. However, in order to assess the possible magnitude of this error, the program was also run assuming a lower temperature reflected beam and background.

Several types of collisions are treated in the model. As mentioned previously, the incident and reflected beams can be attenuated by a Beer's law collisional process (e.g., 3.3-4) (Anderson, 1974). Also, direct collisions between the incident and reflected beam can occur, as noted by Fluendy and Lawley (1973):

$$Z_{ab} = \frac{R_a R_b}{v_a v_b} V v_{ab} \sigma_c \qquad (3.3\text{-}4)$$

where v_a and v_b are incident and reflected beam velocities, respectively, V is the cell volume, and v_{ab} is the relative velocity of the colliding molecules, equal to v_a+v_b in this case.

The effusive flux into and out of unit cells from all directions was accounted for using an expression from Davidson (1962);

$$E = \frac{n_b \bar{v}_{av}}{4} \qquad (3.3\text{-}5)$$

where $\bar{v}_{av}$ is the average background velocity. All collisions were assumed to convert directed species to background species, thus increasing the background density.

The numerical technique used to solve this model begins by introducing the beam at the source end of the cylinder at time t=0. The initial density of the cylinder is that of the background in the chamber prior to initiation of the beam. The beam is followed as it moves forward through the unit cells, is attenuated by background scattering, reflected off the cryo-surface, and collisions begin between incident and reflected species. As the program proceeds, it moves back and forth across the unit cells in the cylinder, accounting for collisions, effusion, and cell density, and continues to do so until the density in the cells attains steady-state, (see appendix B for the program and documentation).

The parameter values used initially are:

(A) Thermal beam velocity, at 300K, is 4.1×10^4 cm s^{-1}.

(B) The total cross section for collisions is 500 $\mathring{A}^2$ (Fluenty and Lawley, 1973).

(C) The initial intensity is 6×10^{17} $cm^{-2}s^{-1}$ -- a high value, but still within the range of interest.

(D) A time step, between iterations, of 5×10^{-7} seconds.

Figure (3.3-26) is a plot of cell density as a function of cell number. Curve A represents the situation when no molecules are captured by the cryosurface located at the end of cell twenty. Note that the density within the cells is significantly above background values, due to beam scattering effects. Figure (3.3-27), curve A, illustrates the effect of this density distribution on the intensity of the incident and reflected beams as a function of cell number. Note that both the incident and reflected beams are highly attenuated.

In order to ascertain whether a difference in accommodation behavior between directed and background molecules is occurring, another boundary condition was imposed on the system; at the cryosurface, it was assumed that 50% of all beam molecules were captured, and 90% of all background molecules were captured. Figure (3.3-26), curve B, illustrates the effect of this new boundary condition on the density distribution in the cells. Note that the number density in the cells has decreased dramatically, and that the change is most apparent in cells near the cryosurface walls.

Figure (3.3-27), curve B, illustrates the intensities of the incident and reflected beams under these new conditions. As shown, the incident beam undergoes much less attenuation, but, due to condensation, the reflected beam at cell twenty is initially at a lower intensity than for the no condensation case. More importantly, however, this curve crosses over the no condensation reflected beam curve, and at cell one is actually greater than its no-condensation counterpart. The lock-in signal calculated from the reflected intensity in cell one,

exhibits a jump of 142% of its initial value. This is precisely what was observed in the data for CO_2, N_2O, and NO experiments during the "first condensation". Thus, a difference in accommodation between directed and background molecules can indeed account for the strange behavior of the lock-in signal. The model also predicts that if the initial beam intensity were lowered significantly, the lock-in "jump" would convert to a drop in intensity, as would be more intuitively expected. Figure (3.3-28) presents the results of a lock-in experiment for CO_2 on the gold-flashed surface, in which the initial intensity was reduced by approximately an order of magnitude below that normally used. The lock-in signal in this case does indeed exhibit the precipitous decrease during the "first condensation", as predicted by the scattering model.

The question now arises as to what can cause the difference in capture coefficient between the directed beam and background molecules. The fact is, that even without LN_2 cryopumping, the background gas is colder on the average (i.e., has less translational energy) than the beam species. The beam is an effusive source, and its molecules travel at a thermal velocity corresponding to 300K. The refrigerated surface, at the point of the first condensation , is at approximately 240K, and the expander housing, although not at 240K, is also below room temperature. Thus background molecules, which collide with these surfaces must exist at a lower average temperature.

In order to check this hypothesis, the scattering program was run with the assumption that all background species were at thermal velocities corresponding to 244K. With $C_{directed} = 0.5$

and $C_{background}$=0.9 during the first condensation, the lock-in signal still jumped to 146% of its pre-condensation value, as compared to 142% for the 300K isothermal case. This implies that the difference between the temperature of the beam and the background molecules has little effect on the beam dynamics, but has a large effect on the capture coefficient during the dirst condensation. Background gas impinging at a lower temperature (e.g., 300K>t>240K) is more likely to be accommodated by the first condensation than are 300K directed molecules. That this does not hold for the true condensation is stated by Bently and Hands (1978). Thus differences in thermal accommodation during the first condensation must be substantially different from the true condensation process. It will be shown in the following section concerned with the true condensation process that the surface properties of the sublayer will also effect the condensation mechanism of the true condensation.

Conclusions: First Condensation

Several conclusions can be drawn from the preceding observations:

(A) A strong adsorption process can and does indeed occur at relatively high (200-250K) surface temperatures in "dirty" systems with non-negligible background.

(B) The cause of this adsorption process is most probably a hydrate agglomerate of the beam species and other background constituents; e.g., a mixed clathrate hydrate.

(C) The clathrate sublayer promotes adsorption primarily due to its charge structure, and the surface is continually renewed. The total polarizability of the beam species is a significant factor in the efficacy of this process.

(D) Clathrate formation is probably a function of at least two competing effects; stabilization by guest molecules, and water vapor availability, the latter of which is also a function of beam dynamics.

(E) The capture coefficient of the clathrate surface for the beam species seems to be a function of its translational energy, in direct contrast to the true condensation mechanism.

(F) The sublayer changes the properties of the surface, and will affect the true condensation mechanism.

An analysis of the true condensation follows.

TABLE (3.3-1)

N_2O ON GOLD-FLASHED STAINLESS STEEL

Run	R ($m^{-2}s^{-1}$)	T(K)
129	3.42×10^{18}	257
130	2.10×10^{19}	250
131	1.36×10^{20}	248
134	2.05×10^{20}	248
135	8.16×10^{20}	252

TABLE (3.3-2)

CO_2 on

(1) Gold-flashed Stainless Steel

Run	R ($m^{-2}s^{-1}$)	% Captured	R_S ($m^{-2}s^{-1}$)	T(K)
140	2.7×10^{19}	27.0	7.3×10^{18}	240
141	1.7×10^{20}	10.9	1.9×10^{19}	228
142	8.9×10^{18}	50.0	4.4×10^{18}	230
143	1.2×10^{20}	10.7	1.3×10^{19}	230
(2)	HMDS-coated Stainless Steel			
194	4.1×10^{19}	42.5	1.8×10^{19}	227
195	1.7×10^{20}	26.0	4.4×10^{19}	241
196	1.4×10^{19}	54.0	7.4×10^{18}	231
197	4.0×10^{20}	9.2	3.7×10^{19}	240
198	3.9×10^{20}	12.5	4.8×10^{19}	230
199	2.9×10^{19}	33.0	9.7×10^{18}	236

TABLE (3.3-3)

N_2O on:

(1) Gold-flashed Stainless Steel

Run	R ($m^{-2}s^{-1}$)	% Captured	R_S ($m^{-2}s^{-1}$)	T(K)
144	4.3×10^{19}	55.0	2.4×10^{19}	240
145	6.4×10^{20}	10.0	6.4×10^{19}	233
146	2.4×10^{20}	15.0	3.6×10^{19}	230
147	1.4×10^{19}	88.0	1.2×10^{19}	227

(2) HMDS-coated Stainless Steel

200	5.1×10^{19}	55.0	2.8×10^{19}	235
201	1.9×10^{19}	80.8	1.6×10^{19}	228
202	1.9×10^{20}	53.0	1.0×10^{20}	224
203	5.5×10^{20}	23.5	1.3×10^{20}	231
208	4.0×10^{20}	25.0	1.0×10^{20}	225

TABLE (3.3-4)

CO_2 ON HMDS-COATED STAINLESS STEEL

Run	R ($m^{-2}s^{-1}$)	Number Captured	Saturation ?
198	3.9×10^{20}	1.2×10^{19}	Yes
197	4.0×10^{20}	9.3×10^{18}	Yes
195	1.7×10^{20}	1.3×10^{19}	Yes
196	1.4×10^{19}	4.5×10^{18}	No
194	4.1×10^{19}	1.1×10^{19}	No

TABLE (3.3-5)

N_2O ON HMDS-COATED STAINLESS STEEL

Run	R ($m^{-2}s^{-1}$)	Number Captured	Saturation ?
203	5.5×10^{20}	1.0×10^{19}	Yes
202	1.9×10^{20}	1.2×10^{19}	Yes
200	5.1×10^{19}	6.7×10^{18}	Yes
201	1.9×10^{19}	7.2×10^{18}	No

TABLE (3.3-6)

NO on:

(1) Gold-flashed Stainless Steel

Run	R ($m^{-2}s^{-1}$)	% Captured	R_S ($m^{-2}s^{-1}$)	T(K)
178	5.6×10^{19}	93.4	5.2×10^{19}	226
179	1.6×10^{20}	83.5	1.3×10^{20}	223
180	4.2×10^{20}	88.0	3.7×10^{20}	230
181	1.1×10^{19}	91.2	1.0×10^{19}	216
182	1.6×10^{19}	92.3	1.4×10^{19}	226
(2)	HMDS-coated Stainless Steel			
209	5.5×10^{19}	91.0	5.0×10^{19}	225
210	2.3×10^{20}	89.0	2.0×10^{20}	227
211	2.2×10^{19}	94.0	2.0×10^{19}	225
212	4.5×10^{20}	88.0	3.9×10^{20}	229

TABLE (3.3-7)

FREON 11 ON HMDS-COATED STAINLESS STEEL

Run	R ($m^{-2}s^{-1}$)	% Captured During Slow Decrease in Signal	R_S ($m^{-2}s^{-1}$)
183	3.8×10^{19}	53	2.0×10^{19}
184	9.7×10^{18}	48	4.7×10^{18}
185	3.4×10^{18}	48	1.7×10^{18}
186	8.9×10^{19}	45	4.0×10^{19}

TABLE (3.3-8)

O_2 ON GOLD-FLASHED STAINLESS STEEL

Run	R_S ($m^{-2}s^{-1}$)	T_{osc} (K)	T_{FC} (K)
160	4.7×10^{20}	-	49
161	7.4×10^{19}	217	48
162	3.5×10^{19}	220	48
163	1.5×10^{21}	225	48
164	1.3×10^{21}	220	46

TABLE (3.3-9)

N_2 ON GOLD-FLASHED STAINLESS STEEL

Run	R_S ($m^{-2}s^{-1}$)	T_{OSC} (K)	T_{FC} (K)
165	3.9×10^{20}	215	40
166	7.5×10^{19}	217	50
167	3.2×10^{21}	212	49.5
168	1.8×10^{21}	208	37
169	3.2×10^{20}	-	37
170	4.1×10^{19}	205	44.5
171	3.0×10^{19}	205	50.5
173	3.0×10^{20}	206	49
174	3.6×10^{20}	215	41

TABLE (3.3-10)

CLATHRATE VAPOR PRESSURE AT T_{FC} AND T_{OSC}

Species	T(K)	Vapor Pressure (torr)
O_2	48	4.1×10^{-8}
N_2	40	2.2×10^{-10}
CO_2	230	1260
N_2O	233	1297
F11	230	2.22
F12	230	15.4
N_2	220	27,000
O_2	220	19,700

TABLE (3.3-11)

CO_2 ON THE HMDS-COATED STAINLESS STEEL SURFACE

Run	Pumping Speed ($cm^2 s^{-1}$)	Saturation Density (cm^{-2})
195	2.12×10^{14}	6.36×10^{17}
197	1.90×10^{14}	4.56×10^{17}
198	2.99×10^{14}	6.08×10^{17}

TABLE (3.3-12)

"FIRST CONDENSATION" TEMPERATURES AS A FUNCTION OF BEAM INTENSITY AND TOTAL SPECIES POLARIZABILITY

Run	Species	Surface	R ($m^{-2}s^{-1}$)	T(K)	Total Polarizability (cm^3)
224	CO_2	(G)	1.0×10^{20}	228	7.35
225	N_2O	(G)	1.4×10^{20}	230	8.25
228	N_2	(G)	1.9×10^{20}	200	4.67
226	O_2	(G)	2.3×10^{20}	200	4.22
229	F11	(G)	3.8×10^{19}	245	30.7
230	F12	(G)	1.9×10^{18}	239	26.2
231	NO	(G)	1.1×10^{20}	206	4.83
213	CO_2	(HMDS)	1.1×10^{20}	234	7.35
215	N_2O	(HMDS)	1.6×10^{20}	230	8.25
221	NO	(HMDS)	1.1×10^{20}	209	4.83

(G) gold-flashed stainless steel
(HMDS) HMDS-coated stainless steel

Figure (3.3-1)
N_2O Condensation Curves For 3 Beam Intensities

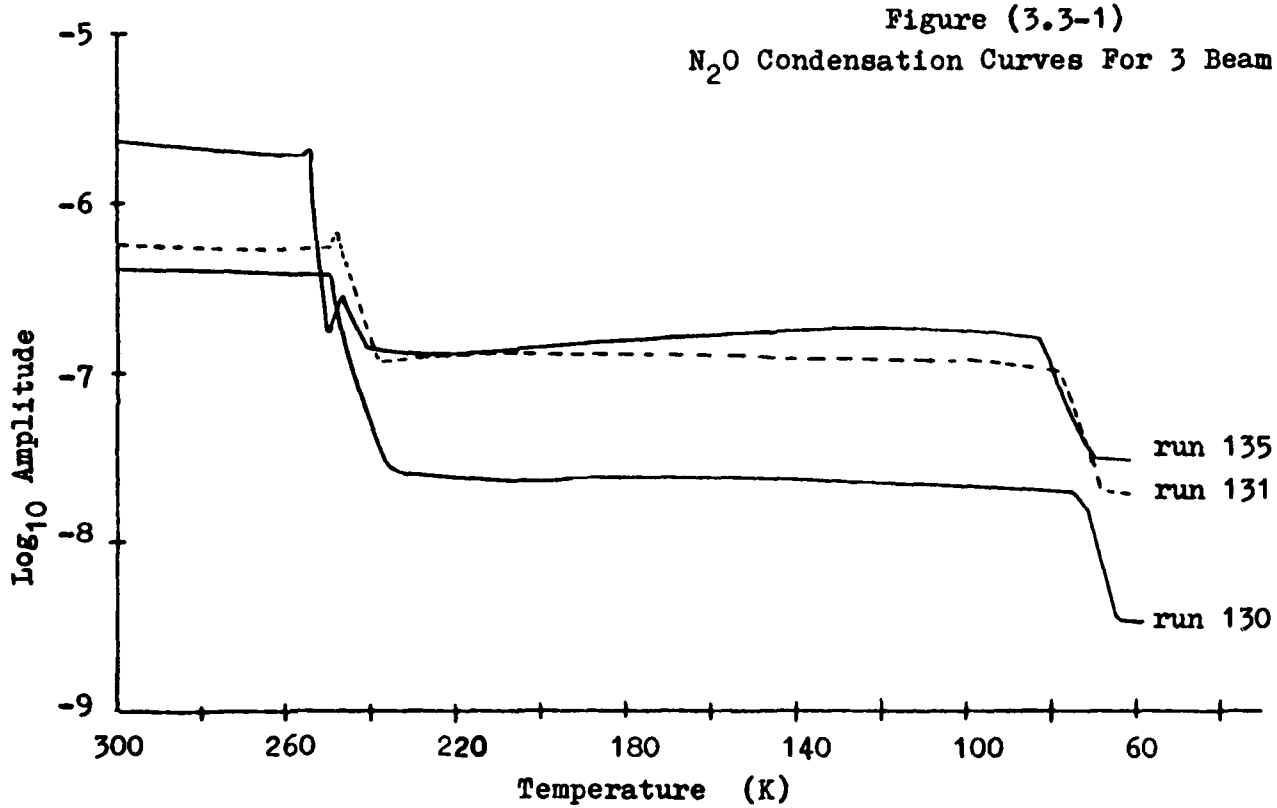

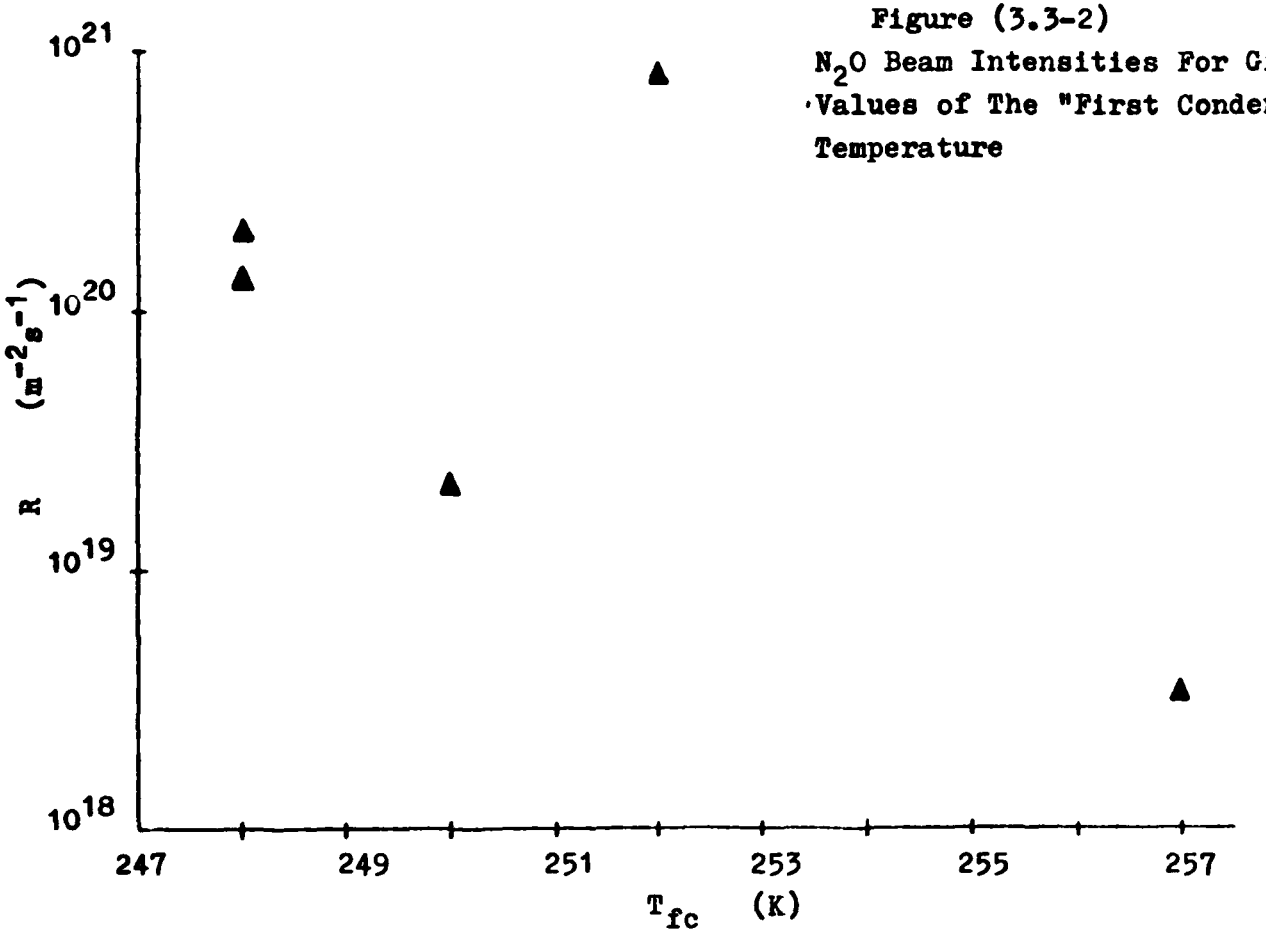

Figure (3.3-2)
N_2O Beam Intensities For Given Values of The "First Condensation" Temperature

Figure (3.3-3) Equivalent Intensity Captured By The First Condensation For CO_2 On Gold-Flashed (O) And HMDS-Coated (Δ) Stainless Steel Surfaces

Figure (3.3-3)

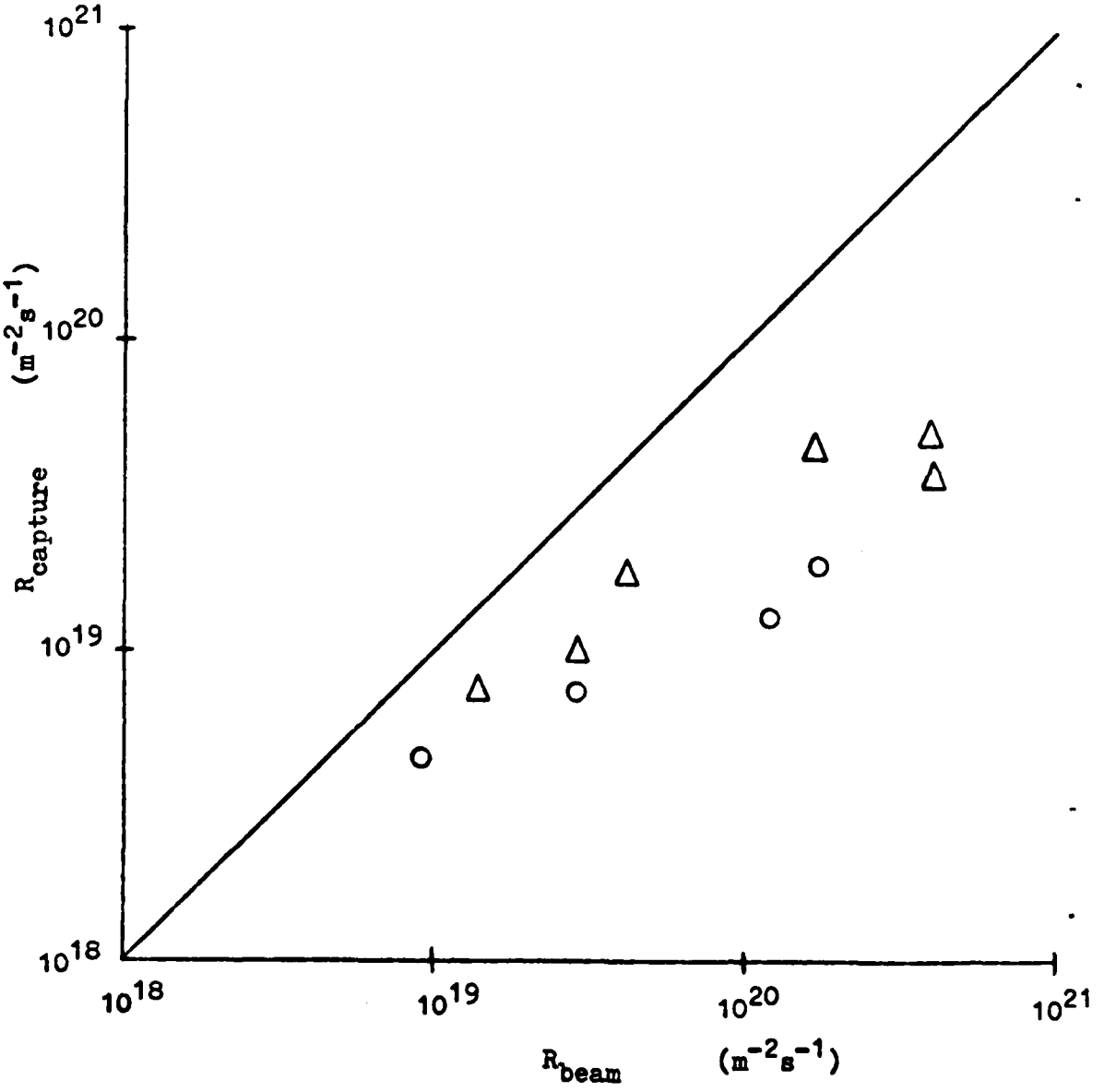
10^{21}
10^{20}
10^{19}
10^{18}
$R_{capture}$ $(m^{-2}s^{-1})$
10^{18}
10^{19}
10^{20}
10^{21}
R_{beam} $(m^{-2}s^{-1})$

Figure (3.3-4) Equivalent Intensity Captured By The First Condensation For N_2O On Gold-Flashed (O) And HMDS-Coated (Δ) Stainless Steel Surfaces

Figure (3.3-4)

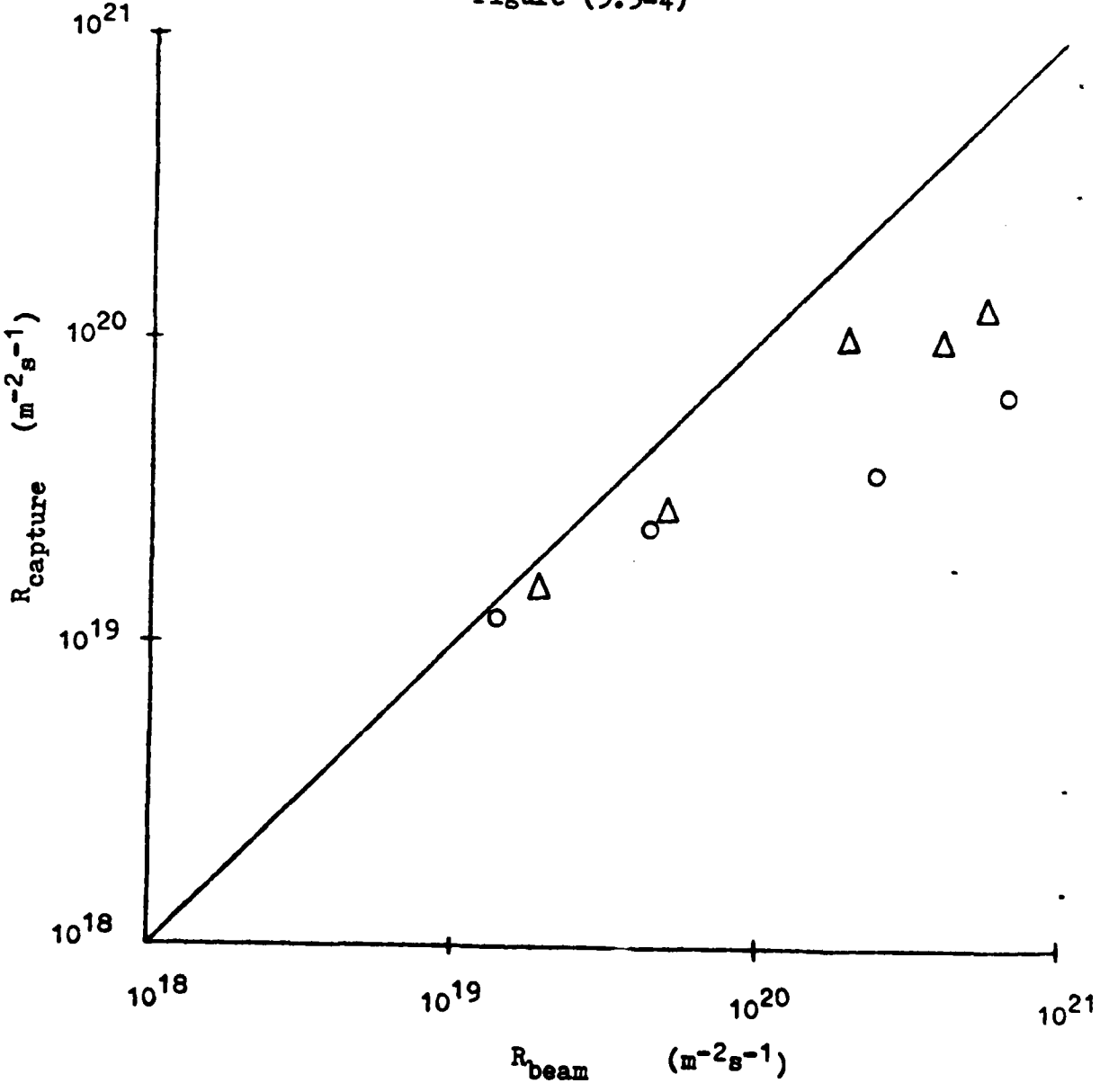
10^{21}
10^{20}
10^{19}
10^{18}
$R_{capture}$ $(m^{-2}s^{-1})$
10^{18}
10^{19}
10^{20}
10^{21}
R_{beam} $(m^{-2}s^{-1})$

Figure (3.3-5)
CO_2 Condensation On The HMDS Coated Stainless Steel Surface

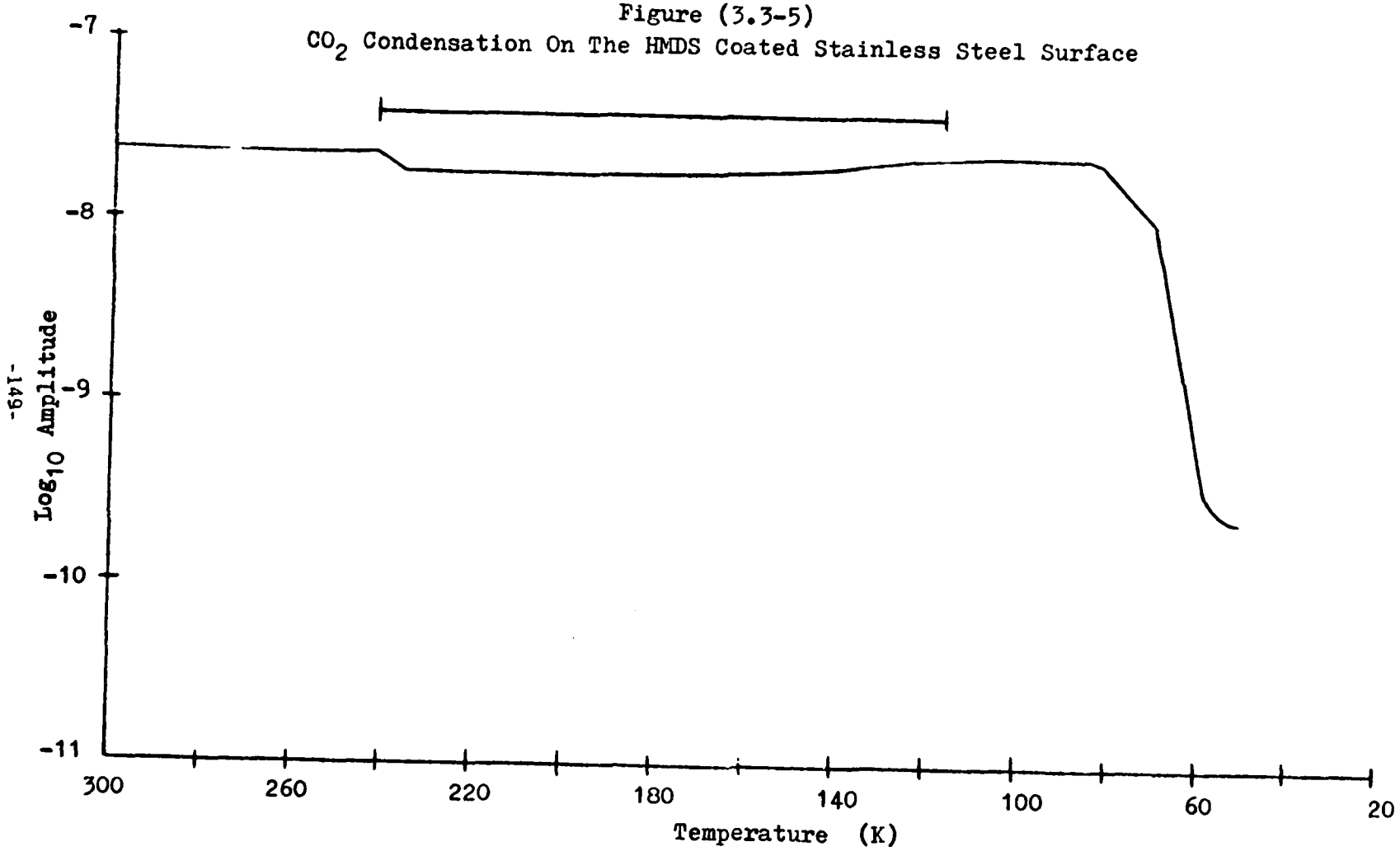

Figure (3.3-6) Equivalent Intesity Captured By The First Condensation For NO On Gold-Flashed (O) And HMDS-Coated (Δ) Stainless Steel Surfaces

Figure (3.3-6)

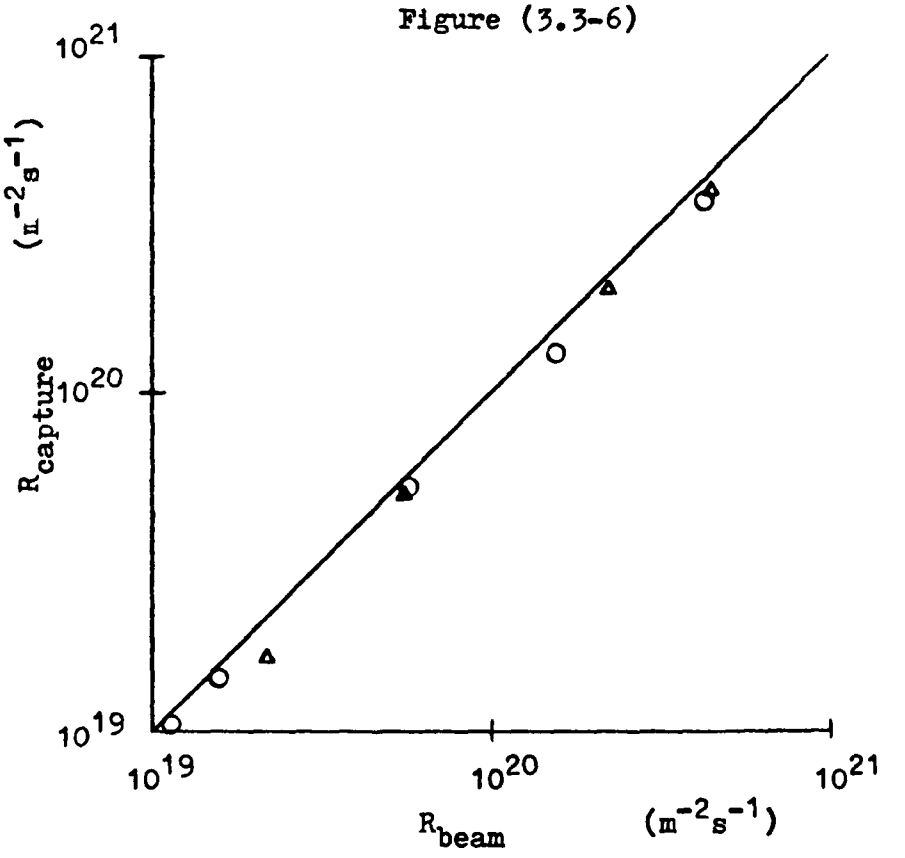

Figure (3.3-7)

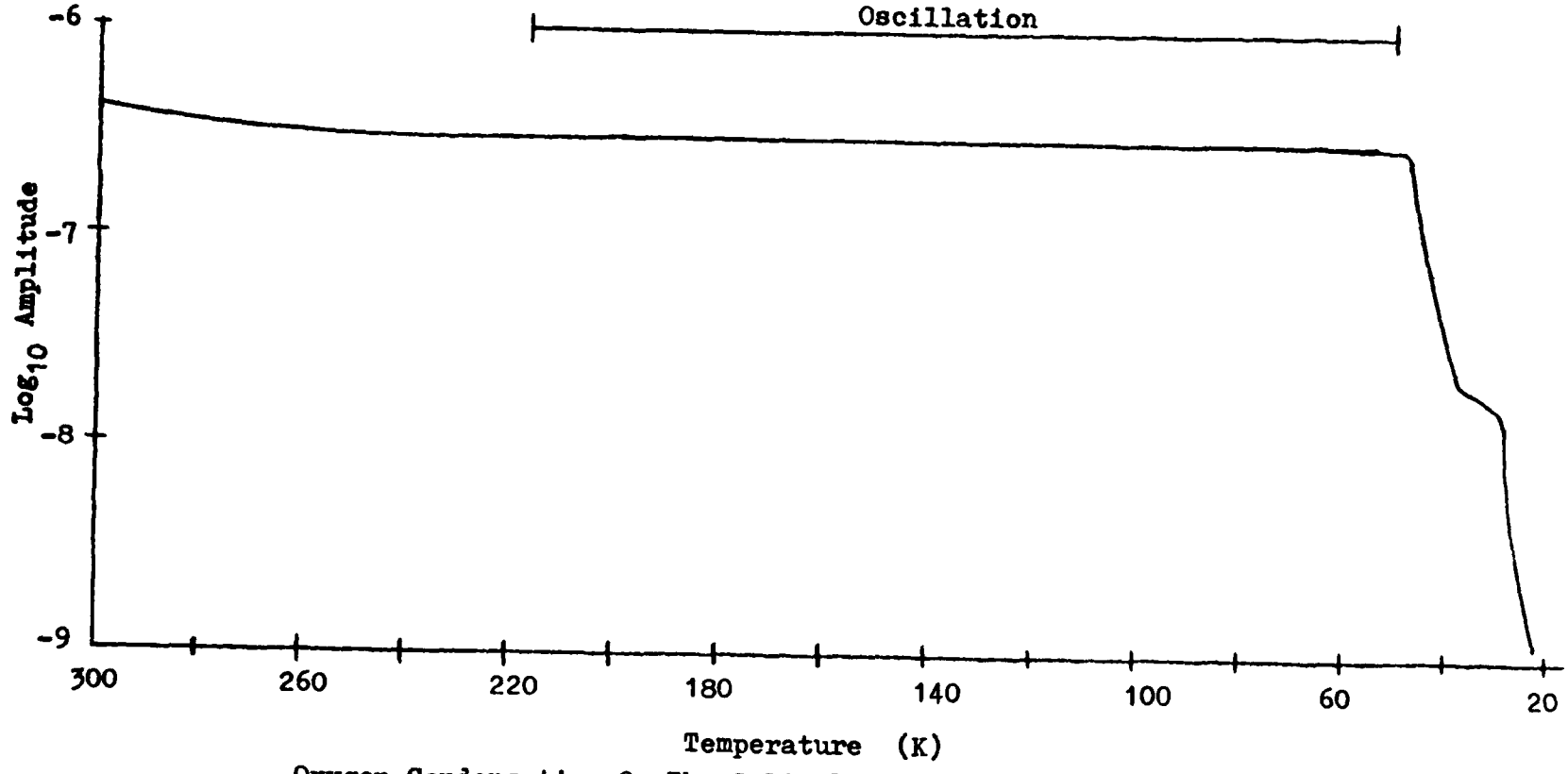

Oxygen Condensation On The Gold-flashed Stainless Steel Surface

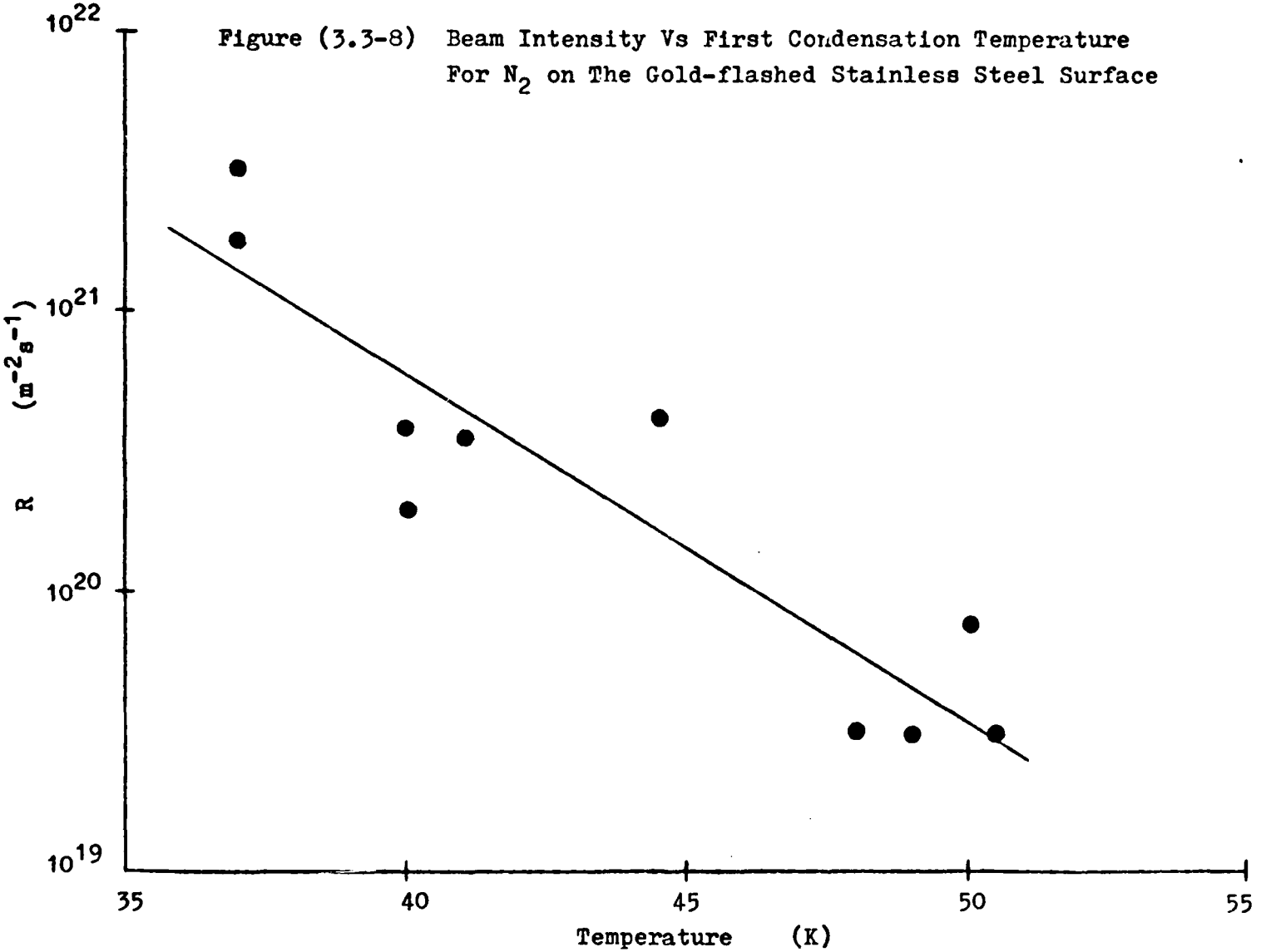

Figure (3.3-8) Beam Intensity Vs First Condensation Temperature For N_2 on The Gold-flashed Stainless Steel Surface

Figure (3.3-9)

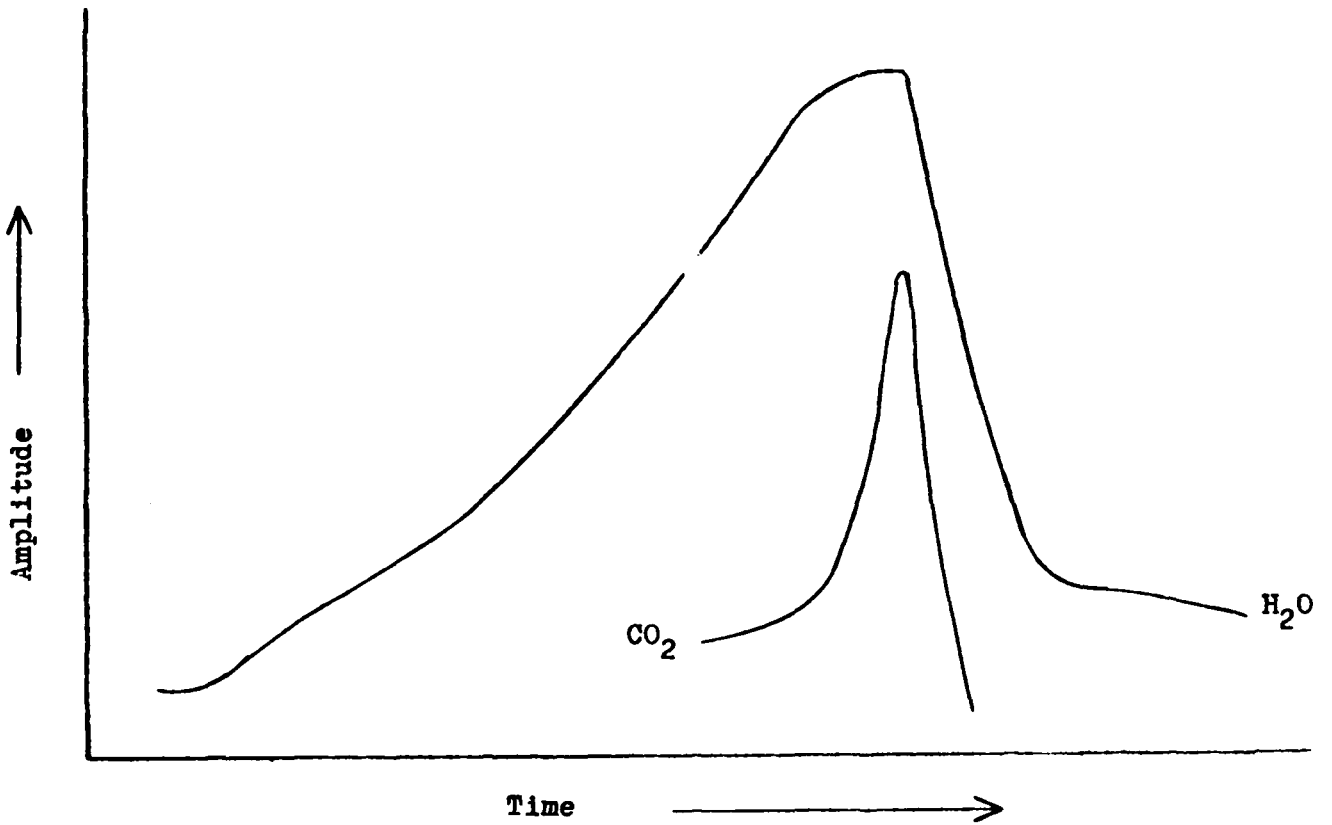

Thermal Desorption Spectra Of H_2O and CO_2 Taken Just Prior To The First Condensation

Figure (3.3-10)

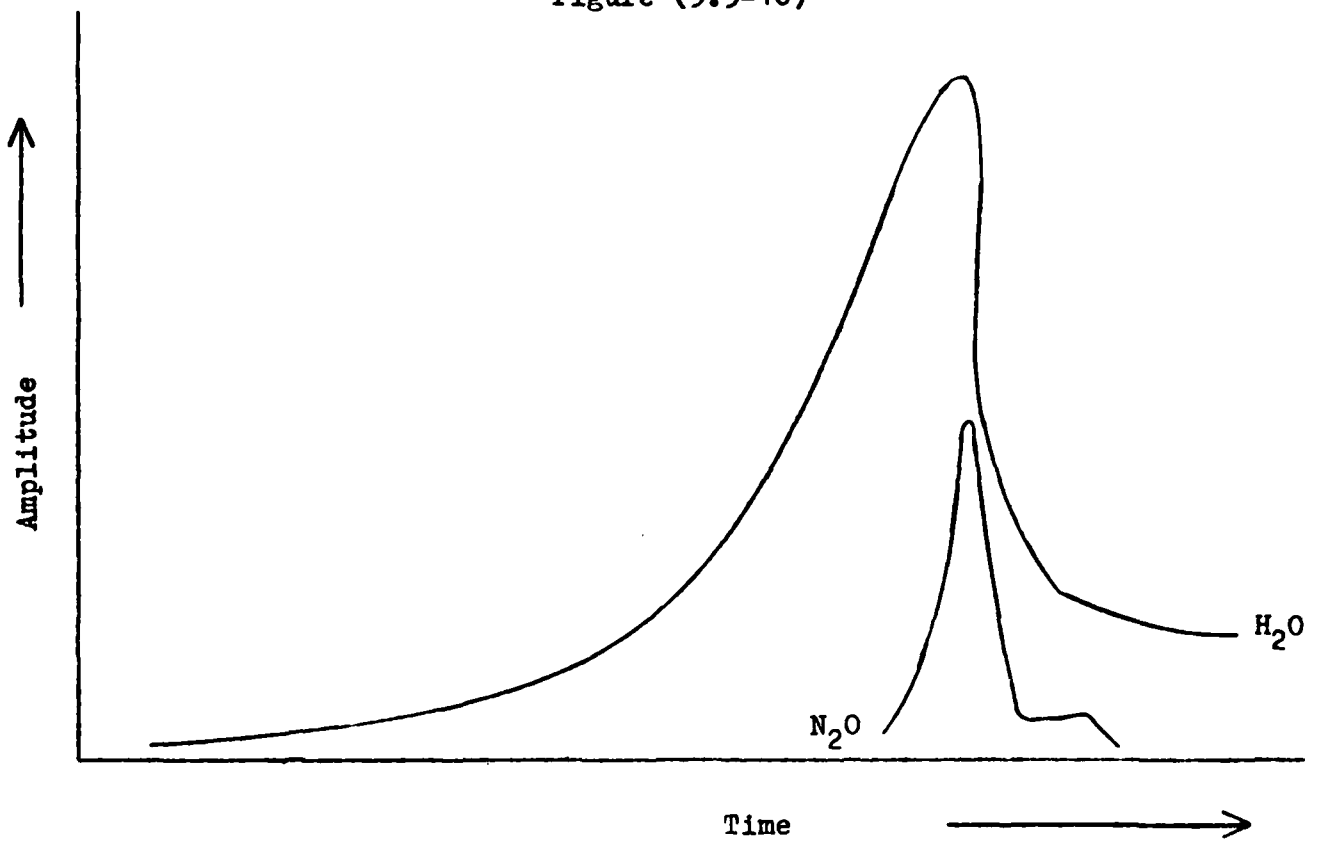

Thermal Desorption Spectra Of H_2O And N_2O Taken Just Prior To The First Condensation

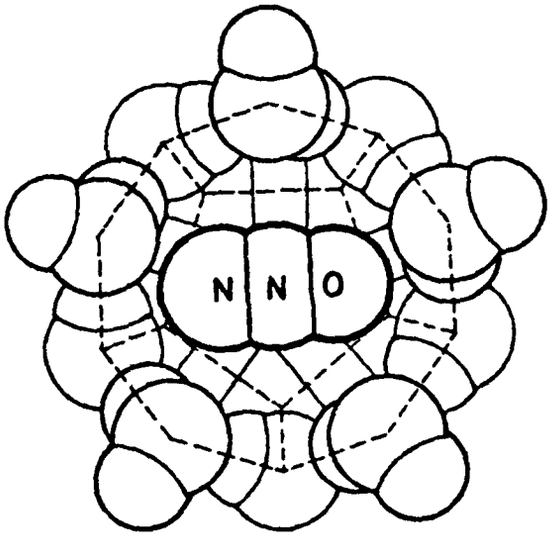

N_2O

Figure (3.3-11)
N_2O Molecule Embedded In An
Opened Water-Clathrate Dodecahedron
(from Siksna, 1973)

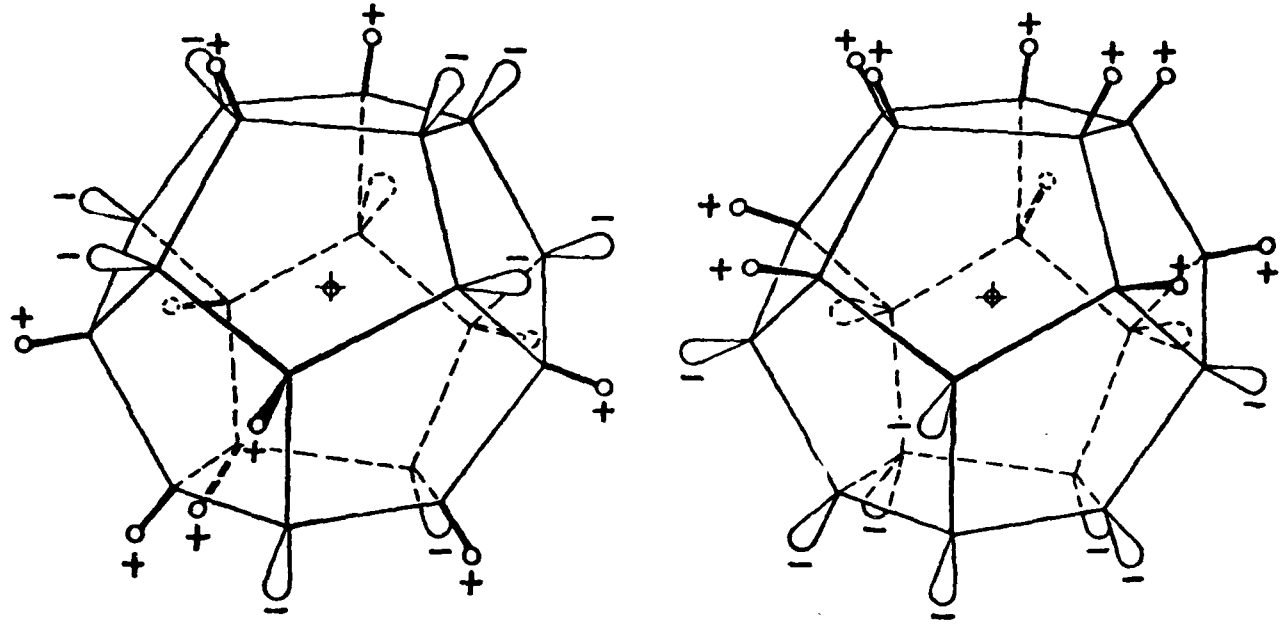

Figure (3.3-12) Distribution Of The Excess Charges On The Surface Of The Water-Clathrate Dodecahedron (from Siksna, 1973)

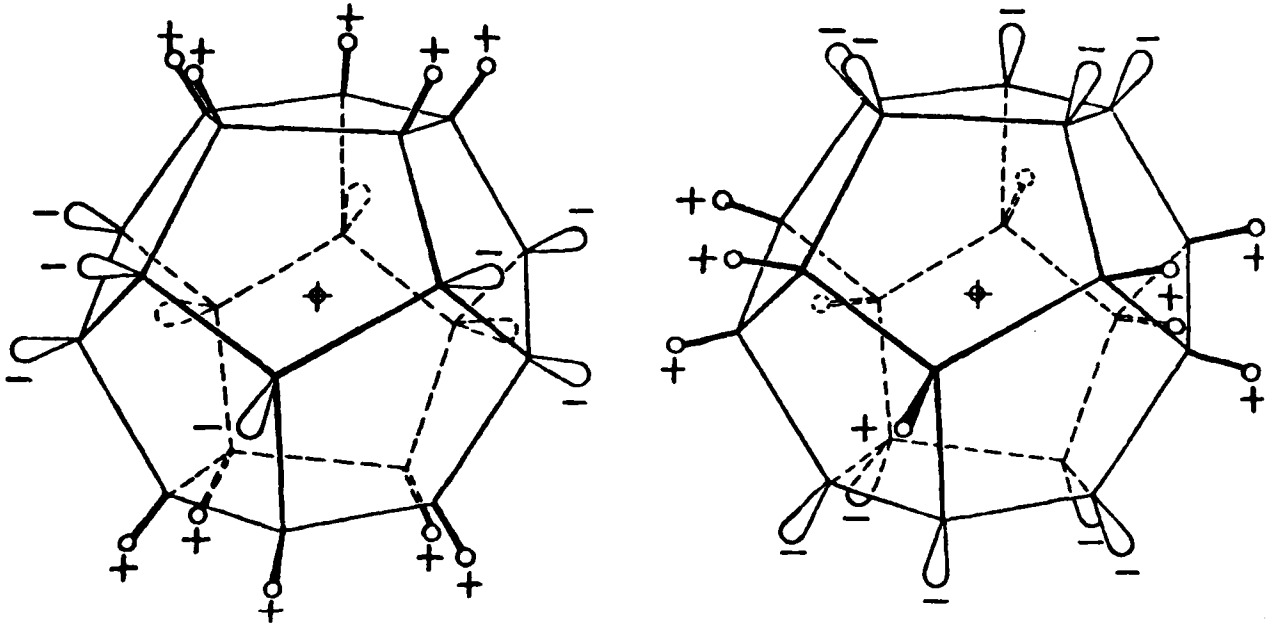

Figure (3.3-13) Distribution Of The Excess Charges On The Surface Of The Water-Clathrate Dodecahedron, Forming Quadrupoles (from Siksna, 1973)

Figure (3.3-14) Condensation Curves For CO_2 On Gold-Flashed Stainless Steel As Given By The Lock-In (----) And Total (——) Signal

Figure (3.3-14)

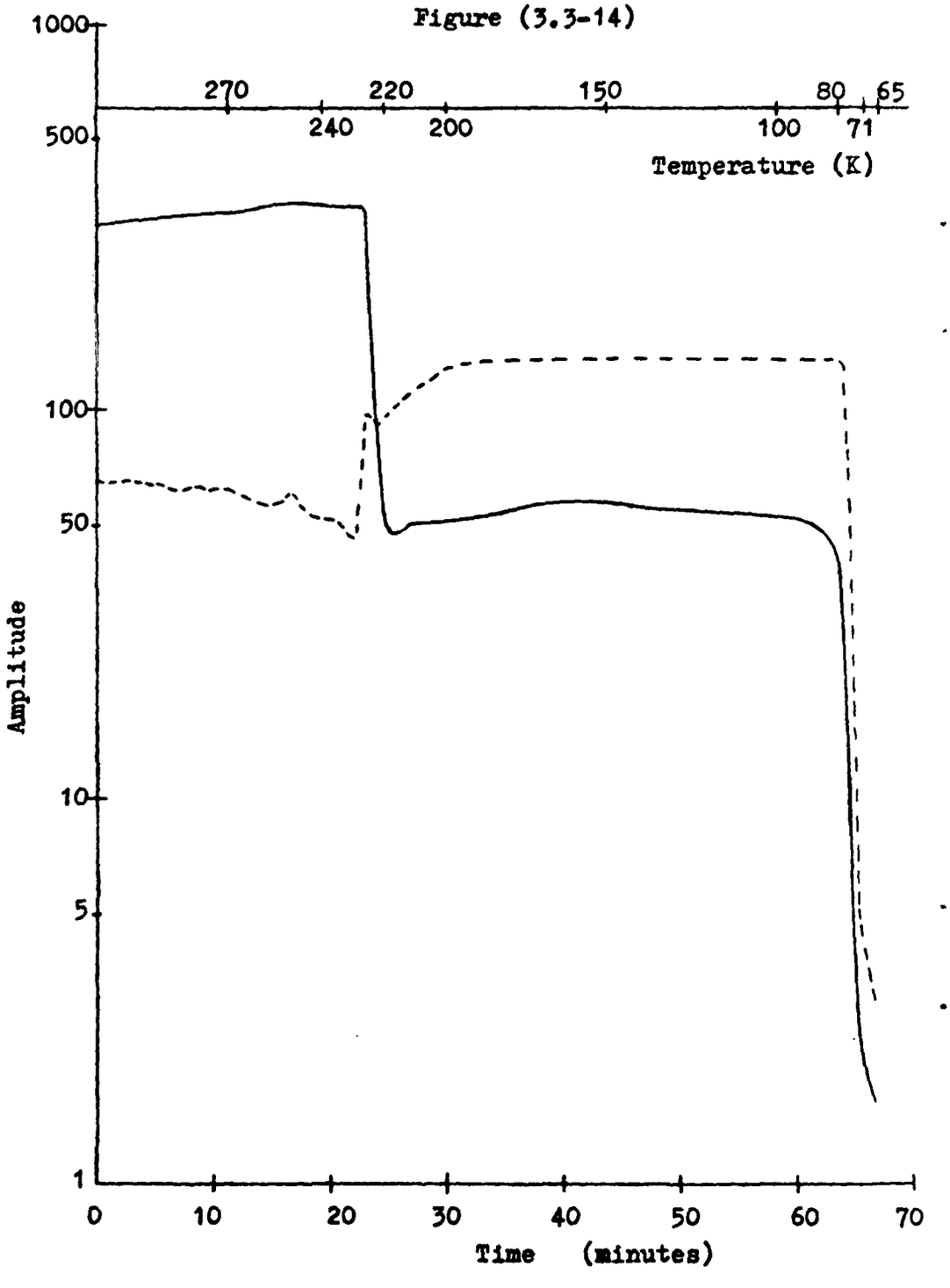
1000
500
100
50
10
5
1
Amplitude
270
240
220
200
150
100
80
71
65
Temperature (K)
0
10
20
30
40
50
60
70
Time (minutes)

Figure (3.3-15) Condensation Curves For CO_2 On HMDS-Coated Stainless Steel As Given By The Lock-In (----) And Total (——) Signal

Figure (3.3-15)

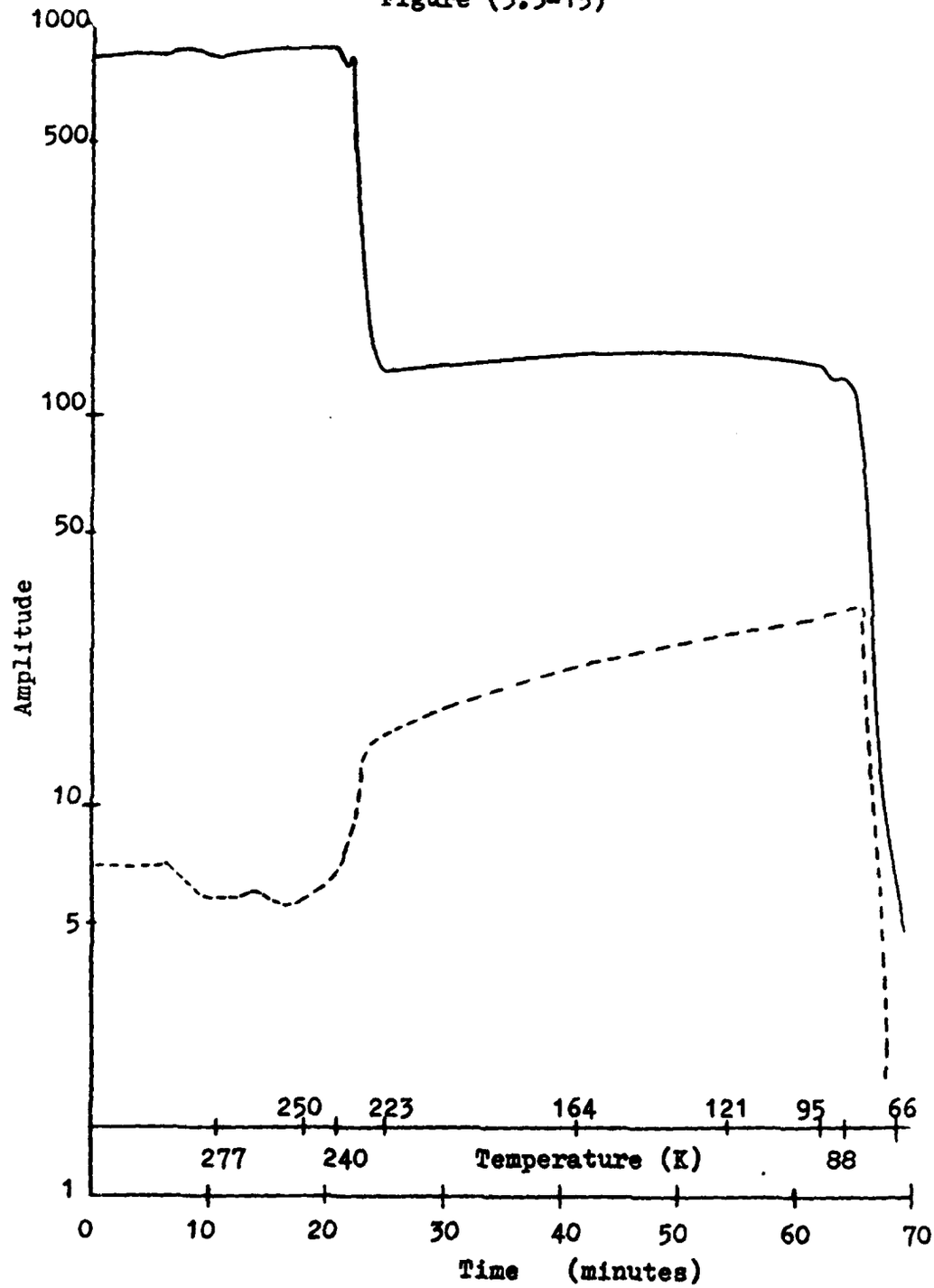
1000
500
100
50
10
5
1
Amplitude
250
223
164
121
95
66
277
240
Temperature (K)
88
0
10
20
30
40
50
60
70
Time (minutes)

Figure (3.3-16) Condensation Curves For N_2O On Gold-Flashed Stainless Steel As Given By The Lock-In (----) And Total (——) Signal

Figure (3.3-16)

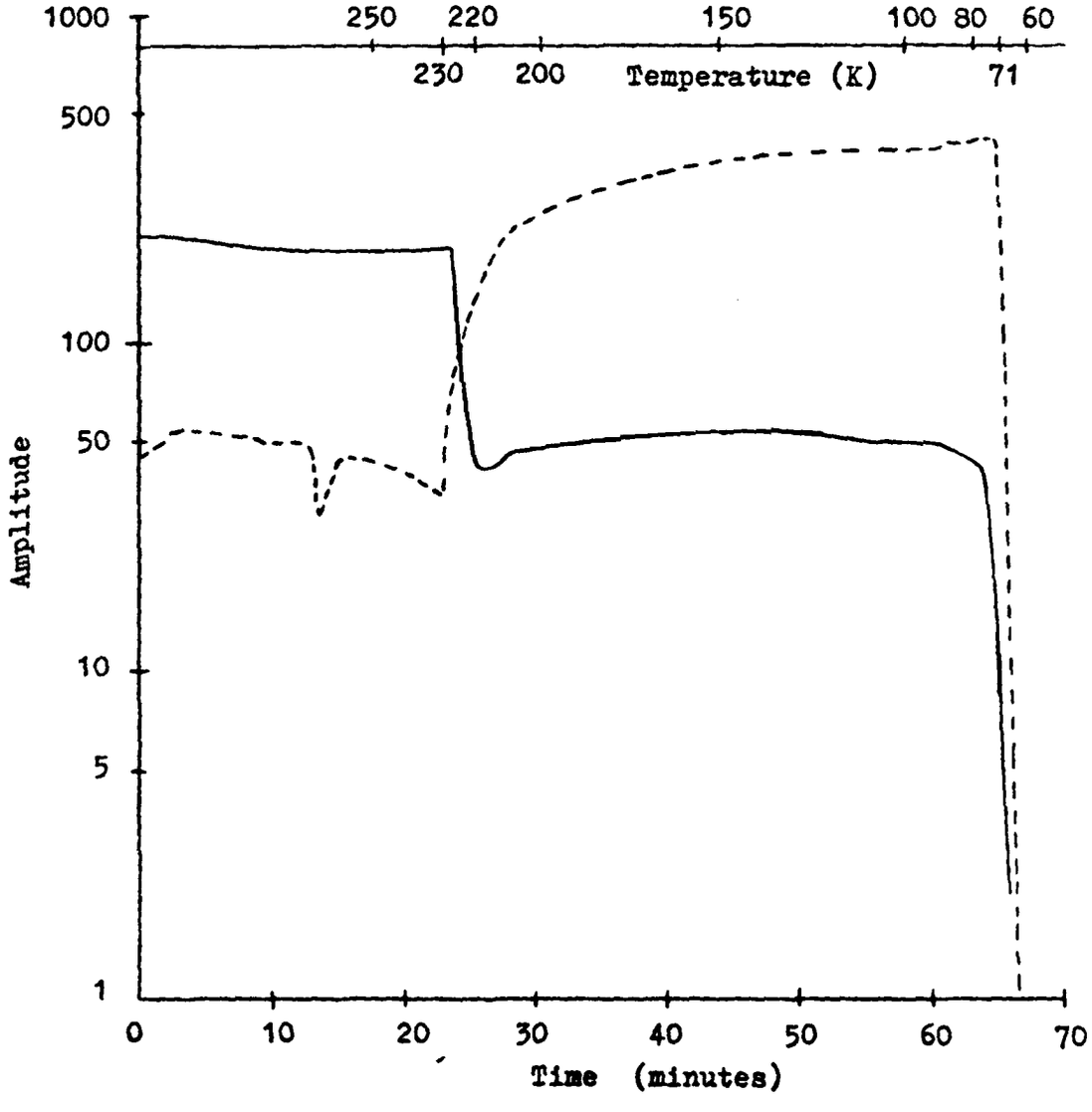
1000
500
100
50
10
5
1
Amplitude
250
220
150
100
80
60
230
200
Temperature (K)
71
0
10
20
30
40
50
60
70
Time (minutes)

Figure (3.3-17) Condensation Curves For N_2O On HMDS-Coated Stainless Steel As Given By The Lock-In (----) And Total (——) Signal

Figure (3.3-17)

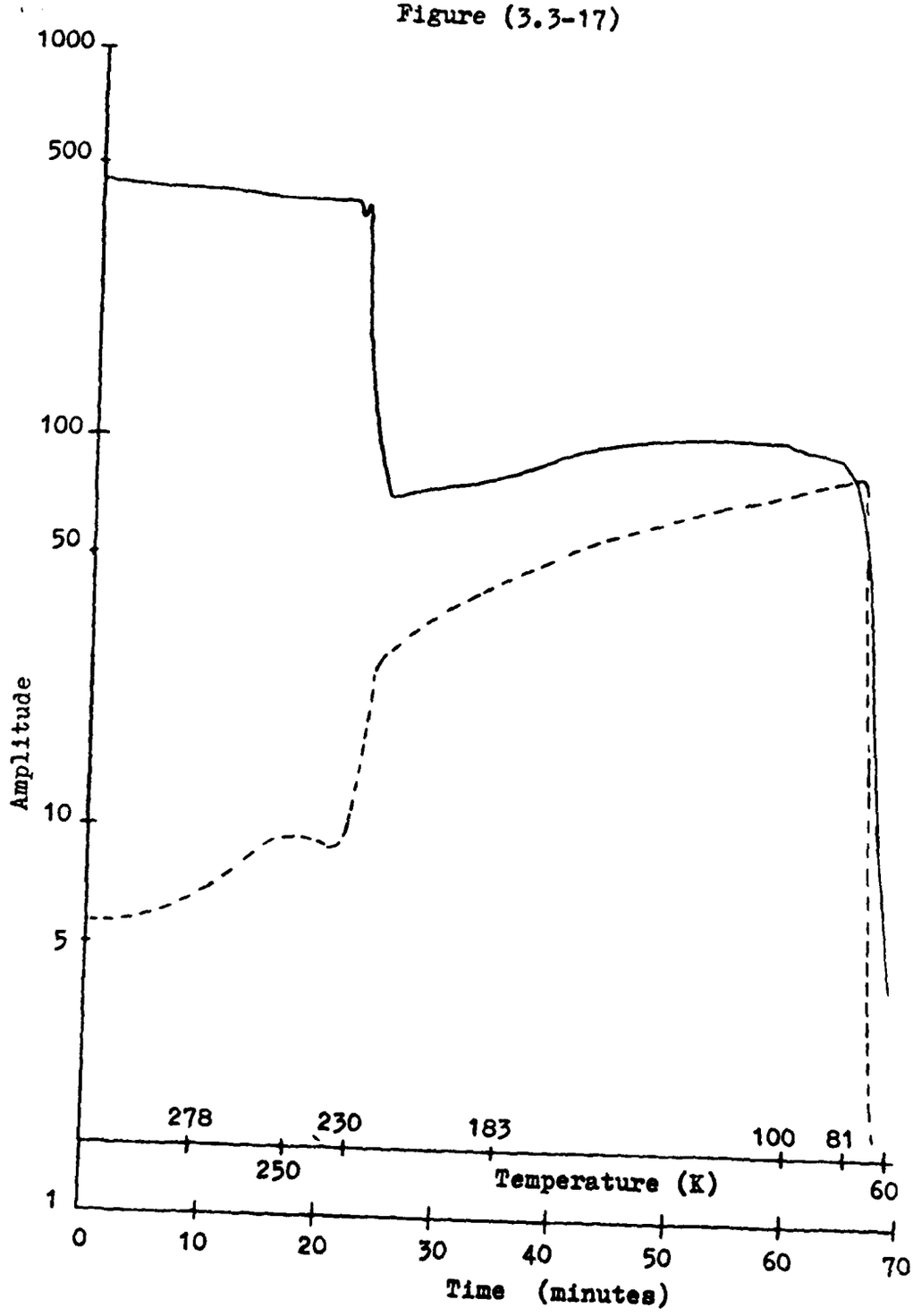
1000
500
100
50
10
5
1
Amplitude
278
230
183
100
81
250
Temperature (K)
60
0
10
20
30
40
50
60
70
Time (minutes)

Figure (3.3-18) Condensation Curves For Freon 12 On Gold-Flashed Stainless Steel As Given By The Lock-In (----) And Total(——) Signal

Figure (3.3-18)

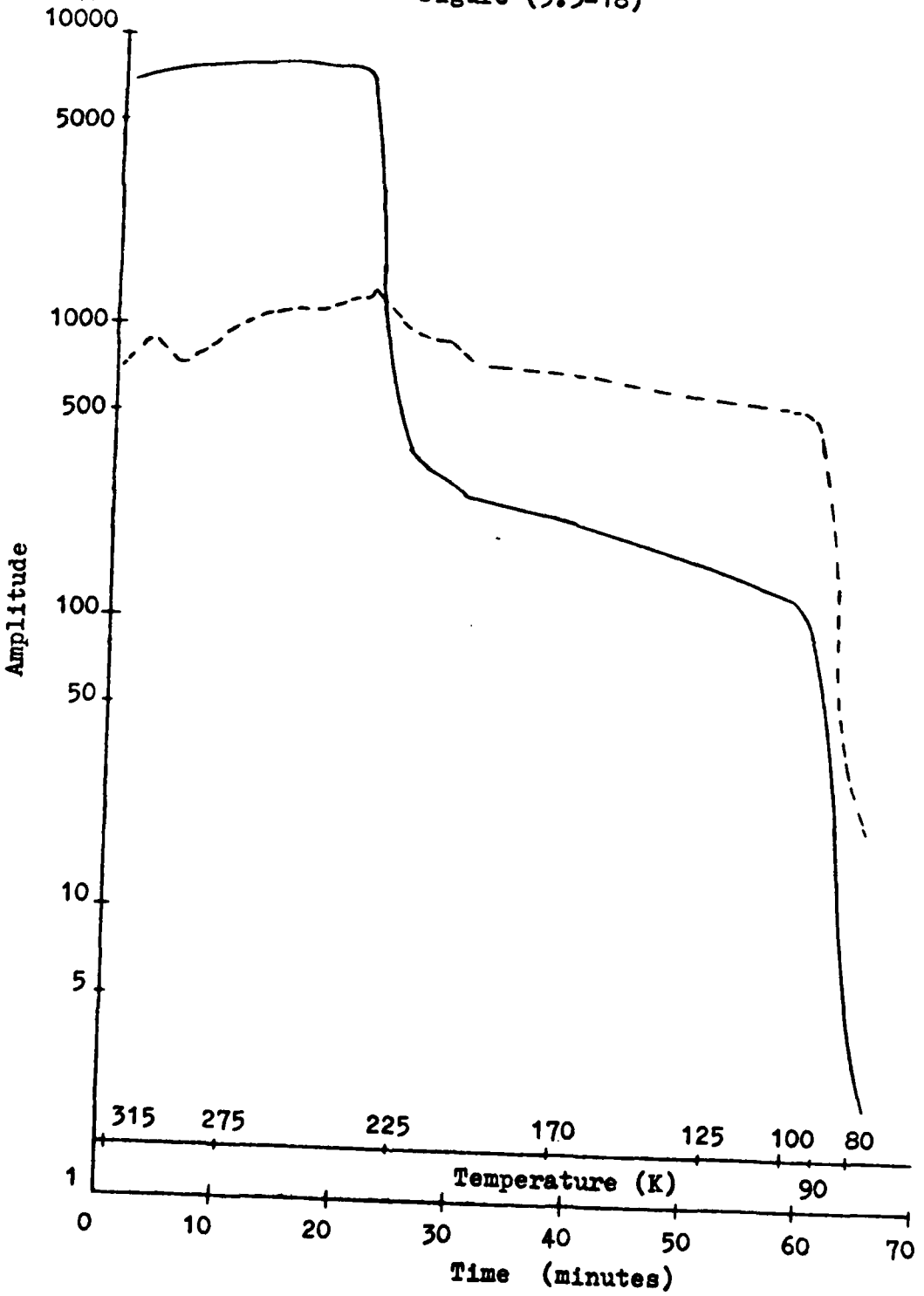
10000
5000
1000
500
100
50
10
5
1
Amplitude
315
275
225
170
125
100
80
Temperature (K)
90
0
10
20
30
40
50
60
70
Time (minutes)

Figure (3.3-19) Condensation Curves For Freon 12 On HMDS-Coated Stainless Steel As Given By The Lock-In (----) And Total (——) Signal

Figure (3.3-19)

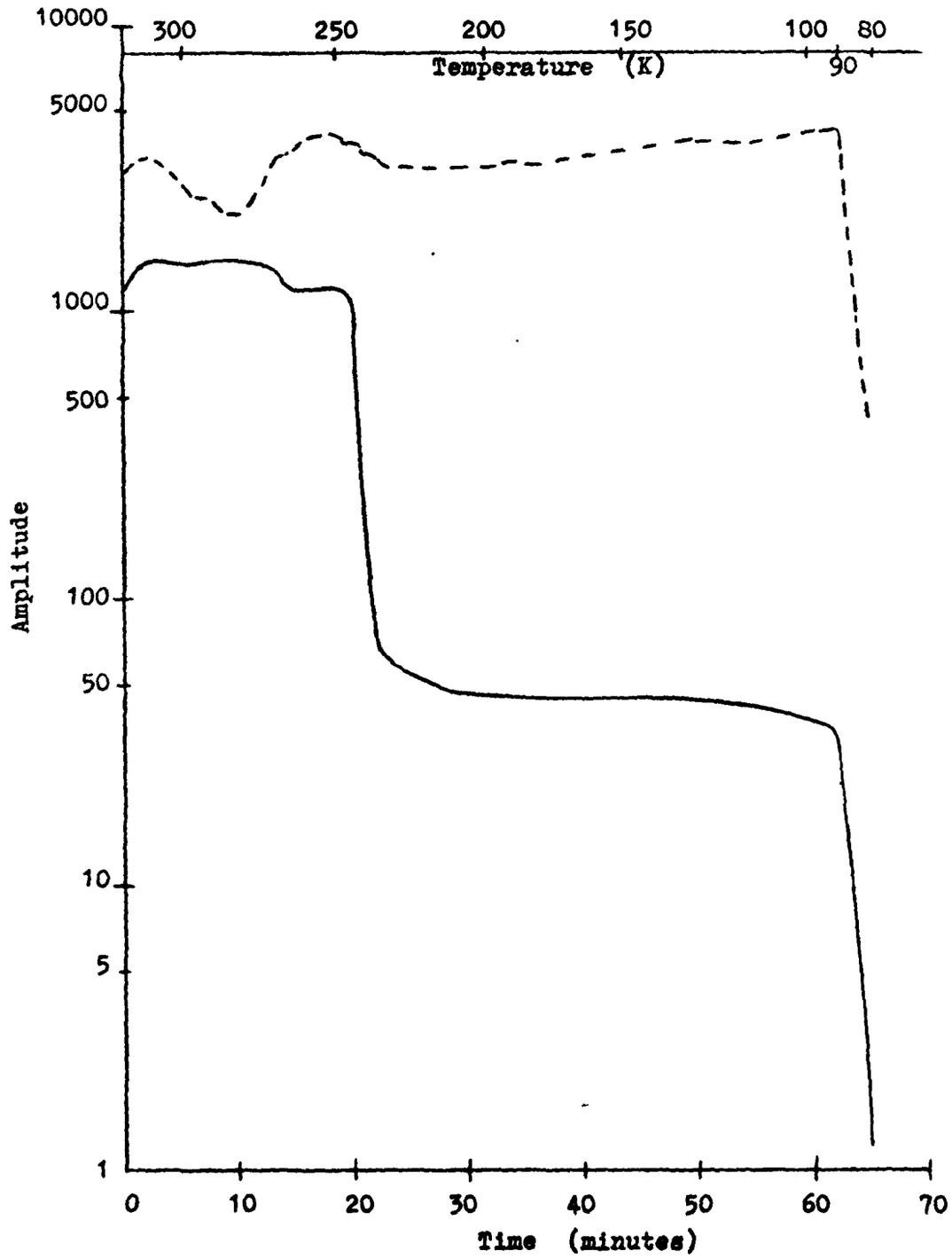
10000
5000
1000
500
100
50
10
5
1
Amplitude
300
250
200
150
100
80
90
Temperature (K)
0
10
20
30
40
50
60
70
Time (minutes)

Figure (3.3-20) Condensation Curves For Freon 11 On Gold-Flashed Stainless Steel As Given By The Lock-In (----) And Total (——) Signal

Figure (3.3-20)

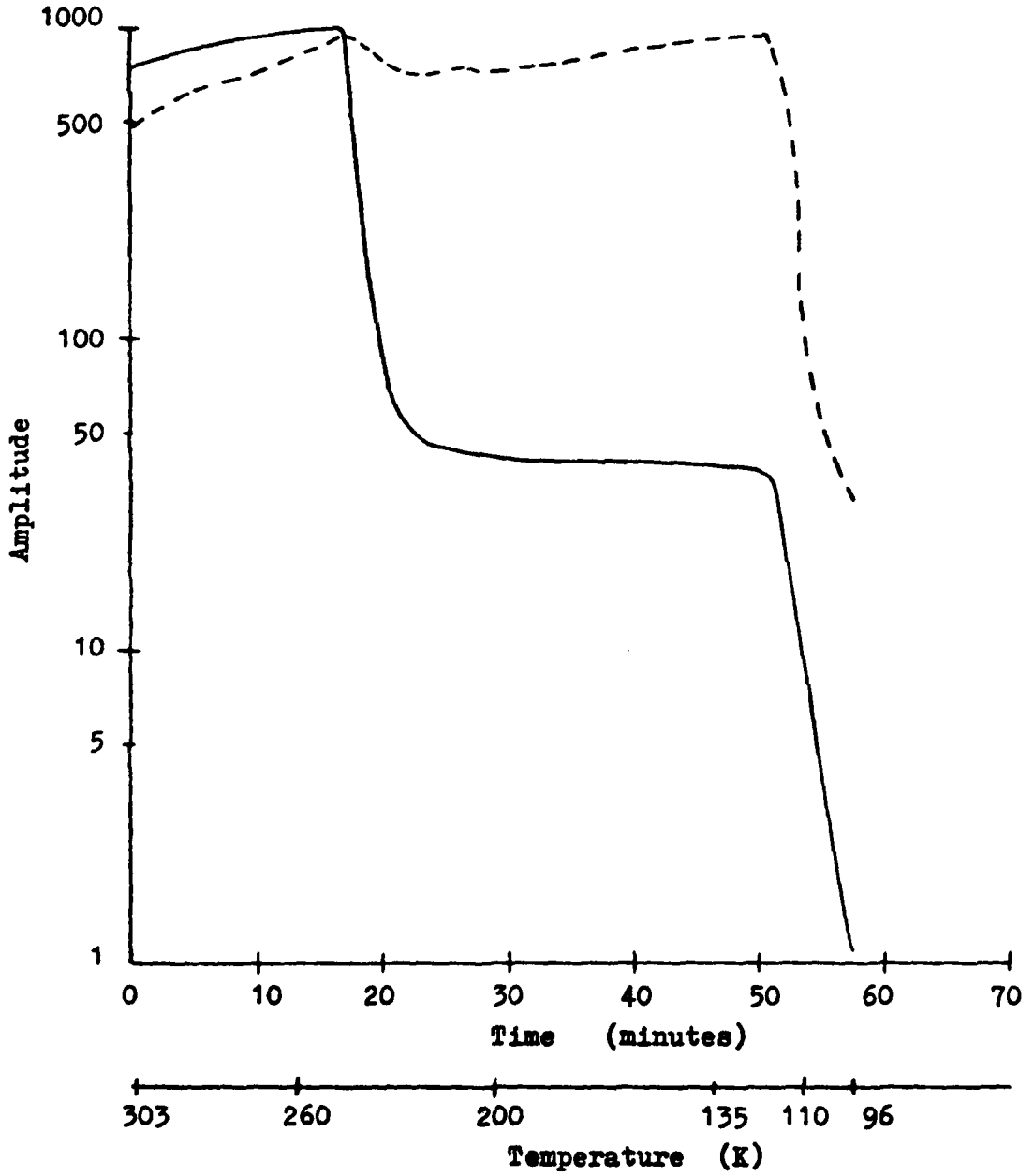
1000
500
100
50
10
5
1
Amplitude
0
10
20
30
40
50
60
70
Time (minutes)
303
260
200
135
110
96
Temperature (K)

Figure (3.3-21) Condensation Curves For Freon 11 On HMDS-Coated Stainless Steel As Given By The Lock-In (----) And Total (——) Signal

Figure (3.3-21)

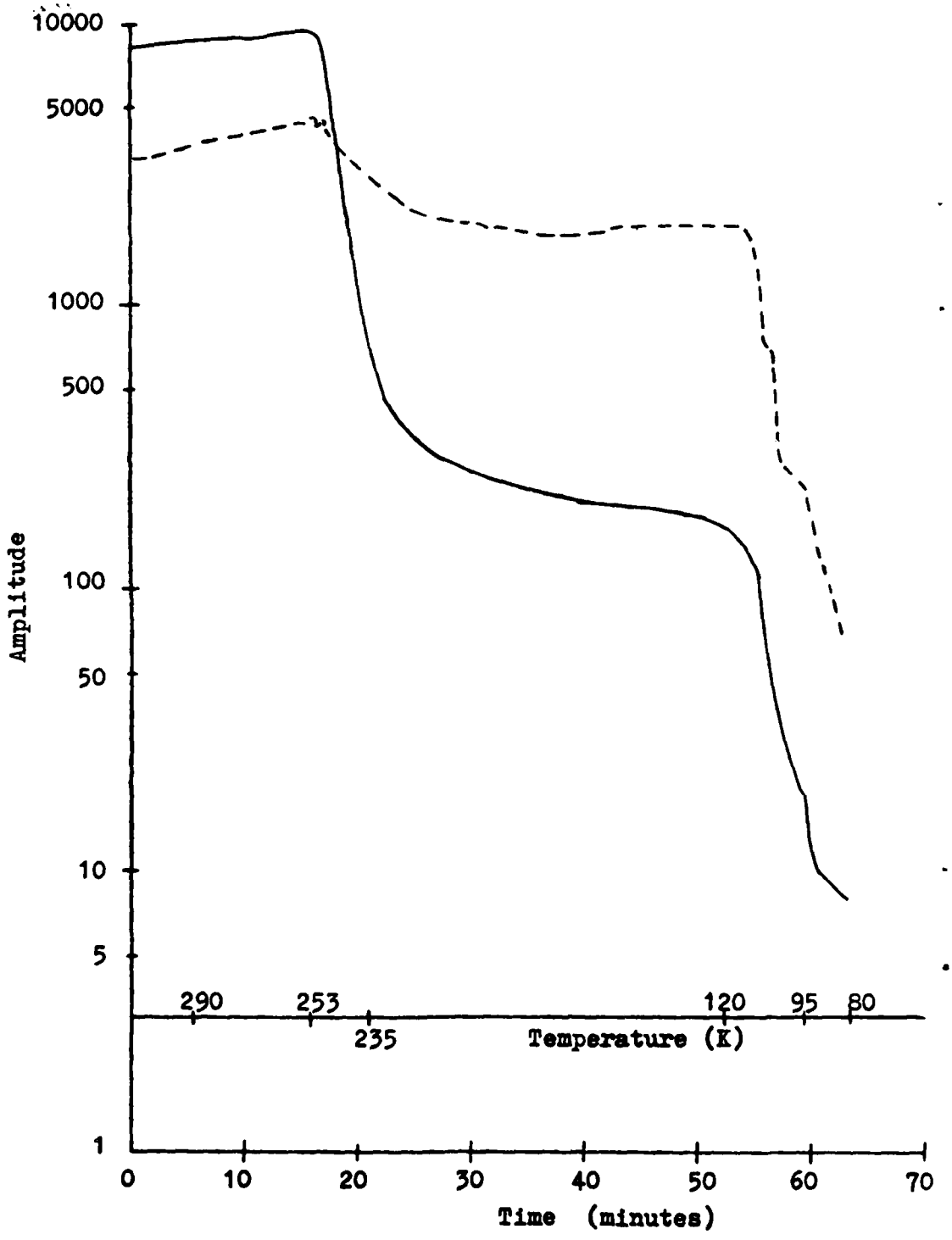
10000
5000
1000
500
100
50
10
5
1
Amplitude
290
253
235
120
95
80
Temperature (K)
0
10
20
30
40
50
60
70
Time (minutes)

Figure (3.3-22) Condensation Curves For NO On Gold-Flashed Stainless Steel As Given By The Lock-In (----) And Total (——) Signal

Figure (3.3-22)

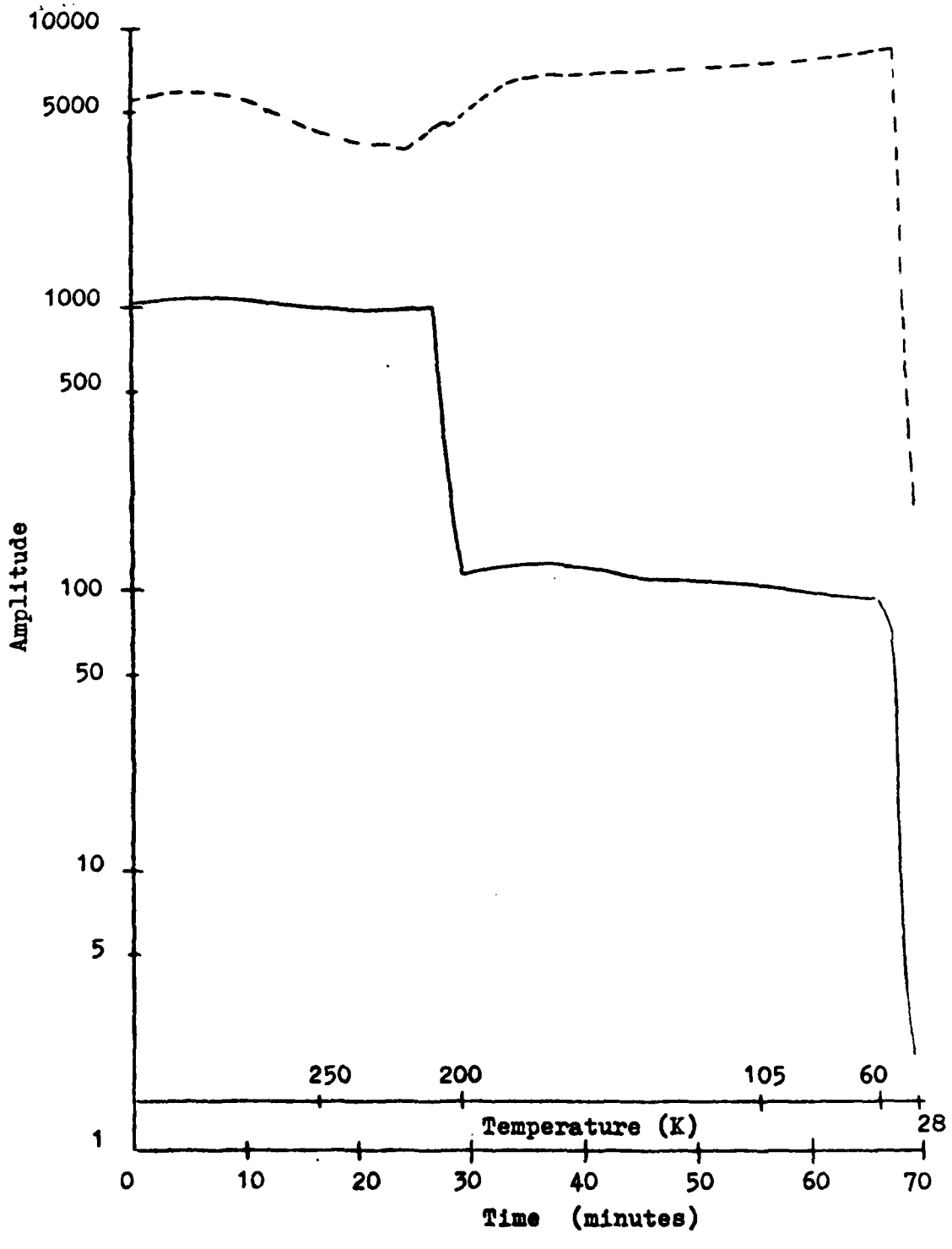
10000
5000
1000
500
100
50
10
5
1
Amplitude
250
200
105
60
Temperature (K)
28
0
10
20
30
40
50
60
70
Time (minutes)

Figure (3.3-23) Condensation Curves For NO On HMDS-Coated Stainless Steel As Given By The Lock-In (----) And Total (——) Signal

Figure (3.3-23)

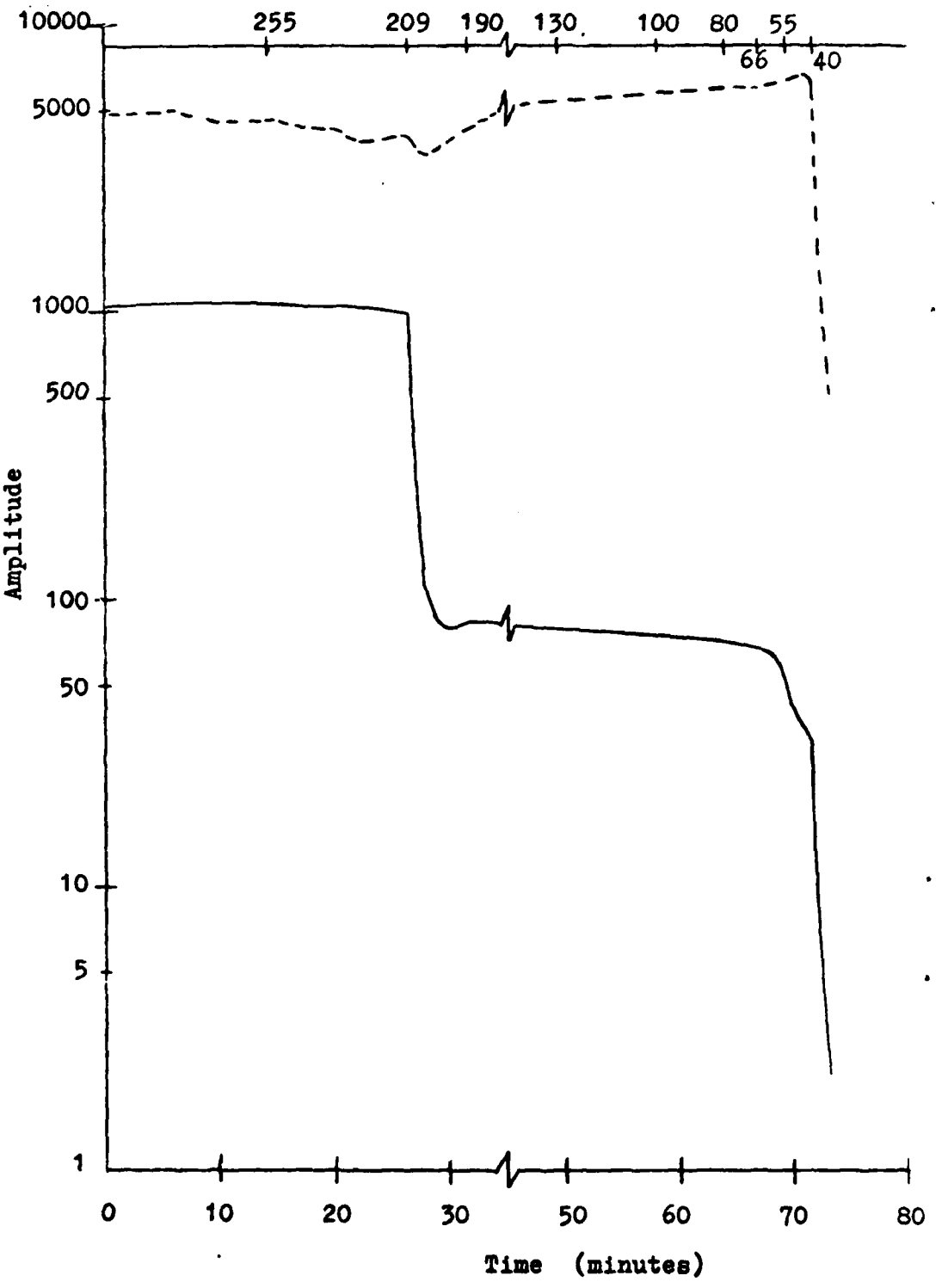
Temperature (K)
10000
255
209
190
130
100
80
55
66
40
5000
1000
500
Amplitude
100
50
10
5
1
0
10
20
30
50
60
70
80
Time (minutes)

Figure (3.3-24) First Condensation Temperature As A Function Of Molecular Polarizability For Various Species On Gold-Flashed (●) And HMDS-Coated (▲) Stainless Steel Surfaces

Figure (3.3-24)

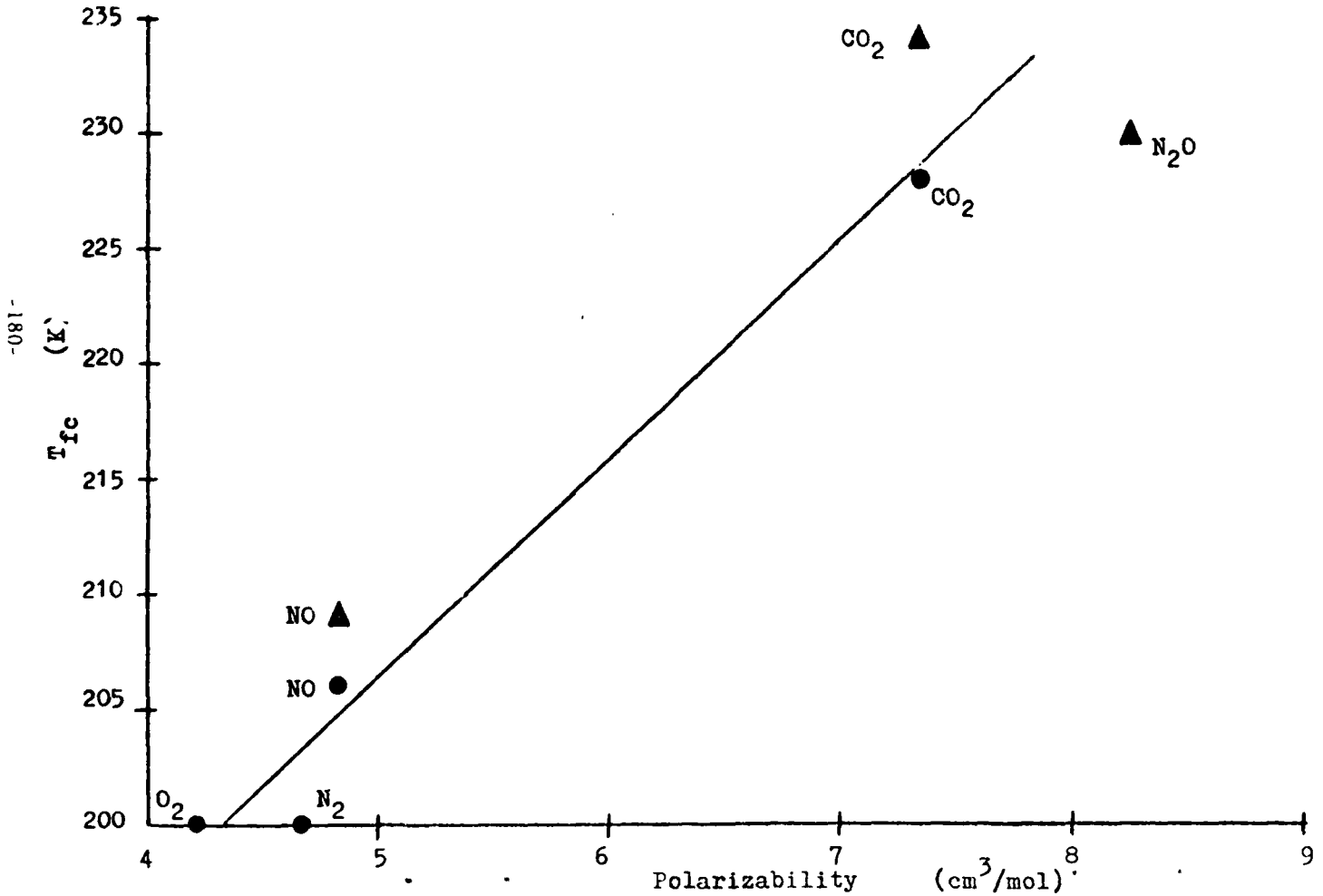
235
230
225
220
215
210
205
200
T_{fc} (K)
CO_2
N_2O
CO_2
NO
NO
O_2
N_2
4
5
6
7
8
9
Polarizability (cm^3/mol)

Figure (3.3-25) CO_2 Desorption Spectra Taken After The First Condensation With The Molecular Beam On, As Given By The Lock-In (----) And Total (——) Signal
(Note: Point A represents the lock-in signal level prior to the first condensation, as does point B for the total signal)

Figure (3.3-25)

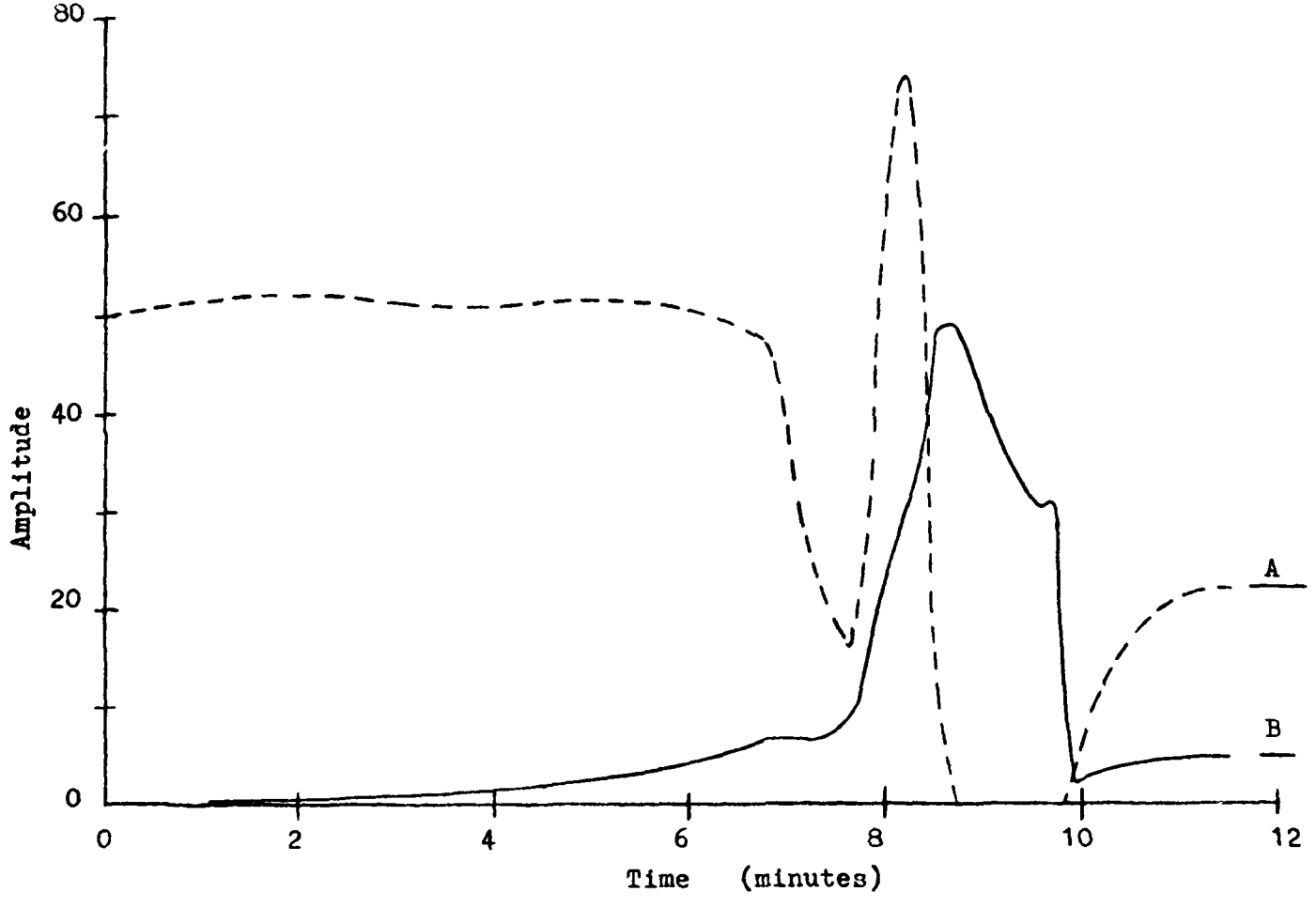

Figure (3.3-26) Density Distributions Calculated By The Cell Model

Figure (3.3-26)

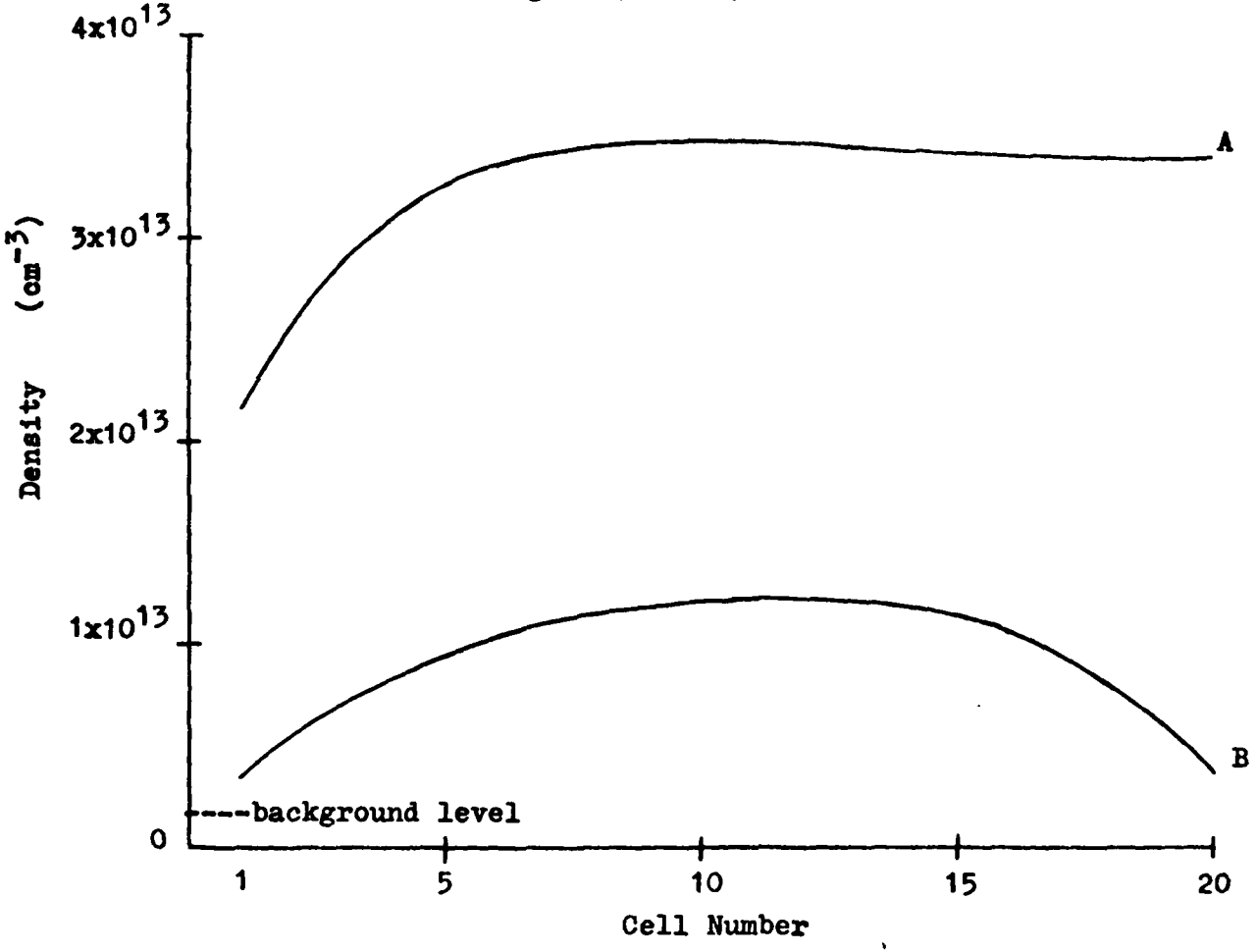
4x10^13
3x10^13
2x10^13
1x10^13
0
Density (cm^-3)
A
B
---background level
1
5
10
15
20
Cell Number

Figure (3.3-27) Incident And Reflected Beam Intensity Distributions Calculated By The Cell Model

Figure (3.3-27)

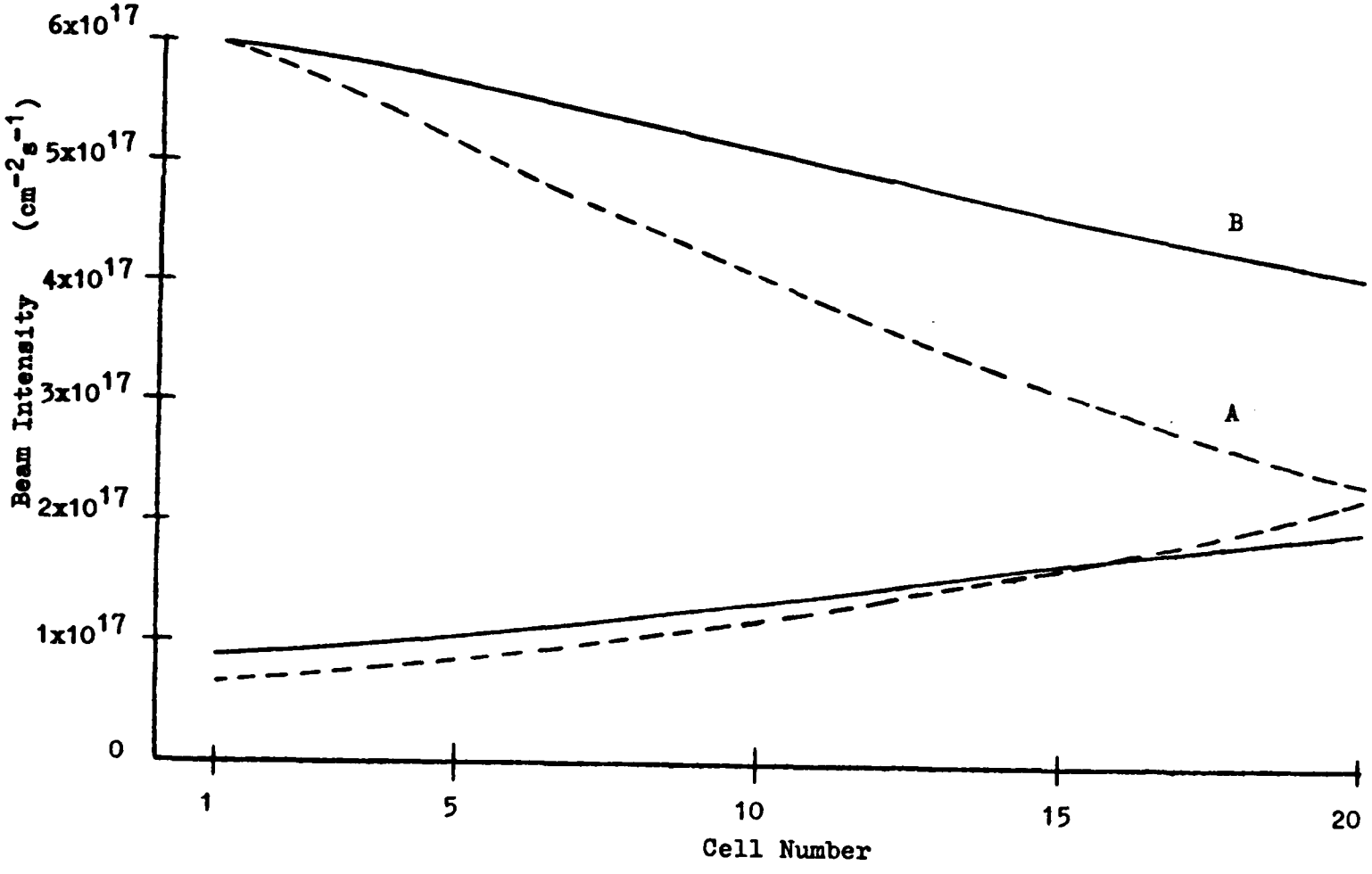
6x10^17
5x10^17
4x10^17
3x10^17
2x10^17
1x10^17
0
Beam Intensity (cm^-2 s^-1)
B
A
1
5
10
15
20
Cell Number

Figure (3.3-28) Condensation Curves For CO_2 On Gold-Flashed Stainless Steel At Low Beam Intensity, As Given By The Lock-In (----) And Total (——) Signal

Figure (3.3-28)

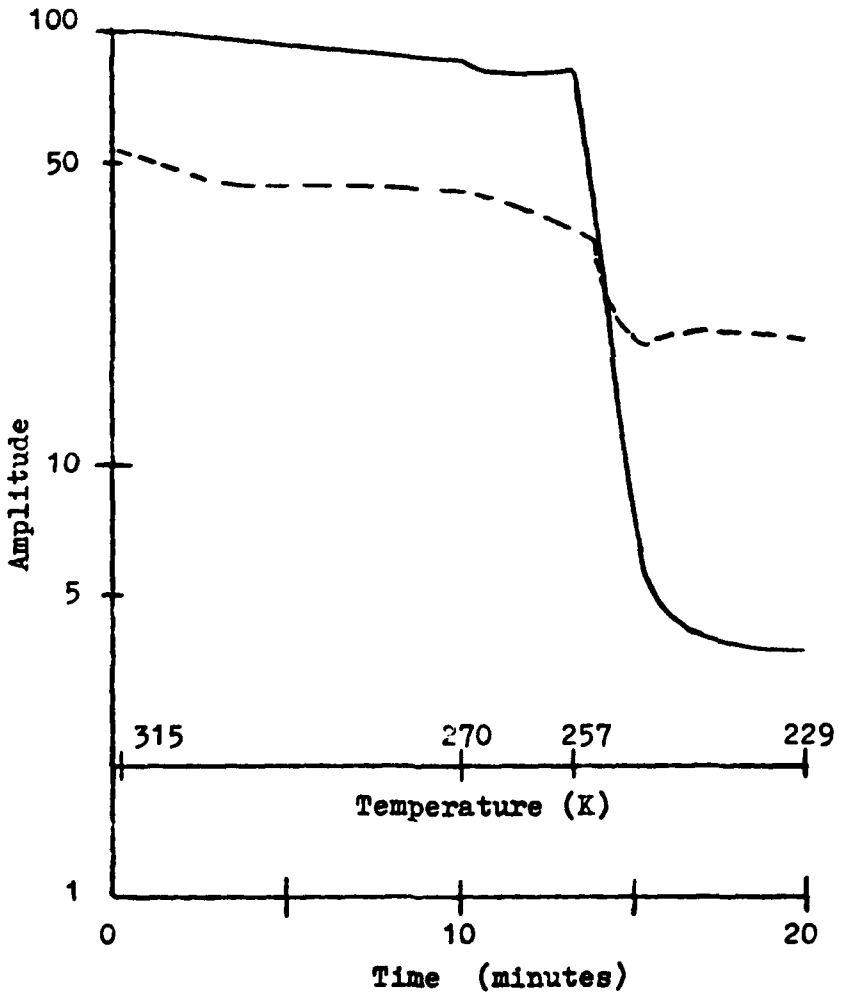
100
50
10
5
1
Amplitude
315
270
257
229
Temperature (K)
0
10
20
Time (minutes)

3.4 THE "TRUE CONDENSATION"

Should Nucleation Occur?

In the literature review section it has been shown that in many instances the "true condensation" occurs only after a significant degree of supersaturation. For example, Heald and Brown (1968) found this to be true for CO_2, N_2, and Ar; Venables and Ball (1971) for Ar, Kr, and Xe; and Bently and Hands (1978) for CO_2. In these papers, the authors all acknowledge that heterogeneous surface nucleation constitutes the initiation step leading to bulk deposition. Yet in all cases, the authors state that nucleation should not occur on the base metal substrate due to the high value of the adsorption energy of the gas species, E_a, on the metal.

Bently and Hands (1978) contend that the deposition of N_2 and Ar on cryogenic surfaces should not be initiated by nucleation, as argued by Heald and Brown (1968). These authors speculate that poor temperature measurements in the low temperature range, as well as surface contamination, are the probable causes of the Heald and Brown results. Yet, the data for CO_2 are quite similar in both works, and both claim that the low adsorption energy observed for CO_2 nucleation is due either to a contaminant sublayer, or possibly even a strongly bound CO_2 sublayer.

In an analysis of the deposition of the species Xe, Kr, and Ar on graphite, Venables and Ball (1971) report adsorption energies of 1860, 1420, and 1080K, respectively, on the base graphite surface, while on a strongly bound monolayer of each species, the corresponding values were 1189, 792, and 578K.

The explanation given was that this sizable decrease in E_a for deposition on a monolayer of the test species was sufficient to cause a transition in the initiation mechanism for condensation from bulk deposition to nucleation. In a subsequent work from the same group (Price and Venables, 1975, and Venables and Price, 1975), however, it was concluded that the strongly bound monolayer was not composed of the test species, as originally assumed, but rather of some unidentified contaminant. Of an even more direct bearing on the present work, Cazcarra et al. (1973), and later Bryson and Levenson (1974) found that nucleation of CO_2 does indeed occur on an H_2O sublayer, and that water clathrate formation is probable.

From these cases, it is apparent that the parameter which primarily controls the condensation mechanism is the adsorption energy, E_a. A pre-adsorbed base layer, such as the one provided by the first condensation (examined at length in section 3.3) can favor nucleation as the initiation mechanism for condensation. As established in section 3.2 on nucleation kinetics, this depends on the adsorption energy of the species for the particular surface. Also, the adsorption energy may change as deposition continues.

Based upon this evidence and the experimental data which will be presented, the first condensation' exhibited in the present work favors nucleation as the initiation mechanism for the crue condensation , in most cases. From the previous section (3.3) it is also evident that E_a is high at the onset of the first condensation , but that it may change as deposition continues, sometimes resulting in saturation. The value of E_a

has been shown to be related to the absolute amount of condensate, background water vapor, as well as other contaminant species in the sublayer, their relative proportions, and probably the morphology of the sublayer, which is in turn dependent on many factors, the foremost of which is the deposition rate. Thus the value of E_a on the sublayer surface is quite difficult to predict with any certainty. However, quantitative estimates of E_a can be obtained from the data using the nucleation kinetics model.

Qualitative predictions of behavior are also provided by the model. For example, the expression for τ (equation (3.2-1)) indicate that for saturation of the first condensation to occur (as observed under certain conditions), E_a must decrease, since temperature continually decreases during cool down (this is evident from the argument of the exponential, E_a/RT). The fact is, as will be illustrated in what follows, that E_a may decrease to such an extent that even when the surface temperature reaches the point at which the vapor pressure of the condensing species equals the pressure exerted by the beam, the species will not condense until the degree of supersaturation available is high enough to allow the nucleation mechanism to occur. It is only then that nucleation becomes competitive with the "first condensation" mechanism, and eventually dominates. It will be shown that this effect is predicted by the model.

Some Preliminary Findings

As noted earlier, Freon 12 did not exhibit a first condensation on either the gold-flashed or HMDS-coated surface when LN_2 cryopumping was employed (with the exception of one

experiment, run 190 on the HMDS-coated surface). This does not mean, however, that the surface was not contaminated, but rather that the conditions for propagation of the first condensation were not present. Indeed, background water vapor must have deposited as an adsorbed layer, just as in all the other experiments. Figure (3.4-1) presents the Freon 12 data on both surfaces. In this figure, the logarithm of beam intensity is plotted vs. the true condensation temperature, the definition of which is dependent on the experimental circumstances. In experiments in which the first condensation has clearly already occurred (e.g., see Figure (3.3-5)), the true condensation temperature is defined as the temperature at which the signal exhibits a precipitous change; i.e., the point at which the derivative of the signal slope undergoes a discontinuity. However, it has also been shown by the modulated reflection experiments (e.g., Figure (3.3-15) for CO_2 on the HMDS-coated surface) that a weak first condensation can precede the true condensation, without a clear indication in the total mass spectrometer signal; i.e., the mass spectrometer signal initially appears steady, then decreases slowly, with an attendant smooth decrease in the derivative, until it attains a large negative value, which remains fairly constant until the rate of condensation reaches steady-state. An examination of the lock-in data, however, shows that the initiation of the true condensation occurs at the point where the mass spectrometer attains its largest negative derivative, and that this usually occurs at approximately 90% of the initial mass spectrometer steady-state signal. Thus care must be

exercised in distinguishing the exact point at which the "true condensation" becomes the dominant mechanism.

Figure (3.4-1) also includes the vapor pressure of Freon 12. Measured values of vapor pressure in the temperature range of interest were not found for Freon 12, and thus the values presented in Figure (3.4-1) are extrapolated from data given by Perry et al. (1973) using a least squares fit of the available data to a third order polynomial (i.e., $\ln (P^\circ) = A+B/T+C/T^2+D/T^3$). The vapor pressures were converted to corresponding intensities according to kinetic theory.

From an examination of the data in Figure (3.4-1), it is clearly evident that the vapor pressure curve falls between the lines representing the data on the gold-flashed and HMDS-coated surfaces. If one assumes that the vapor pressure extrapolation is accurate to within 30% (as indicated by the Freon 11 data, presented later), the fact remains that no significant degree of supersaturation is evident for Freon 12. This is consistent with the fact that Freon 12 did not exhibit a first condensation , except in one experiment where a very weak one was observed (run 190). In this one experiment the data point lies approximately 3K below the value extrapolated from the other HMDS-coated surface data (Figure 3.4-1); i.e., when the 'first condensation does occur, supersaturation is also present, implying nucleation as the growth-initiation mechanism.

From Figure (3.4-1) it is also evident that the data for both surfaces are nearly parallel, but offset by about 6K. that the HMDS-coated surface data are located at correspondingly

AD-A108 255 RESEARCH INST FOR GEODETIC SCIENCES FORT BELVOIR VA F/G 20/12
GAS-SURFACE INTERACTIONS IN CRYOGENIC WHOLE AIR SAMPLING,(U)
MAY 81 J M CALO, R J FEZZA, E J DINEEN F19628-77-C-0071
UNCLASSIFIED AFGL-TR-81-0162 NL

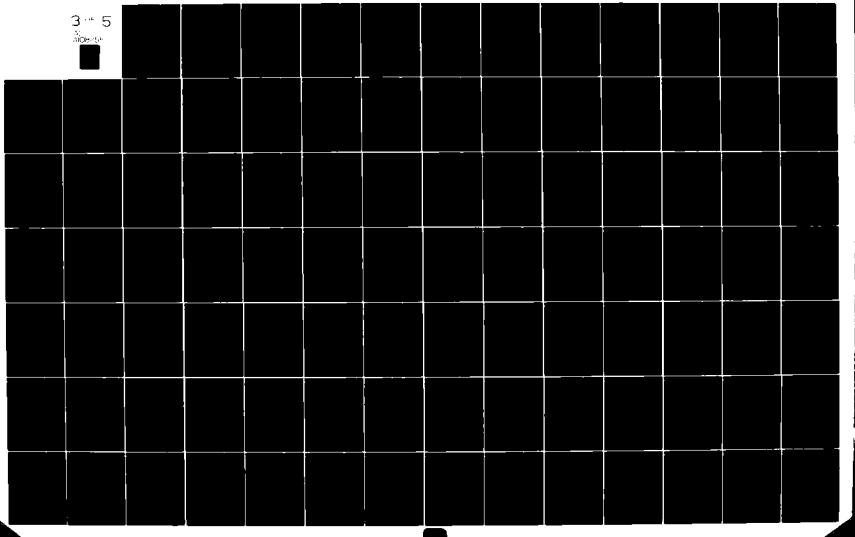

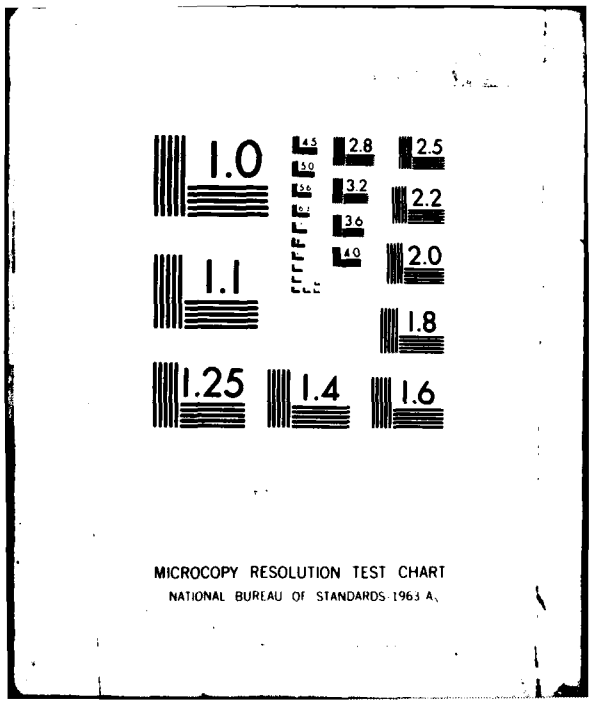
1.0
1.1
1.25
1.4
1.6
1.8
2.0
2.2
2.5
2.8
3.2
3.6
4.0
4.5
5.0
5.6
6.3
7.1
8.0
9.0
MICROCOPY RESOLUTION TEST CHART
NATIONAL BUREAU OF STANDARDS-1963-A

lower temperatures. This same "shift" for the HMDS-coated surface data is apparent in much of the "true condensation" data, implying that a significant difference exists between the two surfaces. In Figure (3.4-1), at 88K, the gold-flashed and HMDS-coated surface intensity data differ by approximately an order of magnitude. The most likely interpretation of these results is that under similar experimental conditions, the HMDS-coated surface provides approximately ten times more adsorption sites, per unit area, than the gold-flashed surface. This may be due to the manner in which background species adsorb on the surface (i.e., the number of surface sites available) and/or the surface structure presented to the adsorbate species. Thus this effect is assumed to be solely a surface property, independent of the beam species. For use in the nucleation model, the HMDS-coated surface will be assumed to have ten times as many adsorption sites per unit area than the gold-flashed surface. Also, this property is assumed to be reflected in the sublayer created by the first condensation".

An alternate explanation of the supersaturation observed is that the first condensation changes the specific surface area of the target. In order to explain the results in this manner, the specific surface area must <u>decrease</u> as a result of the first condensation ; i.e., for the same beam flux, a lower specific surface area dictates a higher intensity, which consequently results in supersaturation. However, based upon pertinent data in the literature concerning the "bare surface" effect, cited previously in section 3.1, this appears unlikely. These data show that the pumping speed, or deposition rate, is

greater on a coated surface than on a bare surface at a constant temperature. If the specific surface area increases upon deposition, the pumping speed would actually decrease, in direct contradiction with the experimental observations. The converse of this argument, i.e., that the specific surface area decreases as a result of the first condensation is contraindicated both by the supersaturation effect observed in the current data, which is quite similar to the data of Bently and Hands (1978), and that the increase in pumping speed has been attributed primarily to the decrease in adsorption energy, E_a, accompanying the deposition, as described as the Stranski-Krastonov growth mode in section 3.2 (Bently and Hands, 1978, Voorhoeve, 1976).

In addition to the preceding, Abe and Schultz (1979) have shown that at the relatively high temperatures where the first condensation occurs in the present work, the deposit should be relatively nonporous as a result of continuous self-annealing; i.e., the specific surface area is not expected to be larger than the base substrate offers. Finally, the aforementioned agreement of the present data for CO_2 with that of Bently and Hands (1978) and Heald and Brown (1968), two works in which no first condensation was observed, supports the conclusion that the first condensation does not appreciably alter the specific surface area. Thus, the significant supersaturations observed do not occur as a result of variations in specific surface area.

Modeling Heterogeneous Surface Nucleation

The data provided by the present study include true condensation temperatures as a function of beam intensity. In addition, the properties of the species investigated are known, or can be estimated fairly accurately. Even so, the nucleation kinetics model presented previously (see section 3.2) requires yet more parameters (e.g., E_a, E_d, E_i, N_o, i) which, in the absence of appropriate data, may be adjusted to agree with the data. Thus the best approach available is to set most of these parameters according to reasonable assumptions consistent with the data and the literature, leaving the primary ones to be determined by fitting the model to the data. If the selection and assignment of parameter values is done in a careful fashion, the computed parameters should provide a reasonable estimate fo the actual values and result in a useful model.

The principal results of the modeling studies are that:

(1) Nucleation is verified as the mechanism which initiates deposition.

(2) The effects of adsorption energy on the first condensation are elucidated.

(3) The assumption of different specific surface areas for the HMDS-coated and gold-flashed surfaces is corroborated.

(4) The relationships among the various parameters of the system and which primarily control condensation are identified.

Prior to proceeding with the analysis of the experimental results, it is appropriate that the method of assigning values to various parameters required by the model be discussed. The number of adsorption sites per unit area, N_o, was estimated by

the method of deBoer (1953), as in the work of Bently and Hands (1978). Assuming the adsorbed molecules are hard spheres arranged on the surface in a hexagonal close packed array, the volume per sphere, $\pi d_{min}^3/6$, would occupy 74% of the available area; i.e.,

$$\pi d_{min}^3/6 = 0.74 \frac{MW}{N_{av}\rho} \qquad (3.4\text{-}1)$$

where ρ is the adsorbate density, MW its molecular weight, and N_{av} is Avagadro's number. DeBoer (1953) found that d_{min}, the minimum in the interaction potential, is approximately equal to 1.37d, where d is the hard sphere diameter. N_o is defined as the inverse of b_2, which is the two-dimensional van der Waals constant, equal to twice the cross sectional area of the sphere; i.e.,

$$N_o = 1/b_2 = 2/\pi d^2 = 2(1.37)^2/\pi d_{min}^2 \qquad (3.4\text{-}2)$$

thus d_{min} can be estimated from Eq. (3.4-1), and N_o from Eq. (3.4-2). The relevant data are given in Table (3.4-1). The atomic volume, Ω, was calculated by dividing the molecular weight of the particular species by its liquid phase density, and is also given in Table (3.4-1). The frequency of vibration of the adsorbed molecules on the substrate, ν_o, is assumed to be $10^{13} s^{-1}$, as discussed by Bently and Hands (1978).

In assigning a value of the activation energy for diffusion along the substrate surface, E_d, the technique of relating E_d to E_a, as presented in Routledge and Stowell (1970) was employed; i.e., E_d=0.25 E_a. Variation of the multiplicative constant, 0.25, over an order of magnitude ((0.0-1.)E_a) has little effect on the results of the modeling studies.

The slope of the temperature-time curve is also required to model the experiments. The temperature-time curve was found to be linear in the range of interest, with slope, dT/dt, of $-0.07\ K\ s^{-1}$.

E_i, the net increase in potential energy upon forming an i-sized cluster from previously adsorbed species, is estimated by first calculating E_b, the intermolecular bond strength in a dimer consisting of two monomers on the surface. This was done in the same manner as in Bryson and Levenson (1974), who employ the Lennard-Jones potential parameter ε/k; i.e.,

$$E_b = N_{av} k\ (\varepsilon/k). \qquad (3.4\text{-}3)$$

Values of ε/k from Bird, Steward, and Lightfoot (1960) are used for all the species except the Freons, for which the parameters are found in Hirschfelder, Curtiss and Bird (1954). The values of ε/k and E_b for the species of interest are given in Table (3.4-2).

Once E_b has been determined, E_i is calculated by determining how many intermolecular bonds must be formed, and how many molecule-surface bonds must be broken, with adsorption energy E_a, to form an i-sized cluster. As in Bently and Hands (1978) and Bryson and Levenson (1974), it was generally found that attachment of all the cluster molecules to the surface requires the largest E_i, and therefore provides the most stable configuration. Thus for i=2,3,4,6,8, and 10, the values of the ratio E_i/E_b are 1,3,4,8,13, and 18, respectively, when the molecules are treated as hard spheres, hexagonal close-packed in two dimensions.

Thus estimates of parameter values used in the present study are based on techniques suggested in the literature. An analysis of the experimental data employing these values follows.

Data and Analysis

The analysis begins with the CO_2 data, since other results are available in the literature for comparison. Figure (3.4-2) is a plot of the logarithm of the beam intensity as a function of the true condensation temperature for CO_2 on both the gold-flashed and HMDS-coated surfaces. The data of Bently and Hands (1978) on a gold-flashed surface, and that of Heald and Brown (1968) on a polished copper surface are also presented in Figure (3.4-2). As is evident, the two data sets from the previous work fall quite close to the current data for CO_2 on the gold-flashed surface. It is emphasized that the current data were obtained with LN_2 cryopumping, and that a first condensation was observed prior to the true condensation , while the other two sources reported no such effect. Thus it must be concluded, as stated previously, that the surface area available to the beam species is not appreciably altered by the first condensation . Also, the fact that the data for the gold-flashed surface are very similar to that for the polished copper surface of Heald and Brown (1968) may imply that a contaminant sublayer was common to both sets of data, which controlled the behavior.

It is also shown in Figure (3.4-2) that the data on the HMDS-coated surface are approximately 18K supersaturated with respect to the data on the gold-flashed surface. It is noted that this HMDS-coated surface data are from experimental runs in

which a first condensation saturation effect was observed. Thus the true condensation temperature was interpreted as the point at which the rapid decrease in signal occurs, as illustrated in Figure (3.3-5) of the previous section.

In order to illustrate the techniques employed in applying the nucleation kinetics model (see section 3.2 and the computer program in Appendix C), reference is made to Figure (3.4-3). This figure includes the experimental data for CO_2 on the gold-flashed surface, as well as model-generated data for values of critical cluster size of i=1,2,3,4,6,8, and 10 for an assumed, constant adsorption energy of E_a=2250 cal/mol. It is evident that for increasing i, the model prediction shifts to lower temperature, with an attendant increase in slope. It is also observed that the resultant slopes are nearly equal for i=6,8, and 10. This property of the slope to approach an asymptotic value at large i will become significant in the interpretation of the experimental data. It is also noted that for constant i, the model predictions can be shifted to higher or lower temperatures by increasing or decreasing, respectively, the value of E_a. However, this slope/intercept fitting method can lead to some problems, as illustrated in Figure (3.4-4). This figure is a plot of the least squares fits of the linear slopes of the model predictions ($d \log R/dT_{cond}$) for discrete values of i for several values of E_a, ranging from 2250 to 2850 cal/mol. As E_a increases, the slopes of the curves also decrease. Thus, changing E_a not only changes the intercept, but also the slope of the model prediction.

As shown in Figure (3.4-4), the slope of the experimental CO_2 data on the gold-flashed surface is 0.117, which corresponds to i=4.45 when E_a is assumed constant at 2850 cal/mol. Since i must reasonably be an integer value, and its exact value is not the desired goal of this approximate model, it is concluded that i=4 with E_a = 2850 cal/mol. The model simulation using these values is presented in Figure (3.4-5), and is seen to fit both the current experimental data, as well as the other data cited quite well. Vapor pressure values for CO_2 from Honig and Hook (1960) are also shown for comparison.

Bently and Hands (1978) reported values of i=9 and E_a=2250 cal/mol for their work with CO_2 using the more simplified nucleation model discussed previously. Although the current data for CO_2 agree quite well with that of these authors, the model predictions do not. Several major differences between models are responsible for these discrepancies. First, it is noted that Bently and Hands (1978) estimated E_b from heat of sublimation data for CO_2, together with a knowledge of the number of nearest neighbor bonds broken when CO_2 sublimates from the bulk phase. With this approach, they obtained E_b=1080 cal/mol as compared to the 377 cal/mol used in the present study estimated according to the method of Bryson and Levenson (1974). Bently and Hands also assumed a cluster configuration which results in twelve intermolecular bonds for a nine molecule cluster. If these parameter values are assumed correct (with E_d=0.01E_a, since Bently and Hands assumed $E_d \tilde{=} 0$ for CO_2), when they are used in the present model, a condensation curve approximately 7K supersaturated with respect to the experimental

data is predicted, as shown in Figure (3.4-6). It is believed that this apparent discrepancy is a result of the oversimplification of the atomistic approach of Venables (1973) undertaken by Bently and Hands, coupled with large uncertainties in parameter estimation. Of particular relevance to the succeeding analysis is the acknowledgement by Bently and Hands that the apparent value of i=9 has a range of 6 to 13, and that with their model, E_a varies little with this variation in i.

As noted earlier, the deposition of CO_2 on the HMDS-coated surface exhibits an enhanced supersaturation effect, in comparison to the gold-flashed surface, as illustrated in Figure (3.4-5). N_o for this surface was estimated at 7.3×10^{19} sites $m^{-2}s^{-1}$ -- an order of magnitude greater than for the gold-flashed surface, as previously discussed. Employing the same fitting techniques as for the gold-flashed surface, and with the parameter values indicated, it was found that i=4 and E_a= 2425 cal/mol represented the experimental data well, as shown in Figure (3.4-7). Thus, although the critical cluster size does not seem to change appreciably, the adsorption energy is less than for the gold-flashed surface. From consideration of the first condensation theory and experiments, it was established that the HMDS-coated surface exhibited a higher initial condensation rate for the first condensation , yet often saturated prior to the true condensation . The higher initial capture rate is attributable to the adsorption sites assumed for the HMDS-coated surface, while the subsequent saturation may be due to an initially lower energy of adsorption. Recalling that the HMDS-coated surface data are approximately

18K supersaturated with respect to that for the gold-flashed surface, and that the propagation of the first condensation is believed to be dependent on the initial stability of the layer and the background water vapor-beam species mixing ratio (which is time dependent), it is consistent that the true condensation of CO_2 on the HMDS-coated surface should exhibit a lower adsorption energy, as indicated by the model results. Thus the clathrate sublayer hypothesized as responsible for the first condensation does not adsorb CO_2 as strongly, when formed on the HMDS-coated surface, as it does on the gold-flashed surface. This effect is reflected in the propagation mechanism, and results in a lower E_a at the true condensation temperature.

In summary, for CO_2:

(1) The current data agree quite well with other data in the literature.

(2) The true condensation on the gold-flashed surface is well represented by the nucleation kinetics model.

(3) On the HMDS-coated surface, the CO_2 critical nucleus size is similar to that found for the gold-flashed surface, but the corresponding value of E_a is lower.

(4) The increased initial first condensation rate and the saturation behavior exhibited by the HMDS-coated surface, are consistent with a larger N_o and a smaller E_a and with the true condensation data.

(5) The lower value of E for the HMDS-coated surface can be explained as follows:

(a) It is possible that the clathrate structure hypothesized as responsible for the first condensation possesses different energy parameters when formed on the HMDS-coated substrate, which tends to lower the initial E_a and is reflected in the propagation mechanism.

(b) Since clathrate formation is a rate process, dependent on contaminant deposition rates, at lower temperatures (i.e., longer times) the composition of the first condensation layer will vary thereby affecting the surface value of E_a.

The results found here for CO_2 will next be applied to the study of other gases of stratospheric interest, not previously analyzed in this manner in the extant literature.

The data obtained for the true condensation of N_2O, a species quite similar to CO_2, with LN_2 cryopumping are presented in Figure (3.4-8). In this figure the circled points are the experimental data, while the triangular points represent model results. Vapor pressure data fron Honig and Hook (1960) are also included.

The same supersaturation effect observed for CO_2 is also quite evident for N_2O in Figure (3.4-8); i.e., gold-flashed surface data are approximately 6K supersaturated with respect to vapor pressure, and near-parallel to it. Data for the HMDS-coated surface are approximately 14K supersaturated with respect to the gold-flashed surface data. It is emphasized that the true condensation was distinguished from the first condensation on the HMDS-coated surface in the manner noted in Figure (3.3-5).

To emphasize this point, in Figure (3.4-9) the first condensation is treated as if it were the true condensation. This erroneous interpretation results in a negative slope, in direct contradiction to both thermodynamics and nucleation theory.

The data for N_2O on the HMDS-coated surface was fit in a manner similar to that for CO_2. The value of N_o, given in Table (3.4-1), was increased by an order of magnitude, (from 8.1×10^{18} to 8.1×10^{19} sites m^{-2}) to account for the higher value of N_o expected for the HMDS-coated surface. Resultant parameter values of i=4 and E_a=2300 cal/mol fit the data well, as shown in Figure (3.4-8). Comparison of these values to those for CO_2 on the HMDS-coated surface indicates that N_2O behaves quite similarly to CO_2 on this surface. This is not surprising in view of the similarities in their physical properties; e.g., Lennard-Jones potential parameters, N_o, atomic volume, vapor pressure, and heat of vaporization.

For N_2O condensation on the gold-flashed surface, the experimental data yield a slope (d log R/d T_{cond}) of 0.167. Yet even with a reasonable value of E_a = 3000 cal/mol, for the temperature range, the largest slope computed, at i=10, was 0.136, which is significantly lower than the experimental value. Since, as shown in Figure (3.4-4), the slope approaches an asymptotic value with increasing i, it is unlikely that a larger critical cluster size will reconcile the measured and predicted slopes. Even so, this approach is attempted first in the following efforts to explain the data.

First the i vs. slope relationship provided by the model was extrapolated to the experimental slope value of 0.167. For E_a=3000 cal/mol., the value of i which results in this manner is 33.4. The next step was to increase the value of E_a to match the intercept obtained for the i=33 model prediction. When this was done, however, the asymptotic value of the slope decreased, as shown in Figure (3.4-4), thereby necessitating a second iteration of the entire procedure. All the succeeding attempts failed in the same manner. This result, coupled with the fact that all the relevant literature (see section 3.2) points to small critical cluster sizes, indicated that the invocation of larger critical cluster sizes is not the solution to the problem.

A second possibility investigated was that the activation energy for surface diffusion, E_d, is not correctly given by the estimate provided by 0.25 E_a. It was established that at this value, the model was not diffusion-limited, and thus decreasing E_d further had little effect on the slope. By raising the value to E_d=E_a, the model did become diffusion-limited, as expected, and the value of the slope decreases, also as might be expected when nuclei growth can occur via direct impingement only. Therefore, an error in the estimation of E_d cannot resolve the problem either. Also, there is no reasonable basis for the variation of the other parameters which are intrinsic properties of the condensing species (e.g., atomic volume, Lennard-Jones constants, etc.).

However, as discussed previously, the value of E_a critically affects the first condensation . The contaminant sublayer

provides a surface that is highly favorable for the adsorption of beam species, i.e., it exhibits a high E_a. Based on observations of saturation of the first condensation on the HMDS-coated surface, with continually decreasing temperature, however, E_a does not remain constant but rather must decrease under these conditions. This effect is probably due to the continually changing ratio of background water vapor to beam species, as well as the movement of the condensation surface away from the metal substrate which originally stabilizes the contaminant sublayer. Also, since the first condensation is a rate process, the beam intensity, R, which is related to the absolute number of molecules the first condensation must accommodate, must affect the value of E_a. Thus, the energy of adsorption, E_a, is related to both the composition and morphology of the base substrate. This conclusion is substantiated by the data of Table (3.4-3), which gives the temperature at which saturation of the first condensation occurred as a function of beam intensity, for both N_2O and CO_2 on the HMDS-coated surface. As the beam intensities increase for N_2O, the saturation temperatures also increase, just as would be expected if E_a were a function of the sublayer composition and structure; i.e., the higher intensity runs deposit the beam species more rapidly, thereby causing E_a to decrease at a greater rate. Illustrations of the effect of deposition rate on frost morphology are given by Meyer (1971) and Hallam and Scrimshaw (1973). This is also consistent with the formulation of the adsorption time; i.e., $\tau = \nu_o^{-1} \exp(E_a/\underline{R}T)$, where $\underline{R}$ is the gas constant.

For CO_2, runs 197 and 198 in Table (3.4-3) of nearly equal intensities, differ in saturation temperatures by approximately 11K. This apparent discrepancy is understandable if the "first condensation effect is also a function of water vapor and contaminant background levels, beam capture coefficients, and beam dynamics, and not merely a simple function of intensity. Yet, in any single case, as R increases E_a should decrease more rapidly during the first condensation .

These observations imply that for the case of N_2O on the gold-flashed surface, the value of E_a used in the model (previously assumed constant with experimental beam intensity), may actually vary, with higher values at lower intensities at the point where the true condensation occurs, and vice-versa. Therefore, the data for N_2O on the gold-flashed surface was fit in the following manner. As stated earlier, Bently and Hands (1978) have shown with their simplified atomistic model that the critical cluster size can be determined from the intercept of a ln R vs. 1/T plot. Although their model is suspected to be oversimplified, this result does predict that the N_2O data on the gold-flashed surface should have a critical cluster size, i, greater than four. Recalling from the previous development that at i=6 the slope of the log R vs. T data is already quite close to its asymptotic value, and that Bently and Hands concluded that a choice of i between 6 and 13 had little effect on E_a, it seems reasonable to choose i=6. As shown in Figure (3.4-8), this approach produces a good fit of the data for E_a values of 2950, 2900, and 2800 cal/mol for beam intensities of 10^{19}, 10^{20}, and 10^{21} $m^{-2}s^{-1}$, respectively. For a two order of

magnitude variation in beam intensity, E_a varies only 150 cal/mol, or $\pm$ 5% of the average E_a value of 2883 cal/mol. This is well within the bounds of experimental error. From these results it is evident that not only does the "first condensation" control the subsequent deposition mechanism (i.e., nucleation), but also its detailed behavior via its effect on E_a.

The analysis of nitric oxide, NO, condensation is considered next. Figure (3.4-10) presents the true condensation temperature versus beam intensity data on both surfaces for NO, along with vapor pressure data from Honig and Hook (1960). Several features of these data are noted. First, for the gold-flashed surface, three points seem to define a line with a very high slope in comparison to the vapor pressure curve. However, the two points at lower intensity on the gold-flashed surface fall to the right of and close to the vapor pressure curve. They appear unrelated to the curve formed by the other three points. The NO data for the HMDS-coated surface also lies to the right of the vapor pressure curve and appears parallel to it. This behavior is the exact opposite of previous results for which the HMDS-coated surface data were located at significantly lower temperatures than the gold-flashed surface data.

A linear fit of the three high intensity NO points for the gold-flashed surface yields a slope (d log R/d T_{cond}) of 0.8813, which, as in the case of N_2O on the gold-flashed surface, it too high to be fit with a constant value of E_a. By varying E_a, and setting i=6 for the same reasons as for N_2O, the data were fit quite well with E_a equal to 2150, 1975, and 1800 cal/mol for beam intensities of 10^{19}, 10^{20}, and 10^{21} m^{-2} s^{-1},

respectively. The range of E_a for these intensities in 350 cal/mol, or 18% of the average E_a value of 1975 cal/mol. In comparison to N_2O, this represents a ver- sharp increase in E_a with decreasing intensity.

In the previous section on kinetics of nucleation, it was noted that the criteria for the occurrence of nucleation are $E_a<E_a'$ or $E_a<E_2$. For most of the data reported here these conditions prevailed due primarily to the nature of the surface properties of the first condensation as it propogated out from the metal surface. For the case of NO on the gold-flashed surface, however, it appears that for the two low intensity points nucleation is not the mechanism for the initiation of the true condensation, but rather bulk deposition initiated by layered growth via equilibrium thermodynamic condensation. The rapid increase in E_a with decreasing R for the remaining three points indicates nucleation at high intensities. Thus, for the low intensity runs, $E_a \not< E_a'$ and/or $E_a \not< E_2$ for the entire temperature range until the beam pressure became equal to the vapor pressure, at which point bulk condensation occurred. Thus these data actually illustrate the transition between thermodynamic and nucleation initiated condensation for NO on a gold-flashed surface. The value of E_a at this transition is approximately 2150 cal/mol.

The data obtained for NO on the HMDS-coated surface is also interesting with respect to its location relative to the vapor pressure curve and the gold-flashed surface data. As shown earlier, (e.g., Figure (3.3-23) for the modulated signal study of NO on the HMDS-coated surface without LN_2 cryopumping)

a dramatic decrease in the mass spectrometer signal occurred just prior to the decrease in the lock-in signal, which marked the onset of the true condensation . This behavior was attributed to the first condensation , which in the lock-in experiments (Figure (3.3-23)) was clearly distinguishable from the true condensation . However, with LN_2 cryopumping, this distinction was not discernible. Thus the data presented in Figure (3.4-10) are most probably representative of just a first condensation , and the true condensation was never attained.

Figure (3.4-11) represents data obtained for Freon 11 with LN_2 cryopumping. In this case, the data on the gold-flashed surface is supersaturated approximately 7K with respect to the vapor pressure, while the HMDS-coated surface data are approximately 8.5K lower than the gold-flashed surface. Both sets of data are parallel to the vapor pressure curve. As in the case of Freon 12, in Figure (3.4-11) the vapor pressure data were extrapolated from data available at higher temperatures (Perry and Chilton, 1973) with a least squares fit, as detailed previously. The extrapolated data agree to within $\pm$30% of data calculated from the Antoine equation, using constants given by Reid et al. (1977). As can be seen from Figure (3.4-11), even with a 30% increase in the vapor pressure (and consequently, the intensity), both data sets remain supersaturated. Therefore, unlike Freon 12, nucleation is the condensation initiation mechanism.

A least squares fit of the Freon 11 data on the gold-flashed surface yields a slope (d log R/d T_{cond}) of 0.128.

This value is again greater than the maximum attainable with the model using a constant value of E_a. In order to explore the role of E_a further, i was set equal to 6 (a value at which the slope approaches its asymptotic limit). The values of E_a found in this manner for intensities of 10^{18}, 10^{19}, and 10^{20} $m^{-2}s^{-1}$, were 4300, 4150, and 4050 cal/mol, respectively. This is a 250 cal/mol or 6% variation from an average E_a value of 4167 cal/mol which is similar to the range calculated for N_2O.

The data for Freon 11 on the HMDS-coated surface exhibited the same type of high slope behavior when model predictions were attempted. N_o was set an order of magnitude greater for the HMDS-coated surface than for the gold-flashed surface (i.e., $3.3 \times 10^{19} m^{-2}$) as indicated by the Freon 12 data. It was found that for i=6, E_a was 4200, 4100, and 4000 cal/mol for beam intensities of 10^{18}, 10^{19}, and 10^{20} $m^{-2}s^{-1}$, respectively. This range of 200 cal/mol, or 4.9% of the mean value of 4100 cal/mol is quite similar to that obtained for the gold-flashed surface.

Freon 11 and Freon 12 are chemically similar species, and as shown in Table (3.4-2) they also have similar Lennard-Jones parameters, which are well above the values for the other species investigated here. Since these parameters are a measure of the attractive potential between like molecules, they are important with respect to multilayer adsorption. It is also noted that Freon 11 and Freon 12 have relatively high total polarizabilities (Table 3.1-1). This suggests that the attraction between the first condensation layer and the beam molecules should be

strong, and remain so during condensate propagation. Recalling that for Freon 11, the range of beam intensity is approximately an order of magnitude less than for the other species, and that the first condensation exhibited a relatively low capture rate, it follows that as the first condensation for Freon 11 propagates, its ability to condense beam molecules, as measured by E_a, does not change as rapidly as for the other gases (e.g., CO_2, N_2O, and NO). Also, the gold-flashed and HMDS-coated surfaces exhibit little difference in E_a, even though their respective temperature ranges differ by 8.5K.

Data for N_2 on the gold-flashed surface are presented in Figure (3.4-12). Only four data points are given because much of the true condensation data were indistinguishable from the first condensation effect, i.e., there was no distinct transition in the mass spectrometer signal that could be interpreted as the onset of the true condensation . Of these four points, three lie on a straight line approximately 3.5 to 4K supersaturated with respect to the vapor pressure (from Honig and Hook, 1960). Also presented in Figure (3.4-12) are the data of Heald and Brown (1968), who found approximately 5K supersaturation. Bently and Hands (1978) also investigated N_2 and found less than a 1K supersaturation, which they attributed to experimental error. These authors claimed that the Heald and Brown (1968) results were due to a contaminant sublayer, as we have also shown.

A fit of the three points yielded a critical nucleus size of i=3 and a constant adsorption energy of 675 cal/mol. This low value of E_a is not surprising since N_2 has no permanent dipole,

and a small Lennard-Jones potential well (ε/k=91.5K). Since the N_2 dipole must be induced, and the interaction potential exhibits a negative exponential dependence on layer thickness (developed in the section on 3.1 on potential theory for induced dipoles) the first condensation cannot propagate at the higher temperatures.

Data for O_2 on the gold-flashed surface, along with vapor pressures from Honig and Hook (1960) are presented in Figure (3.4-13). As shown, a 5K supersaturation with respect to vapor pressure was observed, resembling the data for N_2. The nucleation model fits the data for a critical cluster size of i=10 at a constant E_a of 950 cal/mol. Due to the scatter of these data, it is difficult to determine whether or not this fit is accurate, or whether the data point at 32K is spurious, requiring a fit with varying E_a. O_2 is similar to N_2 in its lack of permanent dipole, low value of induced dipole, and low Lennard-Jones potential well, allowing the same observations concerning its low adsorption energy.

Summary and Conclusions

A considerable amount has been learned about the condensation mechanism in what might be considered a non-ideal experimental system. Some highlights are:

(1) The literature shows that a pre-adsorbed sublayer can cause a change in condensation behavior, from layered equilibrium condensation to nucleation-induced condensation. This occurs in the present system for several gas species, and is similar to Stranski-Krastonov growth.

(2) That when the first condensation does not occur, bulk deposition is initiated by equilibrium thermodynamic condensation (i.e., layered growth) as exemplified by Freon 12.

(3) The HMDS-coated surface appears to offer approximately one order of magnitude more adsorption sites than the gold-flashed surface, and the adsorption energy onto first condensation layers on the HMDS-coated surface appears to be lower than on the gold-flashed surface. This is reflected both in the true condensation data, and in the first condensation data by the fact that the initial first condensation rates are higher on the HMDS-coated surface, yet only this surface seems capable of saturating the first condensation , with the species CO_2 and N_2O.

(4) Data for CO_2 on the gold-flashed surface correspond quite well with literature values, and its behavior on both surfaces is well represented by the nucleation model.

(5) The supersaturation effect cannot be explained by an increase in surface area with the first condensation .

(6) The N_2O data suggest that E_a cannot be assumed constant for all runs on the same surface for a particular species. Its value varies with beam intensity in a manner consistent with the theory of the first condensation developed.

(7) The NO data illustrate a transition between equilibrium thermodynamics (layered) condensation and nucleation-initiated condensation, due to the value of the adsorption energy.

(8) In the case of N_2 and NO, first condensation effects often obscure the onset of the true condensation .

(9) During the propagation of the first condensation for Freon 11, the value of E_a remains fairly constant and the same for both surfaces. This is consistent with the high values of the dipole and dispersive parameters for Freon 11.

(10) Just the opposite is true for N_2 and O_2. In their case, the adsorption energy calculated at the true condensation is low, which corresponds to their low values of dispersive and dipole parameters.

The observations and phenomena encountered in the present research concerning condensation on real, "dirty" surfaces are the type which have been either ignored or supposedly eliminated in the work of other authors. In most cases, however, practical applications are not possible without attendant contamination effects. In the present work, a systematic study of the first condensation and its effects on the true condensation was undertaken which elucidates the mechanisms involved, and their interrelationships.

TABLE (3.4-1)

PROPERTIES OF SPECIES OF INTEREST

	ρ (g/cm^3)	NO ($sites/m^2$)	Ω (cm^3)
NO	1.249	8.1×10^{18}	3.86×10^{-23}
N_2O	1.843	8.1×10^{18}	3.97×10^{-23}
N_2	0.808	6.37×10^{18}	5.75×10^{-23}
O_2	1.118	7.25×10^{18}	4.75×10^{-23}
CO_2	1.560	7.32×10^{18}	4.68×10^{-23}
F12	1.486	3.6×10^{18}	1.35×10^{-22}
F11	1.494	3.33×10^{18}	1.52×10^{-22}

TABLE (3.4-2)

LENNARD-JONES INTERACTION PARAMETER AND BINDING ENERGIES OF SPECIES OF INTEREST

	ε/k [K]	E_o (cal/mol)
N_2	91.5	181.7
O_2	113	224.3
CO_2	190	377.2
NO	119	236.2
N_2O	220	436.8
F11	399	792
F12	345	685

TABLE (3.4-3)

SATURATION TEMPERATURES AT GIVEN BEAM INTENSITIES

Run	$T_{saturation}$ [K]	R_{beam} $[m^{-2}s^{-1}]$
	N_2O	
200	135	5.05×10^{19}
202	164	1.90×10^{20}
203	188	5.49×10^{20}
	CO_2	
198	124.7	3.87×10^{20}
197	135.6	3.97×10^{20}
195	107.7	1.68×10^{20}

Figure (3.4-1) True Condensation Data For Freon 12 On Gold-Flashed (●) And HMDS-Coated (▲) Stainless Steel Surfaces (Note: Vapor pressure data is given (----) and a least square fit of the data is shown)

Figure (3.4-1)

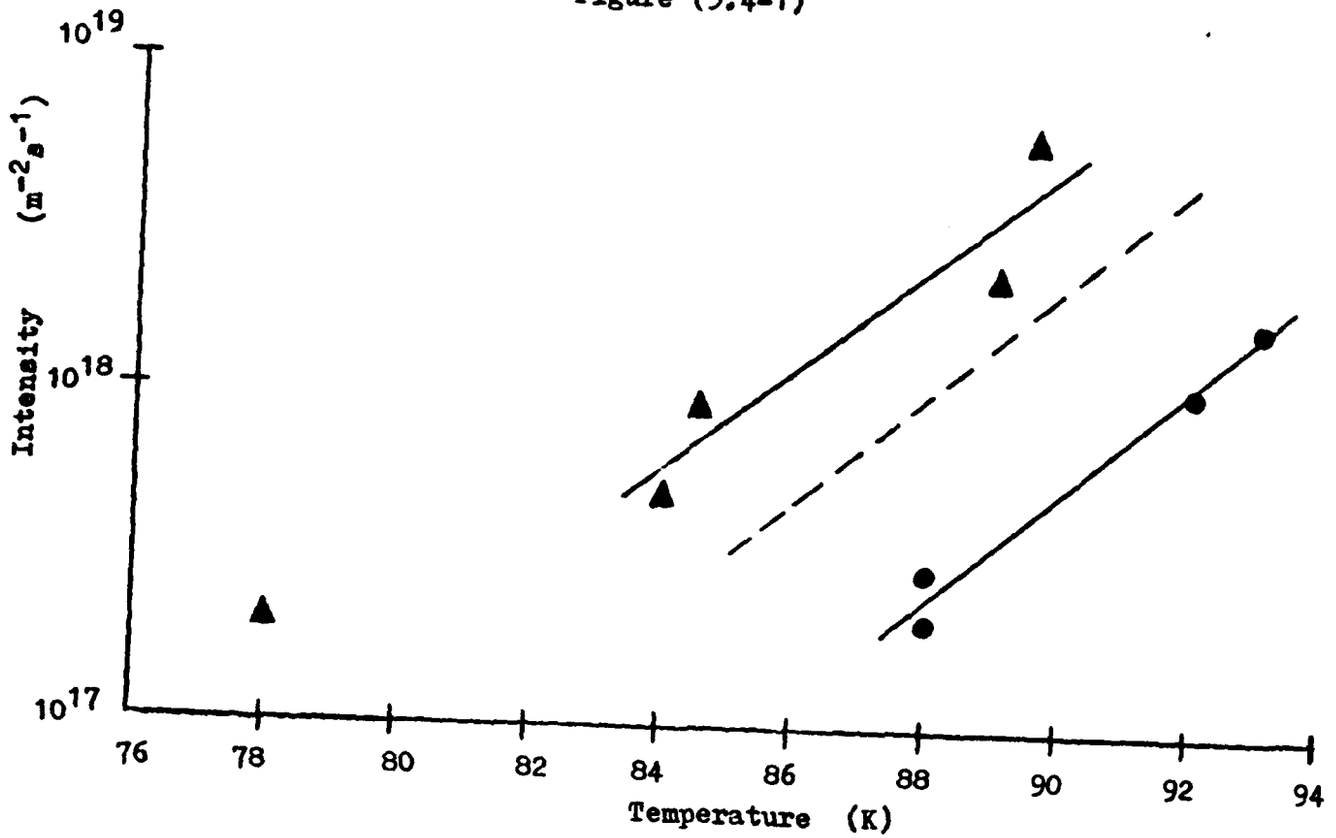
10^{19}
10^{18}
10^{17}
Intensity ($m^{-2}s^{-1}$)
76
78
80
82
84
86
88
90
92
94
Temperature (K)

Figure (3.4-2) True Condensation Data For CO_2 On Gold-Flashed (●) And HMDS-Coated (▲) Stainless Steel Surfaces (Note: Data of Bently and Hands (1978) (■) and Heald and Brown (1968) (+) are given, and a least square fit is plotted)

Figure (3.4-2)

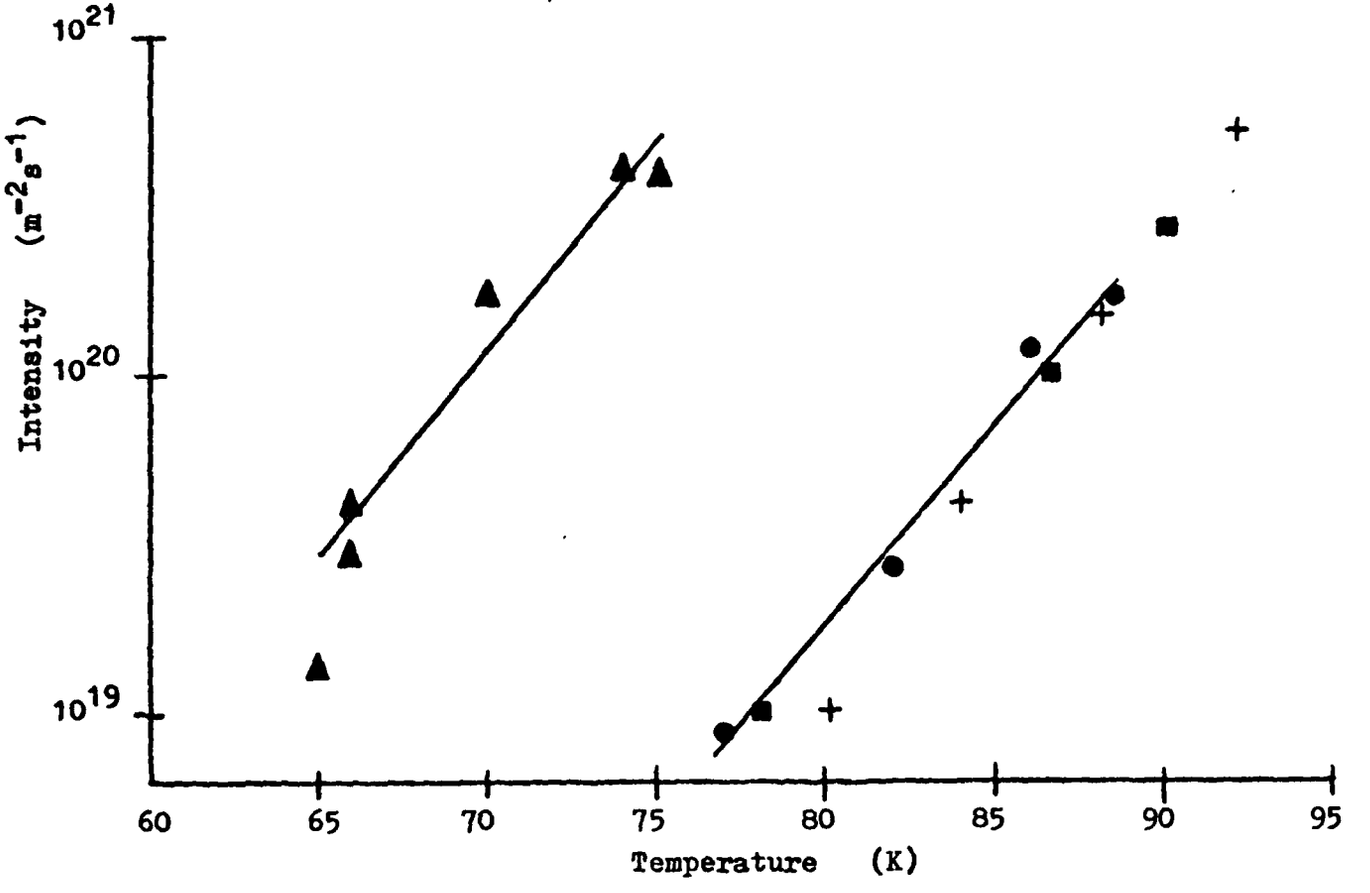
10^{21}
10^{20}
10^{19}
Intensity ($m^{-2}s^{-1}$)
60
65
70
75
80
85
90
95
Temperature (K)

Figure (3.4-3) True Condendensation Curves Predicted By The Nucleation Model For CO_2 For Various Values Of The Critical Cluster Size (Note: E_a=2250 cal/mol, and the experimental data for CO_2 on gold-flashed stainless steel is given (●) for comparison)

Figure (3.4-3)

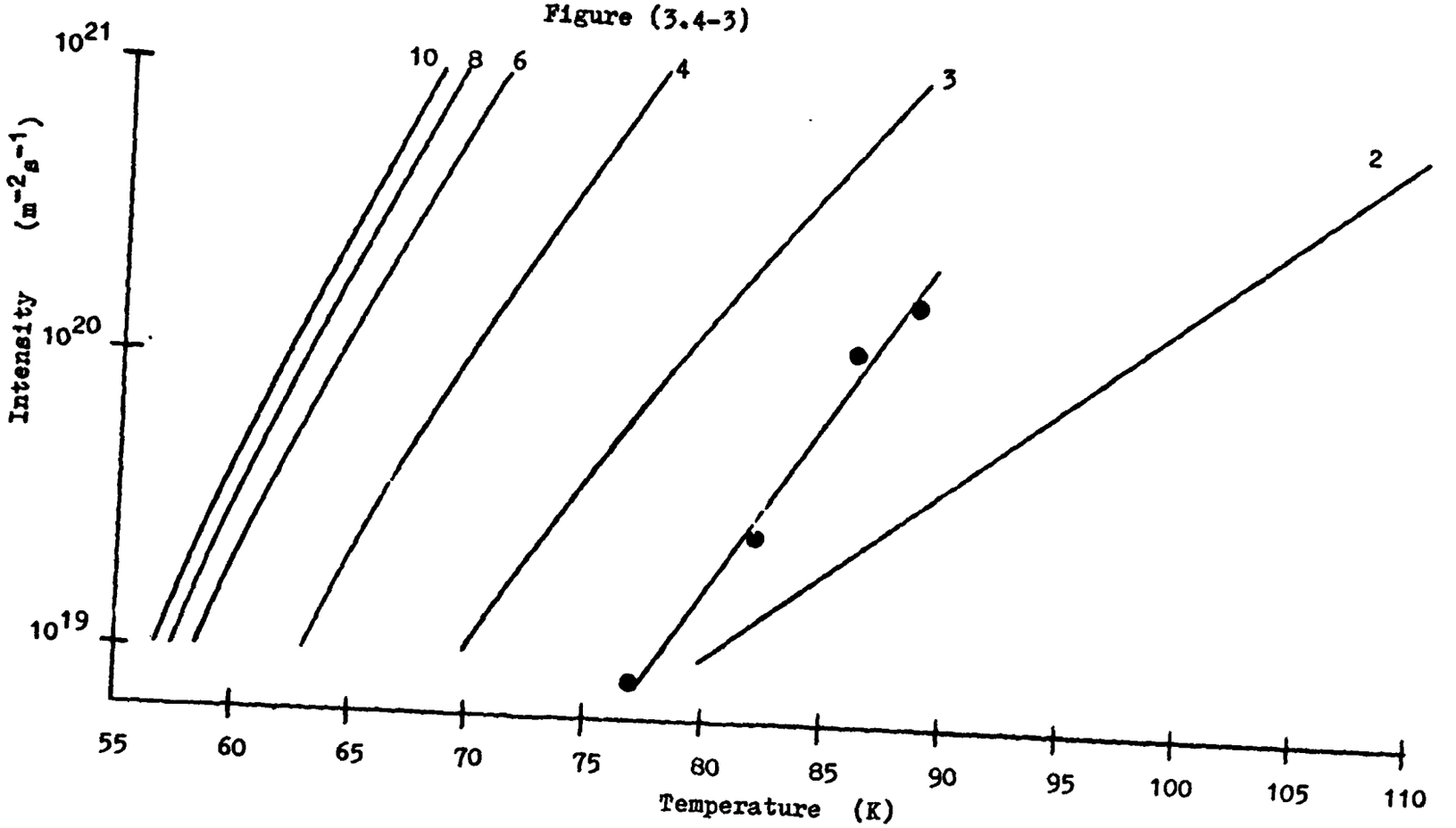
10^{21}
10^{20}
10^{19}
Intensity ($m^{-2}s^{-1}$)
10
8
6
4
3
2
55
60
65
70
75
80
85
90
95
100
105
110
Temperature (K)

Figure (3.4-4) Slopes Of True Condensation Curves Predicted By The Nucleation Model As A Function Of Critical Nucleus Size For Various Values Of E_a

Figure (3.4-4)

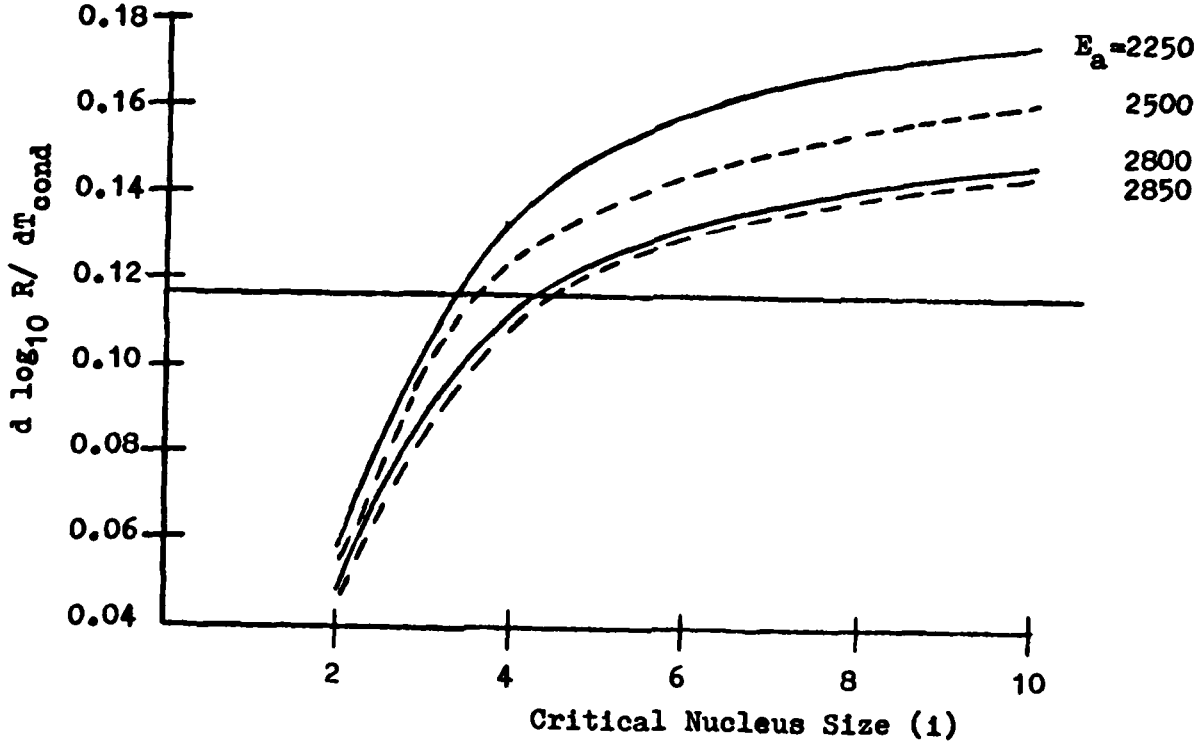
0.18
0.16
0.14
0.12
0.10
0.08
0.06
0.04
d log10 R/ dTcond
2
4
6
8
10
Critical Nucleus Size (i)
Ea=2250
2500
2800
2850

Figure (3.4-5) Nucleation Model Prediction (——) Of Experimental Data (●) On The True Condensation Of CO_2 On Gold-Flashed Stainless Steel (Note: Experimental data for CO_2 on the HMDS-coated surface is given (▲), as well as CO_2 vapor pressure data (----) and the condensation data of Bently and Hands (1978) (■) and Heald and Brown (1968) (+))

Figure (3.4-5)

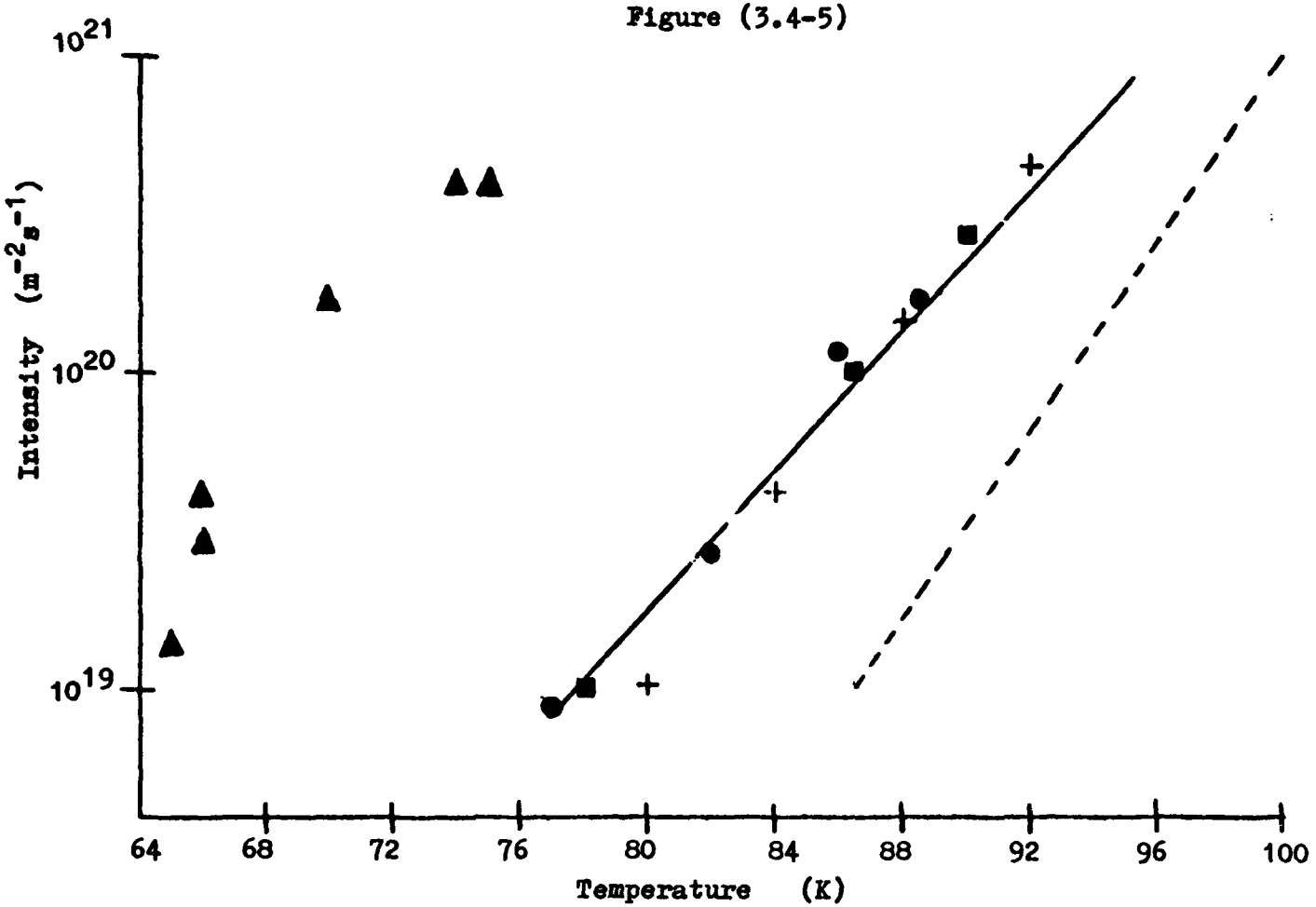
10^{21}
10^{20}
10^{19}
Intensity ($m^{-2}s^{-1}$)
64
68
72
76
80
84
88
92
96
100
Temperature (K)

Figure (3.4-6) A Comparison Of The Nucleation Model Fit For CO_2 Data On The Gold-Flashed Surface (●) Employing Current Parameter Values (——) And Bently And Hands (1978) Parameter Values (----) (Note: The data of Bently and Hands (1978) (■) and Heald and Brown (1968) (+) are also given)

Figure (3.4-6)

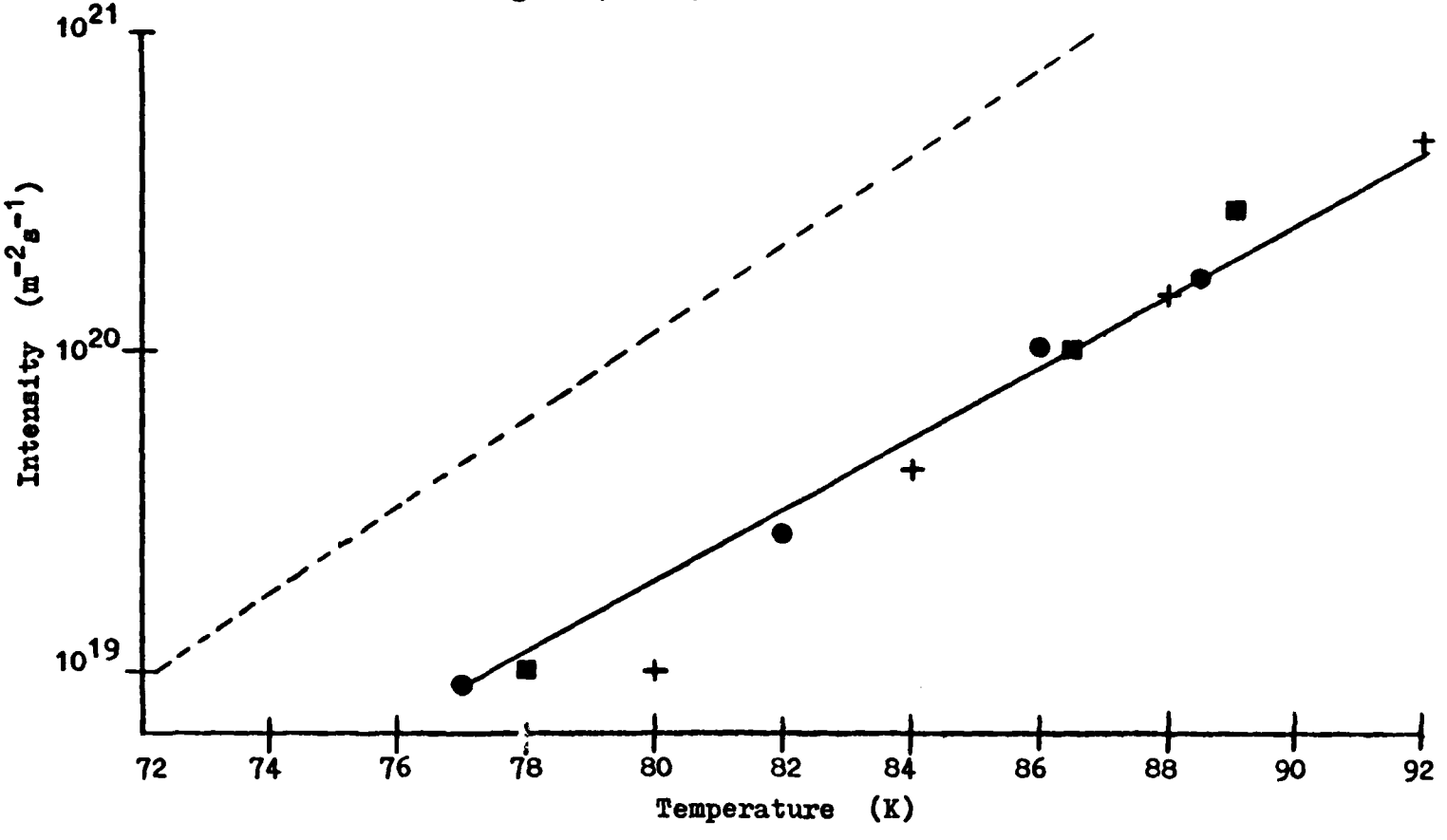
10^{21}
10^{20}
10^{19}
Intensity ($m^{-2}s^{-1}$)
72
74
76
78
80
82
84
86
88
90
92
Temperature (K)

Figure (3.4-7) The Nucleation Model Predictions (——)
For The True Condensation Of CO_2 On The HMDS-Coated Surface

Figure (3.4-7)

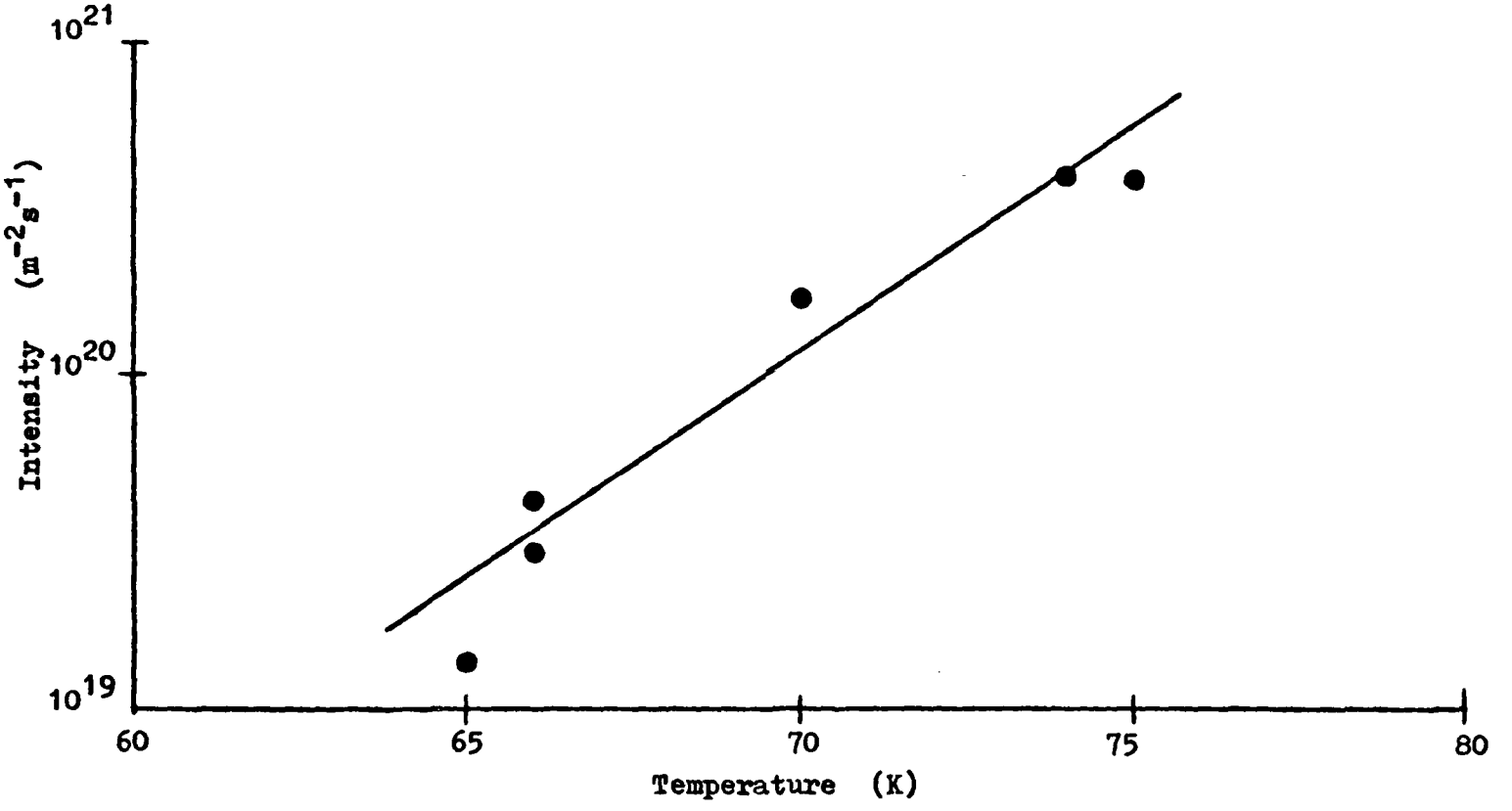

Figure (3.4-8) The Nucleation Model Predictions (—△—) For The True Condensation Of N_2O On The Gold-Flashed And HMDS-Coated Surfaces (Note: Experimental data for the gold-flashed (●) and HMDS-coated (■)surfaces are also given, as well as N_2O vapor pressure data (----))

Figure (3.4-8)

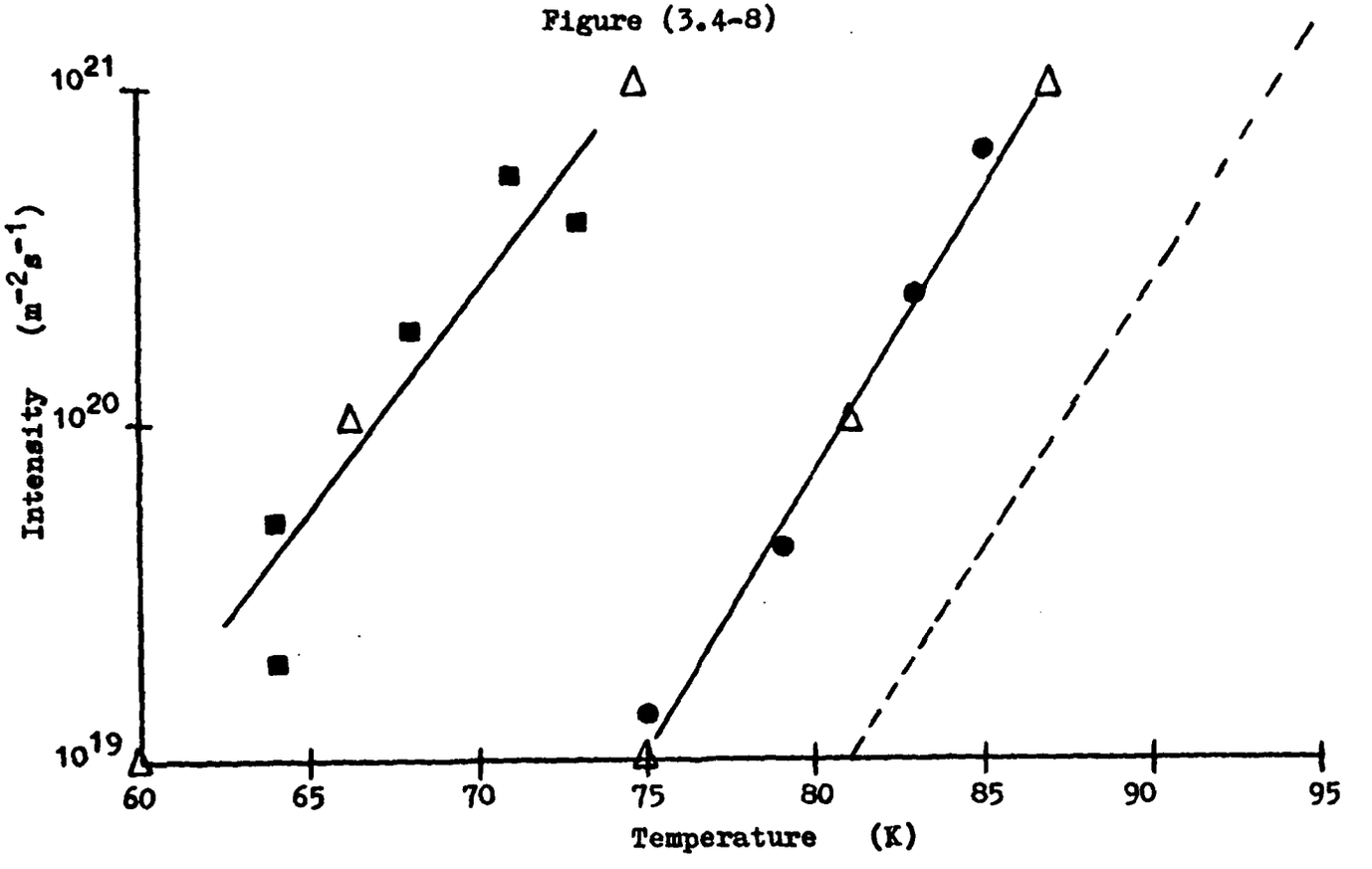
10^{21}
10^{20}
10^{19}
Intensity ($m^{-2}s^{-1}$)
60
65
70
75
80
85
90
95
Temperature (K)

Figure (3.4-9) N_2O First Condensation Data (●) Compared To N_2O Vapor Pressure Data (----)

Figure (3.4-9)

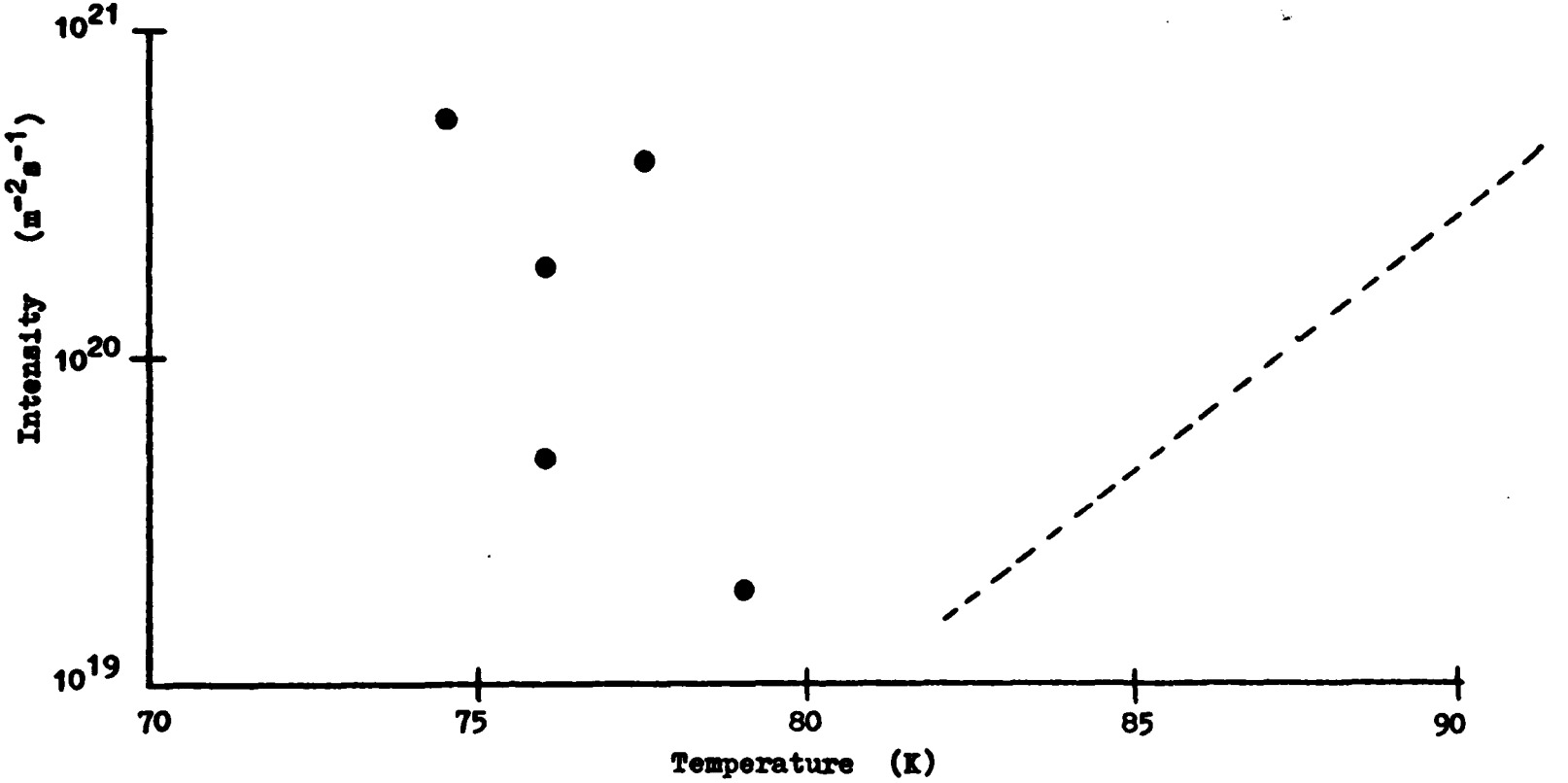

Figure (3.4-10) Nucleation Model Prediction (—△—) Of NO True Condensation Data (●) On The Gold-Flashed Stainless Steel Surface (Note: Data for the HMDS surface is given (■), as well as NO vapor pressure data (----))

Figure (3.4-10)

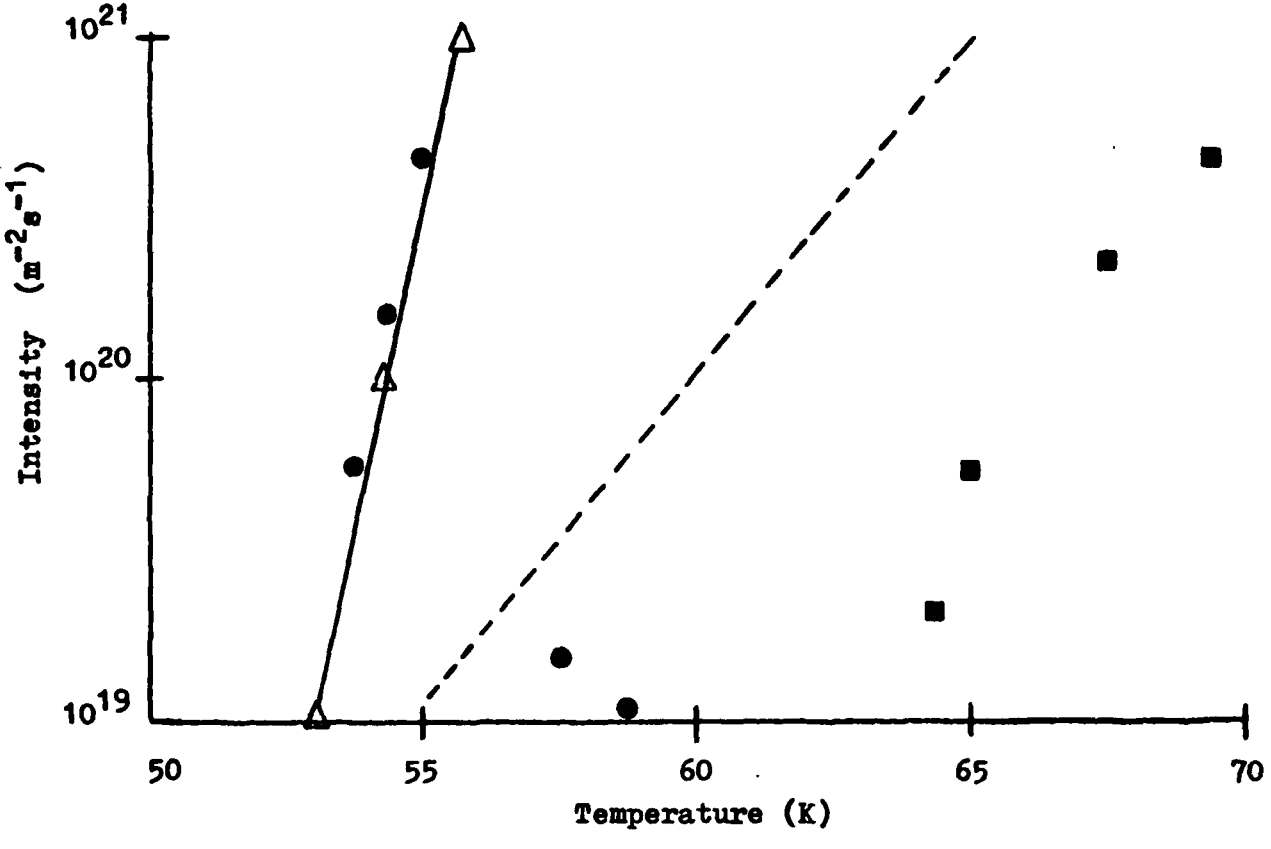

Figure (3.4-11) Nucleation Model Predictions (—△—) For Freon 11 Data On The Gold-Flashed (●) And HMDS-Coated (■) Stainless Steel Surfaces (Note: Vapor pressure data for Freon 11 is also given (----))

Figure (3.4-11)

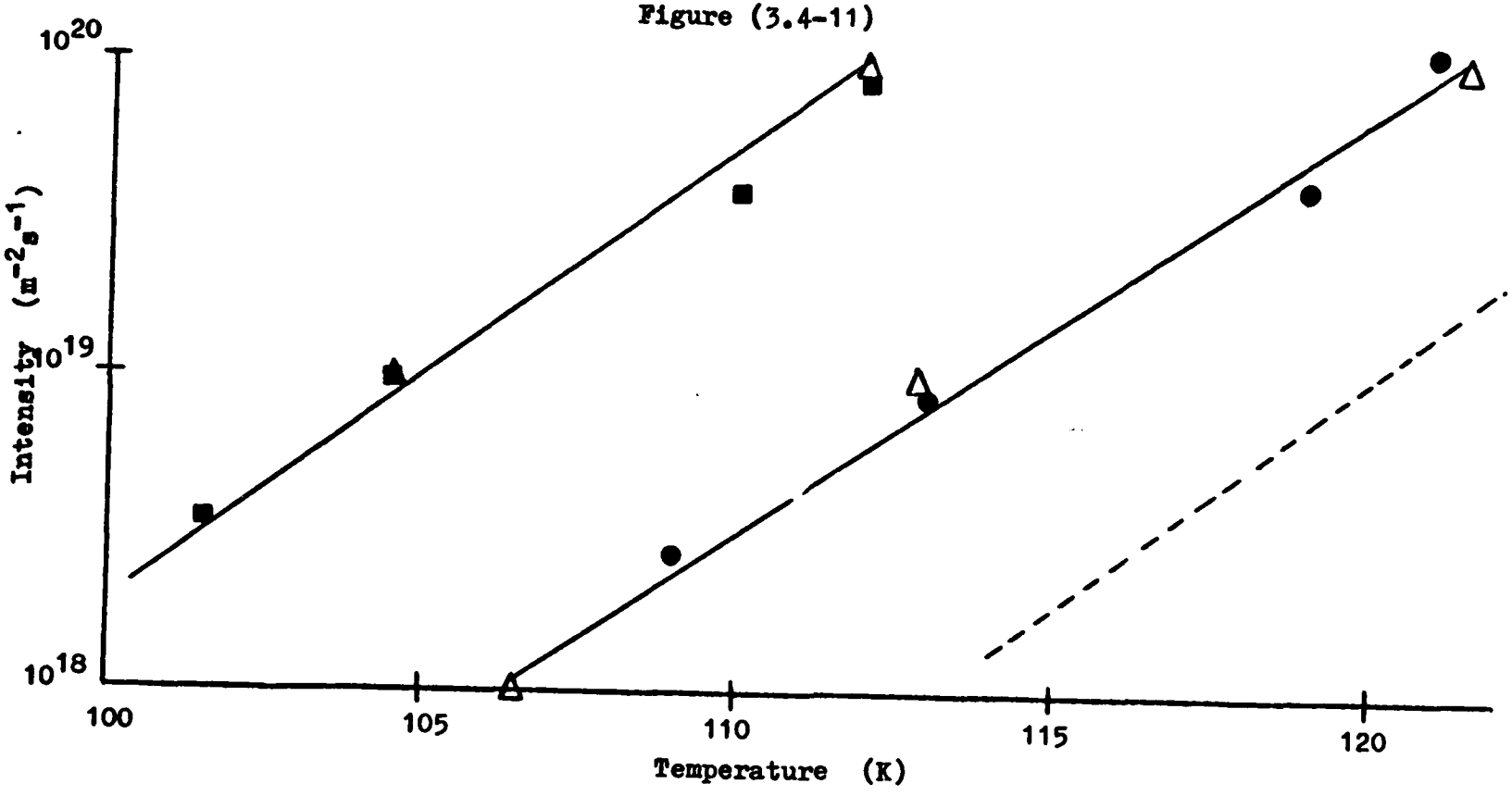
10^{20}
10^{19}
10^{18}
Intensity ($m^{-2}s^{-1}$)
100
105
110
115
120
Temperature (K)

Figure (3.4-12) Nucleation Model Predictions (—Δ—) For N_2 Data (●) On The Gold-Flashed Stainless Steel Surface (Note: The data of Heald and Brown (1968) (■) is also given, as well as N_2 vapor pressure data (----))

Figure (3.4-12)

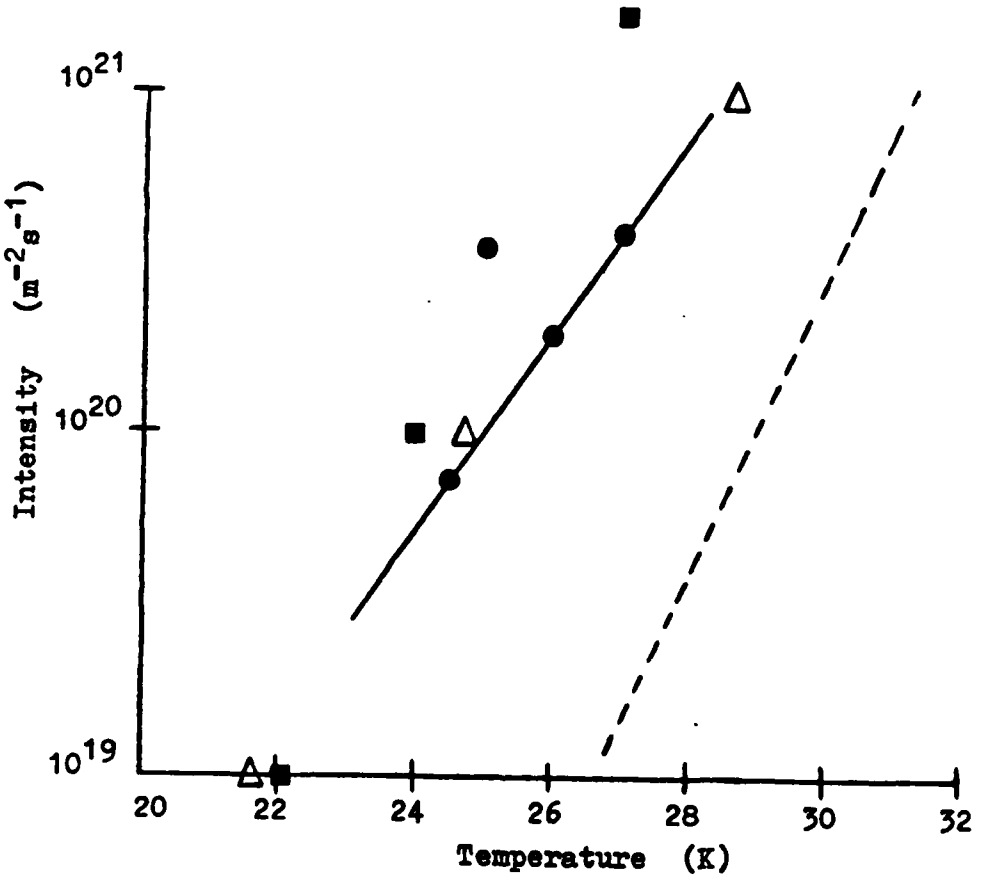
10^{21}
10^{20}
10^{19}
Intensity ($m^{-2}s^{-1}$)
20
22
24
26
28
30
32
Temperature (K)

Figure (3.4-13) Nucleation Model Predictions (—△—) For O_2 Data (●) On The Gold-Flashed Surface
(Note: The vapor pressure data for O_2 is also given (----))

Figure (3.4-13)

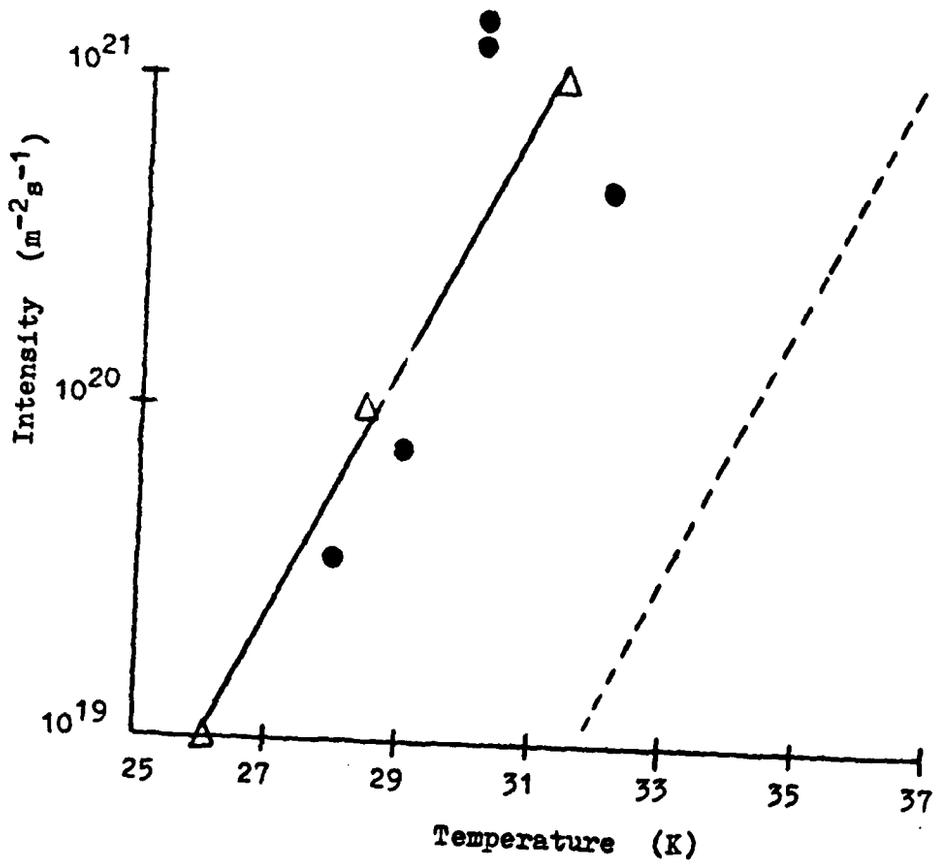
10^{21}
10^{20}
10^{19}
Intensity ($m^{-2}s^{-1}$)
25
27
29
31
33
35
37
Temperature (K)

REFERENCES CHAPTER 3

Abe, H., Schulze, W., Chem. Phys. 41, 257-63 1979

Adamson, A.W., Physical Chemistry of Surfaces, 2nd Ed., Intersciences, N.Y., 1967

Anderson, J.B., Molecular Beams and Low Density Gasdynamics, Wegener, P.D., ed., Marcel Dekker, N.Y., 1974

Barrer, R.M., Zeolites and Clay Minerals as Sorbents and Molecular Sieves, Academic Press, N.Y., 1978, p92-102

Barrow, G.M., Physical Chemistry, McGraw Hill, N.Y., 1973, p401

Becker, K., Klipping, G., Schoenherr, W.D., Schultz, W., Toelle, V., Proc. ICEC (IPC) 4, 319-21, 1972

Becker, K., Klipping, G., Schoenherr, W.D., Schultz, W., Toelle, V., Proc. ICEC (IPC) 4, 323-25, 1972(A)

Benson, S.W., King, J.W., Science 150, 1710-13, 1965

Bently, P.D., Hands, B.A., Rarified Gas Dynamics; Proc. 9th Int. Symp., Vol. 2, Becker, M., ed., 1974, pF14-1

Bently, P.D., Hands, B.A., Proc. R. Soc. Lond. A 359, 319-43, 1978

Bewilogua, L., Jackel, M., Cryogenics 14, 556-8, 1974

Bird, R.B., Stewart, W.E., Lightfoot, E.N., Transport Phenomena, Wiley, N.Y., 1960

Briant, C.L., Burton, J.J., J. Chem. Phys. 63, 2045, 1975

Brown, R.F., AEDC-TRD-63-267, Arnold Eng. Devel. Cent., USAF, 1964

Brown, R.F., Heald, J.H., Adv. Cryg. Eng., Vol. 12, Plenum Press, N.Y., 1967, p243

Brown, R.F., Wang, E.S.J., Adv. Cryg. Eng., Vol. 10, Plenum Press, NY, 1965, p283

Bryson III, C.E., Levenson, L.L., Surf. Sci. 43, 29-43, 1974

Castleman, A.W., Astrophysics and Space Sci. 65, 337-49, 1979

Cazcarra, V., Bryson III, C.E., Levenson, L.L., J. Vac. Sci. Tech. 10, 148-52, 1973

Daee, M., Lund, L.H., Plummer, P.L.M., Kassner Jr, J.L., Hale, B.N., J. Coll. Interface Sci. 39, 65-78, 1972

Davidson, D.W., Water, A Comprehensive Treatise, Vol. 2, Franks, F., ed., Plenum Press, N.Y., 1973, p115-234

Davidson, N., Statistical Mechanics, McGraw-Hill, N.Y., 1962

Dawson, J.P., Haygood, J.D., Collins, J.A., Adv. Cryg. Eng., Vol. 9, Plenum Press, N.Y., 1964, p443

Dawson, J.P., Haygood, J.D., Cryogenics 5, 57-67, 1965

de Boer, J.H., The Dynamical Character of Adsorption, Oxford, England, 1953

Flaim, T.A., Ownby, P.D., J. Vac. Sci. Tech. 8, 661, 1971

Fluendy, M.A.D., Lawley, K.P., Chemical Applications of Molecular Beam Scattering, Chapman and Hall, London, 1973

Foster, P.J., Leckenby, R.E., Robbins, E.J., J. Phy. B 2, 478-83, 1969

Frenkel, J., Kinetic Theory of Liquids, Dover, N.Y., 1955

Fuoss, R.M., J. Am. Chem. Soc., 60, 1633-37, 1938

Griffin, G.L., Andres, R.P., J. Chem. Phys. 71, 2522-30, 1979

Hallam, H.E., Scrimshaw, G.F., Vibrational Spectroscopy of Trapped Species, Hallam, H.E., ed., Wiley, N.Y., 1973. p12-66

Heald, J.H., Brown, R.F., AEDC-TR-68-110, Arnold Eng. Devel. Cent., USAF, 1968

Hirschfelder, J.O., Curtiss, C.F., Bird, R.B., Molecular Theory of Gases and Liquids, Wiley, N.Y., 1954

Holland, P.M., Castleman, A.W., J. Chem. Phys. 72, 5984-89, 1980

Honig, R.E., Hook, H.O., R.C.A. Review 21, 360, 1960

Jeffrey, G.A., McMullan, R.K., Prog. in Inorg. Chem., Vol. 8, Interscience, N.Y., 1967, p43-108

Kay, B.D., Hermann, V., Castleman, A.W., Abstracts of Papers of the Amer. Chem. Soc., 1979, Sept. 256 Phy

Lewis, B., Anderson, J.C., Nucleation and Growth of Thin Films, Academic Press, N.Y., 1978, p24

Meyer, B., Low Temperature Spectroscopy, American Elsevier, N.Y., 1971

Miller, S.L., Science 165, 489, 1969

Miller, S.L., Smythe, W.D., Science 170, 531-33, 1970

Miller, S.L., The Physics and Chemistry of Ice, Whalley, E., ed., Roy. Soc. of Canada, 1973, p42-50

Nikitin, B.A., Z. Anorg. Allegem. Chem. 227, 81-93, 1936

Nikitin, B.A., Zurnal Obscej. Chimiji, 9, 1167-75, 1939

Perry, R.H., Chilton, C.H., Chemical Engineers Handbook, 5th Ed., McGraw Hill, N.Y., 1973, p189-91

Pritchard, J., Nature 194, 38, 1962

Reid, R.C., Prausnitz, J.M., Sherwood, T.K., The Properties of Gases and Liquids, 3rd Ed., McGraw Hill, N.Y., 1977, p629-677

Ross, S., Olivier, J.P., On Physical Adsorption, Wiley-Interscience, N.Y., 1964, p257-275

Routledge, K.J., Stowell, M.J., Thin Solid Films 6, 407-21, 1970

Siksna, R., UURIE: 48-73, Uppsala University, Sweden, 1972

Siksna, R., UURIE: 53-73, Uppsala University, Sweden, 1973

Stowell, M.J., Hutchinson, T.E., Thin Solid Films 8, 41-53 1971

Stowell, M.J., Hutchinson, T.E., Thin Solid Films 8, 411-25, 1971(A)

Stowell, M.J., Phil. Mag. 26, 361-74, 1972

Stowell, M.J., Phil. Mag. 26, 361-74, 1972

Taylor, J.W., Parr, G.R., Jones, G.G., Proc. 4th Int. Conf. Vac. Ultraviolet Rad. Phys., Pergamon, Oxford, 1974, p197

UTI 100C Operating Manual, UTHE Technology International, Calif.

Venables, J.A., Ball, D.J., Proc. Roy. Soc. Lond. A 322, 331-54, 1971

Venables, J.A., English, C.A., Thin Solid Films 7, 369-89 1971

Venables, J.A., Phil. Mag. 27, 697-738, 1973

Venables, J.A., Price, G.L., Epitaxial Growth, Pt B, Matthews, J.W. ed., Academic Press, N.Y., 1975

Vincent, R., Proc. R. Soc. Lond. A 321, 53, 1971

Vogenitz, F.W., Bird, G.A., Broadwell, J.E., Rungaldier, H., AIAA J., 6, 2388-94, 1968

Voorhoeve, R.J.H., Treatise on Solid State Chemistry, Vol. 6A, Hannay, N.B., ed., Plenum Press, N.Y., 1976, p241-342

Walton, D., J. Chem. Phys. 37, 2182-88, 1962

Wang, E.S.J., Collins, J.A., Haygood, J.D., AEDC-TN-61-114, Arnold Eng. Devel. Cent., USAF, 1961

Wang, E.S.J., Collins, J.A., Haygood, J.D., Advances in Cryogenic Eng., Vol. 7, Plenum Press, N.Y., 1962, p44

Watson, H.E., Rao, G.G., Ramaswamy, K.L., Proc. Roy. Soc. Lond. A, 143, 558-88, 1934

Weast, R.C., ed., Handbook of Chemistry and Physics, 55 Ed., CRC Press, N.Y., 1974

Wittstruck, T.A., Brey, W.S., Buswell, A.M., Rodebush, W.H., J. Chem. Eng. Data 6, 343-46, 1961

4. THERMAL DESORPTION PHENOMENA

4.1 INTRODUCTION

In the cryogenic whole air sampling program conducted by the Air Force Geophysics Laboratory (Gallagher and Pieri, 1976, Gallagher, Pieri, and Goldan, 1977), cryogenic fractionation is employed to separate trace components in the sample from major matrix constituents, N_2 and O_2. This manipulation is necessary in order to circumvent saturation of the various analytical techniques employed (e.g., mass spectrometer, gas chromatograph, chemiluminescent analyzer) with the large quantities of N_2 and O_2 present in stratospheric samples. If quantitative analysis of trace species is to be accurate, however, it must be determined whether or not the N_2 and O_2 desorbing during this fractionation process are in fact causing concurrent desorption of less volatile trace species; i.e., "carry-over" of trace species of lower vapor pressure. If significant "carry-over" does in fact occur, can it be attributed to physical entrainment by the major matrix constituents, or are attractive intermolecular forces between the various matrix species primarily responsible? Can such "carry-over" shed light on the structure of the cryofrost? This chapter addresses these possibilities.

Earlier work on these questions (Dineen, 1977) showed that "carry-over" of Freons 11 and 12 by nitrogen and oxygen does indeed occur. Dineen also examined the CO_2-N_2 system (both species being nonpolar) and found no observable "carry-over" effects, leading to the conclusion that dipole-induced dipole interactions between the Freons and nitrogen could be

responsible for the "carry-over" effect. In the current work, Freons 11 and 12 are examined systematically in both N_2 and O_2 matrices, and the system N_2-Ar and N_2-CO_2 are also examined in order to determine if dipole effects are indeed important.

As noted elsewhere in this thesis, the use of concentrations approximating those of actual trace species in the stratosphere (i.e., on the order of ppbv) would make analysis in the present experimental system impossible. Therefore, more highly concentrated samples of the various constituent species were produced, and basic trends were determined. It is reasoned that an understanding of the interactions between matrix species obtained from such experiments could be extrapolated to the ultra-low concentration regimes of practical interest, at least qualitatively.

Since knowledge of the interactions between matrix species is the fundamental goal, experiments were performed in which the trace atmospheric species were the principal cryofrost constituent; e.g., frosts in which Freon 12 was the predominant component in a binary matrix. Experiments such as this do not relate to stratospheric samples directly, but do shed light on the nature of the interactions between species.

Dineen (1977) has shown experimentally that layering of test species onto the cryosurface (i.e., depositing one species as a pure frost, and then the second in a succeeding layer) is a valid approach in the study of species interaction, since the order in which the species are deposited

has little effect on desorption results. This has also been shown in the present work. If the species are premixed, as in the following chapter, the less volatile species (e.g., N_2 in a Freon 12 - N_2 mixture), if in the majority in the frost, can "matrix isolate" the more volatile species, trapping it in a matrix of the low volatility constituent and hindering its desorption. Since in actual air samples the high vapor pressure component is always in the majority (i.e., N_2 and O_2) and the interactions are of primary interest, a layering technique is employed in this work. Thus each species is deposited as a separate layer, and intimate contact between species occurs at the interfaces, which are extensive, due to the porous nature of cryofrosts deposited in such a manner (see Chapter 5). The only barrier desorption of more volatile species is the attractive forces exerted by neighboring, less volatile species. The more volatile species is never trapped in a matrix cage of the more stable species, an effect which would tend to mask the interactions.

Interaction between species in cryofrosts is but little understood, yet can lead to effects of critical importance to the analysis of cryogenic whole air samples. Thus the relevance of this type of work to the understanding of cryogenic whole air sampling is clear.

4.2 EXPERIMENTAL

The species employed in this study were $CFCl_3$ (Freon 11), CF_2Cl_2 (Freon 12), N_2, O_2, CO_2, and Ar. The specifications of these gases and vapors have been noted in Chapter 2.

A typical desorption experiment was performed by cooling the cryosurface to its lowest temperature (usually about 16K), and then exposing it to a directed beam of sample gas until a deposit on the order of $1x10^{-5}$ g mol was condensed. After termination of flow of the first species, the sample supply was changed, and a metered amount of the second species was deposited on top of the first layer. The molar ratio of the two condensed species was determined from the inverse relationship between velocity and molecular weight for sonic flow, which occurs across the variable leak valve; i.e.,

$$\dot{m}_a/\dot{m}_b = P_aV_a/P_bV_b = (P_a/P_b)(M_b/M_a)^{0.5} \qquad (4.2\text{-}1)$$

where

$\dot{m}$ = molar flow rate

P = supply pressure

V = sonic velocity

M = molecular weight

The molar ratio of the deposited species was controlled by varying the deposition time for each species at the same setting of the variable leak valve.

Temperature programmed desorption (TPD) of the cryofrost samples was accomplished by turning off the refrigerator

and allowing the thermal gradient along the refrigerator stem (see Chapter 2) to heat the surface. A typical time-temperature warm-up curve (for run 40) is presented in Figure (4.2-1). The slope of this curve is large at short times, due to the high thermal gradient along the stem. As desorption proceeds and the gradient decreases, the slope declines. Since initially the stem is also at a low temperature, the thermal inertia of the expander causes the surface temperature to rise more slowly.

During desorption, a specific peak was monitored with the mass spectrometer. The selected peaks were chosen such that they produced a strong response, a linear variation with the species partial pressure, and were relatively free of background signal. Applying these criteria, peak 35 was chosen for the halocarbons (i.e., the Cl^+ ion peak), 14 for N_2 (due to CO background at 28), 32 for O_2, 44 for CO_2, and 40 for Ar.

The cryosurface selected for the Freon-N_2 and Freon-O_2 studies was the electropolished stainless steel disk, primarily due to its high affinity for the Freons (Gallagher, Pieri, and Goldan, 1977). Thus if carryover of the Freons at low temperatures by N_2 or O_2 occurs for this surface, the effect would probably be even stronger for other metal cryosurfaces. Since Dineen (1977) discerned no carryover for the CO_2-N_2 system, it was decided to run CO_2-N_2 and Ar-N_2 experiments on the gold-flashed stainless steel cryosurface on which interaction between adsorbed species might be more

visible due to the relatively lower adsorptive capacity of this surface material. Thus two surfaces were employed due to the expected variation in behavior.

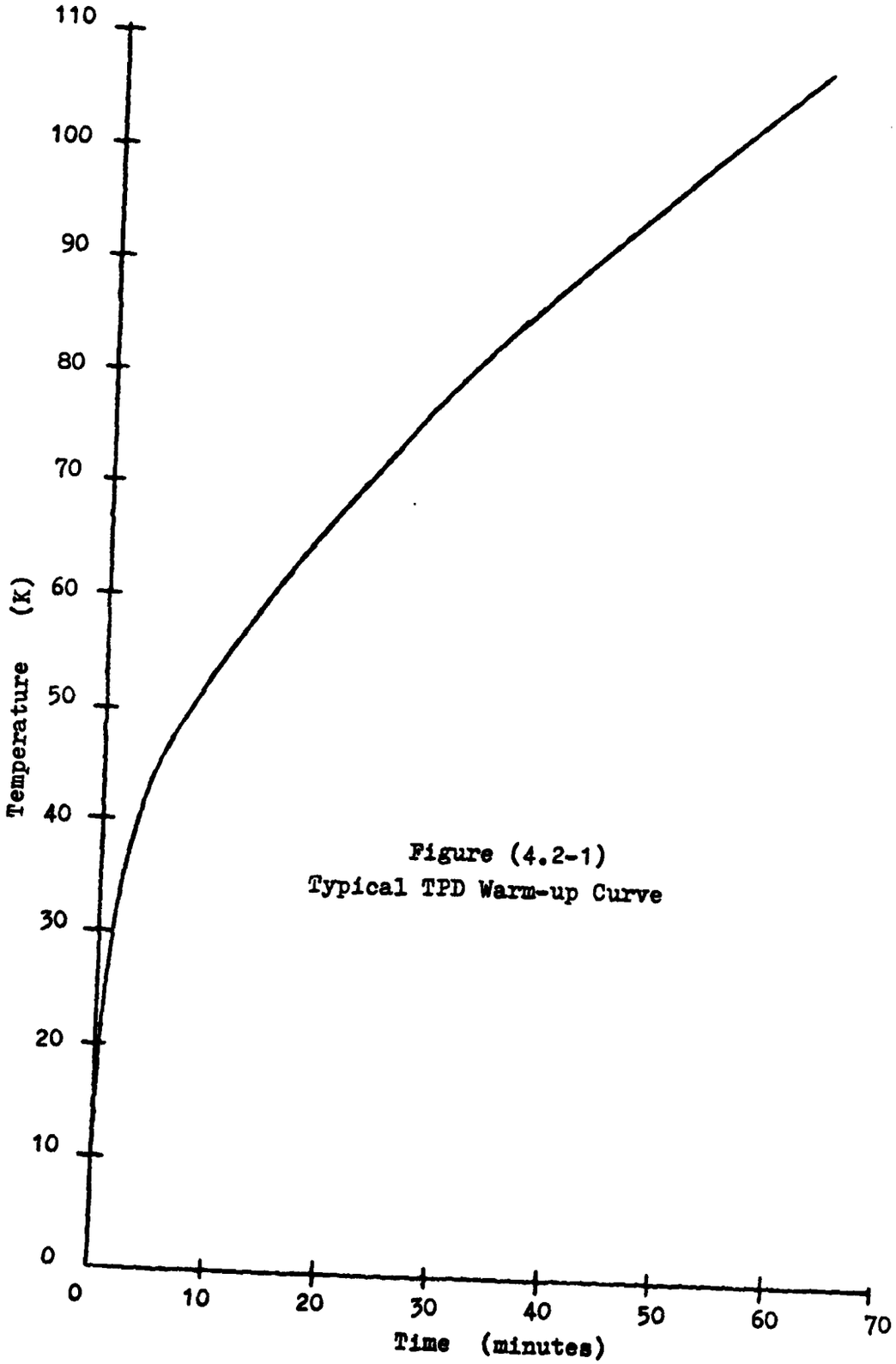

Figure (4.2-1)
Typical TPD Warm-up Curve

4.3 RESULTS AND DISCUSSION

Pure Species Desorption Spectra

We begin the discussion of interactions between species in cryofrosts by examination of the TPD spectra of the various pure components. Figure (4.3-1) is a characteristic desorption spectrum for N_2; i.e., a plot of the logarithm of the mass spectrometer signal versus the cryosurface temperature. It is noted that three distinct peaks, labeled γ(34K), α (38.5K), and β (43K) are evident, and that the bulk of the nitrogen desorbs in the 20-50K temperature range, with the remainder of the signal attributable to background. The labeling of the peaks in this manner is reminiscent of the work of Hickmott and Ehrlick (1958) and Ehrlick (1961), who observed three desorption peaks associated with the desorption of a sorbed layer of N_2 on tungsten at temperatures greater than 115K. It must be noted, however, that the current work deals with multilayer frosts of condensed species, and not monolayers of chemisorbed species, and thus no direct correspondence is intended.

If it is assumed that desorption of a N_2 molecule from an N_2 cryofrost is similar to the desorption of physisorbed and chemisorbed species, then the Polanyi-Wigner equation (Redhead, 1960, King, 1975) can be applied to estimate energies of desorption; i.e.,

$$N(t) = d\sigma/dt = \nu\, \sigma^n \exp(-E_d/RT) \qquad (4.3\text{-}1)$$

where

σ = surface coverage (molecules/cm^2)

ν = first order rate constant (s^{-1}); estimated as

$\nu = kT/h$

N = rate of desorption (molecules/$cm^2 s$)

E_d = activation energy of desorption (cal/g mol)

T = surface temperature (K)

t = time (s)

n = order of the desorption reaction

It has been shown (Redhead, 1962) that for first order desorption (n=1) with a linear time-temperature profile (i.e., $T=Bt + T_o$) at the desorption peak temperature, T_p;

$$E_d/RT_p^2 = \nu/B \exp(-E_d/RT_p) \qquad (4.3\text{-}2)$$

Thus, first order desorption is independent of surface coverage, and desorption energies can be deduced from equation (4.3-2).

The N_2 spectrum in Figure (4.3-1) was found to be quite reproducible except for the β peak, which was observed to shift slightly in temperature, indicating that it may be of higher order than one. The γ and α peaks were determined to be first order, however, with $E_{d\gamma}$ = 2000 cal/mol and $E_{d\alpha}$ = 2300 cal/mol.

In the 20-50K temperature range in Figure (4.3-1), the vapor pressure of N_2 varies from 10^{-11} to 1 torr (Honig and Hook, 1960), while the background pressure in the chamber remains in the 10^{-5} to 10^{-7} torr range. Thus even for pure species desorption, the spectra obtained are more complex than can be predicted from vapor pressure data. It is also

interesting to note that the γ and α peaks are located on either side of the known solid II-I transition of N_2 (ΔH=54.71 cal/g mol) which occurs at 35.61K (Scott, 1959), and could account for the decrease in intensity which defines the two peaks.

The desorption spectrum of pure O_2, presented in Figure (4.3-2), is quite similar to that of N_2 insofar as three major peaks are evident, which, for the sake of consistency, are also labeled γ (40K), α (45K), and β (49K). These three peaks were determined to be first order (i.e., coverage-independent) and with E_d values of 2420, 2780, and 3120 cal/mol, respectively. Also, as for nitrogen, the γ and α peaks are located on either side of the O_2 solid II to solid I phase transition at 43.8K (ΔH=177.6 cal/g mol), and the minor peak at 20K may exist due to the solid III-solid II phase transition (ΔH=22.42 cal/mol) at 23.9K (Scott, 1959). It is also noted that all desorption activity ceases after 55K in Figure (4.3-2), with the remaining signal associated with background.

Figure (4.3-3) is a desorption spectrum of pure Freon 12. Evident are three minor peaks at 55K, 65K, and 72K with associated E_d values of 3525, 4210, and 4690 cal/mol, respectively, and a major peak at 104K with E_d=6950 cal/mol. The latter peak contains the bulk of the desorbing Freon. It is noted that prior to this peak, the mass spectrometer signal constantly increases, reflecting the increasing sublimation pressure with temperature. It is also observed that

the final Freon 12 baseline signal (i.e., above 120K) remains high, primarily due to the high background pressure of Freon 12 resulting from the high affinity of Freon 12 for the vacuum chamber walls. The background Freon 12 signal was eliminated between experiments by baking the vacuum chamber. It is important to note that the desorption behavior of Freon 12, while increasing constantly with temperture, does not exhibit a primary peak until 55K, which is well beyond the desorption temperatures of N_2 and O_2. This point is quite important for the gas mixture desorption studies discussed subsequently.

Figure (4.3-4) presents the desorption spectrum of pure Freon 11. As for Freon 12, Freon 11 exhibits a minor peak at low temperature: 47K with E_d = 2930 cal/mol. The major desorption peak, however, occurs at a higher temperature than that of Freon 12, typically 120K, which corresponds to E_d = 8090 cal/mol. A high background level of Freon 11 after the high temperature desorption peak is also evident, which is again indicative of the strong adsorption of Freon 11 on the stainless steel vacuum chamber walls (Gallagher, Pieri, and Goldan, 1977). Thus care must be taken in integrating the area under these curves. It is also noted that although the minor peak at 47K does overlap those of N_2 and O_2 somewhat, its magnitude and area (approximately 0.2% of the total Freon 11 desorbed) has little effect on the carry-over results.

Binary Mixture Desorption Experiments
Freon-Nitrogen Experiments

Figure (4.3-5) illustrates the results of three separate experments for the binary system Freon 12-N_2; i.e., 100% F12 (run 30), 40% F12 (run 41), and 4% F12 (run 74). Since varying absolute deposit amounts were used, these results should be interpreted as indicative of qualitative trends only. In integrating such desorption spectra, the time-temperature profile is taken into account, and the partial integrals are normalized by the total amount of the species deposited. Baselines are not determined since the signal at low temperatures primarily reflects the sublimation pressure of the cryofrost, and is not just background.

In Figure (4.3-5), a minor peak in the 37-43K temperature range, which is not evident in the pure Freon 12 desorption spectrum, increases with decreasing Freon 12 concentration. Referring to Figure (4.3-1) for pure N_2, it is noted that this minor peak coincides with the α and β desorption peaks of N_2; i.e., as the Freon 12 concentration decreases, a progressively greater fraction is being carried over with the desorbing N_2. Also, in the 50-70K temperature ragne, the three characteristic minor Freon 12 peaks become progressively less well-defined, with decreasing Freon 12 concentration. This can be interpreted in terms of increasing amounts of N_2 held over in F12 agglomerates which alter the distribution of Freon 12 desorption energies, yielding a more continuous pattern. Also, the major desorption peak at 104K shifts progressively to a somewhat lower temperature of 99K,

corresponding to a decrease in E_d of approximately 350 cal/mol. Thus the desorbing Freon 12, in association with some held-over N_2, exhibits a higher effective vapor pressure than pure Freon 12. The normalized partial integrals for 100% and 40% Freon 12 between 14K and 50K are 2.7×10^{-4} and 1.7×10^{-4}, respectively. These results appear anomalous insofar as no carry-over peak at 38K is evident for pure Freon 12, yet the integral is larger. However, the total deposit was far greater in the 40% Freon 12 experiment, and thus the carry-over peak, although relatively larger in magnitude than in the pure Freon 12 data, is a smaller percentage of the entire deposit. This is also a result of the general inability to draw a proper baseline for these experiments. In any case, the same analysis for the 4% Freon 12 data yields a partial integral of 6.8×10^{-4}, which is well above both previous runs, and indicates that, indeed, the magnitude of the N_2 carry-over of Freon 12 increases as the Freon 12 concentration decreases.

Figure (4.3-6) presents additional N_2-F12 experiments in which N_2 desorption was monitored for N_2 concentrations of 100% (run 66), 60% (run 42), and 14% (run 86). As the N_2 concentration decreases, the major pre-50K desorption peak shifts from the γ peak of Figure (4.3-1) at 34K to 41K, a temperature which lies between the α and β peaks of pure N_2 (cf. Figure (4.3-1)). The γ peak itself shifts to approximately 30K, and decreases until it is nearly indistinguishable. Thus Freon 12-N_2 attraction shifts the main N_2 desorption peak from E_d = 2000 cal/mol to 2490 cal/mol. Therefore, it

seems the addition of Freon 12 effectively stabilizes N_2 on the cryosurface, with a ΔE_d well within the range of physical attractive forces. In Figure (4.3-6) it is also evident that: (1) the N_2 desorption pattern gradually assumes the three peak pattern of pure Freon 12 (cf. Figure (4.3-1)) in the 45K to 60K temperature range, with decreasing N_2 concentration; (2) the 60% N_2 mixture develops two additional peaks at 73K and 105K; and (3) the 14% N_2 develops a well-defined peak at 73K and a relatively weak one at 105K. The development of the major peak in the case of 14% N_2 is quite interesting, since, as shown in Figure (4.3-5), Freon 12 does not exhibit a major desorption peak at 73K. This result implies that this particular N_2 desorption peak is not caused by physical entrainment during the desorption of F12 from the surface, but a genuine N_2-F12 interaction which alters the desorption energy for N_2. If entrainment were the case, one would expect the major interaction peak during the desorption of F12 to occur at approximately 103K.

For pure N_2 (cf. Figure 4.3-1), by 50K practically all of the N_2 has desorbed. Choosing 50K as the cutoff temperature, it is calculated that for the 60% N_2 run, 63.5% of the N_2 desorbed by 50K, the remainder desorbing past 50K; while for the 14% N_2 run, only 23.2% of the total N_2 desorbed prior to 50K. Thus, as N_2 becomes less concentrated in the matrix, its desorption pattern in strongly disrupted by interaction with Freon 12, causing it to desorb at much higher temperatures than when pure.

The Freon 11-N_2 system was also investigated. Figure (4.3-7) presents the results of Freon 11 desorption in three runs with Freon 11 concentrations of 100% (run 60), 50% (run 54), and 10% F11 (run 53). As in Figure (4.3-4), the desorption spectrum of pure Freon 11 exhibits a minor peak at 47K and a major peak at 120K. However, the two binary mixture spectra exhibit two additional peaks in the 25-45K range which coincide with pure N_2 desorption peaks (cf. Figure (4.3-1)). These results are quite similar to those for the Freon 12-N_2 system, presented in Figure (4.3-5). One difference, however, is that for Freon 12 (Figure (4.3-5)) the major desorption peak shifted to lower temperatures for low Freon 12 concentrations, while in the case of Freon 11 (Figure (4.3-7)), the major desorption peak remains constant. It is also noted that for Freon 12 (cf. Figure (4.3-5)) and Freon 11 (cf. Figure (4.3-7)), the 25K-45K carryover peaks do not coincide for the moderate and extreme dilution cases; i.e., in Figure (4.3-7) the major pre-45K carryover peak occurs at 38K for the 50% Freon 11 case and 44K for the 10% Freon 11 case. This behavior implies that as the concentration of Freon 11 decreases it becomes increasingly associated with N_2 adsorbed onto higher E_d sites. This is consistent with the porous matrix model discussed in the previous chapter. From integration of the spectra, it was determined that for the 100% Freon 11 case 8.6×10^{-4} of the total deposit desorbed by 45K, as compared to 7.6×10^{-4} for the 50% Freon 11 mixture. These results again illustrate that although the carry-over peak is quite visible for the 50% Freon 11 mixture,

it is not yet strong enough to make a significant difference in the integrated data. However, in the 10% Freon 11 case, the integral becomes 1.3×10^{-3}, which is significantly greater than the two previous cases, and clearly illustrates that as the concentration of Freon 11 decreases in the matrix, the amount of material desorbed as a result of carry-over becomes significant.

The results for the Freon 11-N_2 system for concentrations of 100% (run 66), 50% (run 55), and 20% N_2 (run 59) are presented in Figure (4.3-8). As the concentration of N_2 in the matrix decreases from the pure N_2 case, the γ peak (cf. Figure (4.3-1)), originally located at 34K (E_d=2000 cal/mol), shifts to lower temperatures (e.g., 29K, or E_d=1700 cal/mol for the 10% N_2 case), while simultaneously decreasing dramatically in magnitude. This apparent decrease in the activation energy of desorption is indicative of a change in the local adsorption environment. The major desorption peak for N_2 gradually changes from the γ to the α peak (cf. Figure (4.3-1)), which at 39-40K corresponds to E_d=2400 cal/mol. Thus as the nitrogen concentration in the matrix decreases, the activation energy of the desorption of N_2 increases, primarily due to interaction with Freon 11. In addition, the total amount of N_2 which survives the principal desorption at 39-40K and desorbs at temperatures greater than 50K also increases with decreasing N_2 concentration. The 50% N_2 mixture exhibits some evidence of a Freon 11 carry-over peak coincident with the principal Freon 11 peak at

120K (cf. Figure (4.3-4)), while the 20% N_2 sample does not. In both cases, however, a broad desoption peak develops in the 50-90K temperature range which is not characteristic of pure Freon 11 desorption. This behavior clearly indicates that simple physical entrainment alone cannot explain such striking modifications of the desorption spectra. Integration of the spectra to 50K yielded 0.99, 0.916, and 0.799 of the N_2 desorbed for the 100%, 50%, and 20% N_2 mixtures, respectively. Although not as dramatic as the N_2-Freon 12 effect illustrated in Figure (4.3-6), these data clearly illustrate that reduction of the N_2 concentration increases the percentage of holdover of N_2 by Freon 11, and that the N_2 retained in this manner desorbs over a wider temperature (energy) range.

Freon - Oxygen Experiments

The oxygen-Freon mixtures generally exhibited a greater degree of interaction between the species than was observed for N_2-Freon mixtures. Figure (4.3-9) presents Freon 12 desorption spectra for concentrations of 100% (run 30), 50% (run 29) and 4% (run 75) Freon 12 in oxygen. As for the N_2-Freon 12 mixtures (cf. Figure (4.3-5)), as the Freon 12 concentration decreases, the major Freon 12 peak at 104K steadily shifts to lower temperatures (to 101K for the 4% mixture (run 75), a shift in E_d of approximately 210 cal/mol). The 50-90K region of the Freon 12 desorption spectra, which exhibits only minor peaks for pure Freon 12, progressively blurs with decreasing concentration, while the pre-50K peaks, which, as shown in Figure (4.3-2), coincide

with pure O_2 desorption, increase in magnitude and become more distinct, again as for the N_2-Freon 12 mixtures. Integration of the pre-50K spectra, reveals that 2.7×10^{-4}, 4.2×10^{-4}, and 7.6×10^{-4} of the total Freon 12 desorbs in the low temperature range for the 100%, 50%, and 4% Freon 12 mixtures, respectively. Thus, again as the Freon 12 concentration decreases, carry-over of Freon 12 by the principal O_2 desorption peaks increases.

Figure (4.3-10) presents O_2 desorption spectra for O_2-Freon 12 mixtures of 100% (run 18), 50% (run 26), and 10% (run 31) O_2. As the O_2 concentration decreases, the major desorption pattern in the pre-50K temperature range shifts from a three-peak (cf. Figure (4.3-2)) to a single peak desorption pattern at the same temperature as the α peak in Figure (4.3-2) (45K), while the γ peak decreases to near-zero. This behavior is again similar to that of Freon 12-N_2 desorption in Figure (4.3-6). A significant amount of O_2 holdover past 50K is evident for low O_2 concentration mixtures, which eventually desorbs in a broad series of peaks in the 50-90K range. The binary mixtures also exhibit a series of peaks in the 90-110K range, which is the major desorption region for Freon 12. This is again indicative of a significant degree of Freon 12 interaction with O_2 resulting in stabilization of the adsorbed O_2 to desorb at higher temperatures. The magnitude of the interaction is indicated by the desorption temperatures of the major holdover peaks; i.e., 50-90K. Integration of the data in Figure (4.3-10) to 50K reveals that 0.98, 0.77, and 0.18 of

the oxygen desorbs in the low temperature range for the 100%, 50%, and 10% O_2 mixtures, respectively; e.g., 82% of the oxygen in the 10% mixture is retained by Freon 12 and desorbed at temperatures greater than 50K.

Figure (4.3-11) presents three Freon 11 desorption spectra for Freon 11-O_2 mixtures with 100% (run 60), 50% (run 63), and 10% (run 61) Freon 11. The general characteristics of these curves are similar to those of N_2-Freon 11 mixtures in that the major Freon 11 desorption peak at 120K remains constant, while a Freon 11 carry-over peak steadily develops with decreasing Freon 11 concentration, in the lower temperature range. It is noted here that both pure Freon 11 (Figure (4.3-4)) and pure O_2 (Figure (4.3-2)) have desorption peaks which overlap in the 47-50K temperature range, and thus the distinction between the development of a new carry-over peak and the enhancement of the existing minor peak at 48K is not very clear. Assuming a carry-over cutoff point of 55K (i.e., all material desorbed below 55K is due to carry-over), integration of the spectra to this point reveals that for 100% Freon 11, 2.6×10^{-3} of the total Freon 11 desorbs, in comparison to 7.6×10^{-3} of the deposit for the 50% Freon 11 mixture, and 1.8×10^{-2} of the total deposit for the 10% Freon 11 mixture. This is again clearly consistent with the trend that the fraction of Freon 11 carry-over steadily increases with decreasing Freon 11 concentration.

Figure (4.3-12) presents O_2 desorption spectra for Freon 11-O_2 mixtures with 100% (run 18), 50% (run 64), and 20% (run 67) O_2. In this system, unlike the previous three

examined, decreasing the percentage of oxygen in the matrix shifts the major O_2 desorption peak to the location of the γ peak of pure O_2 (cf. Figure (4.3-2)), which is a less stable peak (lower E_d); i.e., the addition of Freon 11 destabilizes the majority of the O_2 condensate. One explanation for this behavior is that the polycrystalline surface structure of the Freon 11 deposit may provide a less than optimum surface for O_2 stability, although, of course, other explanations are also possible. It is also noted, however, that as the O_2 concentration decreases, the post-55K oxygen desorption (a broad peak varying from 60-95K) increases in relative magnitude, and that the 50% O_2 sample develops an O_2 desorption peak coincident with the major Freon 11 peak at 120K (cf. Figure (4.3-4)), but as in the other system, it disappears at the lowest concentration. Integration of the pre-55K data reveals that 0.995, 0.813, and 0.737 of the total amount of oxygen desorbs in the low temperature range for the 100%, 50%, and 20% O_2 mixtures, respectively. These data clearly show that O_2 is held over to temperatures above its normal desorption range, but still does not desorb with the major Freon 11 peak at 120K, and thus is not being matrix isolated and then entrained by desorbing Freon 11, but rather is being held in the solid due to intermolecular attraction with Freon 11. However, O_2 still desorbs independently of Freon 11 over the temperature ranges where the bulk of the Freon 11 remains condensed.

Thus, it has been shown that carry-over of Freon 11 or 12 mixed with N_2 or O_2 increases steadily with decreasing

Freon concentration at temperatures much lower than normal for the pure Freon. This effect seems to be associated with intermolecular attraction between the two species involved. When either the N_2 or O_2 concentration is decreased, the condensed Freon retains the O_2 or N_2 in the solid to desorb at higher temperatures than for pure N_2 or O_2, but still lower than the major pure Freon desorption peak.

In order to estimate the magnitude of the intermolecular interactions in the cryofrost mixture, the Lennard-Jones potential force constants, ε and $\underline{\sigma}$, along with polarizabilities, $\underline{\alpha}$, and dipole moments of the polar species, μ (Hirshfelder et al., 1964) were used (see Table (4.3-1)). For polar-polar and nonpolar-nonpolar interactions, the geometric combining rule approximation,

$$\varepsilon_{12} = \sqrt{\varepsilon_1 \varepsilon_2} \qquad (4.3\text{-}3)$$

is valid, but for the polar (p)-nonpolar (n) interactions,

$$\varepsilon_{np} = \sqrt{\varepsilon_n \varepsilon_p}\,\zeta^2 \qquad (4.3\text{-}4)$$

(Hirschfelder et al., 1964) where,

$$\zeta = \left[1 + \frac{1}{4}\,\frac{\underline{\alpha}_n\,\mu_p^{*2}}{\underline{\sigma}_n^{3}}\,\sqrt{\frac{\varepsilon_p}{\varepsilon_n}}\,\right] \qquad (4.3\text{-}5)$$

$$\mu^* = \mu/\sqrt{\varepsilon \underline{\sigma}^3} \qquad (4.3\text{-}6)$$

Estimates of energies of interaction between the species considered here using those formulations vary widely, as illustrated in Table (4.3-2). Of the Freon 11/Freon 12-N_2/O_2 systems, Freon 12-N_2 exhibits the lowest interaction, followed by near equal values for Freon 11-N_2 and Freon 12-O_2, and the highest for Freon 11-O_2. From the integrated

data for carry-over of the Freons by N_2 or O_2, an estimate was made of the magnitude of the carry-over effect by subtracting the normalized carry-over integral at the highest Freon concentration (100%) from that at the lowest Freon concentration, which varied from system to system. This procedure yielded values of 4.2×10^{-4}, 4.4×10^{-4}, 4.9×10^{-4} and 153×10^{-4}, for the F12-N_2, F11-N_2, F12-O_2, and F11-O_2 systems, respectively; i.e., in the exact same order as suggested by the interaction energy estimates. It must be noted, however, that the lowest concentrations were not the same for each system, nor were cutoff temperatures equal, and thus this comparison should be treated as qualitative, at best. The fact that the Freon 11-O_2 experimental results exhibit approximately 30 times more interaction than for the other systems, implies that factors other than those reflected by these simple estimates may also be responsible; e.g., steric or geometric, etc. However, without additional data, all that can be said with certainty is that the Freon 11-O_2 interaction seems to be the greatest for those systems tested.

Dineen (1977) suggested that the interactions observed in his experiments were in fact due to dipole-induced dipole interaction, citing an experimental inability to observe the carry-over effect observed for Freon-N_2 systems with CO_2-N_2 mixtures. In order to check this hypothesis, both CO_2-N_2 and Ar-N_2 mixtures were deposited and desorbed from the gold-flashed stainless steel surface.

In Figure (4.3-13), curve A , is a desorption spectrum of pure N_2 from the gold-flashed surface. It is noted that

this spectrum is substantially different than that of N_2 from the electropolished stainless steel surface (cf. Figure (4.3-1)) in that it exhibits two major peaks at 29K (1700 cal/mol) and 42K (2565 cal/mol) as opposed to the three reported earlier on the electropolished stainless steel surface. Figure (4.3-13), curve B, is a background spectrum for mass peak 28 (primarily CO) which shows a minor contribution to the major desorption peak at 42K with a small quantity of desorbate. These data prove that the cryosurface material has a significant effect on the desorption of multilayer cryofrosts.

Figure (4.3-14) presents a desorption spectrum of pure Ar characterized by a broad desorption peak at 35K (2065 cal/mol) and a sharp peak at 47.5K (2960 cal/mol) followed by a rapid drop to the baseline. Also, both peaks are in the same temperature range as for pure N_2 desorption, thereby obfuscating subsequent data interpretation.

Figure (4.3-15) presents a desorption spectrum of pure CO_2 from the gold-flashed surface, characterized by a major desorption peak at 90K (5940 cal/mol), with only minor peak apparent in the lower temperature range, in a manner reminiscent of Freon desorption.

The CO_2 desorption spectrum for a 98% N_2, 2% CO_2 mixture from the gold-flashed surface is presented in Figure (4.3-16). The distinct peaks at 29K and 42K, exactly coincide with the major N_2 desorption peaks from the gold-flashed surface (cf. Figure (4.3-13)). Assuming 50K as the carry-over cutoff temperature, integration of the spectra

reveals that for pure CO_2 (cf. Figure (4.3-15)), 4.5×10^{-4} of the deposit desorbs prior to 50K, while in Figure (4.3-16), 6.9×10^{-4} desorbs in the same range. This result is of the same magnitude as for the Freon-N_2 data, thereby proving that dipole-induced dipole interaction is not the principal source of the observed behavior.

To further illustrate this point, a theoretically weakly-interacting system (cf. Table (4.3-2)), Ar-N_2 was examined. Since interaction effects become more evident with decreasing concentrations, a 46% Ar- 54% N_2 matrix was deposited on the surface and then subsequently desorbed while monitoring Ar desorption. These data are presented in Figure (4.3-17) and clearly show a minor peak at 42.5K, corresponding tothe major N_2 desorption peak at 42K (cf. Figure (4.3-13)) which does not exist in the desorption spectrum of pure Ar (cf. Figure (4.3-14)). As noted previously, the desorption temperature ranges for pure Ar and N_2 overlap, and thus carry-over is not as evident as in the other systems studies and the comparative strength of interaction effects and physical entrainment is difficult to ascertain. Yet, integration reveals that in the 37-45K range where the suspected carry-over peak occurs, 0.115 of the Ar (cf. Figure (4.3-14)) desorbed in the 100% Ar case, while 0.180 of the total Ar desorbed over the same range from the Ar-N_2 mixture (cf. Figure (4.3-17)). Thus the effect does seem substantial, and proves that even in weakly-interacting systems without permanent dipoles, interaction effects are still appreciable.

The formation of heteromolecular complexes, such as dimers and higher multimers, has long been known to occur in cryofrost matrices generated for matrix isolation studies (Guillory and Hunter, 1969, Pimentel et al., 1962, Hallam, 1973; see Chapter 5). Thus it is not surprising that the systems examined in the present studies are susceptible to similar effects; i.e., heteromolecular attractions which may cause carry-over as well as holdover, depending on the concentration of the sample, and the species concerned.

TABLE (4.3-1)

INTERMOLECULAR POTENTIAL FORCE CONSTANTS*

	ε/k [K]	σ_o (A)	$\alpha \times 10^{25}$ (cm^3)	μ (D)
N_2	91.5	3.681	17.6	
O_2	113	3.433	16.0	
CO_2	190	3.996	26.5	
F11	399	4.534		.53
F12	324	4.812		.55
Ar	124			

*Hirshfelder et al. (1964)

TABLE (4.3-2)

ESTIMATED INTERACTION PARAMETERS CALCULATED FROM DATA PRESENTED IN TABLE (4.3-1)

System	ζ	ϵ_{12}
F12-N_2	1.098	214
F11-N_2	1.101	232
F12-O_2	1.098	238
F11-O_2	1.101	258
CO_2-N_2	-	132
N_2-Ar	-	106

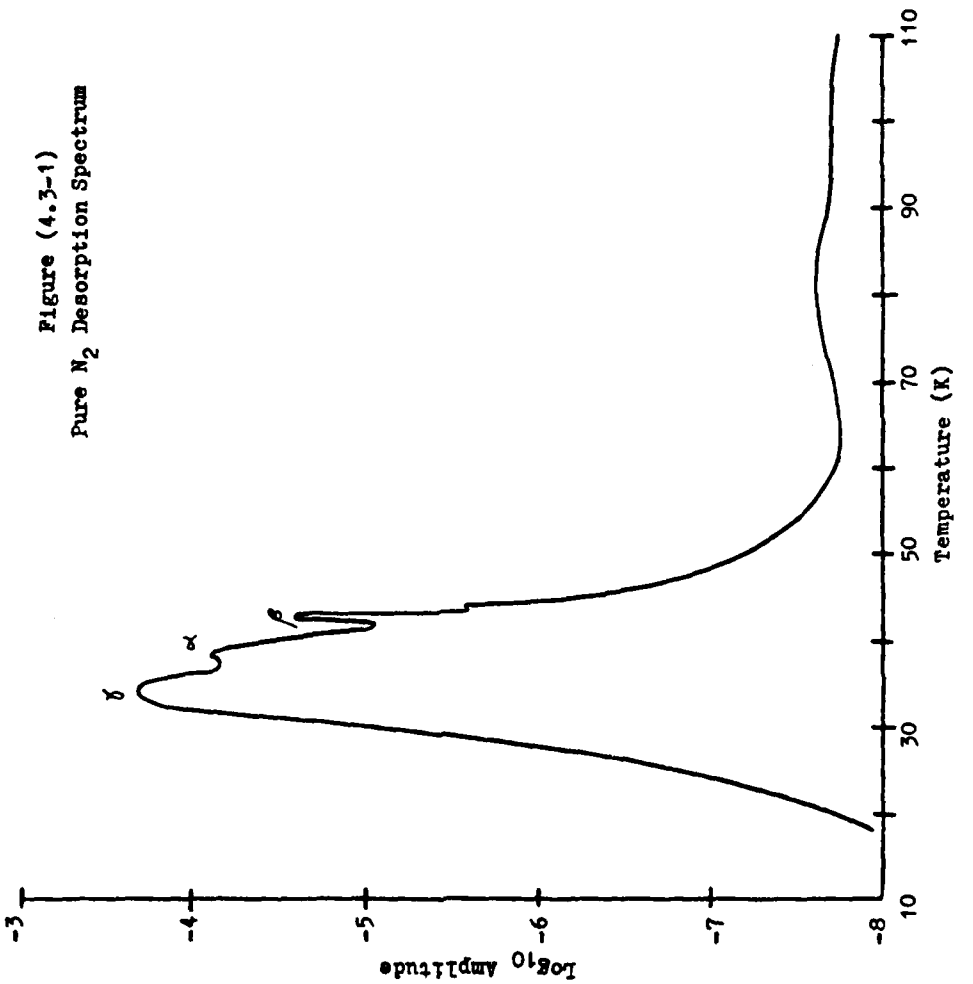

Figure (4.3-1)
Pure N_2 Desorption Spectrum

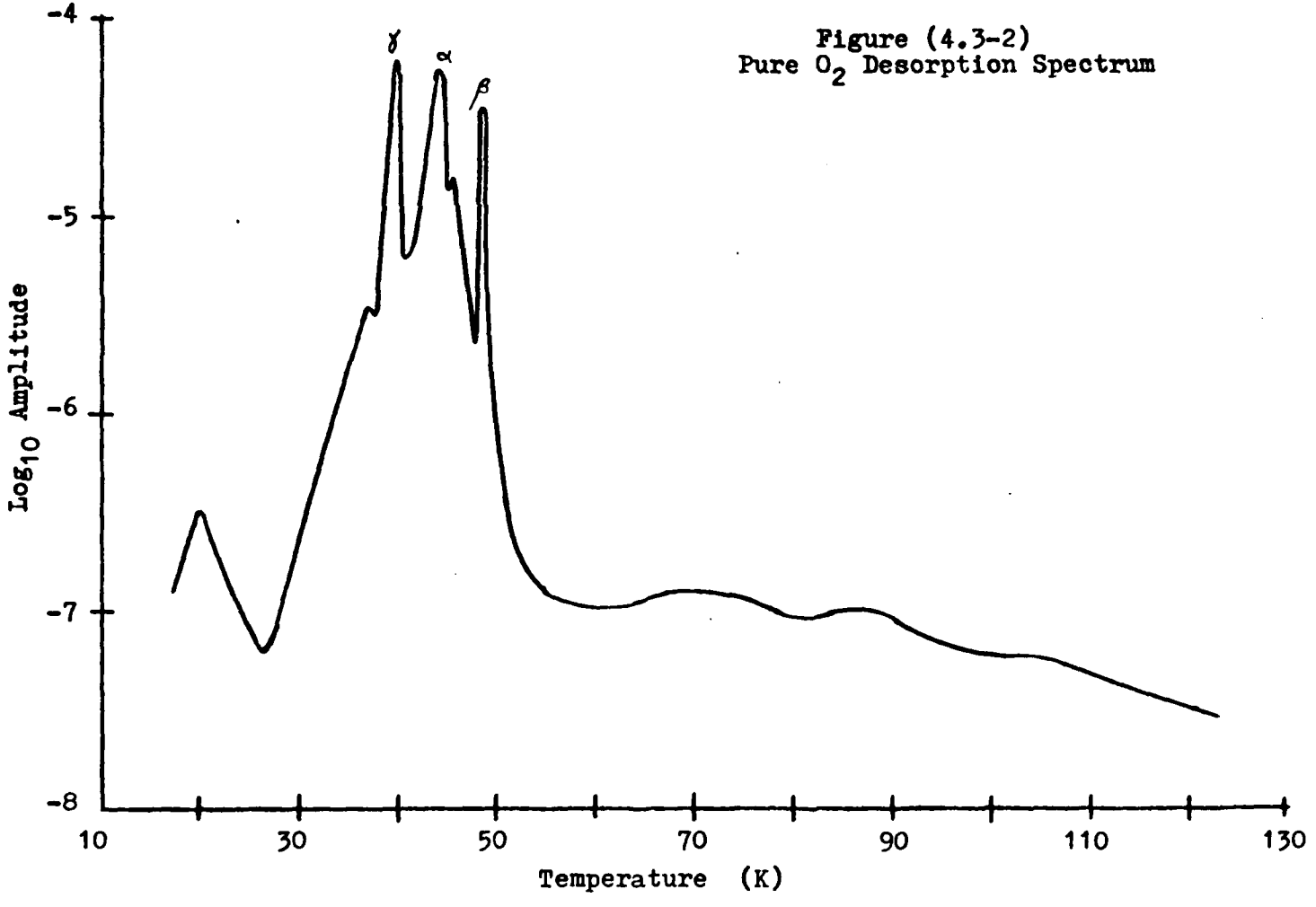

Figure (4.3-2)
Pure O_2 Desorption Spectrum

Figure (4.3-3)
Pure Freon 12 Desorption Spectrum

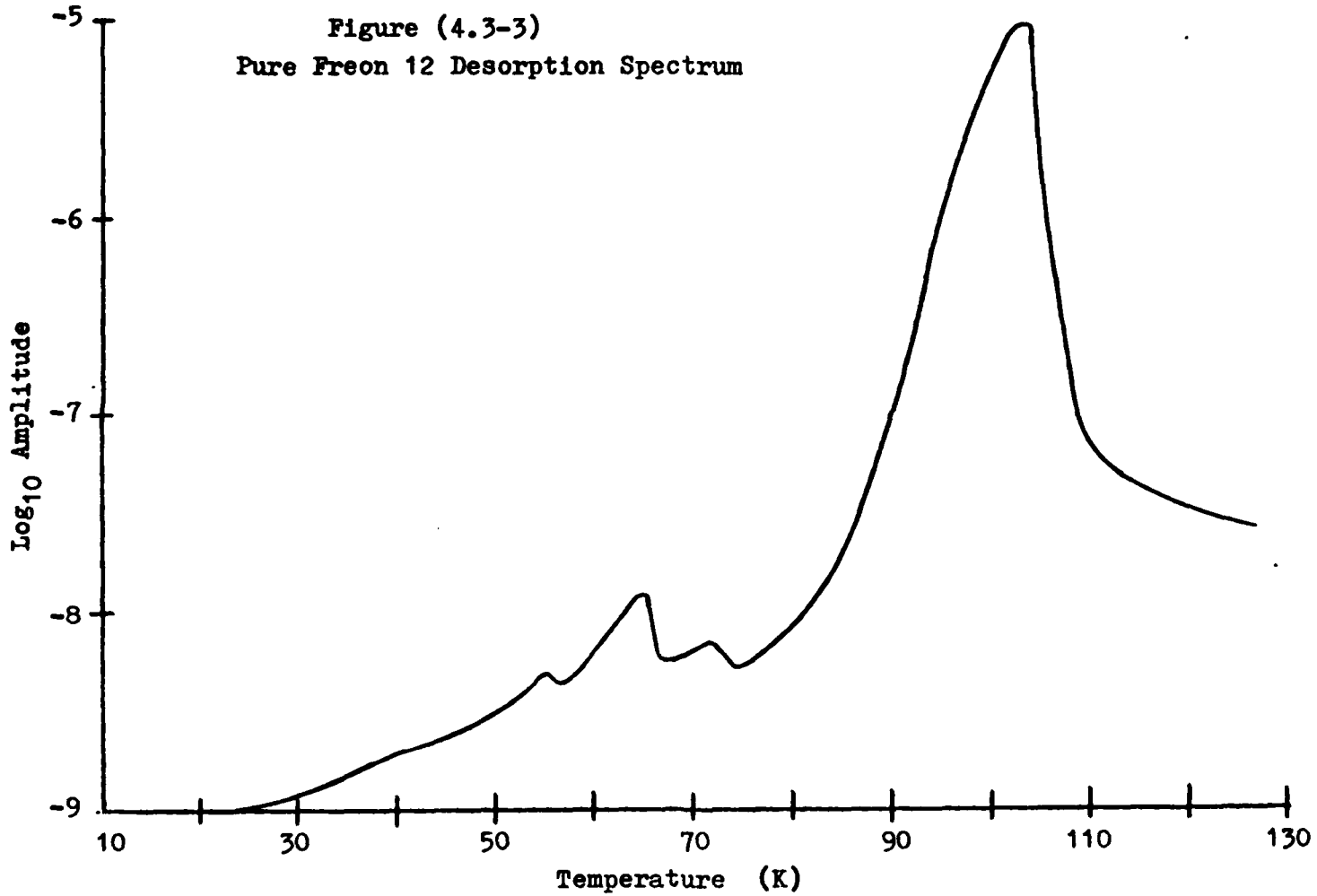

Figure (4.3-4)
Pure Freon 11 Desorption Spectrum

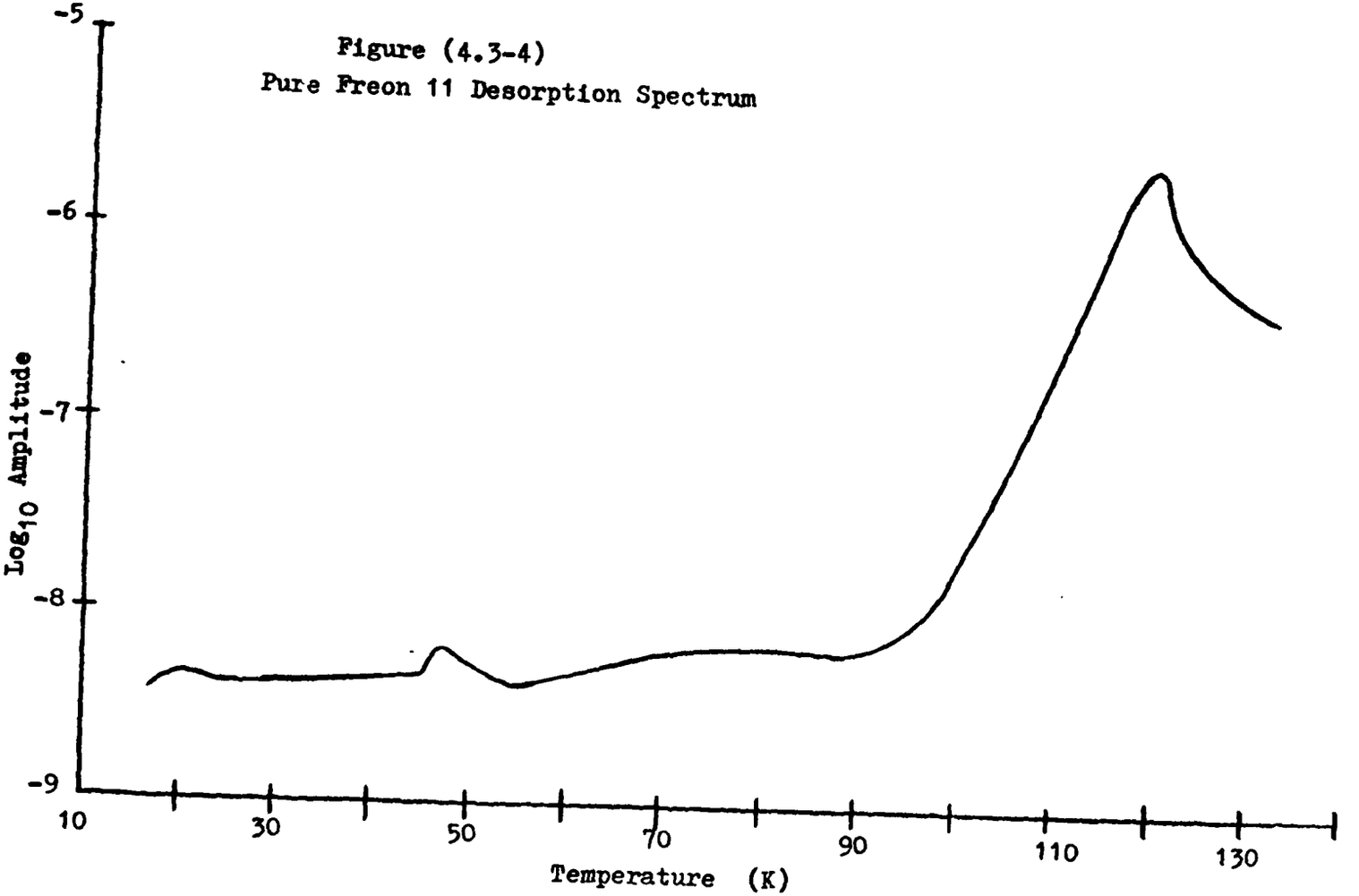

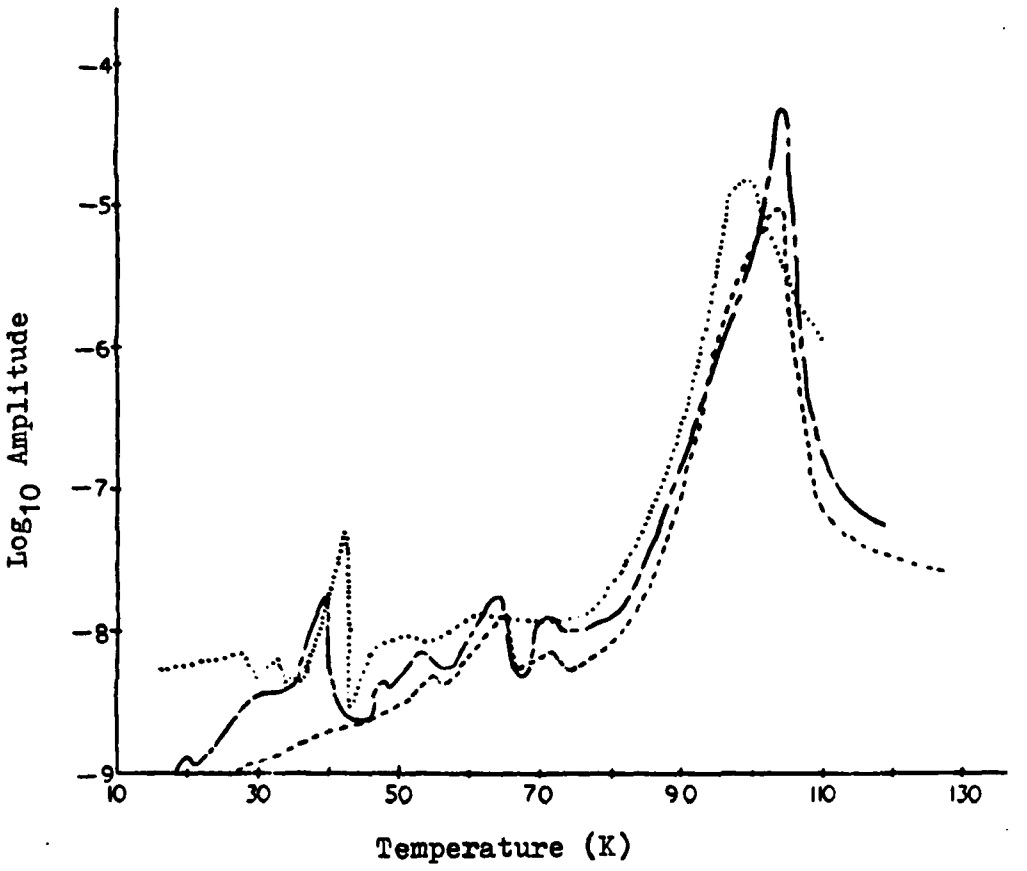

Figure (4.3-5)
Freon 12 Desorption Spectra Of Freon 12/N_2 Cryofrosts
----- (run 30) 100% Freon 12
— - — (run 41) 40% Freon 12
..... (run 74) 4% Freon 12

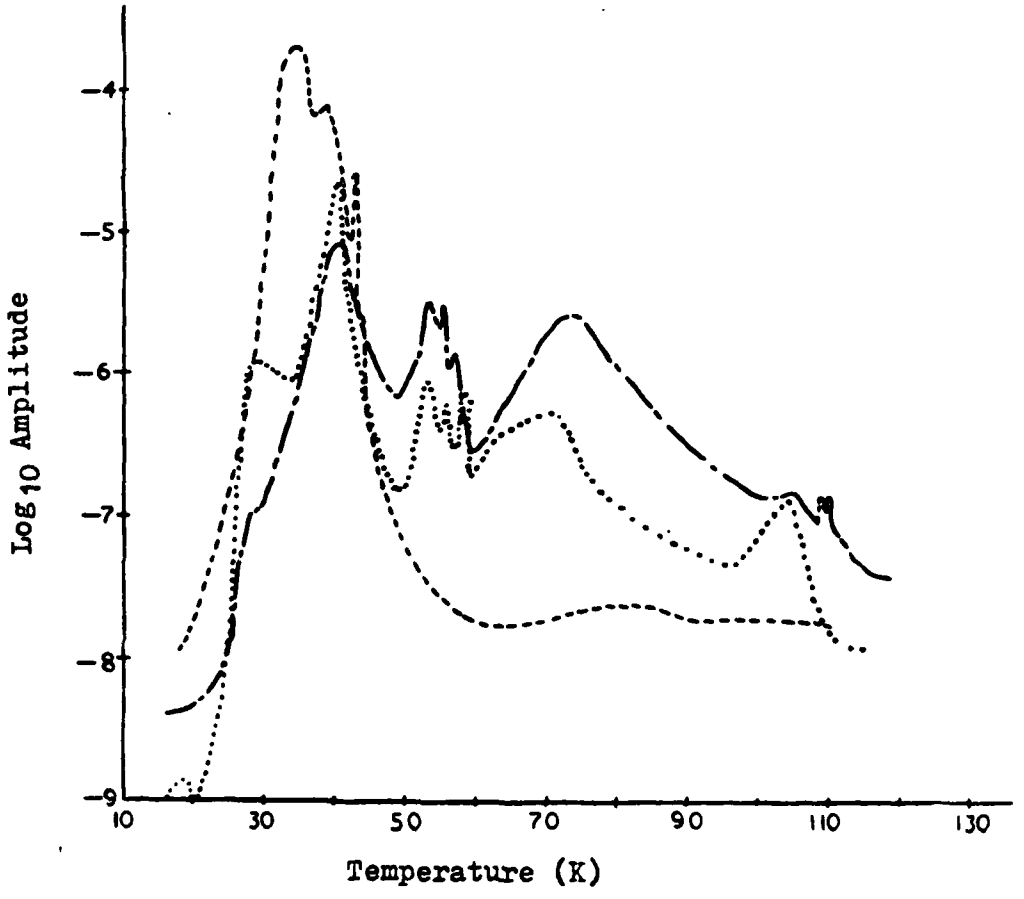

Figure (4.3-6)

N_2 Desorption Spectra Of N_2/Freon 12 Cryofrosts

----- (run 66) 100% N_2

..... (run 42) 60% N_2

—·— (run 44) 14% N_2

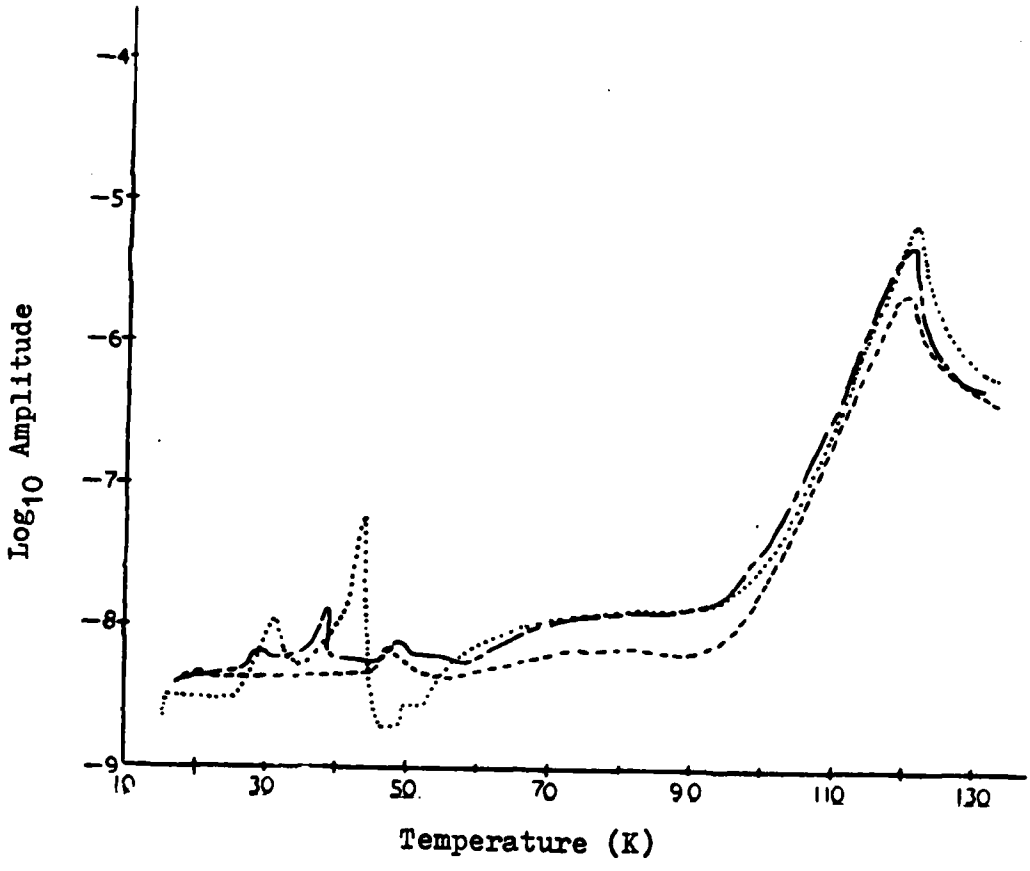

Figure (4.3-7)

Freon 11 Desorption Spectra Of Freon 11/N_2 Cryofrosts

----- (run 60) 100% Freon 11

— — (run 54) 50% Freon 11

••••• (run 53) 10% Freon 11

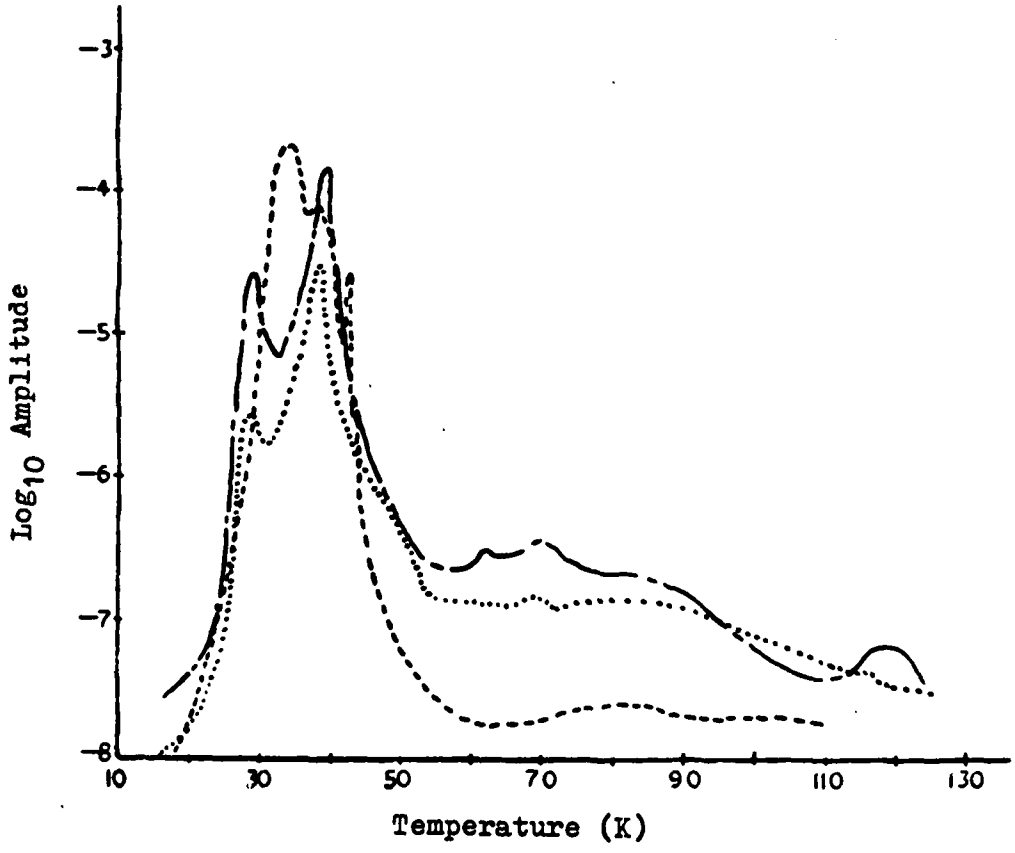

Figure (4.3-8)

N_2 Desorption Spectra Of N_2/Freon 11 Cryofrosts

----- (run 66) 100% N_2

—-— (run 55) 50% N_2

..... (run 59) 20% N_2

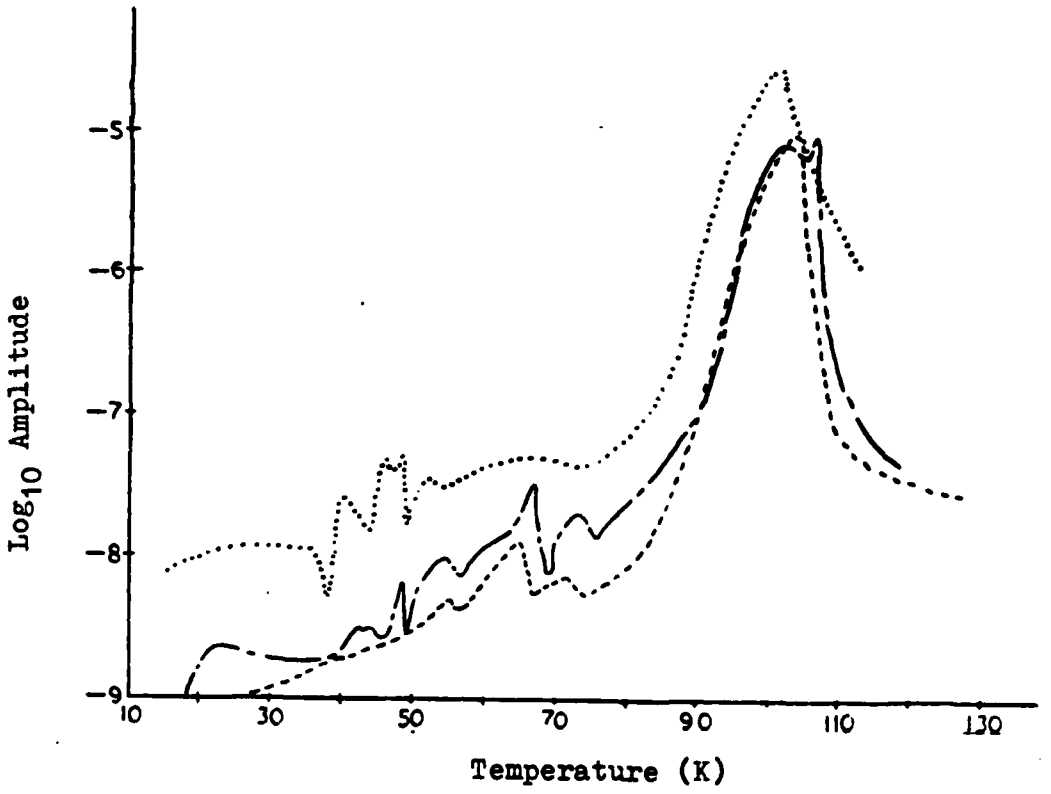

Figure (4.3-9)

Freon 12 Desorption Spectra Of Freon 12/O_2 Cryofrosts

----- (run 30) 100% Freon 12

—-— (run 29) 50% Freon 12

..... (run 75) 4% Freon 12

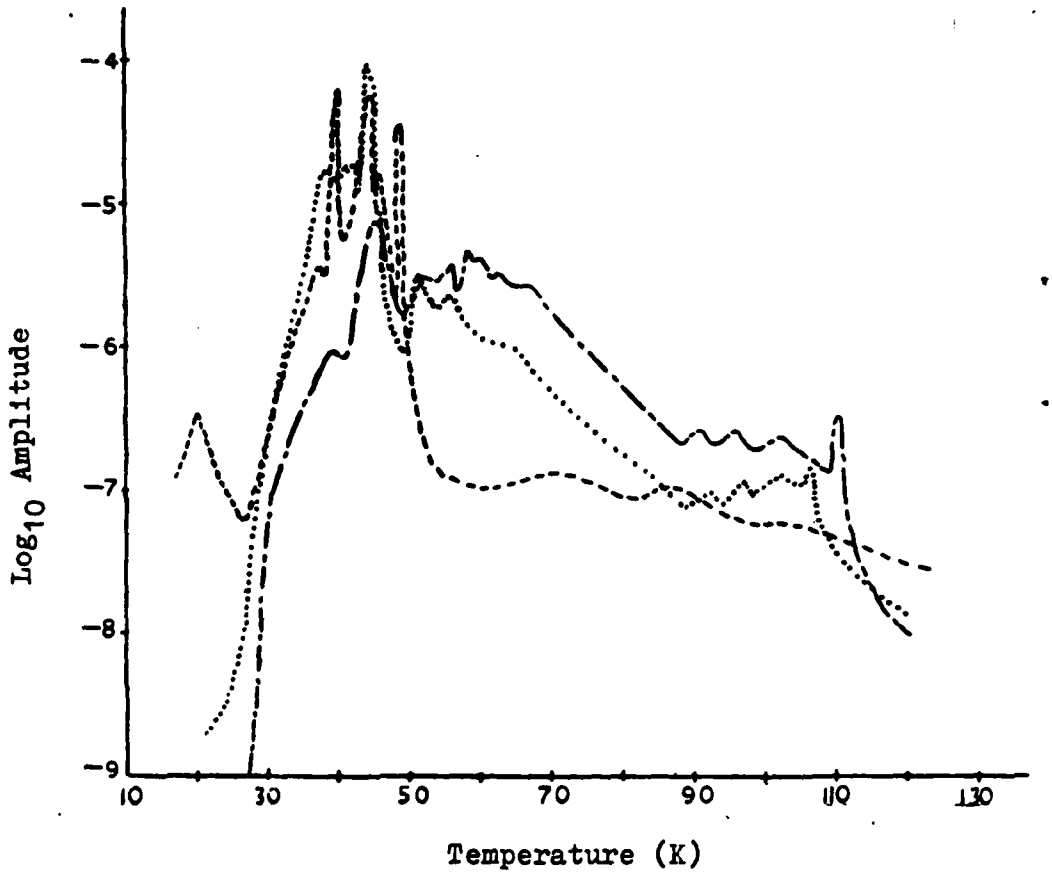

Figure (4.3-10)

O_2 Desorption Spectra Of O_2/Freon 12 Cryofrosts

----- (run 18) 100% O_2

..... (run 26) 50% O_2

—·— (run 31) 10% O_2

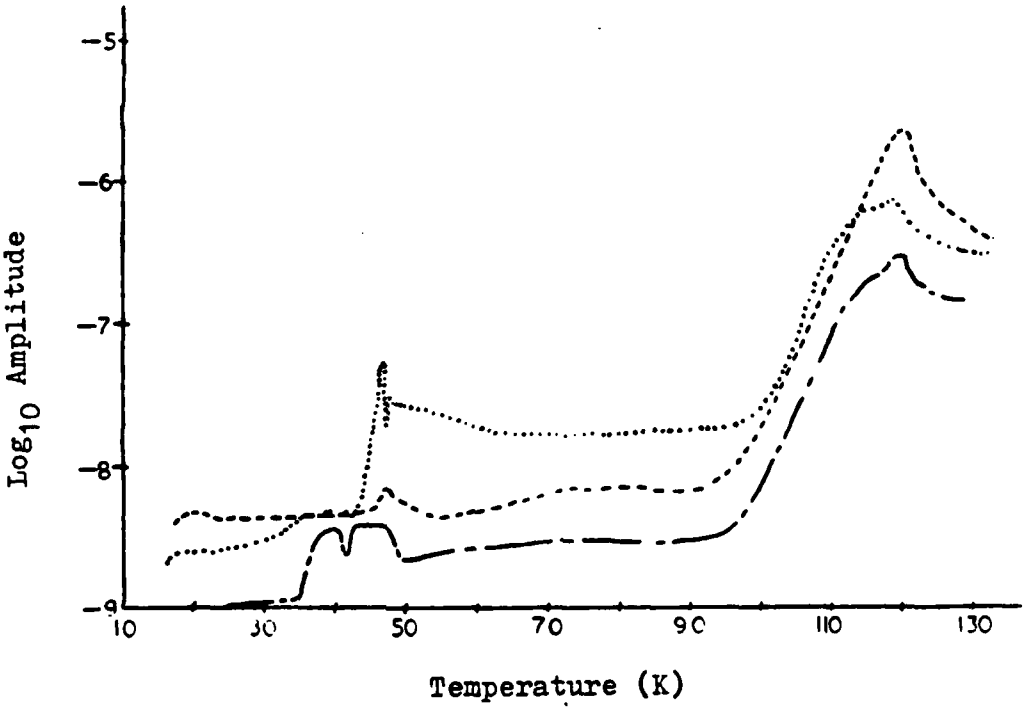

Figure (4.3-11)

Freon 11 Desorption Spectra of Freon 11/O_2 Cryofrosts

----- (run 60) 100% Freon 11

——— (run 63) 50% Freon 11

..... (run 61) 10% Freon 11

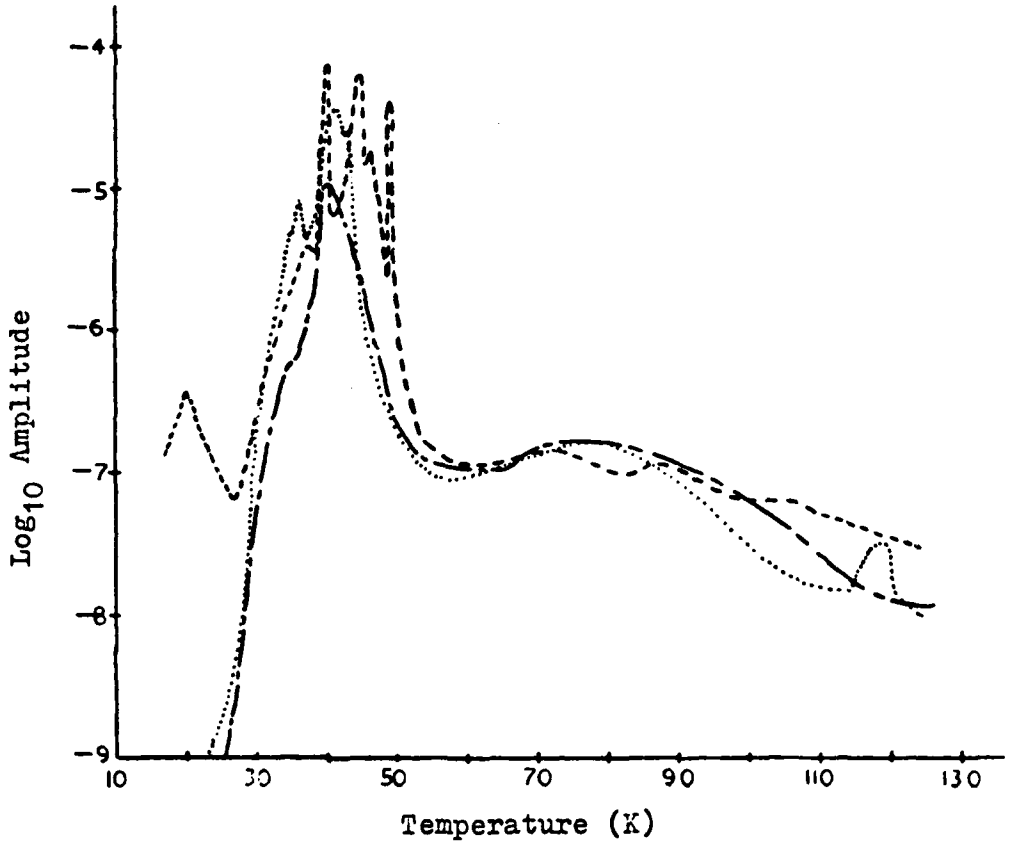

Figure (4.3-12)

O_2 Desorption Spectra Of O_2/Freon 11 Cryofrosts

----- (run 18) 100% O_2
..... (run 64) 50% O_2
—·— (run 67) 20% O_2

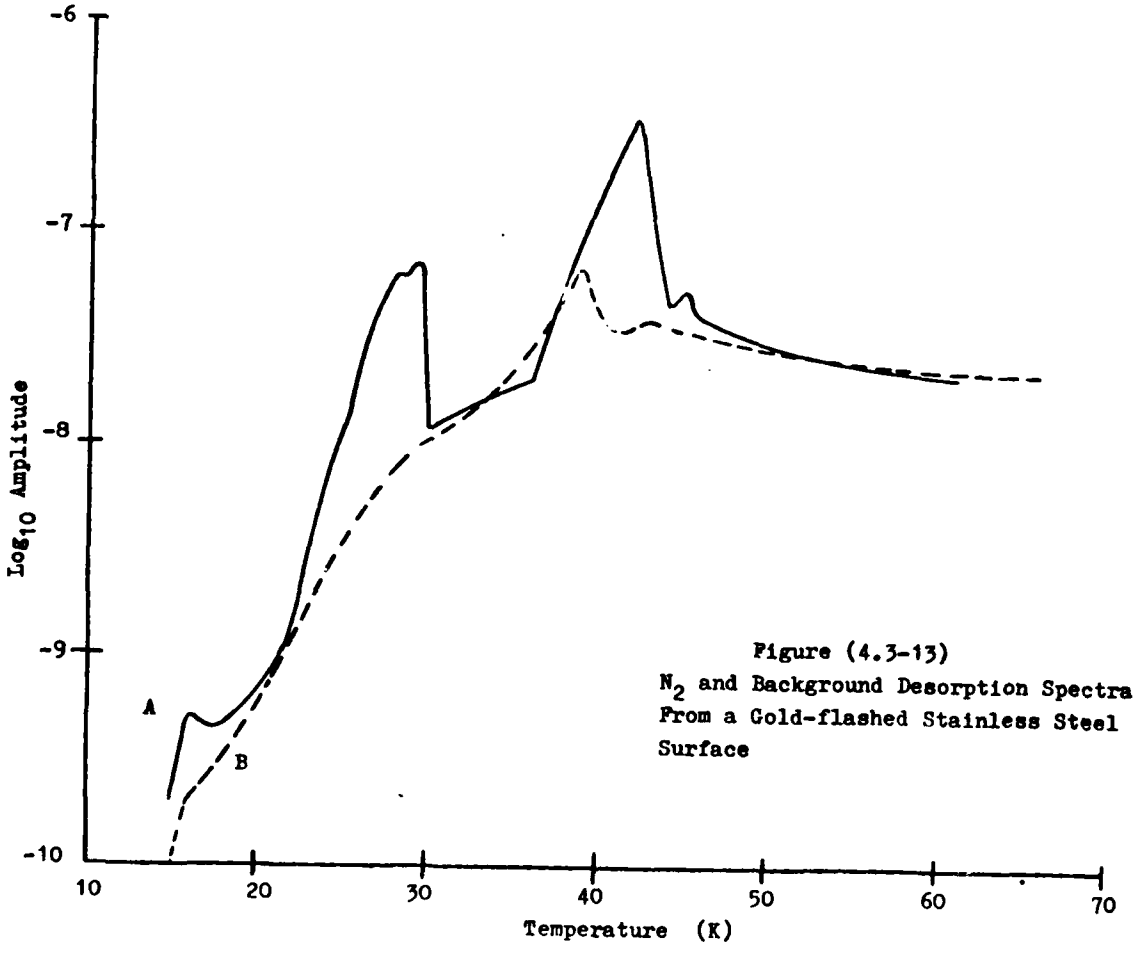

Figure (4.3-13)
N_2 and Background Desorption Spectra From a Gold-flashed Stainless Steel Surface

AD-A108 255 RESEARCH INST FOR GEODETIC SCIENCES FORT BELVOIR VA F/G 20/12
GAS-SURFACE INTERACTIONS IN CRYOGENIC WHOLE AIR SAMPLING.(U)
MAY 81 J M CALO, R J FEZZA, E J DINEEN F19628-77-C-0071
UNCLASSIFIED AFGL-TR-81-0162 NL

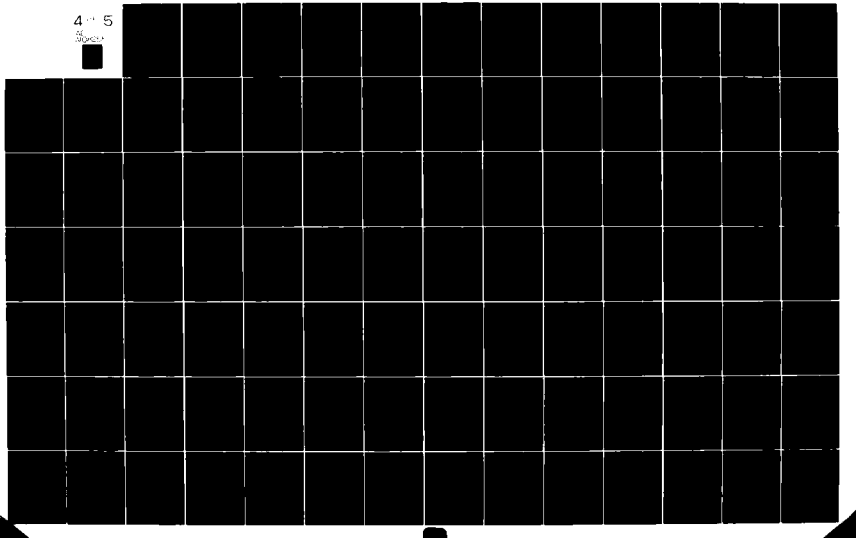

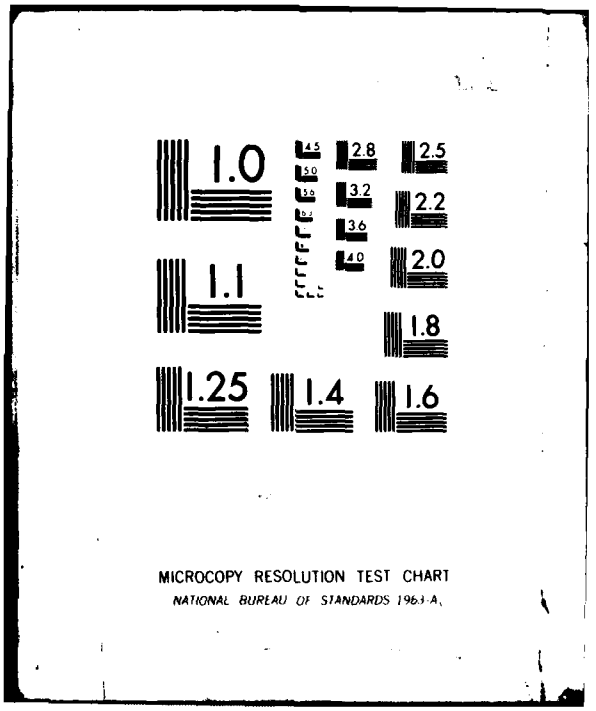
1.0
1.1
1.25
1.4
1.6
1.8
2.0
2.2
2.5
2.8
3.2
3.6
4.0
4.5
5.0
5.6
MICROCOPY RESOLUTION TEST CHART
NATIONAL BUREAU OF STANDARDS 1963-A

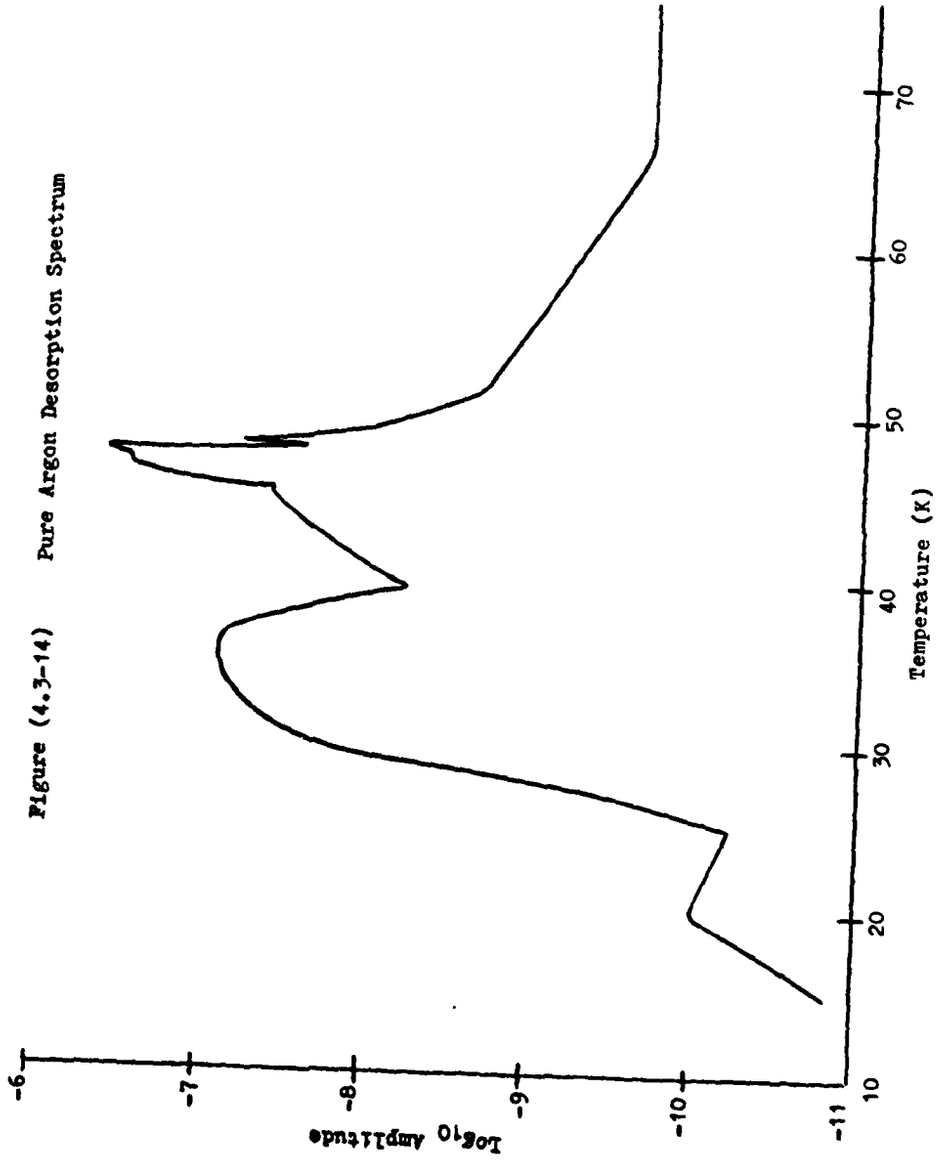

Figure (4.3-14) Pure Argon Desorption Spectrum

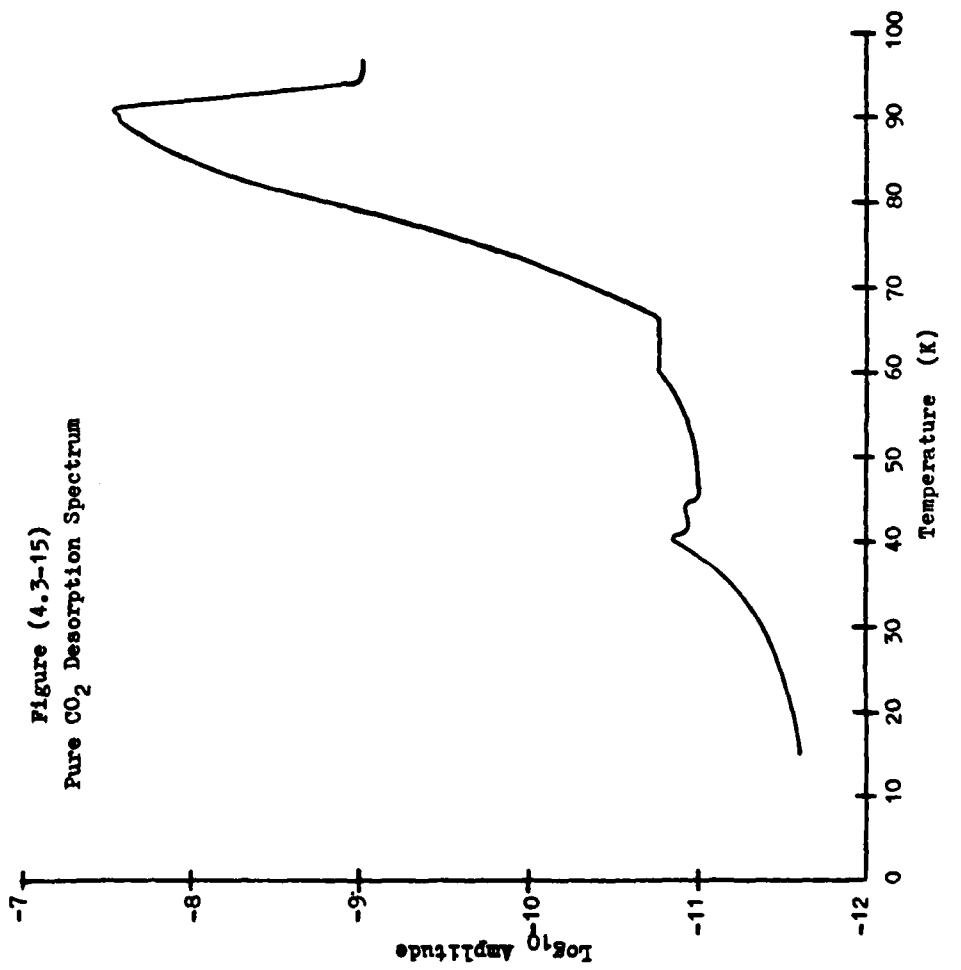

Figure (4.3-15)
Pure CO_2 Desorption Spectrum

Figure (4.3-16)
CO_2 Desorption Spectrum of
a 2% Deposit of CO_2 in N_2

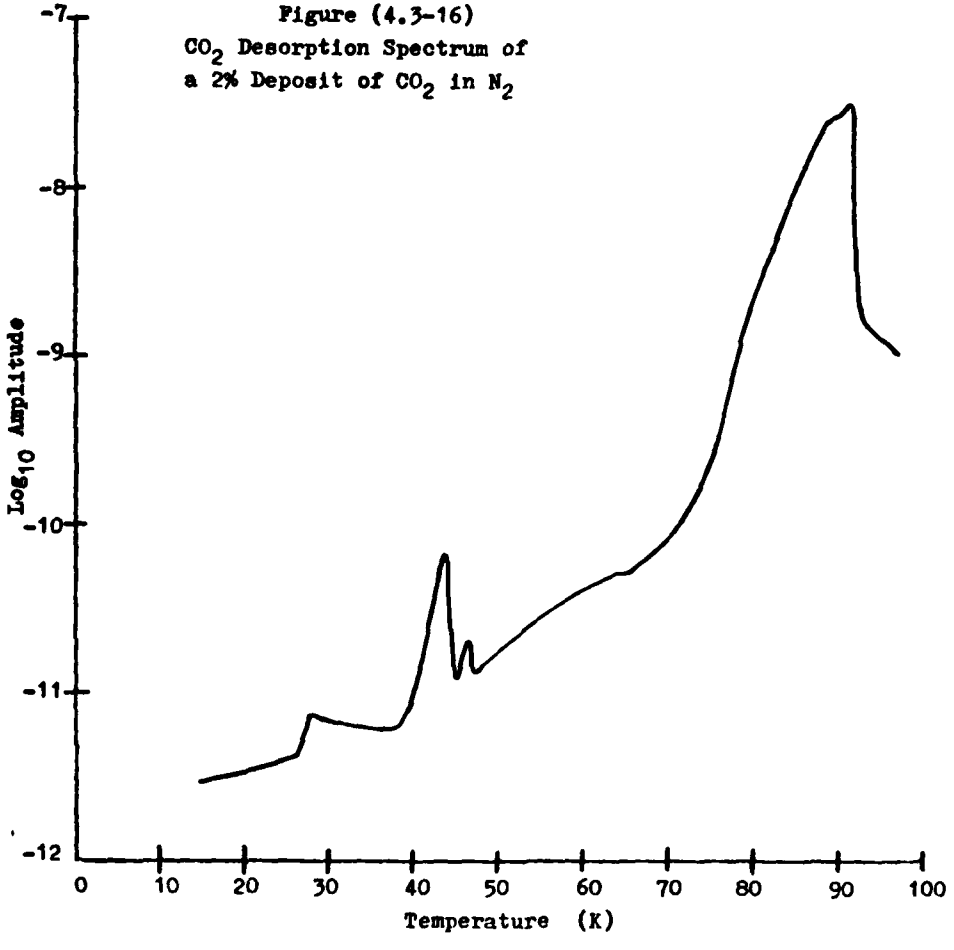

Figure (4.3-17) Argon Desorption Spectrum of a 46% Deposit of Argon in N_2

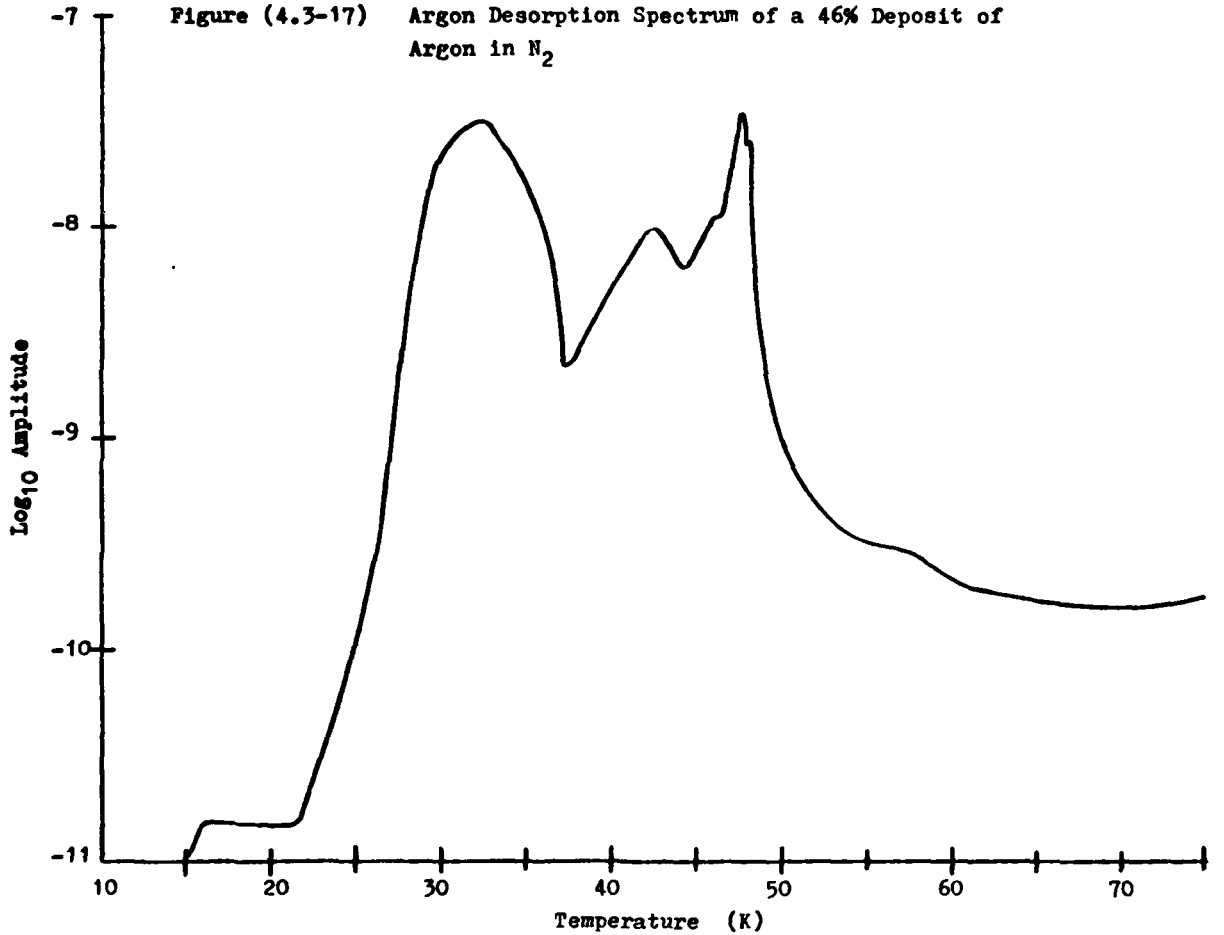

4.4 SUMMARY AND CONCLUSIONS

In summary, the salient points made in this chapter are:

A) Each pure species studied yields a reproducible, characteristic desorption spectra which is dependent on the cryosurface material employed.

B) As the concentration of Freon is decreased in either N_2 or O_2 cryofrosts, an increasing amount of Freon is carried over; i.e., Freon co-desorbs with the desorption of the other species.

C) Reduction of N_2 or O_2 concentration in a Freon matrix increases N_2 or O_2 "hold-over"; i.e., N_2 or O_2 is retained in the solid to desorption temperatures higher than possible for the pure species. Desorption of this held-over material, however, occurs at temperatures below those associated with the main pure Freon desorption peak, thereby proving that desorption of the heldover species is not merely due to physical entrainment in desorbing Freon, but is a function of the strength of the interaction between the species, the cryosurface and the Freon deposit.

D) As the concentration of N_2 or O_2 is decreased in a Freon matrix, the desorption spectra of N_2 or O_2 changes dramatically, usually from multiple peaks to single peaks at higher temperatures, except in the case of Freon 11-O_2, which exhibits a shift to a lower average desorption temperature.

E) The Freon 11-O_2 system exhibits an abnormally high degree of interaction, which is not predicted by the simple interaction estimates.

F) Dipole-induced dipole forces are not the primary forces responsible for these effects, as evidenced by the nonpolar CO_2-N_2 and Ar-N_2 mixture results on the gold-flashed surfaces.

G) The literature supports the theory that heteromolecular complexes can form in such matrices, which may be the basis for the effects observed here.

The implications of these results on the cryogenic fractionation techniques employed in the cryogenic whole air sampling program are obvious and should be taken into account in any cryofrost manipulations- both those currently in practice and/or contemplated.

REFERENCES

Dineen, E.J., Cryofrost Deposition and Desorption As Related to Cryogenic Whole Air Sampling In The Stratosphere, Masters Thesis, Princeton University, NJ, 1977

Ehrlick, G., J.Chem. Phys. 34, 29, 1961

Gallagher, C.C., Pieri, R.V., AFGL-TR-76-0161, Air Force Geophysics Lab, Hanscom AFB, Mass, 1976

Gallagher, C.C., Pieri, R.V., Goldan, P.D., J. Atmos. Sci. 34, 1481-2, 1977

Guillory, W.A., Hunter, C.E., J. Chem. Phys. 50, 3576, 1969

Hallam, H.E., ed., Vibrational Spectroscopy of Trapped Species, Wiley, N.Y., 1973

Hickmott, T.W., Ehrlick, G., J. Phys. Chem. Solids 5, 47, 1958

Hirshfelder, J.O., Curtiss, C.F., Bird, R.B., Molecular Theory of Gases and Liquids, Wiley, N.Y., 1964

Honig, R.E., Hook, H.O., R.C.A. Reviews 21, 360, 1960

King, D.A., Surface Science 47, 384-402, 1975

Pimentel, G.C., Bulanin, M.O., Van Thiel, M., J. Chem. Phys. 36, 500, 1962

Redhead, P.A., J. Chem. Phys. 33, 641, 1960

Redhead, P.A., Vacuum 12, 203-11, 1962

Scott, R.B., Cryogenic Engineering, Van Nostrand, N.J., 1959, p271-9

5. CRYOFROST REACTIONS

5.1 INTRODUCTION

In an early research proposal examining the prospects of cryogenic sampling of the atmosphere, Snelson (1972) exploited the advantage of the naturally high dilution of reactive atmospheric species in an air sample matrix. He noted that a cryofrost of atmospheric species would have nitrogen and oxygen as the primary matrix material with trace species "locked" into the matrix structure at parts per million, and lower, concentrations. Thus these species would be matrix isolated, with N_2 and O_2 as nearest neighbors, and any possible reactions would be severely limited by the low temperature and extremely low diffusion rates. Snelson argued that many species could be studied directly in the solid phase by electron paramagnetic resonance (EPR) spectroscopy (e.g., O_3, CHO, CH_2, CH_3, and other radicals), or after gamma or ultraviolet irradiation (e.g., CO_2, CO, CH_4). Snelson realized, however, that many other species would require alternate analytical techniques, such as gas chromatography (GC) (e.g., O_2, H_2O, N_2O, SO_2), which would entail thermal desorption and possibly fractional distillation of the sample.

The inherent advantages of matrix isolation would be lost with such analytical techniques, and the chemical composition of the sample could be altered. Due to the extremely low concentrations of free radical species in the frost, however, Snelson (1972) argued that reactions would not appreciably alter the other constituents.

In the cryogenic whole air sampling project of the Stratospheric Environment Program of the Air Force Geophysics

Laboratory, as reported by Gallagher and Pieri (1976) and Gallagher, Pieri, and Goldan (1977), the analytical procedure includes:

1) cryogenic fractional distillation to remove the large amounts of N_2 and O_2, and to concentrate trace constituents.
2) NO_x chemiluminescence analysis for the oxides of nitrogen.
3) gas chromatography.
4) mass spectrometry.

All these techniques require regeneration of the cryofrost, and thus loss of matrix isolation. Here we examine the effects of these manipulations on possibly reactive species other than free radicals; in particular, the oxides of nitrogen (NO_x) and ozone, which, as shown in Appendix A, are of primary stratospheric importance.

Many references in the extant literature support the possibility of reactions between what Snelson (1972) considered to be "stable" molecular species. Smith and Guillory (1977) reported the thermal oxidation of dimerized NO by O_2 in the solid phase in the 13K to 29K temperature range. Lucas and Pimentel (1979) cite the thermal oxidation of NO with O_3 while matrix isolated within N_2 in typical $NO/O_3/N_2$ ratios of 1/30/250, between 11K and 20K in the solid phase. Explosion hazards involved with the handling of concentrated, condensed ozone are also well known. For example, Arin and Warneck (1972) noted the rapid reaction of O_3 with CO at low pressure and room temperature, Deitz and Bitner (1973) encountered an explosive reaction while adsorbing O_3 onto charcoal, and Jenkins (1959) reported a spontaneous explosion of liquid O_3 at 90K in which a

catalytic impurity was suspected. Thus, thermal regeneration of cryofrosts involving these species could exhibit similar effects which would serve to alter or mask relative ambient stratospheric concentrations.

The experimental results of this chapter are related to those of the previous chapter insofar as the ability of matrix constituents to phase separate during the desorption process; i.e., the loss of volatile components from the matrix with concomitant concentration of the lower vapor pressure constituents. Relatively high concentrations of possibly reactive species are used, which is justified in terms of manipulation and concentration techniques typically employed in cryogenic whole air sample analysis. This allows more accurate experimental analytical techniques, and results can later be extrapolated to more relevant lower concentrations. The techniques developed during the condensation studies were employed to deposit samples, and the analytical techniques used to determine conversion were mass spectrometry and NO_x chemiluminescence.

In a more specific sense, the current work is novel in that much has been published about matrix isolation at low temperatures, while relatively little has been done concerning the processes which occur upon heating the matrix during desorption, such as catalytic, morphological, and contaminant effects.

5.2 EXPERIMENTAL DESIGN

The gold-flashed stainless steel cryosurface was selected for the current experiments (see Chapter 2) because such surfaces have actually been used in cryogenic whole air sampling flights (Gallagher et al., 1977, Gallagher and Pieri, 1976). Gold is known to be relatively inert catalytically, probably as a result of its filled d-band (Puddephatt, 1978), rendering it incapable of efficiently chemisorbing small molecules (e.g., H_2). Yet some reactions are catalyzed by gold; e.g., partial oxidation of methyl alcohol to formaldehyde (Puddephatt, 1978), and hydrogen-deuterium exchange in some silicon-containing molecules at low temperatures (195-245K) (Bradshaw et al., 1975). The gaseous species employed in the current studies include N_2, NO, N_2O, CO, CO_2, $CFCl_3$ (F11), CF_2Cl_2 (F12), O_2, and O_3.

It has been observed experimentally that NO_2 and O_3 do not exhibit mass spectrometer parent peaks at m/e of 46 and 48, respectively. Their cracking pattern includes fragment peaks located at m/e ratios of other species of interest; e.g., NO_2 exhibits peaks at 30, as for NO; 16 and 14 as for NO; while O_3 has peaks at 16 and 32, as does O_2. Therefore, it is not possible to use the mass spectrometer to distinguish NO_2 from NO, and O_3 from O_2. All attempts at altering the fragmentation patterns of NO_2 and O_3 to obtain a parent peak were unsuccessful. Therefore, NO_x chemiluminescence was employed.

The chemiluminescence analyzer allows independent analysis for NO and NO_2. The analyzer relies on the reaction between ozone and nitric oxide:

$$NO + O_3 \xrightarrow{(\alpha)} NO_2 + O_2 \qquad (5.2\text{-}1)$$

which produces a certain fraction of electronically excited NO_2, $(1-\alpha)$,

$$NO + O_3 \xrightarrow{(1-\alpha)} NO_2^* + O_2 \qquad (5.2\text{-}2)$$

that spontaneously deactivates to the ground state giving off a photon in the 600-2500 nm wavelength range:

$$NO_2^* \longrightarrow NO_2 + h\nu \qquad (5.2\text{-}3)$$

Detection of these photons is used to determine the concentration of NO in the sample gas.

In order to measure the concentration of NO_2 in the sample, the gas is first passed through a stainless steel reactor coil maintained at 650°C which quantitatively thermally reduces NO_2 to NO. As noted in the apparatus description, the chemiluminescence analyzer was modified with lines and valves bypassing the internal ozone generator, thereby also allowing ozone determination by titration with 5% NO in nitrogen.

In modifying the chemiluminescence analyzer for ozone titration; several flow rates and concentrations were changed. Thus, in order to insure accuracy, the analyzer was calibrated against a standard ozone analytical technique as follows. To insure reproducibility of ozone concentrations, the Welsbach ozone generator was always set at an oxygen feed rate of 2 SLPM (standard liters per minute) at 8 psig, and only the primary voltage of the ozonator was changed to vary the ozone concentration. A schematic of the calibration apparatus is presented in Figure (5.2-1). The materials employed were limited to glass, stainless steel, teflon, and tygon, as recommended by

Welsbach (1977). As shown in Figure (5.2-1), the bulk of the ozonated oxygen was fed to a scrubber filled with a potassium iodide solution, which chemically destroys ozone. Upstream of the scrubber, two bleed lines allowed the ozonated oxygen to be fed either directly to the chemiluminescence analyzer, or to the ozone titration apparatus.

The bleed stream to the chemiluminescence analyzer passes through the gas sampling and feed apparatus for the main vacuum chamber (i.e., the leak valve, stainless steel manifold, stainless steel valves, etc.) employed in the actual experiments. Thus any ozone loss due to adsorption and recombination in the equipment feed system, however slight, is essentially nulled in the calibration process. The flow rate into the chemiluminescence analyzer was maintained constant and reproducible by setting the pressure just before the 9 inch length of 0.02 inch I.D. capillary tubing (Figure (5.1-1)) to 19.9 in. Hg, with the sampling system leak valve. Gas flows directly from the capillary to the reactor within the chemiluminescent analyzer, where a second feed containing 5% NO in N_2 (Matheson, unanalyzed) is introduced, and the resultant luminescence is detected by a photomultiplier tube, the signal from which is amplified and read out on a panel meter. Since concentrations and flowrates of the two streams were altered, the analyzer panel meter did not read the concentration of O_3 directly, thereby necessitating recalibration.

The second bleed stream shown in Figure (5.2-1) leads to a wet calibration apparatus, as recommended by Welsbach (1977). The gas flow, regulated by a stainless steel valve, is fed through

a gas bubbler (medium porosity) containing 400 ml of 2% potassium iodide solution at approximately 0.3 ℓ/min. In the bubbler, the reaction:

$$O_3 + 2I^- + H_2O \longrightarrow O_2 + I_2 + 2OH^- \qquad (5.2\text{-}4)$$

takes place. The gas, now stripped of ozone, passes through a pressure gauge and then through a wet test meter, where its volume is recorded as a function of time. The iodine solution produced in the bubbler is then removed and acidified with 10 ml of 1M sulfuric acid and titrated with either 0.1 or 0.01 N sodium thiosulfate solution, depending on the suspected concentration of the iodine solution. Starch solution is used as an indicator, and is added when the bright yellow color of the solution begins to fade.

The information derived from this wet titration, along with the sample gas volumetric flow data (corrected for saturation with water vapor), allows the determination of ozone concentrations in the sample gas stream. Welsbach (1977) contends that this wet titration technique is accurate to $\pm$ 1% of the amount of O_3 in the sample stream in concentrations down to approximately 28 ppm.

Using the wet titration apparatus, the ozone concentration in the product stream was also calibrated against the primary voltage of the Welsbach ozonator (described in Chapter 2). It was found that an ozone concentration of 2.24% $\pm$ 0.1% could be delivered reproducibly. Since high concentrations of ozone in the feed gas were desired, this particular concentration was employed in the experimentation described below.

The actual calibration curve of wet titration results versus chemiluminescent analyzer readings is given in Figure (5.2-2). The entire calibration range is fit reasonably well by a third order polynomial with least squares coefficients:

$$C = 3.887 \times 10^{-2} + 0.130I - 2.322 \times 10^{-6}I^2 + 1.2208 \times 10^{-9}I^3, \quad (5.2\text{-}5)$$

where C is the titrated ozone concentration, in ppm, and I is the chemiluminescent analyzer meter reading, also in ppm. From this calibration (Figure 5.2-2) it can be seen that the chemiluminescence analyzer, when operated in this fashion, is approximately an order of magnitude more sensitive than when operated in its normal mode; i.e., the normal resolution of $\pm$ 0.1 ppm for the lowest range becomes $\pm$ 0.01 ppm for ozone. This increased sensitivity was useful in the experimental work.

In the following description of the experiments performed, reference is made to two types of experiments. The first is temperature programmed desorption (TPD). In TPD experiments, the cryosurface temperature is allowed to increase by conduction of heat along the refrigerator stem. This technique allows a slow, reproducible temperature increase with time, as described in the previous chapter on thermal desorption employing TPD. Mass spectrometry is used to monitor the species of interest. Care must be taken, however, since some parent peaks of the species of interest are also parent or fragment peaks of low level vacuum chamber contaminants; e.g., the N_2 parent peak at m/e 28 is also the parent peak of CO, a common vacuum chamber contaminant. In order to minimize these problems, background desorption spectra

are subtracted from the desorption spectrum of the species of interest. Care must be taken to insure that the absolute sample amount does not cause the vacuum system pressure to exceed desirable limits upon thermal desorption. The typical total deposit amount for a TPD experiment is approximately 10^{-5} g mol.

In order to employ the chemiluminescence analyzer to detect NO, NO_2, and O_3 desorbed in the experimental apparatus, a gas sample at or near atmospheric pressure must be available. In order to meet this requirement, a second type of experiment was devised, which is referred to as flash desorption (FD). For FD, a more massive cryofrost sample, typically 10^{-3} g mol, is deposited on the cryosurface. Then, instead of slow desorption and in situ analysis, as in TPD, the experimental vacuum chamber is sealed off from the pumping system and filled with N_2 to approximately 5 psig through the nozzle system. The final system pressure is measured with a Bourdon gauge, which, together with the chamber volume, allows a quantitative determination of desorbed gas concentrations. This technique has the advantage of an increased desorption rate as compared to TPD, and rapid dilution of components in the gas phase, which limits gas phase reactions, thereby restricting any potential reactive effects to those occurring in the solid state or during the transition to the gaseous state. Figure (5.2-3) illustrates typical temperature versus time curves for both TPD and FD type experiments. Note that the employing FD, the cryosurface reaches approximately 183K in 4 minutes, while with TPD the surface would still be at 44K.

In summary, variable amounts of reactive gases were deposited on a gold-flashed, stainless steel surface at 15K, and then desorbed in one of two ways. Employing TPD, reactant and product species were monitored in situ with the mass spectrometer. Its drawbacks are limits on total deposit quantity and an inability to accurately detect NO_2 and O_3. A second technique, flash desorption, employed the chemiluminescence analyzer modified and calibrated to detect NO_2, NO, and O_3. It allows a quicker desorption time and high dilution in the gas phase. Its limitations are that it is specific to these three species only, and that a minimum sample size must be deposited in order to insure that the final sample gas concentration is within the detectable limits of the chemiluminescence analyzer.

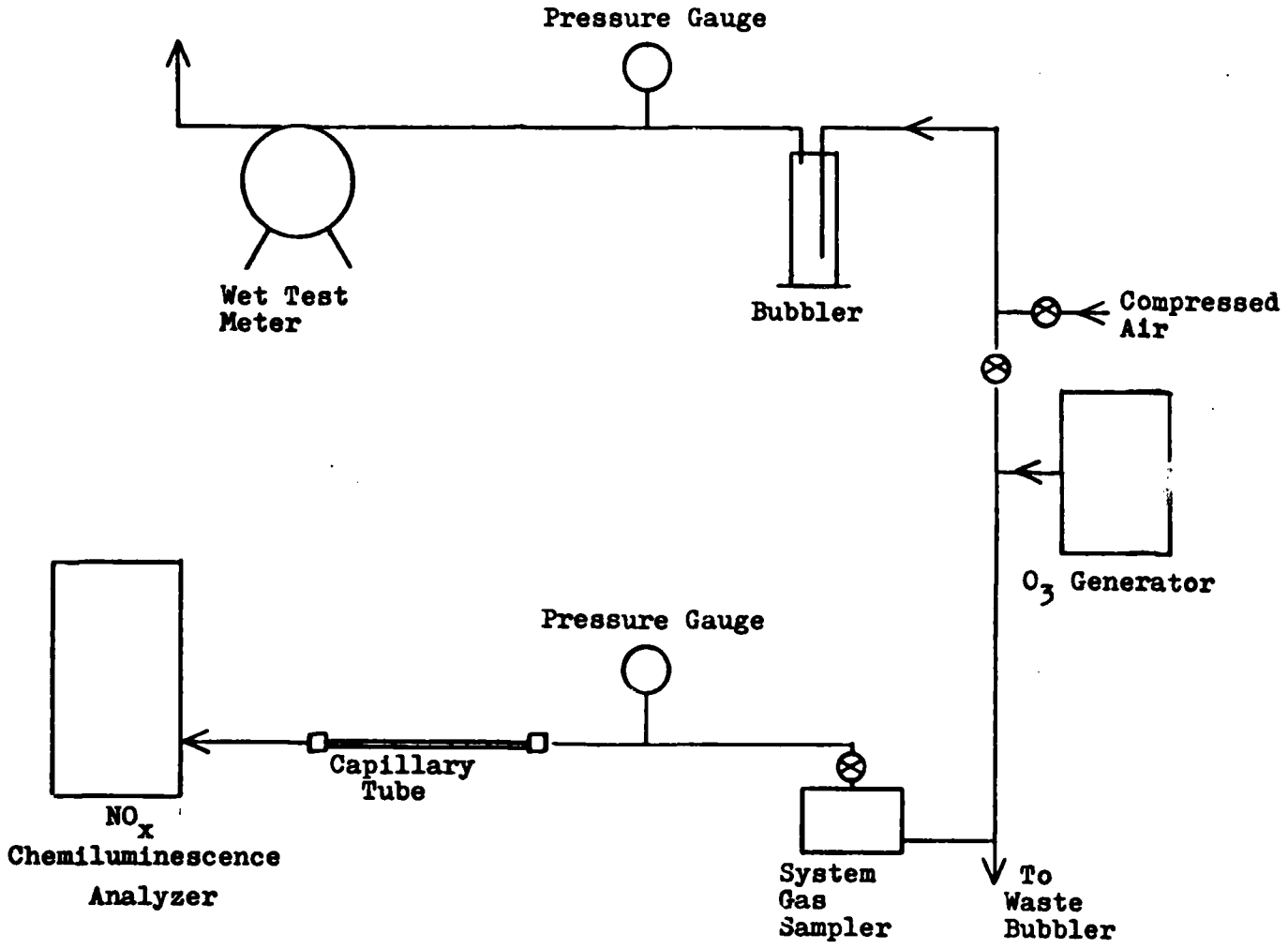

Figure (5.2-1) Ozone Calibration Apparatus

Figure (5.2-2) NO_x Chemiluminescence Analyzer
Calibration Curve for Ozone

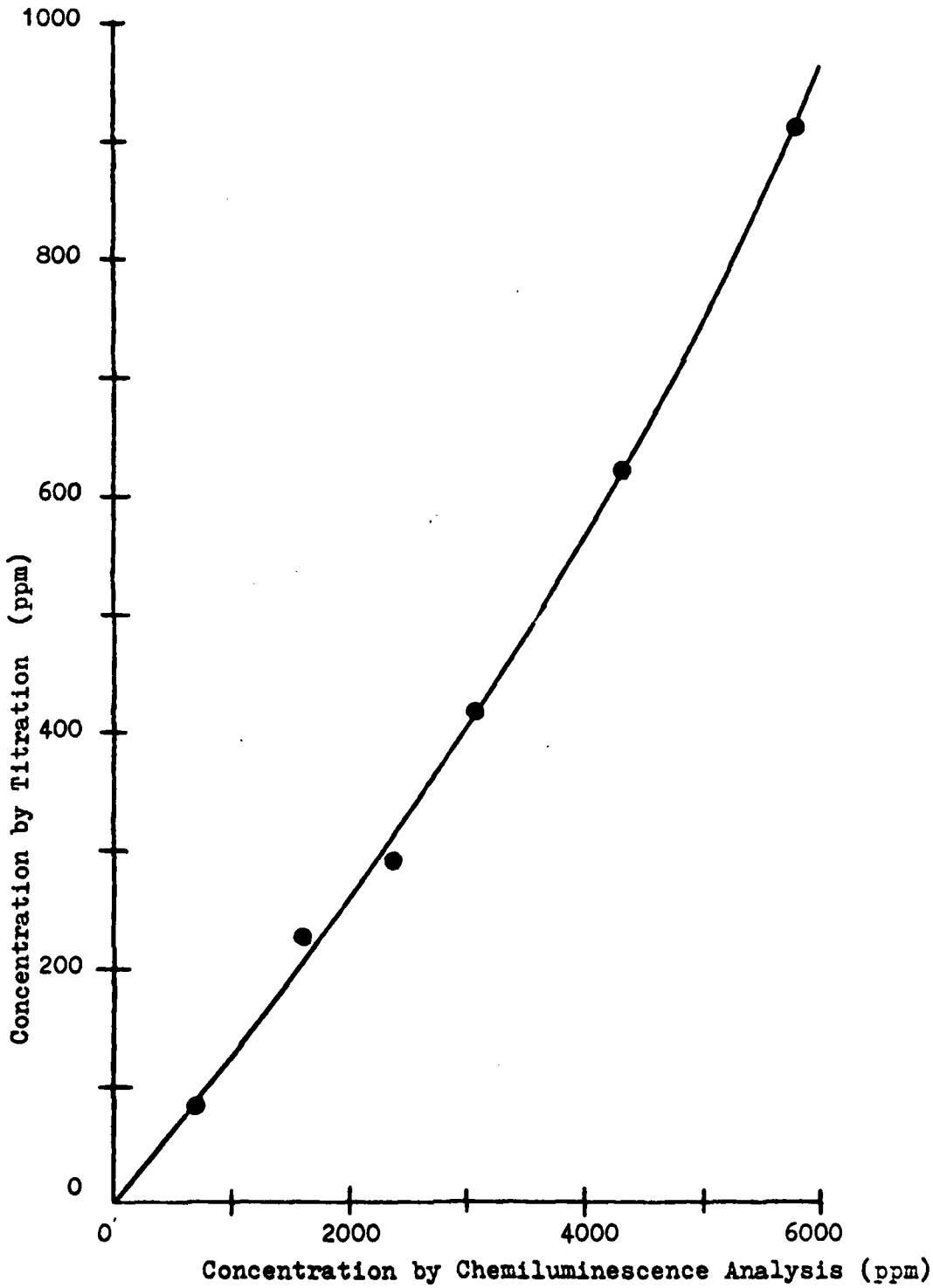

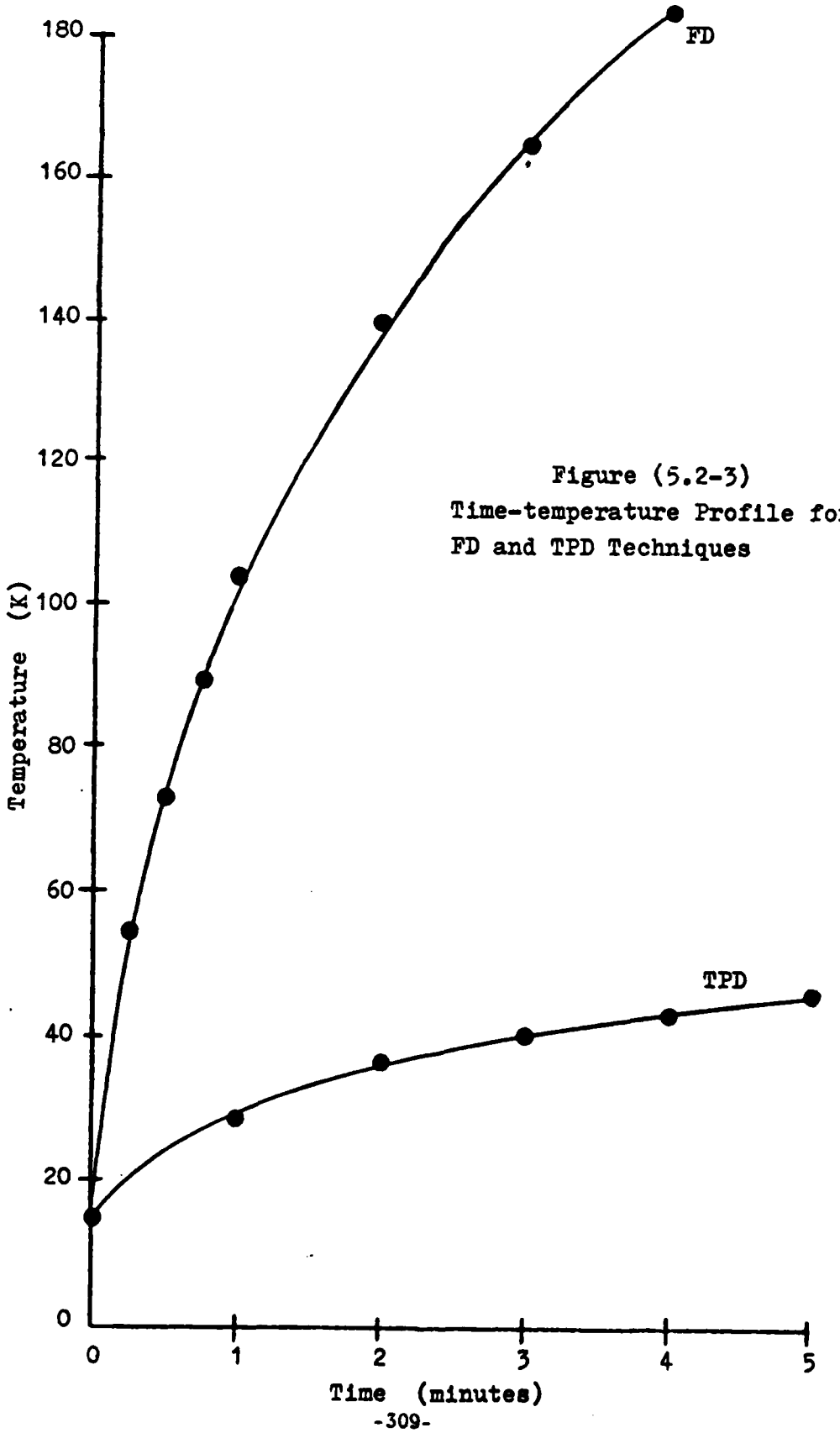

Figure (5.2-3)
Time-temperature Profile for
FD and TPD Techniques

5.3 RESULTS AND DISCUSSION

Desorption of Nitric Oxide - Disproportionation

In devising this experimental program the original intent was to first check the flash desorption procedure (FD) quantitatively with species of interest, e.g., NO and O_3 in O_2. That is, cryogenic deposition, regeneration, detection, and quantitative analysis, followed by the same sequence in the presence of ozone in order to determine whether or not any oxidation reactions occur. The species of interest were primarily NO, and then N_2O, N_2, Freon 11, and Freon 12.

The first experiment performed in this series, run 240, yielded unexpected results. In this run, pure NO was deposited on the cryosurface at a rate of 3.5×10^{-7} g mol/s for 5 minutes, creating a total deposit of 1.1×10^{-4} g mol of NO. After approximately 3 minutes, the NO cryodeposit was flash desorbed with pure N_2, and the composition of the resultant gas mixture was calculated to be 215 ppm NO. The actual results of the chemiluminescence analysis were quite different, however, yielding 72 ppm NO, 133 ppm NO_x, and therefore, by difference, 61 ppm NO_2. Defining the NO/NO_x ratio as the fraction NO remaining in the product gas, $NO/NO_x = 0.54$. Thus, apparently a substantial amount of the NO deposited was converted to NO_2 in the absence of an oxidizing agent in some as yet undetermined mechanism.

Assuming the simple stoichiometry,

$$4NO \longrightarrow 2NO_2 + N_2, \qquad (5.3\text{-}1)$$

for reasons which will become clear later in this development, it follows that 61 ppm of NO_2 corresponds to 122 ppm of NO

deposited. If this stoichiometry is correct, the initial deposit of NO would have been 122 + 72 = 194 ppm NO, which is quite close to the previously computed value of 215 ppm. It is noted that these concentrations are additive only because they are so small. The agreement between these two values is remarkably good in view of the significant errors involved in determining the absolute quantity of gas deposited. This calculation depends on parameter values which are subject to considerable experimental error; e.g., the system pumping speed, ion gauge calibration, leak rate reproducibility, etc. Thus the absolute amount of gas deposited can be determined only within approximately 15%, an accuracy that will have even more significance for the ozone experiments described later. The NO/NO_x ratio determined by chemiluminescence is more accurate, however, to within approximately $\pm 2\%$. Therefore this ratio will be used as the standard measure of conversion obtained for the disproportionation reaction (this is explained in what follows).

This experiment was repeated, in run 241, with similar results. With a NO/NO_x ratio of 0.64, the conversion to NO_2 was slightly less drastic, but still quite substantial. Since this effect would have a significant impact on subsequent NO oxidation experiments, it was decided to investigate it more carefully.

Before continuing, several factors were explored to ascertain the nature of this effect; i.e., whether or not it is genuine and specific to the condensation and regeneration process, or if it could be accounted for by contamination or gas phase

reaction. Thus, the nitrogen used in the flash desorption experiment was analyzed for NO and NO_2 with the chemiluminescence analyzer. Since neither species was detected, contamination was eliminated as a possibility. In a second experiment, a 0.5% NO in N_2 gas mixture, used as a primary calibration standard for the chemiluminescence analyzer, was admitted through the leak valve assembly into the analyzer in order to check for possible conversion of NO to NO_2 in the gas feed system, which includes stainless steel tubing and valves, as well as teflon feed lines. Chemiluminescence analysis yielded $NO=NO_x=5000$ ppm; i.e., no NO was converted to NO_2, thereby eliminating the possibility of conversion in the feed and metering assemblies.

In order to test whether conversion of NO to NO_2 could be occurring on the vacuum chamber walls, the chamber was pumped down to $2x10^{-6}$ torr, sealed off from the pumping system, and with the cryosurface at room temperature, filled with the 0.5% NO in N_2 calibration standard. Again, chemiluminescenee analysis yielded no detectable NO_2, and therefore NO was not oxidized to NO_2 on the vacuum chamber walls.

To determine whether mixing the pure N_2 with NO in the gas phase could result in NO_2 production, the chamber was pumped down to $2x10^{-6}$ torr, sealed off, and with the surface at room temperature, filled to approximately 0.5 atm with the 0.5% NO in N_2 calibration standard, and then brought up to atmospheric pressure with N_2. The subsequent analysis yielded $NO=NO_x=2700$ ppm, and therefore, gas phase mixing of NO and N_2 in the vacuum chamber did not produce NO_2.

In order to ascertain whether the disproportionation reaction might arise as a result of an unknown contaminant in the N_2, active at cryogenic temperatures, run 243 was performed. In this experiment, 1.0×10^{-4} g mol of NO was deposited on the 15K cryosurface, and then flash desorbed with the 5.6 ppm NO in the N_2 primary calibration standard. This resulted in an NO/NO_x ratio of 0.80, when corrected for the NO in the primary standard. Although this conversion is relatively low, the disproportionation reaction was not prevented. This proves that disproportionation during flash desorption is not due to a contaminant in the gas used to flash desorb the system.

The only shortcoming of the preceding tests is that the use of high NO concentrations could mask low levels of conversion to NO_2, since only the total NO_x and NO concentrations are actually measured, with the NO_2 concentrations found by difference. Also, the pure NO could have low levels of NO_2 as a contaminant. Both of these points were addressed as follows. The chamber was pumped down to 2×10^{-6} torr, sealed, and with the cryosurface at room temperature, the pure NO was admitted to the system. The NO feed was terminated after a few moments, and the chamber filled to atmospheric pressure with pure N_2 (similar to a FD experiment performed at room temperature). Chemiluminescence analysis of the final gas composition yielded $NO = NO_x = 68$ ppm, thereby proving that; (a) the pure NO was not contaminated with NO_2; and (b) low levels of NO_2 were not being formed in the feed system or the vacuum chamber at room temperature. Thus one must conclude that the conversion of NO to NO_2 is genuine, and that it is a direct result of the condensation

and desorption process. In order to explore this phenomenon further, the literature was examined for similar reports.

Disproportionation - Extant Literature

The oxidation of NO with O_2 at cryogenic temperatures (-192°C) was reported as early as 1924 by Briner et al. Catalytic oxidation of NO with O_2 over silica gel was reported in 1931 by Szego and Guacci. However, the first thorough investigation of catalytic disproportionation (i.e., conversion of NO to NO_2 in the absence of any other oxidant) was reported by Addison and Barrer (1955). This latter work was initiated as a study of adsorption/desorption properties of various gases on zeolites, particularly calcium and sodium-rich forms of chabazite and faujasite, as well as mordenite. The authors found that N_2O adsorbed on these zeolites was remarkedly stable up to 350°C. NO, however, reacted strangely, particularly in faujasites and chabazites. Large quantities were adsorbed, relative to N_2O, and underwent the disproportionation reactions:

$$4NO \longrightarrow N_2O + N_2O_3 \qquad (5.3\text{-}2)$$

$$3NO \longrightarrow N_2O + NO_2 \qquad (5.3\text{-}3)$$

with remarkable ease to near completion at cryogenic temperatures. Table (5.3-1), taken from a more recent reference to this work (Barrer, 1978) illustrates the relationship between percent reaction in Ca-chabazite and initial sorption temperature. Note that in the first series, performed at 0°C, the percent conversion did not increase with residence time in the zeolite; i.e., the contact time has no observable influence on the extent of reaction. Yet, as the second series clearly shows, the sorption temperature did have a great deal of influence, with a calculated

conversion of near 100% at -78°C. Runs performed at -183°C also resulted in nearly complete conversion. In fact, Addison and Barrer (1955) speculated that disproportionation did not occur at the sorption temperature, but rather during desorption, perhaps at temperatures below -63.5°C, the sorption temperature at which conversion deviated significantly from 100% (Table (5.3-1)).

These authors also worked with charcoal, in order to determine if the disproportionation reaction would occur on other sorbent materials. They found that charcoal also adsorbed NO copiously at 0°C (e.g., 80 cm^3/g at STP) and upon thermal desorption, a large quantity of NO_2 was evolved. These authors further suggested that the reactions

$$4NO \longrightarrow N_2 + 2NO_2 \qquad (5.3\text{-}4)$$

$$6NO \longrightarrow N_2 + N_2O_3 \qquad (5.3\text{-}5)$$

might be occurring. However, no further work on charcoal was performed since the primary objective was N_2O production on zeolites. In addition, the authors hypothesized that disproportionation might also occur in NO in the compressed state or in a condensed phase. Yet, a blank experiment (i.e., with no adsorbent), involving the condensation of NO for 100 hours at -183°C yielded no detectable traces of any disproportionation products. Little information was reported concerning this blank experiment, however (e.g., adsorbents used, pressure, solid or liquid phase, detection scheme, etc.) and many differences between their blank and the present experiments are possible, and these will be subsequently discussed.

Addison and Barrer (1955) were also able to show expermentally that NO adsorbed on chabazite was inactive towards oxidation by oxygen.

In these papers, disproportionation was attributed to the intracrystalline environment of the zeolite, particularly its polar nature and comparatively intense fields which exist within zeolite crystals, and may favor catalytic activity. This work was patented (Barrer and Addison, 1958), and the disproportionation reaction on zeolites was presented as an efficient method of producing N_2O and higher oxides of nitrogen from NO.

Alekseev et al. (1962) employed infrared spectrophotometry in a study of the adsorption of NO on zeolite X. These authors found the 1876 cm^{-1} band of NO shifted upon adsorption, due to NO-surface bond formation. Bands at 2250 cm^{-1}, 1300 cm^{-1}, and other low frequencies were also obtained, which were attributed to N_2O formation. Bands at 1940 and 2110 cm^{-1} were also observed, and attributed to NO_2 decomposition. Thus, this surface species analysis technique employed by an independent group of workers verified the disproportionation reaction in zeolites. More recently, this reaction was noted by Lunsford (1970), who employed electron paramagnetic resonance to study nitric oxide adsorbed on alkaline earth zeolites.

In summary, disproportionation of NO on adsorbents at low temperatures has been observed and reported extensively in the literature. When zeolites are employed, N_2O, N_2O_3, and NO_2 are produced. When charcoal is employed as an adsorbent NO_2, N_2, and N_2O_3 are produced. Thus it is quite natural to

suspect these or similar reactions as occurring in the present work. It was also reported, however, that low temperature adsorption resulted in near complete conversion, and also that a blank experiment without an adsorbent yielded no conversion. Thus why should conversion occur in the present system without use of an adsorbent medium (e.g., zeolites)? Is the reaction catalyzed by the gold-flashed, stainless steel surface, or perhaps by the frost itself? These questions were examined via the experiments which follow.

Further Disproportionation Experiments

Since chemiluminescence analysis showed NO_2 was a significant product in the present system, a test of the stoichiometry

$$4NO \longrightarrow N_2 + 2NO_2 \qquad \text{(as 5.3-4)}$$

is obvious. Thus, in run 244, a TPD experiment was performed by depositing approximately 8.8×10^{-6} g mol of NO on the cryosurface at 15K, followed by desorption while monitoring m/e peak 28 for the N_2 parent peak. (Peak 14 was not employed since NO also has a fragment at this m/e ratio.) It is noted that CO, a common vacuum system contaminant, also has its parent peak at an m/e of 28. This necessitated a second experiment, in which no NO was deposited, but the surface was cooled to 15K and then regenerated, in order to determine the background CO desorption spectrum.

Results of experiment 244 are presented in Figure (5.3-1). Curve A represents the desorption of peak 28 following deposition of NO, while curve B is the background desorption pattern. Note that curve A exhibits three major peaks at 40K, 64K, and 82K, while curve B, the background spectrum, exhibits only one major

peak, at 40K, which coincides very closely in both height and area with the 40K desorption peak of curve A. Thus, the 40K desorption peak of curve A is attributed to the desorption of CO condensed from the vacuum chamber background. This leaves curve A with two peaks, at 64K and 82K, which are not due to background contamination. These could be due to either N_2, N_2O, or N_2O_3, since all three have fragments at peak 28.

Assuming, for the moment, that these peaks are due to desorption of N_2 only, the following calculation was performed in accordance to the stoichiometry of eq. (5.3-4). The area under the two peaks, was determined as a function ot time. Knowing that the ratio of the chamber pressure (in torr), as determined by the ionization gauge, to the current (in amperes) given by the mass spectrometer, is approximately 36.3, it was determined that 9.8×10^{-7} g mol of N_2 could have been generated from the calculated 8.8×10^{-6} g mol of NO deposited. Thus, 1.96×10^{-6} g mol of NO_2 were formed and 3.92×10^{-6} g mol of NO were converted, if the assumed stoichiometry is correct. Therefore, the corresponding NO/NO_2 ratio is 2.49, and the NO/NO_x ratio would be 0.71. This latter value compares quite favorably with the NO/NO_x values of 0.54 and 0.64 reported for the flash desorption experiments discussed previously. Differences in the types of desorption technique (FD vs. TPD), quantities deposited, and analytical techniques (chemiluminescence vs. mass spectroscopic desorption patterns) could account for the observed differences in conversions.

Since peak 28 can also be a N_2O and/or N_2O_3 fragment peak, the identity of the two remaining peaks of Figure (5.3-1) have

yet to be determined. In runs 249, 250, and 251, TPD experiments were performed in which NO was deposited on the cryosurface and then desorbed while peak 44, the N_2O parent peak, was monitored. In run 249A, 4.3×10^{-6} g mol of NO were deposited initially and desorbed. A small amount of peak 44 material was generated, but increasing the deposit by approximately a factor of three to 1.3×10^{-5} g mol NO in run 248B did not increase the amount of desorbed material at peak 44, thereby implying that the desorbate was probably a condensed background species, possibly CO_2. In runs 250 and 251, approximately 1.3×10^{-5} g mol of NO were deposited, and the desorption pattern of peak 44 compared to blank experiments (i.e., no NO deposited) conducted before and after the deposition experiment. In each experiment, the area of the peak desorbed and detected at m/e 44 in the 80-90K range remained the same, both with and without NO deposition. Thus it was concluded that a minute quantity of background CO_2, (which is known to desorb in the 80-90K range) was primarily responsible for the peaks observed at m/e = 44, and that no appreciable amount of N_2O was produced.

Since mass 44 may also be a fragment of N_2O_3, there is little reason to believe, in light of the previous experiments, that this species was produced during disproportionation. To confirm this conclusion, run 252 was performed, in which 1.3×10^{-5} g mol of NO were deposited and then desorbed by TPD, while mass 76, the N_2O_3 parent peak, was monitored. As expected, the results were negative.

Thus the conclusions drawn from these experiments are that N_2 is a product of the disproportionation in the current system,

while N_2O and N_2O_3 are not. Thus one must also conclude that the reaction stoichiometry is indeed that of eq. (5.3-4). Since it has been shown experimentally that NO_2 and N_2 are generated during disproportionation, the work of Chapter 4, on desorption as a fractionation technique, would lead one to suspect that much of the N_2 formed at low temperatures would not be trapped (i.e., held over to higher temperatures) by the NO or NO_2. Yet in run 244, N_2 desorbed at 64K and 82K. Thus an experiment was devised to explore this point further.

In run 247, approximately $5x10^{-6}$ g mol of 5% NO in N_2 were deposited on the cryosurface, and mass 28 was monitored during desorption. The results are shown in Figure (5.3-2), curve A. As can be seen from this figure, two peaks were generated, corresponding to N_2 desorption at 28K and 40K. Curve B illustrates a blank background run, in which the level of CO (peak 28) contamination on the cryosurface was determined. Note that this peak also occurs at approximately 40K. No 64K peak is evident, and a faint peak is observed at 82K. Both of these peaks are characteristic of disproportionation. Actually, the absence of these two peaks is understandable, since only $2.5x10^{-7}$ g mol of NO was deposited, or approximately 3% of the quantity deposited in run 244 (Figure 5.3-1). This fact, when combined with a high mass 28 background, would tend to obscure any low levels of N_2 produced during disproportionation. An important point made here is that the N_2 deposited desorbed readily at 28K and 40K, while practically none desorbed at 64K and 82K. This strongly suggests that the N_2 desorption peaks at 64K and 82K of run 244 were due to spontaneous N_2 generation at these temperatures.

In run 256, 1.2×10^{-5} g mol of pure NO was deposited, and a TPD experiment was performed while monitoring mass 30 for NO. The resultant desorption pattern in presented in Figure (5.3-3), along with that of N_2 (mass 28), obtained during run 244. It is obvious that the 64K and 82K peaks of run 244 correspond to the two major mass 30 desorption peaks. Since mass 30 is also a fragment of NO_2, it cannot be determined whether either or both of the run 256 peaks are either partially or entirely due to NO_2. Yet it can be hypothesized that since N_2 would have desorbed at a lower temperature if it had already formed, it did not exist until the desorption of the NO deposited; i.e., that the disproportionation reaction occurs just prior to, or during the desorption of NO from the cryosurface. This hypothesis is consistent with the reasoning of Addison and Barrer (1955), who believed that the disproportionation they encountered in zeolites occurred during thermal desorption. These authors noted that when NO was adsorbed between -78°C and -183°C, and then regenerated, the conversion remained the same, but that conversion decreased if NO was adsorbed above -63.5°C. These results imply that the reaction occurred during the heating process, as the molecules developed enough mobility just prior to their desorption. Our evidence is similar. One possibility is that clusters of NO are being formed which redistribute their atomic constituents during desorption, aided by the catalytic influence either of the cryosurface or a sublayer of condensate. Thus the next experimental study was aimed at developing an understanding of the influence of the cryosurface during the disproportionation; i.e.,

whether its influence could be inhibited by pre-coating it with a presumably more inert layer of a condensed gas.

An attempt was made to isolate a NO deposit from the cryosurface by coating the surface with N_2. In run 245, 1.6×10^{-4} g mol of N_2 were deposited on the 15K cryosurface, followed by 1.2×10^{-4} g mol of NO, and then flashed desorbed with N_2. The product gas was analyzed by chemiluminescence and was found to have a NO/NO_x ratio of 0.82. Thus the conversion to NO_2 was less than found with the bare cryosurface, but was not eliminated. It is difficult to say whether or not the reduction was significant, due to the wide range of conversions found during other disproportionation experiments. It was noted, however, that the N_2 probably desorbed at approximately 40K, allowing at least some of the NO to contact the surface prior to desorption. Thus it was decided to use another gas species with a lower vapor pressure than NO, which conveniently turned out to be CO_2 (Honig and Hook, 1960).

In run 248, 10^{-4} g mol of CO_2 was deposited to coat the 15K cryosurface, and then 1.1×10^{-4} g mol of NO were condensed. The deposit was flash desorbed, resulting in a product gas with an NO/NO_x ratio of 0.46. This conversion was just as high, if not actually greater, than the conversion obtained on a bare cryosurface. Since CO_2 remains condensed on the surface until the 85-95K temperature range (as shown in the following development), it is apparent that coating the surface with CO_2 did not produce the desired effect. It is quite possible that in the case of the N_2 coating, carryover became important as the

N_2 base layer desorbed. Effects such as this have not been explored for flash desorption type experiments.

It is concluded from these two experiments that:

A) Coating the cryosurface does not halt NO disproportionation, and therefore this reaction is probably not dependent on the cryosurface for catalytic action.

B) If a volatile sublayer is used, followed by flash desorption, carryover of the NO frost by N_2 leaving the surface may reduce the extent of reaction.

While the metal surface does not seem to catalyze this reaction, it is still possible that the cryofrost structure itself does. The following discussion explores the relevant literature with an eye towards establishing the catalytic nature of the frost with respect to the disproportionation reaction.

Disproportionation - Self Catalyzed?

Addison and Barrer (1955) noted that conversion due to disproportionation increases as sorption temperature decreases. This implies that multilayering of sorbed NO in the pore structure of the adsorbent seems to be important. Since these authors propose the four-body reactions;

$$4NO \longrightarrow N_2O + N_2O_3 \qquad \text{(in zeolites)} \qquad (5.3\text{-}6)$$

$$4NO \longrightarrow N_2 + 2NO \qquad \text{(in charcoal)} \qquad (\text{as } 5.3\text{-}4)$$

the greater the number of available NO molecules in the adsorbent pores, the more likely the reaction. This reaction is not likely in the gas phase, where four body collisions are for all practical purposes nonexistent.

Alekseev et al. (1962) have shown that NO physisorbs on zeolite surfaces, forming weak physical bonds with the surface which probably stabilize not only the NO molecule, but also the intermediates formed during the disproportionation reaction. Combining this information with Addison and Barrer's (1955) contention that disproportionation occurs during heating to desorption, implies that these reactions occur in NO agglomerates, physisorbed onto the zeolite pore surface, which dissociate just prior to desorption. Thus the phase change during desorption may be the critical step. However, this still leaves open the question of whether or not the sublayers of adsorbed NO can act as a stabilizing surface. Thus, similarities between the cryofrost and adsorbents should be examined in order to ascertain whether the cryofrost can indeed be self-catalytic.

It was mentioned in section (3.1) that Kohin (1960) attributed the crystal structures of solid CO and N_2 to quadrupolar interactions, anisotropic molecular polarizability, and short range repulsive forces. Venables and English (1971) suggested that the crystalline structure of NO is not due to van der Waals forces but to quadrupole-quadrupole interactions. As also reported in the condensation chapter, many of the separations properties of zeolites are due to the electrostatic aspects of physical adsorption (Benson and King, 1965, Barrer, 1978); i.e., the same electrostatic forces believed to be responsible for the crystalline form of frozen gas matrices.

Abe and Schultz (1979) have shown that rare gases deposited at intensities of approximately 5×10^{20} $m^{-2}s^{-1}$ onto low temperature (4-22K) surfaces are quite porous. These conditions

correspond quite well to be the beam intensities and temperature ranges employed in the TPD experimental depositions. These authors also note that increasing the beam intensity may also increase cryofrost porosity at higher (22K) temperatures. The flash desorption technique employed deposition intensities of approximately $4x10^{21}$ $m^{-2}s^{-1}$ at 15K. Thus it is probable that our cryofrost, in both TPD and FD experiments is quite porous. As also shown in section (3.1), rare gas matrices (Abe and Schultz, 1979) and CO_2 matrices (Becker et al., 1972) adsorb H_2 in proportions similar to zeolites. It has been calculated that in porous rare gas matrices, the adsorption energy of H_2 is approximately 0.6 kcal/mol greater than the evaporation energy of pure H_2, while in porous CO_2 matrices the H_2 adsorption energy is approximately 1 kcal/mol greater than the evaporation energy of pure H_2. These energies are quite similar to the estimated 0.8 kcal/mol Benson and King (1965) calculate as necessary to separate ortho and para hydrogen in Linde 5A and 13A molecular sieves, an effect they attribute to electrostatic effects in zeolite pores. This comparison implies that, for H_2 the electrostatic environment in zeolite pores may be comparable to that in the pores of cryofrosts.

Is it possible that the frost itself might meet the requirements for the disproportionation to occur? The frost does provide a source of highly concentrated NO (since in most of these cases it was pure NO) in the close proximity required for a four-body reaction. Although the pore structure might decompose somewhat during heating to desorption, the literature does in fact show that an electrostatic field exists in the

cryofrost matrix and on its surfaces, and thus the cryofrost matrix surface could serve as a stabilizing environment for intermediates formed in the disproportionation reaction. This may be the critical difference between this work and the blank experiment of Addison and Barrer (1955). Though their description was not clear, it was implied that the blank was NO liquified in glass, which would not have the stabilizing influence of the crystalline solid phase NO matrix.

A rough, first order calculation of the heat of reaction of disproportionation, using heat capacity data from Reid et al. (1977) and heats of formation, fusion, and vaporization from Dean (1973) was performed. In the solid phase at 50K, reaction (5.3-4) is exothermic with a ΔH_R of approximately -64 kcal/mol, making it thermodynamically favorable. Since the reaction is exothermic, it is also possible that a thermal quasi-chain reaction could occur; i.e., the energy liberated upon reaction could cause additional reaction. Since the cryofrost layer is pure NO, there are no heat transfer limitations; i.e., any energy liberated would be transferred directly to potential reactants.

Thus it is hypothesized that the disproportionation observed experimentally is in fact a result of desorption of NO from the solid phase, where the NO sublayer acts as a stabilizing medium for reaction intermediates as desorption progresses; i.e., the crystalline state provides a medium for self-catalysis.

Matrix Isolation

The original intent in the current work was to study the possible oxidation of NO with O_3 during the deposition and

desorption process. The disproportionation reaction renders such a study difficult by masking the production of NO_2 by oxidation with the NO_2 produced via the self-catalysis mechanism. In an attempt to eliminate this undesired reaction, matrix isolation was attempted. (Matrix isolation techniques have been reviewed by Cradock and Hinchcliffe (1975), Hallam and Scrimshaw (1973) and Meyer (1971)).

The first experiment performed in this manner was run 246, in which 1.4×10^{-3} g mol of a 5% NO in N_2 gas mixture (NO=7×10^{-5} g mol) were deposited and subsequently flash desorbed with N_2. The resulting NO/NO_x ratio of 0.5, found by chemiluminescence confirmed that matrix isolation by N_2 did not reduce the conversion due to disproportionation. The next logical step was to run TPD experiments to ascertain the reason why this occurred.

In run 247, approximately 5×10^{-6} g mol of the 5% NO in N_2 mixture (2.5×10^{-7} g mol of NO) were deposited onto the 15K surface. Figure (5.3-2), the mass spectrometer desorption pattern at mass 28, which has already been discussed, shows that the vast majority of N_2 desorbs by 50K. In run 247B, the same amount and type of deposit was desorbed except that the NO parent peak (mass 30) was monitored. The resultant desorption curve is presented in Figure (5.3-4). The low level carryover of NO during the desorption of N_2 in the 20-45K (shown in Figure (5.3-2)) and the subsequent drop in NO signal at approximately 42K, signaling the end of NO carryover by desorbing N_2, are noted. Thus, as expected from the results of the previous chapter, N_2 phase separates from NO and desorbs with little quantitative carryover of NO, although they were initially well mixed, leaving

essentially pure NO on the cryosurface. Figure (5.3-4) also exhibits the characteristic NO peaks in the 64K and 82K temperature ranges, as in Figure (5.3-3) for pure NO. Thus once the N_2 matrix has desorbed, the remaining NO desorbs exactly as pure material. Note that due to the low quantitative deposit of NO, these peaks are only slightly above background; i.e., the desorbed NO can linger in the background for some time, due to adsorption onto vacuum chamber walls.

As noted in the previous discussion of Figure (5.3-2), there is evidence of low levels of N_2 production at 82K, even though mass 28 background levels are relatively high. Along with the FD evidence of run 246, this illustrates the fact that matrix isolation of NO in N_2 at this concentration (5%) is ineffective in halting the disproportionation reaction; i.e., N_2 phase separates and desorbs first, leaving pure NO on the surface. Therefore, carbon dioxide was chosen as a matrix material due to its low vapor pressure in comparison to NO, which allows it to remain rigid and to continue to isolate NO above its normal desorption temperature (Redhead et al., 1968, Honig and Hook, 1960). (The vapor pressure of CO_2 is 10^{-5} torr at 91.5K, while for NO, the vapor pressure is 10^{-5} torr at 57.6K.) Thus the CO_2 matrix should survive at temperatures above the point at which NO first desorbs. Cradock and Hinchcliffe (1975) define the onset of annealing to occur (discussed later) at 30% to 50% of the normal melting point, which is 216.6K for CO_2 (Hallam and Scrimshaw, 1973). Thus the CO_2 matrix should begin to lose rigidity between 65K and 108K.

To test this theory at high concentrations, run 253 was performed, in which 3.3×10^{-4} g mol of a 30.5% mixture of NO in CO_2 were deposited on the 15K cryosurface and then flash desorbed with N_2. This procedure resulted in a NO/NO_x ratio of 0.41, which is somewhat lower than previous runs, implying a more effective disproportionation conversion than in previous runs.

In run 254, 5.7×10^{-4} g mol of 8.2% NO in CO_2 were deposited on the 15K cryosurface and flash desorbed. The results were similar to run 253, in that a NO/NO_x ratio of 0.42 was found. Thus lowering the concentration of NO in the CO_2 by more than a factor of three had little effect on conversion due to disproportionation. Thus it must be concluded that matrix isolation is not effective at these dilution ratios during the desorption process. It is possible, as evidenced by the NO/NO_x ratios, that the CO_2 matrix acts as superior catalyst for NO disproportionation than does pure NO. Thus TPD experiments employing 8.2% NO in CO_2 were performed to determine if matrix isolation in CO_2 has any effect.

In run 257A, approximately 1.3×10^{-5} g mol of 8.2% NO in CO_2 were deposited and then desorbed by TPD, while monitoring mass 30. Run 257B was similar in that the mixture deposited was taken from the same gas sample to insure the identical concentration, but the foreline sample pressure was unknown. It is estimated that approximately 1.4×10^{-6} g mol of the 8.2% mixture were deposited. Since temperature dependence of the desorption peaks was the desired data, knowledge of the exact deposit quantity was not critical. In this run (257B), mass 44 was monitored for CO_2 desorption. In run 258, 10^{-5} g mol of

pure CO_2 were deposited, and mass 44 was monitored. The results of these three experiments are presented in Figure (5.3-5), where curve A is the desorption pattern of NO in the NO-CO_2 mixture, curve B is the desorption pattern of CO_2 in the NO-CO_2 mixture at lower deposit quantities, and curve C is the desorption pattern of pure CO_2. Note that curves B and C show that the CO_2 desorbed from the NO-CO_2 mixture begins to peak at the same temperature as pure CO_2, but that the peak width is narrower, due to the small amount of CO_2 desorbed. Thus the CO_2 behavior is unaffected by the NO in the matrix.

The nature of the desorption pattern of NO from the NO-CO_2 mixture, as illustrated in curve A of Figure (5.3-5) is substantially different from the desorption spectra of pure NO shown in Figure (5.3-3). In Figure (5.3-3), pure NO exhibits two maxima of nearly equal area, at 66K and 83K. In Figure (5.3-5) of matrix isolated NO, the low temperature (63K) peak has an area approximately two orders of magnitude less than the higher temperature peak, which is shifted to approximately 88K, coincident with the CO_2 desorption temperature. Thus the attempted matrix isolation in CO_2 was partially successful in that a major desorption peak of pure NO at 66K was reduced substantially (and shifted slightly), trapping the NO in the CO_2 matrix until that matrix began to sublimate, resulting in a wider desorption peak at 88K, corresponding approximately to both NO and CO_2 desorption. Thus a low vapor pressure matrix material can trap the more volatile NO. Yet, flash desorption experiments show that this effect does not stop disproportionation. Thus aggregation of NO must occur prior to desorption, if the solid

phase disproportionation theory is valid. Reasons why this technique did not stop the disproportionation reaction are explored below.

Matrix Isolation - Does It Apply?

The term matrix isolation is actually a misnomer for the effect sought in the present work. It has been shown that disproportionation occurs just before or during the desorption of NO, primarily by the N_2 byproduct desorption peaks. In classic matrix isolation experiments, reactions are minimized by careful control of the matrix temperature, and thereby the diffusivities or mobilities of the reacting constituents. These conditions are clearly not obtained here, where the cryofrost is heated to complete desorption. Cradock and Hinchcliffe (1975) have shown that the probability of CO in a rare gas matrix being completely isolated (i.e., no CO nearest neighbors) is given by $(1-r)^{12}$ for CO isolated in a matrix with 12 nearest neighbors, where r is the inverse of the matrix ratio (r=moles solute/moles solvent). Complete isolation is even more difficult if the trapped species interacts strongly with the matrix material. Thus a matrix containing NO:CO_2 as 1:100 would only have 88.6% of the NO completely isolated. In the present case the ratio is $(1-(8.2/91.8))^{12}=0.325$, and thus approximately 67.5% of the NO in the NO:CO_2 mixture deposited as cryofrost has NO as a nearest neighbor. Thus, most of the NO interacts with other NO molecules.

In order to achieve true isolation, much higher dilution ratios are necessary. A matrix ratio of 1000 (solvent/solute) will yield 98.8% isolation of solute species, while a matrix

ratio of 10,000 will yield 99.9% isolation. These higher dilution rates are impractical for both TPD and FD experiments in the current work. For TPD type desorption, the absolute quantity deposited is limited by the vacuum system pumping speed. Thus small quantities of highly dilute sample render solute desorption spectra practically impossible to detect above background levels.

In the case of flash desorption type experiments, deposition times on the order of several days would be necessary to deposit enough solute to be visible employing chemiluminescence analysis. Thus for true matrix isolation type experiments, a surface specific analysis technique such as IR (Calo, 1979, Hallam and Scrimshaw, 1973, Meyer, 1971) becomes a necessity.

The basic purpose of the "matrix isolation" experiments performed here was to determine the effect of dilution of NO by CO_2 in a range appropriate to the limits of the current experimental system. Since a four-NO molecule aggregate is believed to be the minimum size necessary for disproportionation, dilutions in the ranges feasible for the current apparatus should have induced at least some reduction of the extent of reaction.

During deposition of the cryofrost, care must be taken in controlling the deposition rate. If the rate becomes too high, local hot spots may develop due to poor thermal conduction to the refrigerator heat sink for the heat of sublimation, and local diffusion and aggregate formation can occur. Cradock and Hinchcliffe (1975) recommend a deposition rate of 18 mg mol/hr. as the rate that best balances the diffusion problem against

opacity problems associated with very low growth rates (although IR transmittance is not a problem here), while Meyer (1971) recommends a rate of 1 to 2 mg mol/hr. In the present work, the maximum deposition rate was approximately 2 mg mol/hr. for flash desorption experiments and 0.1 mg mol/hr. for TPD type experiments. Though these rates would seem to comply with those recommended, there is evidence that NO may be more sensitive to aggregate formation during deposition. For example, Varetti and Pimentel (1971) reported that in studies of highly dilute matrices of NO and NO_2 in N_2 ($N_2/(NO+NO_2)=500$) deposited on a 20K surface at 10 mg mol/hr., IR bands of NO dimers and higher aggregates were readily observed. Since the high NO concentration in matrices in the present work require a substantially shorter diffusion path to aggregate, aggregation of NO during deposition is a distinct possibility. However, a technique such as IR spectrophotometry would be required to unequivocally confirm this conjecture. Thus, it seems that the working concentration range in the current work is too high to prevent dimerization, and that matrix deposition probably leads to aggregate formation.

The process of thermal desorption causes a considerable degree of diffusion in the frost. In matrix isolation studies, diffusion in matrices is usually treated in terms of matrix rigidity. Cradock and Hinchcliffe (1975) note the common rule of thumb for matrix rigidity: viz., below $0.3T_m$ (where T_m is the normal melting point), the matrix is considered rigid; i.e., it remains essentially in its initial state, as formed during deposition, without rearrangement. Between $0.3T_m$ and $0.5T_m$ diffusion becomes important.

Hallam and Scrimshaw (1973) elaborate on this notion of rigidity as a barrier to solute diffusion. These authors list actual temperatures at which diffusion effects become important (T_d) for several common matrix gases. While the values of T_d for N_2 and O_2 are 30K and 26K (approximately one half of the normal melting points of 63.2K and 54.4K, respectively), it was found that CO_2 is an exception. For CO_2, T_d = 63K, while T_m = 216.6K. Thus for CO_2, the T_d/T_m = 0.29. This T_d value (63K) corresponds well with the minor desorption peak at 63K for CO_2-isolated NO given in Figure (5.3-5).

Guillory and Hunter (1969) employed IR spectroscopy in a study of the dimerization and aggregation of NO in N_2 matrices. With matrix ratios of 500:1 (N_2:NO) and deposition onto a 4K cryosurface, complete isolation of NO resulted; i.e., no dimer or higher aggregate bands were observed spectroscopically. Heating the cryofrost to 15K and rapidly recooling to 4K brought about limited dimerization. Heating to 40K and then recooling to 4K resulted in an IR spectrum identical to that of bulk NO. Thus, starting with a very dilute matrix and heating it to 10K above its T_d value, total aggregation of the solute NO, as measured by IR absorption, occurred. It must be noted here that Guillory and Hunter (1969) found CO_2 too rigid for their experiments, though they were interested in the 15K to 40K temperature range, where the CO_2 matrix would be highly rigid.

Smith and Guillory (1977, 1977A) investigated NO isolated in O_2 at O_2:NO ratios of 100 to 300:1 on a CsI window initially at 13K. They found that NO deposited in this manner yielded IR spectra indicative of complete isolation. However, by heating

the matrix to 35K in a six second interval and then recooling to 13K, limited migration was induced. In this experiment, IR analysis revealed NO dimer formation, as well as products of NO oxidation (discussed later in this chapter). Cis-$(NO)_2$ was found to be the most stable dimer. Thus again in this case, rapid dimerization (and reaction) occurred when the isolated matrix containing NO was heated to 9K above its diffusion temperature (T_d).

Thus far, it has been shown that:

A) Matrix compositions possible for the present system do not completely isolate NO in the matrix frost.

B) Aggregation may occur during deposition.

C) Aggregation can occur by diffusion prior to desorption of the CO_2 matrix.

The process steps by which NO can aggregate in the CO_2 cryofrost matrix and disproportionate have now been hypothesized.

The most realistic conceptualization of the cryofrost structure would be the microcrystalline state (Cradock and Hinchcliffe, 1975); i.e., small crystals surrounded by regions unoriented with respect to each other. Multilayer deposits of O_2 and Xe, grown by Horl and Suddeth (1961), and studies by electron diffraction, reveal a crystallite size of approximately 100Å. Venables and Ball (1971) grew rare gas crystals in the 40K to 50K temperature range, and found grain sizes of $\leq$2000Å by electron microscopy. Thus crystallite sizes should range from 100Å to 1000Å in radius, on the average.

As in the work of Chadwick and Glyde (1977), a mean penetration depth (MPD) can be defined as

$$MPD = (Dt)^{0.5} \qquad (5.3\text{-}7)$$

where D is the diffusion rate and t a characteristic time. Estimating the average radii of the crystallites obtained by deposition as 500Å and the characteristic time as 100 seconds, a conservative estimate of the time available for diffusion, a diffusion rate of approximately 2.5×10^{-13} cm^2/s would be necessary for the MPD to be equal to the crystallite radius; i.e., at this diffusion rate, much of the trapped NO would be able to migrate to the grain boundaries.

Although diffusion rate expressions are not available in the literature for the NO-CO_2 system, examination of a different system should allow an order of magnitude estimate for the possible diffusion rates. Self-diffusion in Kr, which has a T_d of 50K (Hallam and Scrimshaw, 1973) has been shown to be well represented by

$$D = 5 \exp(-4800/\underline{R}T), \qquad (5.3\text{-}8)$$

where D is the diffusivity in cm^2/s, $\underline{R}$ is the gas constant, and T is the temperature in K (Chadwick and Morrison, 1970). At 80K, this expression yields a diffusion rate of 3.8×10^{-13} cm^2/s, which is of the correct order of magnitude for the mean penetration depth desired. Thus in this rare gas solid, the order of magnitude of the diffusion coefficient is high enough to allow diffusion to the grain boundaries.

Parker et al. (1969) reported that the activation energy for diffusion along grain boundaries is approximately half of its value for crystalline lattices. Thus grain boundary diffusion coefficients are approximately 10^6 times larger than those for lattices, making lattice diffusion the only effective barrier.

In this work on self-diffusion in Ar, it was assumed that the concentration of isotopic Ar in the grain boundaries is equal to that in the vapor during the experiment; i.e., there is no effective barrier to diffusion along the grain boundaries.

Meyer (1971), in a general review of diffusion in cryofrosts, noted that diffusivity should be dependent on relative solute-solvent molecular size. Thus a small solute in a larger solvent matrix, such as NO in CO_2 in the current work, should exhibit a larger diffusion coefficient than in self-diffusion, for example. Thus, the estimate of Kr self-diffusion rates at 80K may actually underestimate that for the NO-CO_2 system, with the NO diffusion coefficient being significantly greater, thereby allowing even greater mobility during desorption, which again leads to aggregate formation and ultimately, disproportionation.

Thus it is reasonable to assume that during heating of the NO-CO_2 matrix, diffusion of NO can occur readily prior to CO_2 desorption, and that during this process NO diffuses to the crystalline grain boundaries, where it meets with little diffusional resistance, leading to agglomeration which provides the necessary four-body sites for the disproportionation reaction. From the experimental evidence, it is likely that the actual disproportionation reaction occurs during the desorption process. Predicting a mechanism for this reaction would be sheer speculation without the aid of further analysis using surface analysis techniques, such as IR spectrophotometry.

It is interesting to note that in Figure (5.3-5), a NO desorption peak does occur at 64K, but is only approximately 2.4%

of the main peak at 88K. It is possible that this minor peak represents that portion of the NO deposited that phase-separates upon deposition, or perhaps originally resided in the grain boundaries, while the majority of the NO deposited is still locked in the CO_2 matrix and thus cannot desorb until agglomeration and disproportionation occur.

In summary, it is concluded that:

(A) Disproportionation occurs when pure NO desorbs from the solid state, yielding NO_2 and N_2 as the primary products.

(B) The disproportionation reaction appears to occur at or near the point of NO desorption.

(C) This reaction has been previously been reported in the literature.

(D) Coating the gold-flashed stainless steel surface with an inert gas does not halt the reaction.

(E) The extant literature supports the hypothesis that the solid state cryofrost may act as the disproportionation catalyst.

(F) Dilution of NO in a rigid matrix cannot stop the reaction in the range of concentration practical for the current apparatus.

(G) The extant literature provides ample evidence that in the viable concentration ranges, NO is not fully matrix isolated, that NO can agglomerate during deposition, and that it can readily agglomerate during heating of the matrix to desorption.

Thus as long as concentrated stratospheric cryosamples are desorbed to the gaseous state as part of the analysis

procedure, the disproportionation reaction may occur. This is particularly relevant to cryodistillation and subsequent manipulation and desorption processes. This finding also limits the present experimental study, in that, if the disproportionation reaction cannot be halted, nor its products accurately predicted quantitatively, this causes problems in the analysis of NO-O_3 oxidation experiments, which are described in the following section.

Ozone Regeneration

In view of the unexpected disproportionation of NO, it is evident that reactions can occur at cryogenic temperatures. Thus, if O_3 is to be employed as a reactant, it must be determined whether or not O_3 recombines during the deposition and desorption process. With a normal boiling point of 161.9K in comparison to 90.2K for oxygen (Dean, 1973), O_3 has a significantly lower vapor pressure than O_2. Thus, even though O_3 does not exhibit a parent peak at mass 48, it is possible that O_3 deposited as a mixture in O_2 can survive the desorption of the more volatile O_2 and remain on the cryosurface, only to sublimate at a temperature at which its vapor pressure is close to the system pressure. By depositing such a mixture and following the oxygen parent peak during desorption ty TPD, one should thus be able to observe an "extra" desorption peak at relatively high temperatures corresponding to O_3.

In run 235, 1.1×10^{-5} g mol of a mixture of 1.59% O_3 in O_2 were deposited on the gold-flashed, stainless steel surface and desorbed by the TPD method. Run 236 was a blank, in which 9.3×10^{-6} g mol of pure O_2 were deposited and desorbed in a similar

fashion. The resultant TPD spectra are presented in Figure (5.3-6). These spectra show that there is no substantial difference in desorption patterns between ozonated and non-ozonated oxygen. An extra desorption peak due to O_3 occurring after the main O_2 desorption peaks would have been clearly visible. This implies that either O_3 desorbs with O_2, (i.e., is carried over, as for other species in Chapter 4), or that it survives on the surface during the desorption of O_2 but concentrates and decomposes immediately to form O_2. Since the product of the recombination, O_2, is indistinguishable from either the reactant (O_3) or the matrix (O_2) with this analytical technique, and the concentration of O_3 in O_2 in the feed stream has a maximum of 2.25%, it is evident that this technique cannot be employed satisfactorily to study O_3 regeneration.

Due to these findings, the following series of O_3 regeneration experiments utilized chemiluminescence as the O_3 detection technique, employing the titration method, as described in section 5.2. Thus a procedure was developed in which a known quantity of O_3 in O_2 at a known concentration on the 15K cryosurface, flash desorbed with N_2, and the resultant gas mixture analyzed for O_3 using chemiluminescence. The number of g mol of O_3 both deposited and recovered after desorption could be calculated, and this information employed to determine whether or not O_3 could be deposited and then desorbed in a quantitative manner.

In experimental run 239, 3.17×10^{-4} g mol of approximately 1.6% O_3 in O_2 were deposited on the cryosurface and subsequently

flash desorbed with N_2. By calculating the amount of O_3 deposited, it was determined that the resultant gas would have a NO_3 concentration of 12.8 ppm if 100% of the deposited O_3 was recovered. Since a direct reading of the panel meter during chemiluminescence titration overestimates the concentration of O_3, as illustrated by the calibration curve of Figure (5.2-2), the uncorrected meter reading would be on the order of 98 ppm with a raw sensitivity on the lowest scale of approximately 0.2 ppm. The result of the experiment was surprising in that the O_3 reading obtained upon desorption was zero, implying that all of the ozone deposited had recombined.

This lack of ozone recovery could not be due to calibration errors. Since the ozone generator and chemiluminescence analyzer were calibrated while feeding the sample stream through the same valves, fittings, and tubing involved in feeding the sample gas to the cryosurface, any small O_3 loss in this system should have been compensated for. With an uncorrected panel meter reading of 98 ppm expected, with a sensitivity of 0.2 ppm, the ozone loss experienced, if due to a calibration error, would require an error on the order of a factor of 500; i.e., the deposit actually made had to be on the order of 1/500 of the amount calculated. Possible calibration errors include the vacuum system pumping speed, the ionization gauge corrections for the various gases, and the initial O_3 composition in the feed stream. The pumping speed, however, is conduction limited, and thus cannot change appreciably. The ion gauge response to N_2 as compared to the mass spectrometer readings was consistent,

making error on its part unlikely. The ozone concentration in the feed stream was also shown to be reproducible by wet titration. Thus it was concluded that for an ozone loss this pronounced, O_3 must have decomposed during the desorption process, similar to NO disproportionation. Therefore, it was decided to increase the ozone concentration in the feed stream and the deposit thickness, with an eye towards ascertaining whether or not any O_3 could indeed by deposited and then recovered from the solid state.

Runs 262-266 were made by depositing 2.25% O_3 in O_2 and varying the deposit time, and thus the amount of mixture deposited, and were subsequently flash desorbed. Table (5.3-2) gives the amounts of gas deposited and recovered, while Figure (5.3-7) displays the same information graphically. A linear fit of these data yields a slope of 0.6096, and ordinate intercept of -3.29×10^{-6}.

There are several features to note in Figure (5.3-7). The abscissa intercept is at 5.4×10^{-6} g mol O_3. Thus it appears that below this amount of O_3 deposited, all of the O_3 decomposes, as in experiment 239, in which 5.05×10^{-6} g mol were deposited and none recovered. It was shown previously, as in the case of NO in N_2, that if a matrix material is more volatile than the solute species, phase separation will occur; i.e., the matrix material will sublimate, leaving concentrated solute on the surface. Small amounts of O_3 concentrated in this manner seem to recombine completely. This is also supported by the TPD results of run 235, where 1.7×10^{-7} g mol of O_3 were deposited, and the desorption spectra revealed no distinctive desorption peaks

at high temperatures (>45K). It is possible that O_3 separates from the O_2 matrix in this manner, recombines immediately and desorbs at the tail end of the desorption spectrum.

The line drawn in Figure (5.3-7) also has a slope of approximately 0.61, implying that although ozone is recovered at higher absolute quantities deposited, the relationship is still not one to one; i.e., a percentage of the ozone deposited in the quantity over that necessary to overcome the initial disappearance, is also converted. Figure (5.3-8) is a plot of percent conversion of O_3 to O_2 (moles deposited-moles recovered)/ moles deposited) versus the number of moles of O_3 in the deposit. Note that conversion decreases with increasing deposit layer thickness, which may imply that competition for a limited number of catalytic sites may be occurring. Conversion seems to level off at approximately 55% at higher deposits, which may reflect the fact that thicker deposits effectively enjoy a longer residence time on the surface. Catalytic limitations and variations in reaction time may compensate, yielding a near constant percentage conversion at the higher deposit thickness.

An estimate of the heat of reaction for decomposition at 50K in the solid phase shows it to be exothermic, with ΔH_R= -69.5 kcal/g mol, calculated from data given by Reid et al. (1977) ($C_p(T)$) and Dean (1973) (heats of formation, fusion, and vaporization). This reaction is therefore thermodynamically favorable, and thermal chain reactions are again possible. As for the previous experiments, it appears that O_3 decomposition may also be self-catalytic.

In the next series of experiments, annealing the O_3 in O_2 matrix was attempted a la Smith and Guillory (1977), in an effort to determine if increased aggregation induced by this process would increase the conversion of O_3 to O_2. In run 273, an attempt was made to oxidize N_2O with O_3, which is discussed in a later section. The data relevant to this section are that $5x10^{-5}$ g mol of O_3 were deposited in an O_2 matrix at a concentration of 2.25% O_3 in O_2, the matrix was annealed to 35K and instantly recooled to 15K, and then held at 15K for 7 hours.

Flash desorption and chemiluminescence analysis yielded no NO or NO_x in the product gas, but did produce a recovery of $1.82x10^{-5}$ g mol of O_3. If the previous desorption results are extrapolated to the deposit quantity used here, they would predict that $2.7x10^{-5}$ g mol of O_3 would have been recovered, or 1.5 times more than the amount actually found. Thus the possibility arose that additional O_3 had been lost due to the annealing treatment and longer residence time.

In order to test this hypothesis, run 274 was performed, in which $2.3x10^{-5}$ g mol of O_3 were deposited at 15K (2.25% O_3 in O_2), and then annealed to 35K, recooled to 15K and held at 15K for 5 minutes. Flash desorption yielded $6.6x10^{-6}$ g mol of O_3 recovered in the resultant gas, as compared to an estimated value of $1.07x10^{-5}$ g mol, or a factor of 1.6 greater than the amount of O_3 recovered experimentally. Thus it seems that annealing does have some affect in increasing decomposition of ozone. The data for these two experiments are shown in Figure (5.3-9, curve B). Curve A of this figure is the data of Figure (5.3-7). There is a substantial difference between these data sets.

In order to attempt to prove that annealing was in fact responsible for this reduction in O_3 recovered, runs 275 and 276 were performed, depositing 4.39×10^{-5} and 3.4×10^{-5} g mol of O_3, respectively, in an O_2 matrix at a concentration of 2.25%. Flash desorption and subsequent analysis yielded 1.58×10^{-5} and 1.04×10^{-5} g mol of O_3 recovered. These data are presented in Table (5.3-3), along with those for the two previous experiments (runs 273-276). These points are also shown in Figure (5.3-9) as part of curve B. It is noted that the experiments performed with and without annealing fall on the same straight line, with a least squares slope of 0.44, on ordinate intercept of -3.79×10^{-6}, and correlation coefficient of 0.99. Thus annealing cannot be the cause of the increased decomposition of O_3 which occurred during this experimental set.

These results can be explained in terms of surface aging with a concommitant increase in catalytic activity with respect to O_3 decomposition. Although gold should be inert, the original gold flashing may not have been complete, leaving parts of the underlying surface exposed and subject to thermal cycling and exposure to concentrated oxidants, which might have caused chemical transformations. The experiments listed in Tables (5.3-7) and (5.3-8) were run approximately 2 to 3 weeks apart, with many other experiments occurring in between.

The work of Jenkins (1959) dealing with high concentration liquid ozone handling techniques reports that hydrocarbons, as well as other contaminants, are thought responsible for initiating O_3 recombination in liquid ozone. Arin and Warneck (1972) investigated gas phase O_3 decomposition and tested CO as

an initiator of a thermal chain reaction, resulting in the decomposition of O_3 by O_3-O_3 recombination. These authors found that rapid reaction occurred when CO and O_3 were mixed, but after further testing concluded that a low level contaminant in the CO was actually the chain initiator (discussed in more detail later). Since CO is one of the major background species in oil diffusion-pumped vacuum systems, it was decided to test CO as a decomposition initiator by using it as a base sublayer for the O_3-O_2 mixture deposition and subsequent flash desorption.

In run 290, 1.9×10^{-4} g mol of CO were deposited on the 15K gold-flashed surface, followed by 2.1×10^{-5} g mol of O_3 in a 2.25% O_3-O_2 mixture. Upon flash desorption, approximately 1.1×10^{-6} g mol of O_3 were recovered, an amount substantially less than would be expected from the previous experiments (Figure (5.3-9) curve B). The experiment was repeated with a larger deposit in run 291, in which 4.8×10^{-4} g mol of CO were first deposited, followed by 5.76×10^{-5} g mol of O_3 deposited in a 2.25% mixture with O_2. This experiment resulted in 1.1×10^{-5} g mol of O_3 being recovered, again a decrease with respect to the amount expected as a given by Figure (5.3-9), curve B. Thus the preliminary results suggested a significant increase in O_3 decomposition can be induced by depositing CO on the cryosurface as a base layer.

In order to confirm this result, experimental runs 292 and 293 were performed as blanks without CO deposition. For these runs 2.5×10^{-5} and 3.7×10^{-5} g mol of O_3 in a 2.25% mix with O_2 were deposited, respectively, and 3.42×10^{-6} and 3.08×10^{-6}

g mol of O_3 were recovered. These results are listed in Table (5.3-4) (runs 290-293), and presented in Figure (5.3-9), curve C. They show that although there again was a significant decrease in the amount of O_3 recovered, the effect was independent of the CO deposit sublayer. The slope of the straight line drawn through the data of Figure (5.3-9), curve C is 0.25, and its ordinate intercept is -4.03×10^{-6}, quantifying the difference between these data and that of curves A and B. It should be noted here that the data of curve C were taken approximately 4 months after runs 270-273, represented by curve B of Figure (5.3-9).

Thus, over a period of five months, it was found that ozone decomposition on the same cryosurface increased significantly, yielding a linear relationship within any single set of experiments, but with constantly decreasing slope between experimental sets (Figure 5.3-9). Calibration drifts cannot account for this phenomenon. The most likely changes in calibration would occur in either the ozone generator or the chemiluminescence analyzer. In order to determine if this was the case, the 5.6 ppm calibration standard was introduced to the reaction chamber of the chemiluminescence analyzer, and the panel meter read 5.6 ppm, proving that a drift in the analyzer calibration was not at fault. The ozone generator was then recalibrated by the wet titration procedure, described previously, and the calibration curve was found to be reproducible to within 7% of the original calibration. Thus, it is not likely that an experimental calibration shift in the ozone generator was responsible. Therefore, it appears that the

condition of the cryosurface is the most likely factor which could account for the significant change in decomposition behavior. A review of the known literature on this subject follows.

Ozone Decomposition - Literature Survey

The early work of Platz and Hersh (1956) and Jenkins (1959) on producing and purifying pure liquid O_3 are replete with reports of explosions; i.e., rapid decomposition of O_3 to O_2 with the subsequent stoichiometric increase in volume and thermal energy. It was believed at the time that the principal sensitizers for the decomposition reaction were organic contaminants, and that liquid ozone was only stable when the level of sensitizers was restricted to below 20 ppm. Since the decomposition is exothermic, it was believed that a thermal chain occurred, i.e., the energy necessary for neighboring molecules to react. It was also noted that explosions usually occurred during a phase change (usually boiling or vacuum evaporation).

Ardon (1965) noted that liquid O_3 is highly explosive, and is sensitized by small amounts of hydrocarbons as well as species such as H_2. He also reported that some metals, particularly in the Fe and Pt groups, metal oxides, peroxides and hydroxides are active O_3 decomposition catalysts.

Relevant work on this type of experimental system has been performed and reported by Emel'yanova et al. (1964, 1964A). This work deals with the catalytic decomposition of liquid O_3 at cryogenic (77K and 99K) temperatures. It was found that Pt and Pd catalysts were highly active in this regard,

and it was implied that the conversion was nearly complete. Fe_2O_3 and NiO were found to be relatively inert, although they have been reported as active in gas phase decomposition. The authors postulated a mechanism by which the activation energy for the liquid phase reaction was supplied by the exothermic decomposition of neighboring O_3 molecules. It was also found that dilution of O_3 with liquid N_2 or O_2 had no influence on the decomposition rate, which implies that the surface reaction was the rate-determining step.

The catalytic activities of NiO (Houzelot and Villermaux, 1976) and Fe_2O_3 (Neely et al., 1975) towards decomposition of O_3 in the gas phase are well known. In fact, Fe_2O_3 (Neely et al., 1975) is so effective, that a room temperature stream of 2 to 3% O_3 in O_2 was found to decompose to the extent that no ozone was detectable, at a sensitivity of 10^{-8} parts of ozone to oxygen in the exit stream, when the sample was run through a packed bed of Fe_2O_3 mesh. Thus, Fe_2O_3 and NiO were found to be active in the gas phase, but relatively inactive in the bulk liquid phase. This suggests that these two metal oxides may be orientationally hindred from catalysis in the bulk liquid phase by electrical double layer constraints (Marron and Prutton, 1965), an effect which should not prevail in very thin films of cryofrost, the orientation of which is determined by different factors. Thus, catalytic activity of NiO and Fe_2O_3 on the base stainless steel in the cryofrost experiments may be responsible for this behavior. It is entirely possible that the gold flashing on the stainless steel disk was not completely success-

ful in covering the stainless steel surface. This in turn allowed slow oxidation of the surface, from repeated exposure to concentrated oxidants and repeated rapid thermal cycling. Stainless steel is an alloy of Fe, Ni, Cr, and other elements, and thus oxidation of the surface layer would indeed yield Fe_2O_3 and NiO. With the absence of a significant double layer effect, as might occur for liquid O_3, and for very low absolute deposit quantities, catalytic activity of this surface is possible. Thus, it is hypothesized that repeated O_3 deposition and desorption on the gold-flashed surface increased its catalytic activity towards O_3 recombination by increasing the surface concentration of NiO and Fe_2O_3, formed by oxidation of the exposed stainless steel with concentrated O_3, a resultant of phase separation of O_2 from the O_2-O_3 mixture. This hypothesis is supported by the apparent increasing catalytic activity illustrated by the three curves in Figure (5.3-9). In addition, visual inspection of the surface revealed that the gold-flashed cryosurface had lost much of its original luster in areas of high condensate loading.

The question of whether or not the decomposition of O_3 on the surface is initiated by the exothermic reaction of O_3 with some low level contaminant species yet remains. The primary identifiable contaminant species in the current system are H_2O and CO. The oxidation of CO with ozone has been considered as a possible atmospheric reaction, and has, as mentioned previously, been studied by Arin and Warneck (1972). These investigators studied this reaction on a laboratory scale, and found that that the initial mixing of O_3 and CO in the gas phase

at low pressures produced an immediate intense reaction. Strangely enough, however, they found that the reaction proceeded almost to completion and then stopped abruptly, with little additional conversion occurring subsequently. This led the authors to hypothesize that either the products formed, (CO_2 and O_2) were inhibitors of the reaction, or that an impurity in one or more of the feed streams was acting as an initiator. By dilution studies, they were able to prove that the gaseous products were not inhibitors, thereby leaving the second possibility open. In this regard they noted that if an excess of CO was employed and the reaction allowed to exhaust the initial O_3 added, and the excess CO was separated from the reaction products by adsorption on charcoal, the CO thus recovered would not react with ozone significantly. Therefore, the authors claimed that the initiator was a contaminant in the CO feed gas, even though the CO had been carefully prepurified. The possible contaminant remained unidentified.

This sample illustrates that low levels of unidentified contaminants which exist in the background of the vacuum chamber, as a result of introduction in the feed gas or cracking of vacuum pump oil, may indeed initiate ozone decomposition on the cryosurface.

Thus it has been found that the differences in curves A, B, and C of Figure (5.3-9) may be due to oxidation of the exposed portion of the gold-flashed surface to Fe_2O_3 and NiO, which have been shown to be gas phase O_3 decomposition catalysts. This does not exclude the possibility that the reaction is initiated by a volatile impurity in the background or O_3 feed

itself, but it does cast doubts on the effectiveness of CO as the initiator, an effect which has been confirmed experimentally here.

Some conclusions drawn about the behavior of O_3 in the present system include:

1) O_3 is concentrated by the initial desorption of O_2.
2) Low level deposits decompose entirely, once they are concentrated.
3) A fraction of the O_3 deposited survives the desorption process with larger deposits.
4) Repeated cycling of the surface with ozone concentrated in this manner activates the surface catalytically, presumably by oxide formation, towards ozone decomposition.

Thus, both NO and O_3 undergo reaction during the deposition and desorption process, rendering attempts to study the NO-O_3 oxidation reaction employing this technique rather tentative in nature.

Oxidation Reactions

Will N_2O Oxidize?

This section deals with the first group of experiments designed to test whether various species of atmospheric interest can be oxidized during desorption by O_3. The first species tested was N_2O. From the vapor pressure data of Honig and Hook (1960), it was ascertained that N_2O is far less volatile than O_2. Thus, when N_2O is deposited on a surface of O_3-O_2 cryofrost and desorbed, the more volatile O_2 will desorb first, leaving a mixture of O_3 and N_2O on the cryosurface. Thus dilution of

O_3 by O_2 is not at issue, and intimate contacting of N_2O and O_3 results.

The reaction

$$N_2O + O_3 \longrightarrow 2NO + O_2 \qquad (5.3\text{-}9)$$

at 50K in the solid phase, is exothermic with a heat of reaction, ΔH_R of -13 kcal/mol, making it thermodynamically favorable (e.g., see Reid et al., 1977, Dean, 1973 for thermodynamic properties).

The experiments performed in this group employed the technique of flash desorption. In run 260, 1.5×10^{-5} g mol of N_2O were deposited on top of 9.2×10^{-6} g mol of O_3, and then desorbed by sealing the system and allowing it to heat slowly by thermal conduction to 100K. This was done to attempt to increase the reaction time before dilution. Once 100K was attained, the chamber was raised to atmospheric pressure and room temperature by the addition of N_2. This experiment again resulted in no NO_x as measured by chemiluminescence analysis, even though a conversion as low as 0.4% would have been detectable.

Another experiment was performed to test if annealing, *a la* Smith and Guillory (1977), is effective in promoting the as yet unobserved oxidation of N_2O by O_3. Run 268 involved the deposition of 4.8×10^{-5} g mol of N_2O on top of 2.3×10^{-5} g mol of O_3 in a 2.25% mixture with O_2. The resultant cryofrost was annealed to 35K and immediately recooled to 15K and allowed to age for 30 minutes. Subsequent flash desorption and analysis revealed no NO_x production.

In run 273, a variation of this procedure was attempted, in which 1.3×10^{-4} g mol of N_2O was deposited on top of 5.0×10^{-5} g mol of O_3 in a 2.25% O_3 in O_2 mixture. The cryofrost was then

allowed to warm to 35K, and was then recooled to 15K and held at this temperature for 7 hours. After flash desorption and analysis, this procedure again revealed no NO_x production.

Thus it has been shown that N_2O is not oxidized by O_3 in the current system, and that this result is unaffected by annealing.

Will N_2 Oxidize?

This series of experiments was designed to determine if N_2 can be oxidized by O_3 in the system under discussion. An estimate of the thermodynamics of the reaction

$$N_2 + 2O_3 \longrightarrow 2NO + 2O_2 \qquad (5.3\text{-}10)$$

shows that it is exothermic, and at 50K in the solid phase, $\Delta H_R = -31$ kcal/mol (from data taken from Reid et al. (1977) and Dean (1973)).

Harteck and Dondes (1954) have observed the reaction

$$N_2 + O + M \longrightarrow N_2O + M \qquad (5.3\text{-}11)$$

in the gas phase at 295°C upon heating O_3 and N_2 mixtures. The conversion, however, was reported to be very low, and was dominated by the thermal decomposition of O_3.

The experimental approach chosen was TPD, with mass spectrometer analysis focused on mass 30, the NO parent peak and an N_2O and NO_2 fragment peak. In experimental runs 269 to 273, approximately 2.3×10^{-6} g mol of N_2 were deposited, followed by 10^{-6} g mol of O_3 as a 2.25% mixture in O_2. TPD was performed for all four runs, with none yielding any trace of mass 30 above background. Thus, within the sensitivity of this technique, no NO, N_2O, or NO_2 was formed as an oxidation product of N_2.

Will The Freons Oxidize?

As in the previous cases, the oxidation reactions of Freons 11 and 12 are thermodynamically favored. For the Freon 12 reaction

$$CF_2Cl_2 + 2O_3 \longrightarrow F_2 + Cl_2 + CO_2 + 2O_2 \qquad (5.3\text{-}12)$$

ΔH_R = -55 kcal/mol, calculated for the solid phase at 100K (near the desorption temperature) from the data of Reid et al. (1977) and Dean (1973). The equivalent reaction for Freon 11,

$$2CFCl_3 + 4O_3 \longrightarrow F_2 + 3Cl_2 + 4O_2 + 2CO_2 \qquad (5.3\text{-}13)$$

yields ΔH_R = -196 kcal/mol at 100K in the solid phase, again using data from the same references.

Since it was not known whether CO or CO_2 would be the final carbon oxidation product for the Freons, TPD was performed while monitoring mass 28 for the CO parent peak and the CO_2 fragment peak.

In run 277, 2.0×10^{-7} g mol of F12 were deposited on top of 2×10^{-7} g mol of O_3 in a 2.25% mixture with O_2. Since the vapor pressures of F11 and F12 are substantially lower than O_2 (see previous chapter on cryogenic fractionation), O_2 desorption would again yield essentially pure O_3-Freon mixtures on the cryosurface. In run 278, a similar deposit of 6×10^{-7} g mol of F11 and 6×10^{-7} g mol of O_3 in a 2.25% mixture with O_2 was made. Both of these runs resulted in desorption patterns due to CO contamination, but comparisons of these runs to blank runs conducted on the same days indicated no peak enhancement due to oxidation products of the Freons. Thus, attempts at oxidizing the Freons also yielded negative results.

In summary, it has been shown experimentally that:

1) NO disproportionates
2) O_3 decomposes
3) N_2O, N_2, F11, and F12 do not oxidize when exposed to concentrated ozone, within the detectable limits of the experimental apparatus.

It remains to be seen, therefore, whether or not NO reacts with O_3, and if so, if this can be distinguished from the disproportionation and decomposition reactions.

Oxidation of NO?

As was the case for the previous species investigated, the thermodynamics of the NO-O_3 oxidation reaction

$$NO + O_3 \longrightarrow NO_2 + O_2 \qquad (5.3\text{-}14)$$

indicate the reaction to be thermodynamically favorable. An estimate of the heat of reaction at 83K in the solid phase, employing data given by Reid et al. (1977) and Dean (1973), yields a value of -48 kcal/mol.

This reaction has been studied by IR spectroscopy employing matrix isolation techniques by Lucas (1977) and Lucas and Pimentel (1979), and will be discussed in more detail after a description of the current experimentation. Again, it must be noted here that the disproportionation reaction of NO, and O_3 decomposition described earlier have a direct bearing on these experiments.

In run 279, 4.6×10^{-5} g mol of NO were deposited on top of 4.6×10^{-5} g mol of O_3, in a 2.25% mixture of O_3 in O_2. In this case, as in those previous, the data of Honig and Hook (1960) show that the vapor pressure of NO is less than that of

O_2, thereby allowing concentrated O_3-NO mixtures to form upon initial desorption of O_2. The deposit was flash desorbed with N_2 and analyzed with the chemiluminescence analyzer. The resultant NO/NO_x ratio was 0.224, a value lower than those found in the disproportionation series, thereby indicating a higher percentage conversion of NO to NO_2. The lowest NO/NO_x ratio noted previously was 0.41, which was the result of run 253, the matrix isolation experiment of 30.5% NO in CO_2. However, in view of the complications of the ozone decomposition experiments, no hypothesis was made until a blank experiment was conducted.

In run 280, $2x10^{-3}$ g mol of pure O_2 were deposited on the cryosurface without ozonation, followed by $4.5x10^{-5}$ g mol of NO deposited on top, as a blank experiment for run 279. Flash desorption yielded an NO/NO_x ratio of 0.48, which is well within the range of the disproportionation reaction results described earlier. Thus the oxidizing effects of the added ozone seemed genuine.

In order to test this result once again, run 281 was performed as a repetition of run 279. In this experiment, $4.1x10^{-5}$ g mol of O_3 were deposited as a 2.25% mixture of O_3 in O_2, followed by a deposit of $5.1x10^{-5}$ g mol of NO. This deposit was flash desorbed and analyzed, resulting in a NO/NO_x ratio of 0.16, for an even higher conversion of NO to NO_2 than in run 279. Thus, even though masked by the disproportionation reaction and possibly affected by O_3 decomposition, the flash desorption experiments imply that O_3 does in fact oxidize NO. This result is explored in the context of the extant literature below.

Relevant NO Oxidation Literature

A previous section on matrix isolation illustrated that NO in N_2 (Varetti and Pimental, 1971, Guillory and Hunter, 1969) and O_2 (Smith and Guillory, 1977, 1977A) matrices readily aggregate when heated above their characteristic diffusion temperature, T_d. Just as in run 247, in which NO and N_2 were co-deposited on the cryosurface, and the more volatile N_2 desorbed first, leaving pure NO on the cryosurface, by the same token a deposit of NO, O_3, and O_2 deposited on the cryosurface will first desorb the higher volatility O_2, thereby concentrating NO and O_3 on the cryosurface, which should enhance the oxidation reaction.

In the work of Smith and Guillory (1977, 1977A), it was found that NO is oxidized by O_2 in an NO-O_2 matrix if the NO is first allowed to dimerize by annealing it to 35K followed by subsequent recooling. In the solid phase they determined the rate to be first order with respect to the concentration of cis-$(NO)_2$, unlike the gas phase rate, which is given by

$$- dNO/dt = 2\, k_{gas}\, [NO]^2\, [O_2] \qquad (5.3\text{-}15)$$

The rate constant found for the solid phase experiment, defined as

$$k_{solid} = 4.25 \times 10^{-2} \exp(-103/RT),\ s^{-1} \qquad (5.3\text{-}16)$$

was also understandably quite different from the rate constant for the gas phase reaction,

$$k_{gas} = 0.8299T \exp(996/T),\ \ell^2/mol^2 s \qquad (5.3\text{-}17)$$

in the 273 - 662°C temperature range. It is important to note here that the gas phase oxidation rate is slow in the gaseous product phase which results from the flash desorption procedure,

due to dilution with N_2. For example, assuming final NO and O_3 concentrations of 100 ppm and 4,400 ppm, respectively (concentrations possible if disproportionation does not occur), the resultant concentration of reactant species would be approximately 5.6×10^{-6} g mol/l and 2.5×10^{-4} g mol/l, respectively. At 295K, this concentration yields a gas phase reaction rate of

$$- dNO/dt = 1.12 \times 10^{-10}, \text{ mol/l s} \qquad (5.3\text{-}18)$$

assuming the rate constant expression is correct at this temperature. Thus on the experimental time scale of 10 minutes, the gas phase reaction rate would be approximately 1% of the initial NO deposited, as verified by blank experimental run 280, which gave no detectable conversion above that predicted from disproportionation.

Smith and Guillory (1977, 1977A) have also noted that in the solid state, the concept of concentration is somewhat nebulous, as well as the fact that the term activation energy may be better described as a gross temperature dependence of the rate constant. These authors attempted to convert gas phase data to an equivalent expression for the solid phase reaction, and found that their technique, when extrapolated to their experimental temperatures, yielded a pre-exponential factor six orders of magnitude greater than the factor for the solid phase reaction derived from their experimental data. This result was explained in terms of tunneling and orientation constraints, but the principal feature of this result which is relevant to the current work is that the solid phase NO-O_2 oxidation rate is far lower than might be expected from gas phase data.

The literature most relevant to the present work is that of Lucas (1977), Pimentel (1977), and Lucas and Pimentel (1979). The original work of Lucas (1977) consisted of co-depositing NO/N_2 and O_3/N_2 gas mixtures in order to prevent gas phase reaction, producing cryofrosts with final compositions typically in the range of $NO/O_3/N_2$ of 1/30/250. Typical deposits were of order of 0.9 mg mol deposited at 12K, and held at constant temperature. In this work, the growth of the 1617 cm^{-1} IR band was attributed to the increasing NO_2 oxidation product. As the reaction proceeded, the rate slowed with time, although no appreciable change was observed in the reactant concentrations. This fact was interpreted as being due to a loss of $NO-O_3$ reactant pairs in the matrix, which were hypothesized as the reaction intermediates. Employing this hypothesis, the reaction rate data were observed to be first order with respect to the $NO-O_3$ complex concentration. It was also shown that even in matrices with concentrations on the order of $NO/O_3/N_2$ of 1/1/150, with no $NO-O_3$ being formed by diffusion, only 8% of the deposited NO would have O_3 as the nearest neighbor, and if 25% had reacted, the resultant change in the reactant concentration would be barely discernible with their analytical technique. Thus, at even high dilution, measuring reactant losses in their experiment would be highly unlikely. The reaction proved to be neither IR nor background radiation sensitive; thus decomposition of O_3 by a photolytic mechanism is not a substantial contributing mechanism. It was also experimentally verified that the oxidation reaction of NO with O_2, studied by Smith and Guillory (1977), was far slower than the oxidation with ozone,

and only becomes appreciable in the event of high $(NO)_2$ concentration and substantially decomposed O_3 i.e., the O_2 oxidation dominates when little O_3 exists.

Kinetic analysis of the rate constant, treated as first order in $(NO-O_3)$ concentration, yielded a pre-exponential factor of 1.4×10^{-5} s^{-1} at 12K, with an activation energy, E_a, of 106 cal/mol in the solid phase. This is compared to an E_a of 2.3 kcal/mol in the gas phase, and it is noted that the solid phase E_a is quite similar to the E_a for the solid phase $NO-O_2$ oxidation found by Smith and Guillory (1977). In a subsequent work, Lucas and Pimentel (1979) noted that a lack of a substantial isotope effect argued against a tunneling explanation, thereby leading the authors to hypothesize that orientation constraints imposed by the structure of the cryofrost matrix were responsible for the reduced value of the activation energy in the solid phase. This argument is supported by the fact that the E_a value of 106 cal/mol is of the order of magnitude of the energy necessary for orientational rearrangement processes in rare gas matrices. Thus the matrix geometry may be imposing the reaction constraints, i.e., thermal reorientation is necessary in order to proceed by this reaction path. Thus, raising the matrix temperature will accelerate the reorientation process, as well as increase the number of reaction pairs of $NO-O_3$ by limited diffusion, thereby greatly increasing the overall reaction rate. The detailed mechanism for such a reaction, however, is beyond the scope of this work.

It now remains to relate the results of these cited works to that of the present oxidation study. It has been shown

that the O_2 oxidation reaction of Smith and Guillory (1977) should be negligible in the current experiments. This is supported by the result that the O_2 and NO deposited in run 280 did not result in NO_2 production above that predicted for the disproportionation reaction, while experiments 279 and 281, performed with O_3, measurably increased the resultant NO_2 concentration.

The literature has shown that in a matrix maintained at 12K, the reaction of NO-O_3 aggregate pairs was substantial, with reaction limited by the formation of these reactive pairs by diffusion. In the present system, NO is deposited on a 2.25% matrix of O_3 in O_2. As desorption proceeds, the matrix O_2 is lost due to its high volatility, leaving O_3 and NO concentrated on the gold-flashed stainless steel surface. This should result in a high number of reactive pairs, and at elevated temperatures with the cryosurface as a possible catalyst, the oxidation of NO to NO_2 by O_3 could be significant, as born out by the experimental results. Thus the literature supports the experimental finding that NO:O_3:O_2 mixtures deposited and desorbed in such a manner as described here will lead to the oxidation of NO to NO_2.

(a) Effect of initial sorption temperature upon NO disproportionation in Ca-chabazite[56]

T (°C)	Time (h)	NO sorbed (cm^3 at s.t.p.g^{-1})	N_2O recovered (cm^3 at s.t.p.g^{-1})	% reaction of NO
0	1	16·03	3·18	79·3
0	7	14·51	2·91	80·2
0	24	16·35	3·16	77·3
0	25	16·74	3·31	79·1
0	119	14·45	2·91	80·6
0	1	10·35	2 01	77·7
−22·5	1	24·11	5·29	87·8
−63·5	1	24·10	5·70	94·6
−78	1	34·48	8·47	98·3
−78	31	54·98	13·78	100·2

(b) Disproportionation of NO sorbed at 0°C in several zeolites

Zeolite	NO sorbed (cm^3 at s.t.p./g)	N_2O recovered (cm^3 at s.t.p./g)	% reaction of NO
Ca-X	21·45	4·82	89·7
Na-X	22·0	4·08	72·8–83·6[a]
Na-chabazite	15·68	3·52	89·8–92·7[a]
Na-A	16·31	1·07	26·2–42·7[a]

[a] Results of several runs.

Table (5.3-1)

Literature Values Of NO Conversion
Due To Disproportionation
(from Barrer, 1978)

TABLE (5.3-2)

INITIAL OZONE DECOMPOSITION EXPERIMENTS

Date	Run	Deposit (g moles O_3)	Recover (g moles O_3)	Initial Concentration (%)
7/10/80	239	5.05×10^{-6}	0	1.59
8/19/80	262	2.14×10^{-5}	8.49×10^{-6}	2.25
8/20/80	263	1.81×10^{-5}	8.84×10^{-6}	2.25
8/21/80	264	1.24×10^{-5}	4.26×10^{-6}	2.25
8/22/80	265	2.19×10^{-5}	1.05×10^{-5}	2.25
8.26/80	266	7.93×10^{-6}	1.30×10^{-6}	2.25

TABLE (5.3-3)

OZONE DESORPTION EXPERIMENTS

Date	Run	Deposit (g moles O_3)	Recover (g moles O_3)	Initial Concentration (%)
9/11/80	273	5.00×10^{-5}	1.32×10^{-5}	2.25
9/12/80	274	2.29×10^{-5}	6.62×10^{-6}	2.25
9/16/80	275	4.39×10^{-5}	1.58×10^{-5}	2.25
9/17/80	276	3.40×10^{-5}	1.04×10^{-5}	2.25

TABLE (5.3-4)

OZONE DESORPTION EXPERIMENTS

Date	Run	Deposit (g moles O_3)	Recover (g moles O_3)	Initial Concentration (%)
1/14/81	290	2.14×10^{-5}	1.08×10^{-6}	2.25
1/16/81	291	5.76×10^{-5}	1.08×10^{-5}	2.25
1/19/81	292	2.47×10^{-5}	3.42×10^{-6}	2.25
1/23/81	293	3.66×10^{-5}	3.08×10^{-6}	2.25

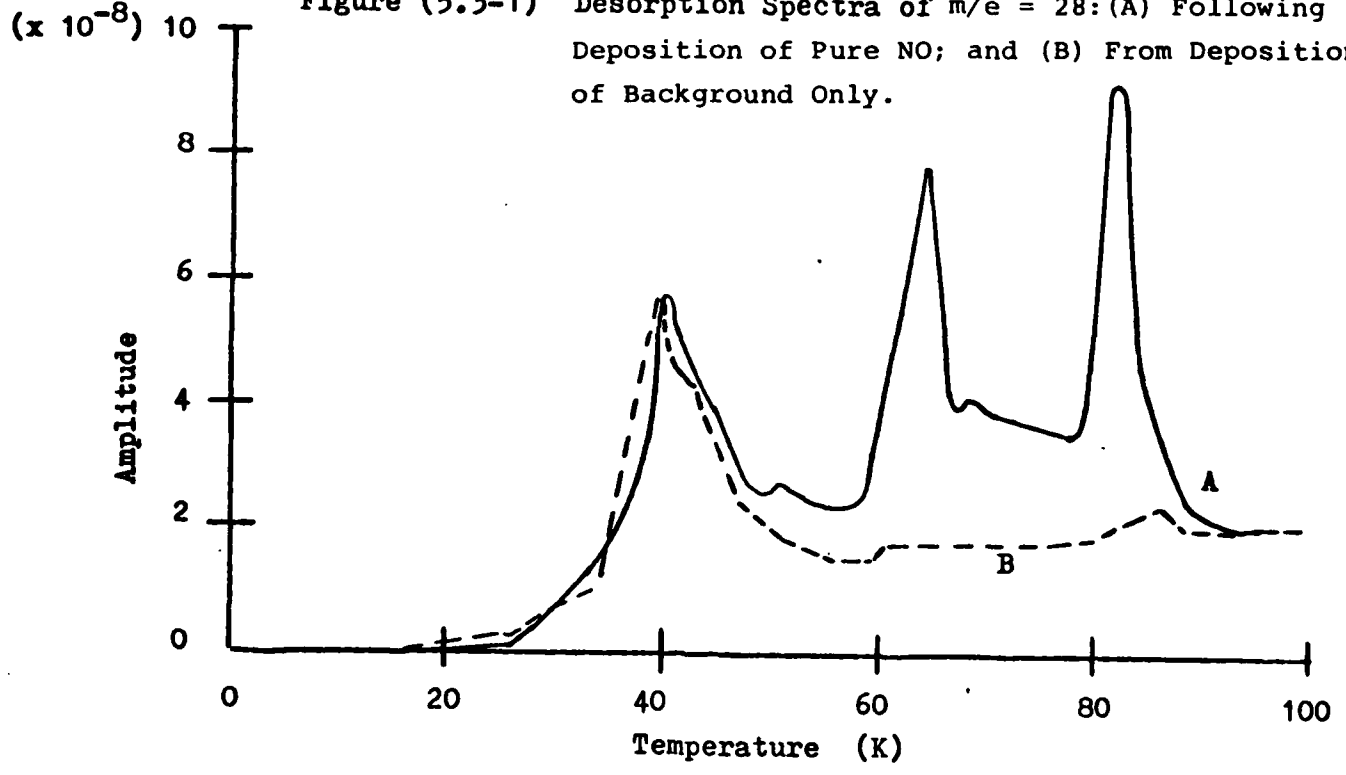

Figure (5.3-1) Desorption Spectra of m/e = 28: (A) Following Deposition of Pure NO; and (B) From Deposition of Background Only.

Figure (5.3-2) Desorption Spectra of m/e = 28: (A) Following Deposition of 5% NO in N_2; and (B) From Deposition of Background Only

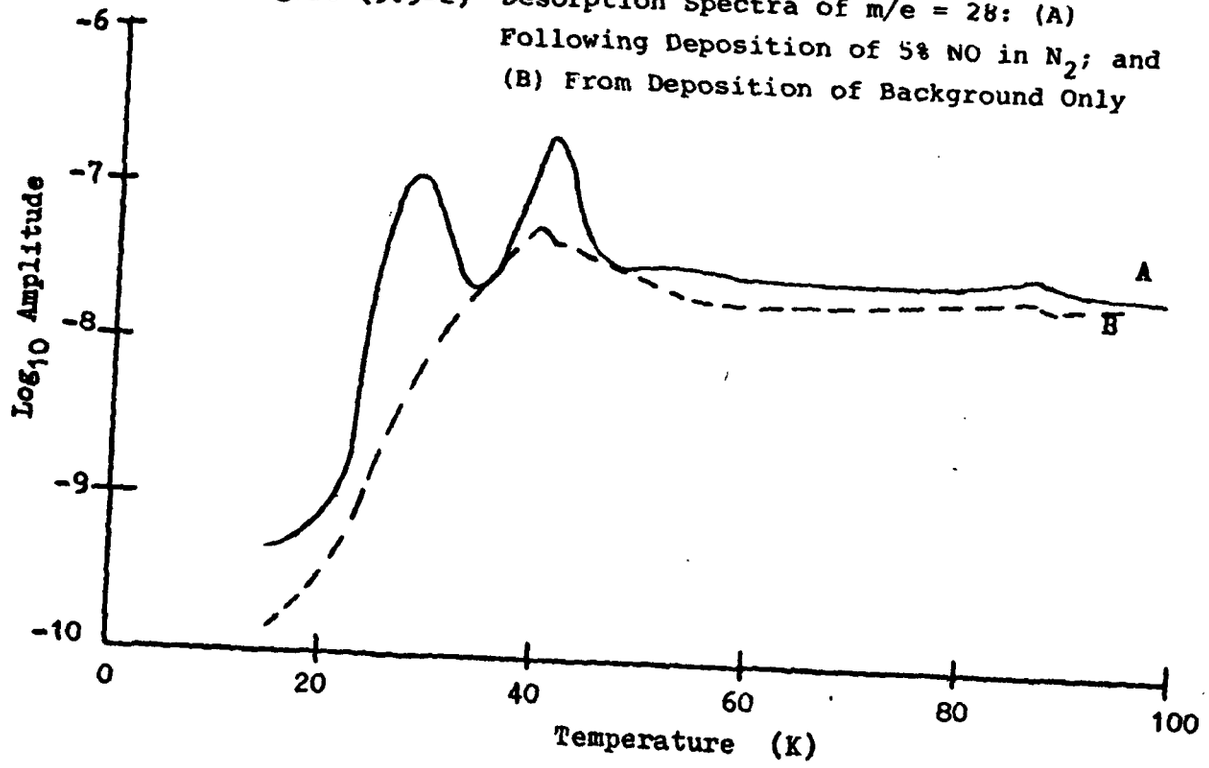

Figure (5.3-3) Spectrum of N_2 Resulting From Disproportionation Compared To NO Desorption Spectrum

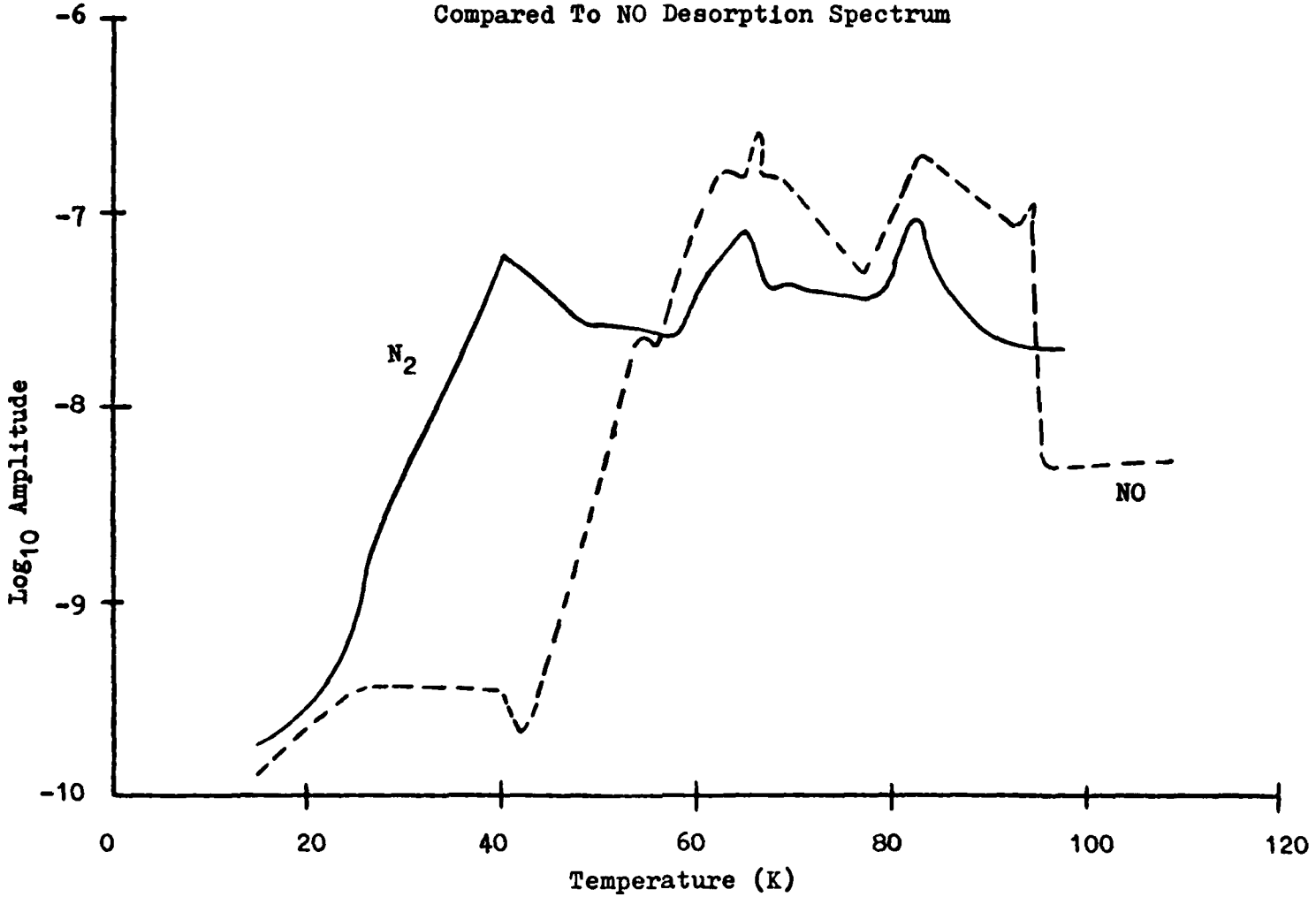

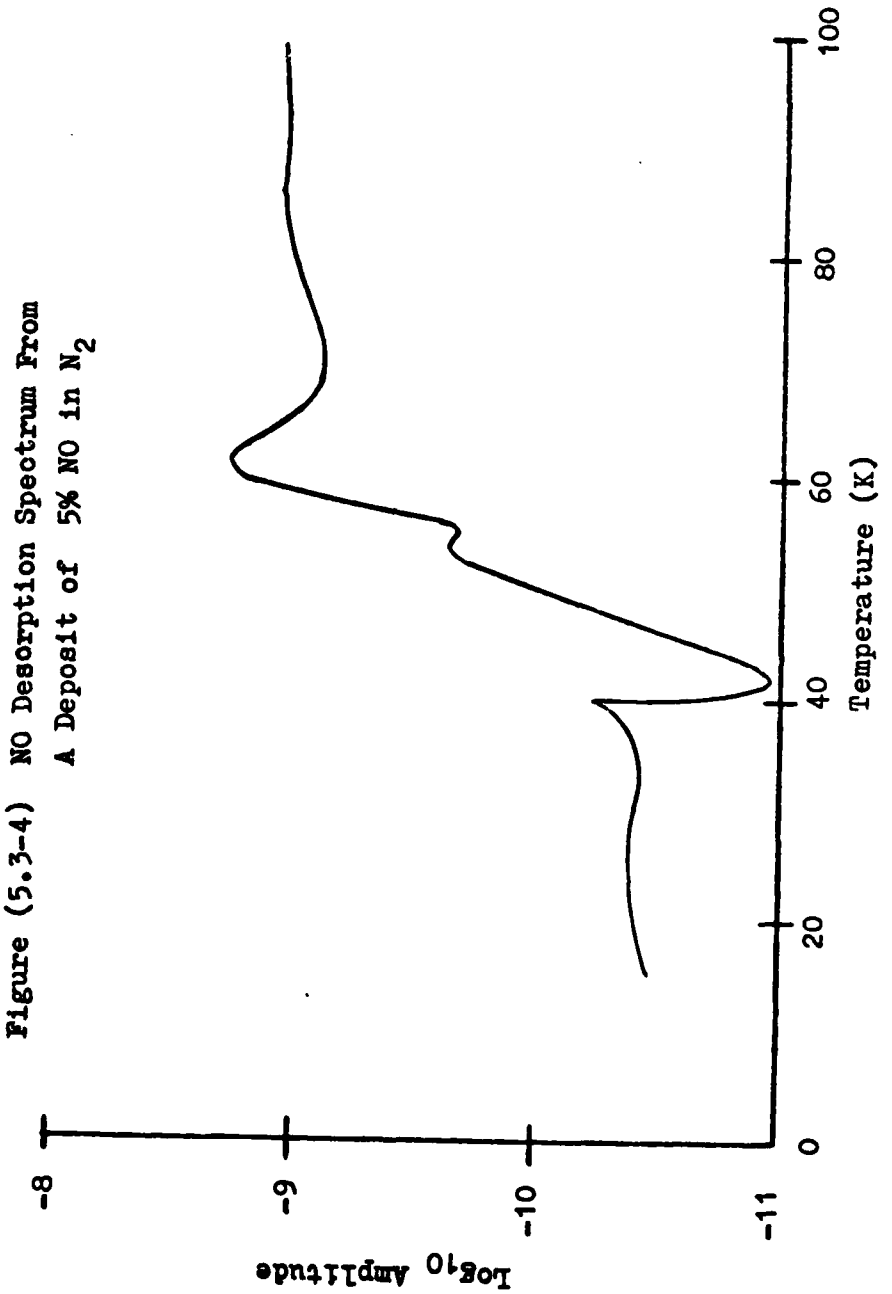

Figure (5.3-4) NO Desorption Spectrum From A Deposit of 5% NO in N_2

Figure (5.3-5) Desorption Spectra of NO In A NO-CO_2 Mixture (A), CO_2 In A NO-CO_2 Mixture (B), And Pure CO_2 (C)

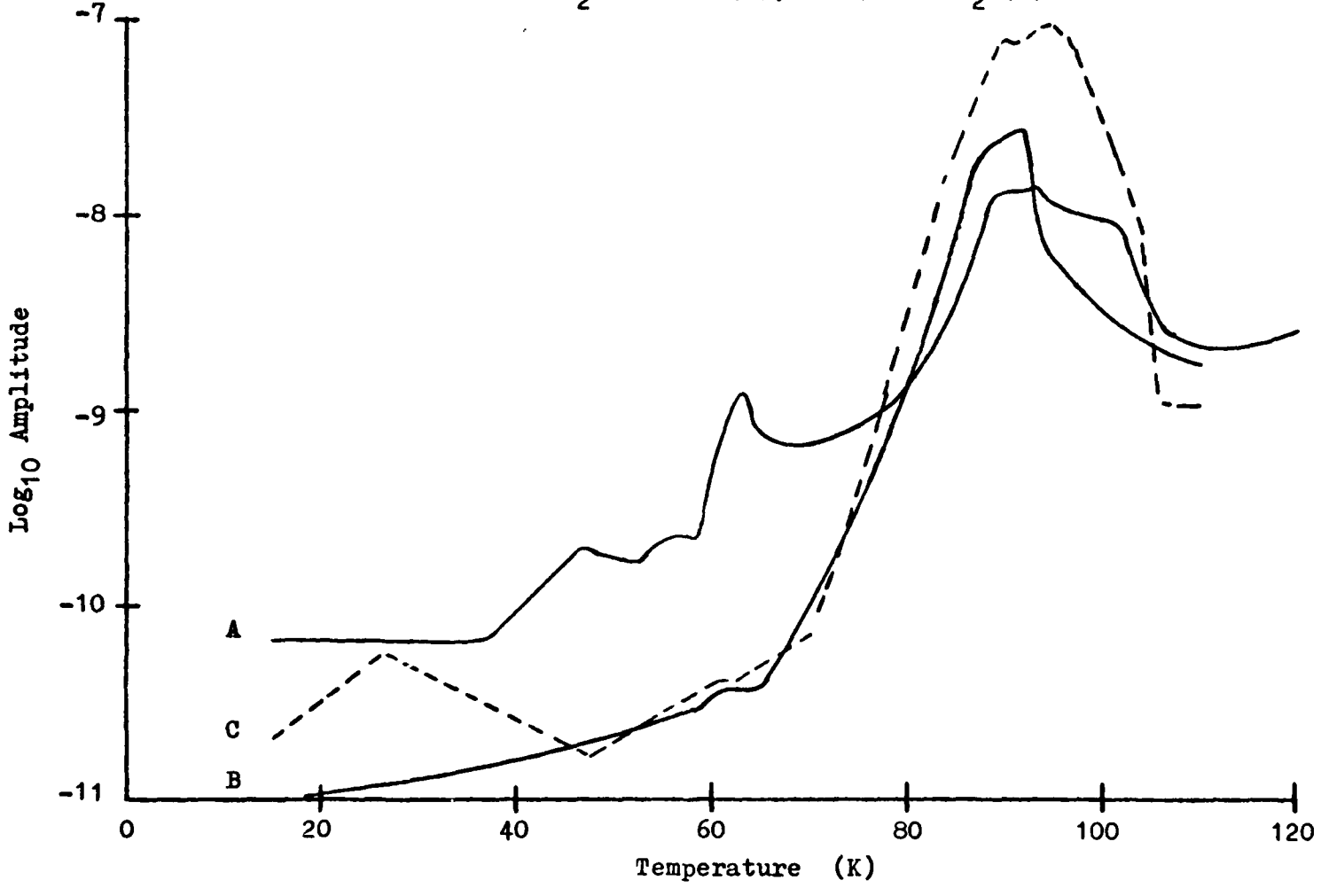

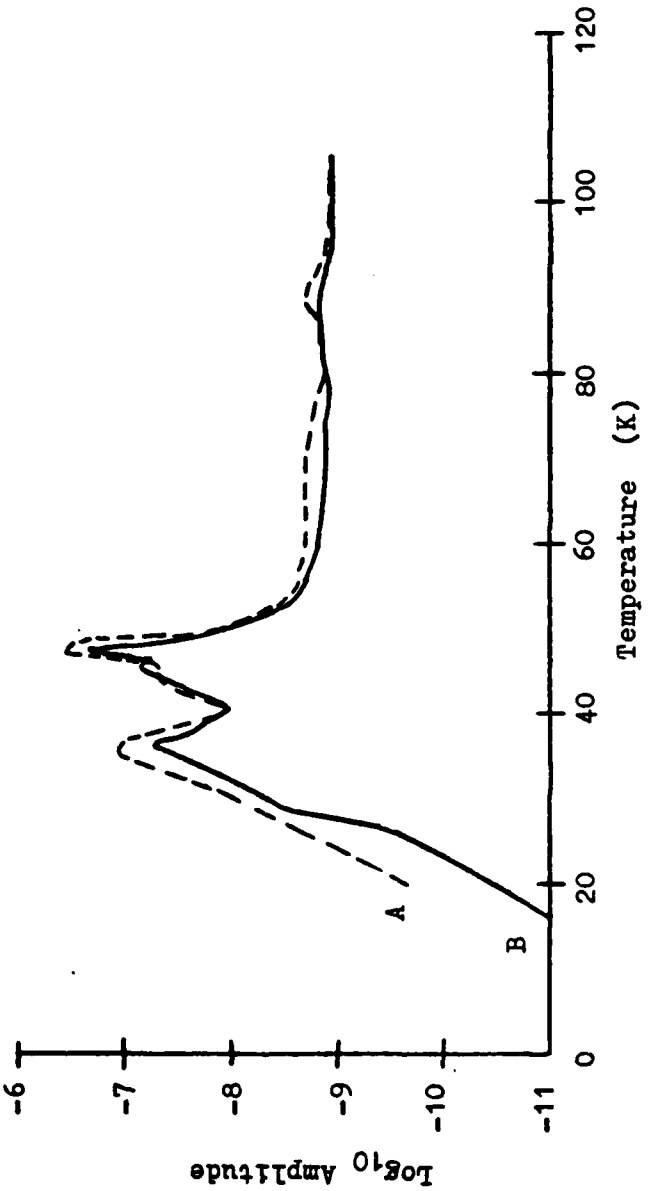

Figure (5.3-6) Peak 32 Desorption Spectra For Pure O_2 (A) And A 1.59% O_3 In O_2 Mixture (B)

Figure (5.3-7) Ozone Regeneration Data

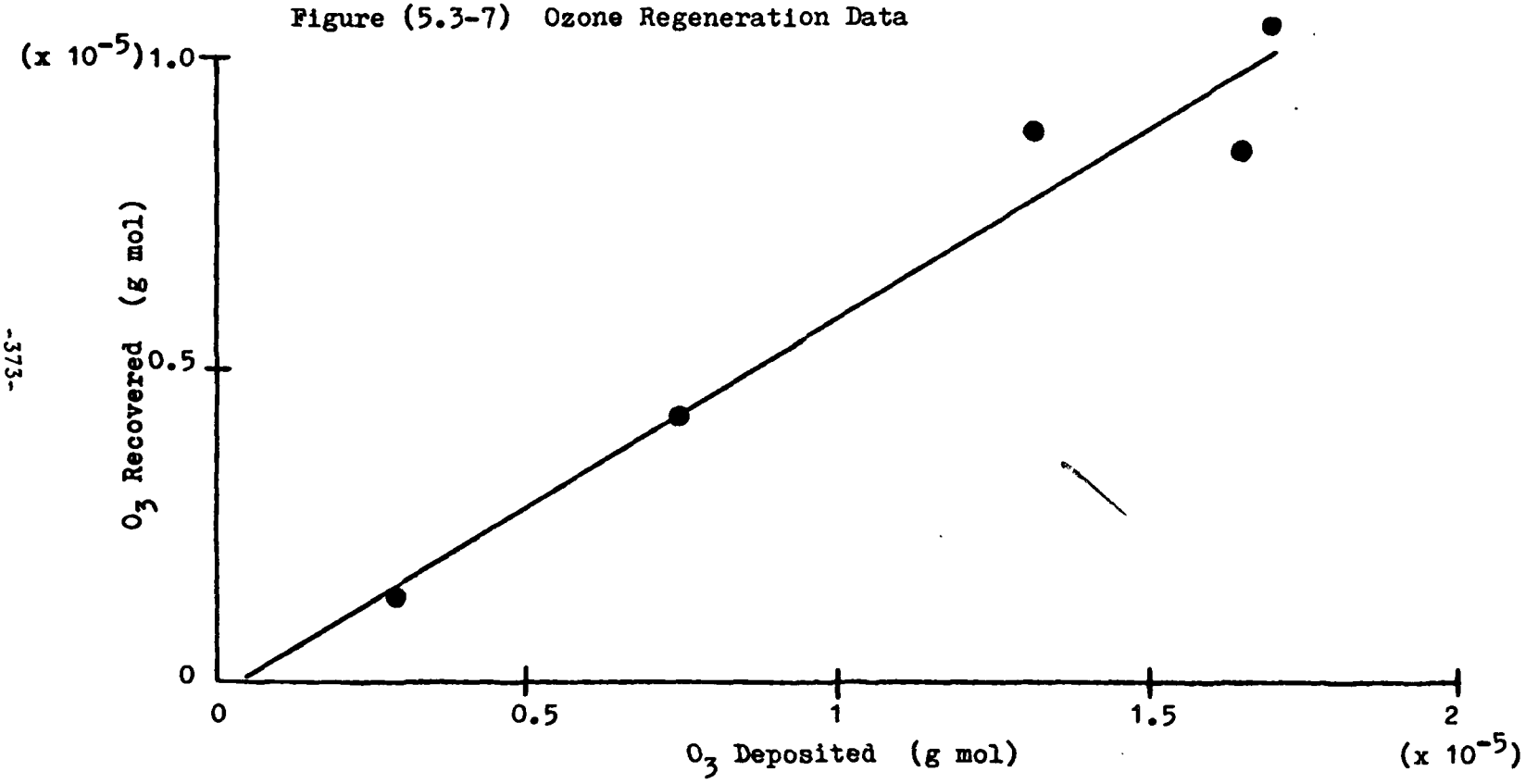

Figure (5.3-8) Ozone Conversion Versus Deposit Quantity

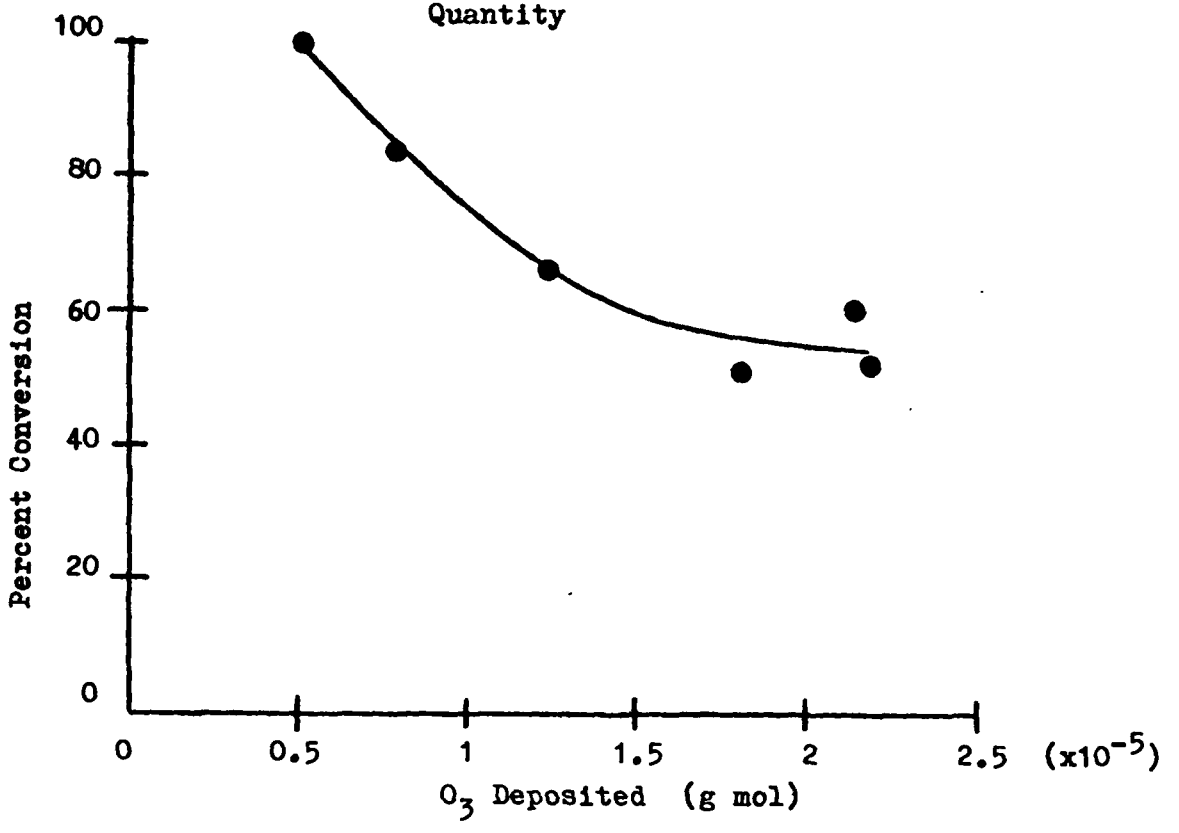

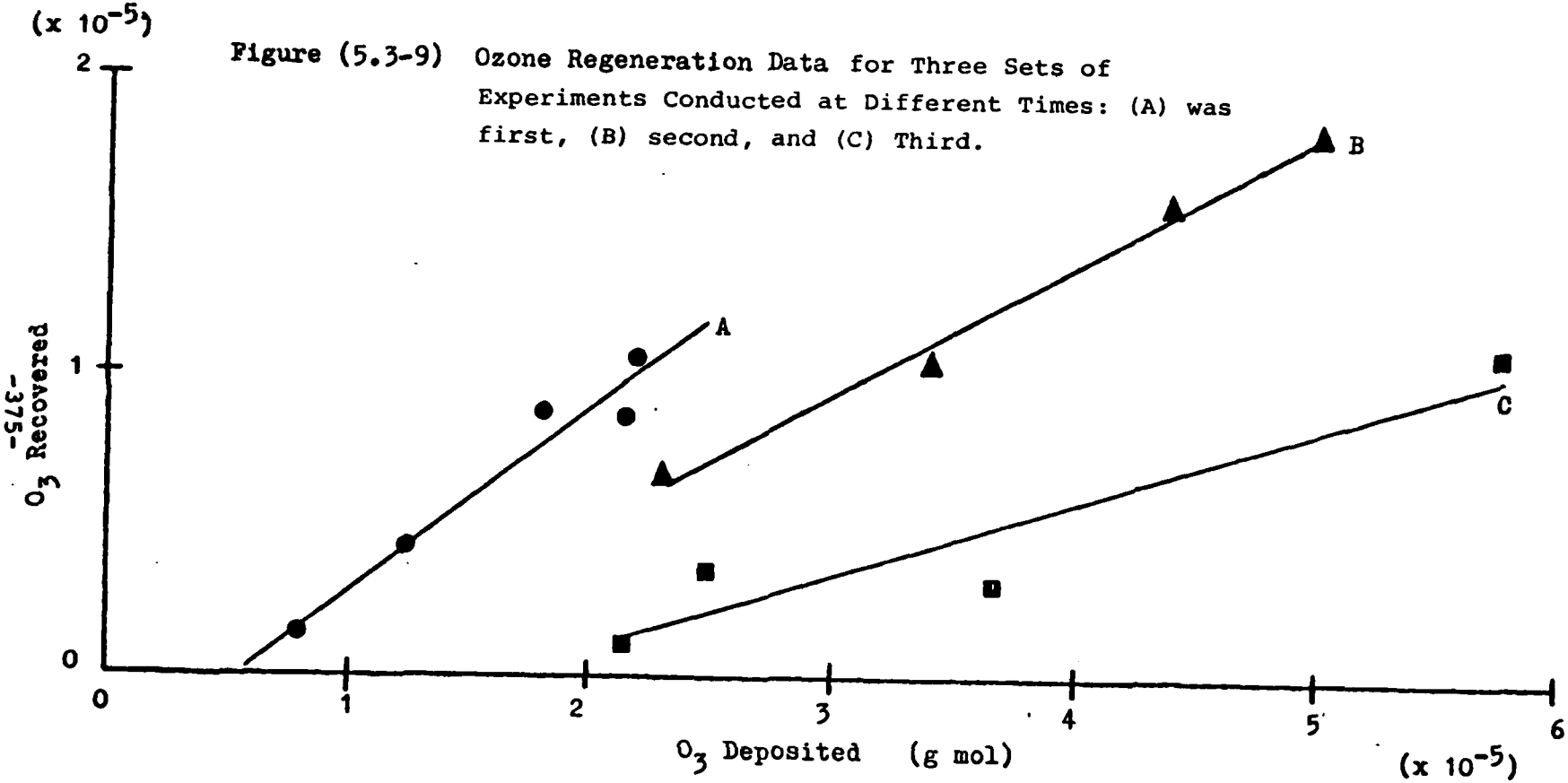

Figure (5.3-9) Ozone Regeneration Data for Three Sets of Experiments Conducted at Different Times: (A) was first, (B) second, and (C) Third.

5.4 SUMMARY AND CONCLUSIONS

In summary, it has been shown that:

A) NO disproportionates; the reaction occurring on the cryosurface just before, or during the desorption process. The primary products of this reaction are NO_2 and N_2.

B) Disproportionation of NO has been reported in the literature on zeolites and charcoal at cryogenic temperatures.

C) Isolation of NO from the gold-flashed, stainless steel cryosurface does not prevent the disproportionation reaction. The reaction is therefore not primarily metal surface-catalyzed, but, as born out by the literature, the structure of the cryofrost itself may be responsible for a self-catalytic process.

D) Dilution of NO in either N_2 or CO_2 does not stop the disproportionation reaction. This result is consistent with the matrix isolation literature when deposition conditions, matrix concentration, and diffusion parameters during heat-up to desorption are considered. The results are also consistent with the experimental observations in the literature concerning dimerization and agglomeration of NO in N_2 and O_2 matrices.

E) Ozone decomposed to O_2 during desorption when the outlined procedure was performed. TPD experiments did not reveal a specific O_3 desorption peak, probably due to O_3 recombination after concentration due to sublimation of the O_2 matrix. Small deposit quantities decompose completely, but O_3 does partially survive desorption when deposited in larger

quantities. The extent of reaction attained may be a factor of both the reaction time and catalytic site availability.

F) Annealing O_3 in an O_2 matrix to 35K does not increase the extent of the decomposition reaction.

G) CO does not act as an initiator for O_3 decomposition, but the stainless steel surface may act as a catalyst, if the gold-flashed layer was not sufficient to completely cover the stainless steel surface. Specifically, Fe and Ni oxidation may have led to an increase in catalytic activity.

H) N_2, N_2O, Freon 11, and Freon 12 are not oxidized by ozone upon desorption within the limits of detection, although the thermodynamics are favorable for all these reactions.

I) NO oxidizes during the desorption process when contacted with O_3. The conversions obtained are significantly greater than those expected from just disproportionation. The literature supports this effect in light of matrix isolation studies which show that the rate of reaction is dependent upon the formation of $NO-O_3$ reaction pairs and their subsequent re-orientation and reaction, processes which should be significantly accelerated at higher temperatures in highly concentrated matrices, like the ones studied here.

The conclusions of the current work which are relevant to cryogenic whole air sampling are obvious. Concentration of reactive species, particularly O_3 and NO during analysis of cryogenic samples by fractionation can lead to several possible reactions when the concentrated sample matrix is desorbed to the

gas phase for analysis. Thus extreme care must be taken in attempting to analyze the resultant gas phase mixtures.

Future work in this field should include, as in the extant literature, surface-specific analytical techniques, such as reflectance or transmittance IR. Such methods will allow quantitative analysis of the possible reactions, as well as define kinetic rates necessary to correct atmospheric sample data. As in the work of Calo (1979), such research would help in unraveling the puzzle of the quantitative behavior of condensed stratospheric gas species on cryogenic surfaces.

REFERENCES: CHAPTER 5

Abe, H., Schultze, W., Chem. Phy. 41, 257-63, 1979.

Addison, W.E., Barrer, R.M., J. Chem. Soc. Lond. 757-69, 1955

Alekseev, V.N., Filimonov, V.N., Terenin, A.N., Dokl. Akad. Nauk. SSSR 147, 1392-5, 1966, Chem. Abs. 58:6341d

Ardon, M., Oxygen-Elementary Forms and Hydrogen Peroxide, W.A. Benjamin, N.Y., 1965, p58-67

Arin, L.M., Warneck, P., J. Phys. Chem. 76, 1514-16, 1972

Barrer, R.M., Addison, W.E., U.S. Patent 2,853,365 Sept. 23, 1958

Barrer, R.N., Zeolites and Clay Minerals as Sorbents and Molecular Sieves, Academic Press, N.Y., 1978, p366-369

Becker, K., Klipping, G., Schoenherr, W.D., Schulze, W., Toelle, V., Proc. ICEC 4 (IPC), 1972, p323-325

Benson, S.W., King, J.W., Science 150, 1710-13, 1965

Bradshaw, D.I., Moyes, R.B., Wells, P.B., J. Chem. Soc. 5, 137-8, 1975

Briner, Pfeiffer, Malet, J. Chim. Phys. 21, 25, 1924

Calo, J.M., Chemical Reactions and Molecular Aggregation In Cryogenic Whole Air Sampling Matrices, Research Proposal submitted to AFGL, Hanscom AFB, Mass., July 1979

Chadwick, A.V., Glyde, H.R., Rare Gas Solids, Vol. 2, Klein, M.L., Venables, J.A., eds, Academic Press, N.Y., 1977, p1152-1252

Chadwick, A.V., Morrison, J.A., Phy. Rev. B 1, 2748, 1970

Cradock, S., Hinchcliffe, A.J., Matrix Isolation, A Technique For The Study of Reactive Inorganic Species, Cambridge Univ. Press, London, 1975

Dean, J.A., ed., Langes Handbook of Chemistry, McGraw-Hill, N.Y., 1973

Deitz, V.R., Bitner, J.L., Carbon 11, 393-401, 1973

Emel'yanova, G.I., Lebedev, V.P., Kobozev, N.I., Chem. Abs. 60:9957e, 1964

Emel'yanova, G.I., Lebedev, V.P., Kobozev, N.I., Zh. Fiz. Khim. 38, 170-5, 1964(A), Chem. Abs. 60:11412b, 1964

Gallagher, C.C., Pieri, R.V., AFGL-TR-76-0161, Air Force Geophy. Lab., Hanscom AFB, Mass., 1976

Gallagher, C.C., Pieri, R.V., Goldan, P.D., J. Atmos. Sci. 34, 1481-2, 1977

Guillory, W.A., Hunter, C.E., J. Chem. Phys. 50, 3516-23, 1969

Hallam, H.E., Scrimshaw, G.F., Vibrational Spectroscopy of Trapped Species, Hallam, H.E., ed., Wiley, N.Y., 1973, p12-66

Harteck, P., Dondes, S., J. Chem. Phys. 22, 758, 1954

Honig, R.E., Hook, H.O., RCA Reviews 21, 360, 1960

Horl, E.M., Suddeth, J.A., J. Appl. Phys. 32, 2521-25, 1961

Houzelot, J.L., Villermaux, J., J. Chem. Phys. Phys-Chem. Biol., 73, 7-8, 1976, Chem. Abs. 86:22313g, 1976

Jenkins, A.C., Ozone Chemistry and Technology, Adv. In Chem. Series, A.C.S., Wash., D.C., 1959, p13-21

Kohin, B.C., J. Chem. Phy. 33, 882, 1960

Lucas, D., Fast Reactions, Free Radicals, and Molecular Complexes Studies By The Matrix Isolation Technique, PhD Thesis, Univ. of Calif., Berkley, 1977, Univ. Micro. 77-31, 448

Lucas, D., Pimentel, G.C., J. Phys. Chem. 83, 2311-16, 1979

Lunsford, J.H., J. Phys. Chem. 74, 1518-1522, 1970

Maron, S.H., Prutton, C.F., Principles of Physical Chemistry, MacMillan, London, 1965, p847-849

Meyer, B., Low Temperature Spectroscopy, American Elsevier, N.Y., 1971

Neely, W.C., West, A.D., Hall, T.D., J. Phy. E 8, 543, 1975

Parker, E.H.C., Glyde, H.R., Smith, B.L., J. Phys. E 2, 691-5, 1969

Pimentel, G.C., Vibrational Spectroscopy-Modern Trends, Barnes, A.J., Orville-Thomas, W.J., eds., Elsevier Scientific, N.Y., 1977, p79-82

Platz, G.M., Hersh, C.K., Ind. and Eng. Chem. 48, 742-44, 1956

Puddephatt, R.J., The Chemistry of Gold, Elsevier Scientific, N.Y., 1978, p254

Redhead, P.A., Hobson, J.P., Kornelsen, E.V., The Physical Basis of the Ultrahigh Vacuum, Chapman and Hall, London, 1968

Reid, R.C., Prausnitz, J.M., Sherwood, T.K., The Properties of Gases and Liquids, McGraw Hill, N.Y., 1977

Smith, G.R., Guillory, W.A., Int. J. Chem. Kinetics 9, 953-68, 1977

Smith, G.R., Guillory, W.A., J. Mol. Spect. 68, 223-35, 1977(A)

Snelson, A., The Chemical Composition of The Atmosphere At 40,000 to 65,000 Feet Using A Modified Matrix Isolation Technique, Project Suggestion IITRI-72-107CX, IIT Res. Inst., Chicago, 1972

Szego, Gaucci, Gazzetta 61, 333, 1931

Varetti, E.L., Pimentel, G.C., J. Chem. Phys. 55, 3813-21, 1971

Venables, J.A., Ball, D.J., Proc. Roy. Soc. Lond. A 322, 331-54, 1971

Venables, J.A., English, C.A., Thin Solid Films 7, 369-89, 1971

Welsbach, Basic Manual of Applications And Laboratory Ozonation Techniques, Welsbach Ozone Systems Corp., Pa., 1977

APPENDIX A - STRATOSPHERIC CHEMISTRY

The previous decade witnessed a growing concern over the effects of atmospheric pollutants on the concentration of ozone in the stratosphere. The possibility of reduction of the ozone column, with its attendant health and environmental implications, has already had a significant impact on several industries. The development of the Boeing supersonic transport, which depended on federal funding, was halted in the early seventies at least partially due to concern over projections of ozone depletion caused by oxides of nitrogen emitted in the exhaust of the aircraft. Additional legislation has sharply curtailed the use of chlorofluoromethanes (Dupont trade name Freons) for use in blow molding of plastic foams and as propellants in aerosol cans, due to their suspected involvement in catalytic ozone destruction. Related atmospheric chemistry research has increased dramatically, and many of the results are controversial. It seems that these phenomena will be under scientific and public scrutiny for quite some time to come.

Much of the controversy derives from the fact that the problem is fraught with technical complexities. Chemical mechanisms and rates of reaction for stratospheric species are not well known. Transport parameters, and the types of models themselves, vary from worker to worker. Atmospheric sinks for various species remain to be clarified, and physical effects, such as the CFM (chlorofluoromethane) greenhouse effect, are often not included in models of ozone depletion. In many instances, concentration profiles of stratospheric species are actually estimates provided by imperfect models, rather than by

physical measurements. When concentration measurements are available, they are subject to error, and even if they are accurate, they represent only point measurements for a particular location at a particular time, which may or may not reflect global or even regional time-averaged values. These complexities challenge man's understanding of the atmosphere, and the environment in general.

The objectives of this section are to briefly examine some of the work which has been done since the emergence of the ozone problem, to clarify current thinking on catalytic ozone destruction, and to point out the possible effects of such losses. This is intended as a basis for understanding the need for cryogenic whole air sampling.

The Stratosphere

The stratosphere is the region of the atmosphere bounded by the tropopause at an altitude of approximately 16 km (in the tropics), and the stratopause at about 50 km (NAS Report, 1976). The tropopause and stratopause are, respectively, local minima and maxima in temperature with altitude, which separate regions of decreasing temperature with altitude above and below the stratosphere, from a region of increasing temperature with altitude in the stratosphere. This stratospheric thermal inversion results in slow vertical transport, since the colder, denser air remains at lower altitudes, and thus provides a stable, almost cloudless region. Circulation occurs primarily by large-scale horizontal motion of air which provides the mixing of all stratospheric constituents.

The chemical composition of the stratosphere consists mostly of nitrogen, oxygen, and water vapor, but also includes a wide variety of minor and trace species, including free radicals formed by absorption of solar radiation. The most notorious of the minor species in ozone, largely due to the fact that it strongly absorbs damaging ultraviolet radiation (DUV), thereby shielding the lower atmosphere.

Perhaps the first model to explain ozone chemistry in the stratosphere was formulated by Chapman (1930), and consisted of a series of five reactions, including:

1) Photodissociation of O_2 by UV light:

$$h\nu + O_2 \rightarrow 2O \quad (\tau < 240nm) \qquad \text{(A-1)}$$

2) Recombination, which occurs below 80 km:

$$O + O_2 + M \longrightarrow O_3 + M, \qquad \text{(A-2)}$$

where M is a third body, usually nitrogen or oxygen.

3) Photodissociation:

$$h\nu + O_3 \longrightarrow O_2 + O \ (\tau=200\text{-}350\text{nm, UV}) \qquad \text{(A-3)}$$

which is a biologically important reaction due to the wavelength adsorbed.

4) Two body recombination below 50km:

$$O + O_3 \longrightarrow 2O_2 \qquad \text{(A-4)}$$

5) Three body recombination at higher altitudes:

$$O + O + M \longrightarrow O_2 + M \qquad \text{(A-5)}$$

This section scheme has proven useful for qualitative predictions, such as the ozone concentration maximum at 25 km, but not quantitative effects, such as concentrations or the total ozone column. It ignores natural diurnal cycles, and atmospheric transport phenomena, as well as the role of trace species other than odd oxygen in atmospheric chemistry. Trace species are particularly important if they become involved in catalytic ozone destruction cycles, which greatly magnify their effect.

There are several natural ozone sinks in the stratosphere (NAS Report, 1976) other than those assumed by Chapman. Almost 10 percent of the natural O_3 sink is provided by hydrogen-containing species such as hydrogen (H), hydroxyl (OH), and hydroperoxyl (HO_2) radicals; i.e.

$$O + HO_2 \longrightarrow HO + O_2 \qquad \text{(A-6)}$$

$$HO + O_3 \longrightarrow HO_2 + O_2 \qquad \text{(A-7)}$$

AD-A108 255 RESEARCH INST FOR GEODETIC SCIENCES FORT BELVOIR VA F/G 20/12
GAS-SURFACE INTERACTIONS IN CRYOGENIC WHOLE AIR SAMPLING,(U)
MAY 81 J M CALO, R J FEZZA, E J DINEEN F19628-77-C-0071
UNCLASSIFIED AFGL-TR-81-0162 NL

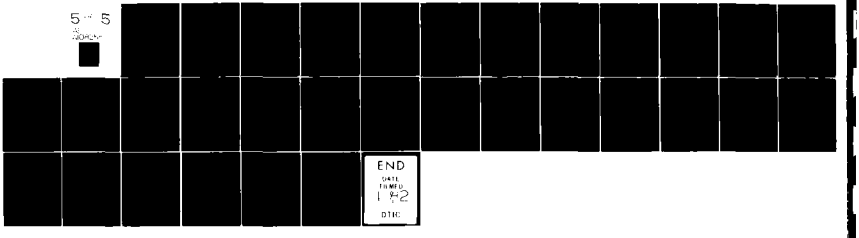

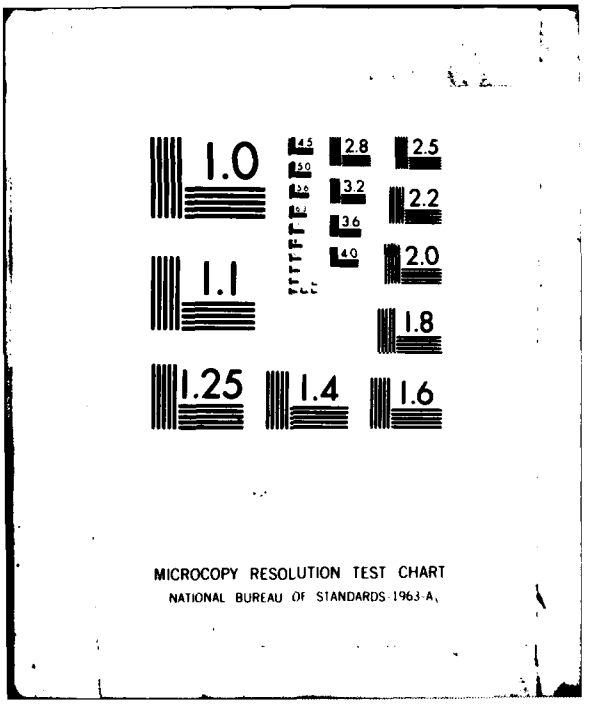
1.0
1.1
1.25
1.4
1.6
1.8
2.0
2.2
2.5
2.8
3.2
3.6
4.0
4.5
5.0
5.6
MICROCOPY RESOLUTION TEST CHART
NATIONAL BUREAU OF STANDARDS-1963-A

which lead to the overall destruction of ozone via

$$O + O_3 \longrightarrow 2O_2 \qquad \text{(A-8)}$$

Another 70% of the natural ozone sink is provided by oxides of nitrogen, as illustrated by Crutzen (1970) for example:

$$O + NO_2 \longrightarrow NO + O_2 \qquad \text{(A-9)}$$

$$NO + O_3 \longrightarrow NO_2 + O_2 \qquad \text{(A-10)}$$

which again results in

$$O + O_3 \longrightarrow O_2 + O_2 \qquad \text{(A-11)}$$

The natural source of NO is from nitrous oxide via

$$O_3 + h\nu(\lambda < 310nm) \longrightarrow O_2 + O(^1D) \qquad \text{(A-12)}$$

$$O(^1D) + N_2O \longrightarrow 2NO \qquad \text{(A-13)}$$

The fundamental removal mechanism for HO and NO_2 is by nitric acid formation via

$$HO + NO_2 + M \longrightarrow HNO_3 + M \qquad \text{(A-14)}$$

There are many other reactions which couple these species together, making the system more complex than presented here. It would appear obvious, however, that the ozone balance could be upset by injection of NO_x into the stratosphere. It is also possible that other trace species, introduced into the stratosphere as pollutants, could cause similar effects.

The Controversy Begins

The concern regarding supersonic transport (SST) aircraft involves the facts that they cruise at stratospheric altitudes, and that the engines produce higher concentrations of oxides of nitrogen (NO_x) than do conventional aircraft. These aspects cause direct injection of significant amounts

of NO_x directly into the stratosphere, circumventing the attendant loss mechanisms provided by the troposphere. One of the first workers to publish on this problem was Johnston (1971) who noted that although water vapor injection by these engines was carefully considered, NO_x pollution was initially deemed unimportant. Johnston's approach involved the formation of a simplified steady state model of the atratosphere which neglected transport effects but included what he considered to be the key reactions. He found that a fleet of 500 SST's with exhaust concentrations of 1000 ppm NO could reduce the ozone column by 77% of its original value. Although the model was admittedly unsophisticated in comparison to subsequent work, it focused attention on the theory that NO_x injection by SST's could cause a serious reduction in the ozone column, a basic trend substantiated in later work.

Johnston's work helped to focus the attention of the Climatic Impact Assessment Program (CIAP), a U.S. Department of Transportation - sponsored research program directed at the possible environmental effects of the SST, onto the NO_x - ozone problem. One aspect of this program involved the improvement of the model predictions.

Atmospheric modeling problems include selecting the important reactions from the thousands possible, deciding on concentration profiles which in many cases have never been measured but have been calculated by other models, inclusion of radiation effects such as scattering, photolysis, and radical formation, and determining eddy diffusivity profiles

and transport phenomena. A one-dimensional model assumes the general form

$$(1/n)\ (\partial C_i/\partial t) = S - L + T/n \qquad \text{(A-15)}$$

where $T = -\text{div}\ (C_i\ V)$

$$T = \partial/\partial z\ (n\ K(z)\ (\partial C_i/n)/\partial z) \qquad \text{(A-16)}$$

where

- n = mean number density
- C_i = species i concentration
- S = sources of species i
- L = loss mechanisms for species i
- K = eddy diffusivity
- z = altitude

Two and three-dimensional models were also used under CIAP sponsorship. Since the chlorine radical - ozone loss mechanism was not yet recognized, it was not generally included in CIAP modeling efforts.

The results of the various CIAP-sponsored modeling efforts (Hoffert et al. 1975; Grobecker et al. 1974) predicted similar trends. A log-log plot of reduced ozone (percent) versus global NO_x emissions yielded a smooth curve which predicted a 0.6% reduction in O_3 at a 0.1×10^9 kg/yr. global NO_x injection rate, and a 40% reduction at a 1×10^{10} kg/yr. injection rate. On the basis of 100 aircraft, the Concord/TU144, burning 4×10^8 kg/yr. of fuel with a NO_x emissions index (g NO_x/kg fuel) of 18 would cause a 0.39% O_3 reduction, per 100 aircraft, while the advanced Boeing SST, burning 3×10^8 kg/yr. of fuel with an equal emissions index

would cause a reduction of 1.74% O_3. It was this type of result that prompted the legislative committees of the congress to refuse further federal funding for SST development.

Enter the Chlorofluoromethanes

In 1974, Stolarski and Cicerone (1974) published a catalytic ozone sink mechanism employing the chlorine free radicals Cl and ClO; viz.

$$Cl + O_3 \longrightarrow ClO + O_2 \qquad \text{(A-17)}$$

$$ClO + O \longrightarrow Cl + O_2 \qquad \text{(A-18)}$$

Thus, as for NO_x, the overall effect leads to ozone destruction by ClO_x via

$$O_3 + O \longrightarrow 2O_2 \qquad \text{(A-19)}$$

at a rate apparently five times faster than for the NO_x scheme. These workers concluded that there were few natural sources of chlorine-containing compounds in the stratosphere other than volcanic emissions and sea salt spray. Their concern centered on the space shuttle, the engines of which are fueled by ammonium perchlorate and aluminum powder, which emit exhaust with chlorine-containing compounds. The space shuttle, however, eventually proved to be a relatively minor source of these pollutants.

A subsequent study conducted by Molina and Rowland (1974), concerning the eventual fate of chlorofluoromethane (CFM's) in the atmosphere, was the first to point out the potential threat of this major source of atmospheric chlorine. They reported that the only major sink for CFM's released at ground level was photodissociation in the stratosphere, at

solar radiation wavelengths in the far ultraviolet (175-200nm); viz.,

$$h\nu + CFCl_3 \longrightarrow CFCl_2 + Cl \qquad \text{(A-20)}$$

$$h\nu + CF_2Cl_2 \longrightarrow CF_2Cl + Cl \qquad \text{(A-21)}$$

Since CFM's were believed to be inert to all other possible loss mechanisms, they would remain in the atmosphere until dissociated, thereby providing a source of chlorine free radicals to fuel the catalytic loss mechanism. A time-dependent, one dimensional vertical diffusion model with eddy diffusion coefficients of $3x10^3$ to $1x10^4$ cm^2/s was employed, which resulted in a prediction of 40-150 years for the atmospheric lifetime of CFM's. It also predicted that at constant injection rates, the stratospheric concentration of CFM's would eventually accumulate to 10-30 times the 1973 value at steady state, with the maximum in chlorine free radical concentration at 25 to 35km, which is the altitude of the region of highest ozone concentration. Thus a major source of chlorine free radicals was discovered, triggering a sizable scientific effort to understand this newly perceived threat to the ozone layer.

Reporting on the results of a model employing this chlorine source, Wofsy, McElroy, and Sze (1975) found that when they allowed for a 10 percent growth of the CFM industry per year, that there could be a 2% ozone reduction by 1980, and a 20% reduction by the year 2000. Of particular concern, however, was the fact that the time constants involved were quite large. Depending on the scenario employed, the major reduction in the ozone column would appear from 10 to 50

years after the termination of CFM release, and the effects could last for centuries. This result underscored the need for early decisions, since the major negative effects of CFM release would be felt only after a considerable time delay.

A National Academy of Sciences panel (1976) commissioned to review the work done on the O_3-CFM loss mechanism, reported that at steady state, 7.5% of the ozone column would be depleted with a 2-20% range for a 95% confidence interval, if CFM release rates remained constant at their 1973 levels. This estimate was based on a survey of the current work and on model predictions made by individual members, which included the chlorine nitrate reaction (see below). The report also noted that while concentrations of most major reactants, such as NO and NO_2 had been measured, and were within 50% of model predictions, concentrations of other species such as HO_2 and Cl were only model estimates, which could lead to considerable inaccuracies. Passing mention was also made to possible problems arising from nitrous oxide produced by the decomposition of nitrate fertilizers in the soil (see below).

The question then arose as to whether or not Molina and Rowland had overlooked major tropospheric sinks for CFM's in their original work. Some possible sinks, such as dissolution into the oceans or polar ice masses, photolytic reactions in the troposphere, or heterogeneous catalytic reduction on atmospheric particulates were discussed. In examining this facet of the problem, Rowland and Molina (1976)

considered the total calculated release of CFM's from anthropogenic sources and compared it to observed CFM concentrations. They found that the actual concentration exceeded the calculated concentration by 20%, when only a stratospheric sink was used in the model. Only by stretching the manufacturers estimated release rates to their upper limits, and the concentration measurements to their lower limits were they able to justify a tropospheric sink which had a rate of the order of magnitude of the suspected stratospheric sink. Thus a large tropospheric sink, which would greatly reduce the impact of CFM's on the ozone column, was thought to be incompatible with observed concentrations.

But there were disagreements. Sze and Wu (1976) noted that temporal and spatial distributions of CFM concentrations in the atmosphere are not well understood, and that assumed concentrations had to be adjusted for such distributions. Their calculations showed that the data at the time did not rule out a 10 year tropospheric lifetime, which would mean that the amount of CFM's in the stratosphere would only double the 1975 concentration at steady state at constant 1975 production rates.

A series of papers from DuPont's Central Research Laboratories supported the theory of a tropospheric sink. These workers began by making their own estimates of the total CFM release from the 1930's to the present (McCarthy et al. 1977) and found their number to be about 45% above that of Rowland and Molina (1976). They also disagreed with Rowland

and Molina's method of conversion of concentration data to a global mean (Jesson et al. 1977), and found that the most probably tropospheric lifetime for CFM's was approximately 15 to 20 years, assuming a Hunten eddy diffusion profile. When different eddy diffusion profiles were examined (Meakin et al. 1978), the degree of uncertainty in the calculation became even more apparent. The most probable tropospheric lifetime was calculated to be 25 years, but the limits of certainty ranged from a 10 year lifetime to infinity. A 25 year tropospheric lifetime would reduce O_3 depletion by Freon 11 by a factor of 1.7 to 4.5, and reduce ozone depletion by Freon 12 by a factor of 3 to 6.5 (Glasgow et al. 1978). It was also noted that their model predicted a ClO_x concentration of 1.5 ppb, while the actual, recently measured value was in the range of 1.2 to 5.5 ppb. This led them to speculate about other anthropogenic sources of stratospheric chlorine compounds, and points out the difficulty, and inaccuracy of such efforts. It is evident that there is still a great deal of disagreement about the existence and extent of a tropospheric sink.

The role of chlorine nitrate (Rowland et al. 1976 (b); 1976 (c)) chemistry was also re-examined with an eye towards judging its effects on stratospheric ozone concentrations. This compound couples the two ozone destruction cycles together via the reaction,

$$ClO + NO_2 + M \rightarrow ClONO_2 + M \qquad \text{(A-22)}$$

Rowland found the product to be stable in the laboratory at

room temperature, thereby providing a stable sink for the two contaminants. Chlorine nitrate is dissociated by solar radiation of wavelengths longer than 460nm, and thus the ClO concentration is assumed to go to zero after sunset and to be regenerated during the day. The N.A.S. study (1976) found the projected reduction in the ozone column was reduced by a factor of 1.85 when chlorine nitrate chemistry was included in the modeling effort. Thus interaction between the two catalytic cycles becomes quite important.

The Return of NO_x

During the mid-seventies, Johnston (1977) again emphasized ozone loss due to the NO_x catalytic cycle, with the primary source now being nitrogen fertilizer denitrification. Nitrogen fertilizers in the soil, under correct pH conditions, interact with water, bacteria, and the local oxygen concentration to form nitrous oxide (N_2O) as well as other products; i.e.,

$$NO_3 + \ldots \longrightarrow N_2O \qquad \text{(A-23)}$$

The fraction of fertilizer which forms nitrous oxide as its product is designated by α, where α can range from 0.025 to .4. In the stratosphere, the reaction

$$O + N_2O \longrightarrow 2NO \qquad \text{(A-24)}$$

can form nitric oxide which can then participate in the well-known ozone loss mechanism. If nitric oxide has an atmospheric lifetime, τ, from 5 to 160 years, and β is the fraction of the total fertilizer production which is actually denitrified, Johnston showed that a simplified model yields

$$-\Delta O_3/O_3 = 1/5(\Delta N_f/1300)(\alpha\beta\tau) \qquad \text{(A-25)}$$

which predicts reductions in ozone concentration similar to much more complex models. In this simplified model, the CIAP NO_x-ozone loss kinetics were employed, and ΔN_f was the nitrate fertilizer production rate in Mtons/yr. In comparing this analysis to that of other workers, Johnston found agreement, insofar as that for the upper limit of atmospheric lifetime (τ=130 years), ozone reduction at steady state would range between 14 and 16%, whereas if τ = 10 years, a 1.5-10% ozone reduction could be expected if α lies in the range of 0.07 to 0.5. If more likely values of τ and α are chosen to be 20 years and 0.26, respectively, the ozone reduction is calculated to be 1.8 to 10% when β is varied from 0.1 to 0.6. These predicted O_3 depletion values agree with the results of other workers, and help to define what might be another area of growing concern. The solution to such a problem, however, would have far reaching implications concerning agricultural production.

In a more recent paper, Turco, Whitten, Poppoff, and Capone (1978) claim that NO_x pollution will actually increase atmospheric ozone. They point to recently published evidence that the rate coefficient for the reaction

$$HO_2 + O_3 \longrightarrow OH + 2O_2 \qquad \text{(A-26)}$$

is actually four to six times larger than assumed in previous models. Thus the natural HO_x-ozone destruction cycle

$$HO_2 + O_3 \longrightarrow OH + 2O_2 \qquad \text{(A-27)}$$

$$OH + O_3 \longrightarrow HO_2 + O_2 \qquad \text{(A-28)}$$

becomes the dominant loss mechanism below 25km and above 40km, while the NO_x cycle is dominant between these altitudes. This fact again makes water vapor injection by SST's a significant factor, since water is the principle source of HO_x radicals. If this is combined with the result that the rate of reaction for

$$HO_2 + NO \longrightarrow OH + NO_2 \qquad \text{(A-29)}$$

is approximately forty times faster than previously assumed, it is found that NO_x inhibits HO_x catalytic destruction of ozone, which is presently believed to be the major natural loss mechanism. Therefore, direct NO_x injection by SST's could actually increase the amount of ozone in the stratosphere. The authors note, however, that water vapor injection by SST's would reverse this effect by increasing the concentration of HO_x radicals, and that H_2O concentration in the exhaust is fixed by combustion reaction stoichiometry, and therefore are impossible to lower. Thus if SST's could inject 1.4×10^9 kg NO_x/yr. with no H_2O, there would be an ozone increase of 4.2%, while if water vapor effects were included in the model, the increase would be only be 0.3%. Another prediction is that a 50% increase in N_2O concentration in the atmosphere due to nitrogen fertilizer would lead to a 2.7% increase in total ozone, although above 30km, there would be a 5% net decrease. These predictions are also strongly dependent on Cl-ClO radical concentrations due to coupled reaction mechanisms, with the increase in ozone due to NO_x and the decrease due to H_2O both accelerated by

increases in Cl-ClO radical concentrations. This illustrates how volatile the field truly is, insofar as that a change in a predicted reaction rate can completely reverse earlier conclusions regarding NO_x injection.

Many other effects can influence ozone concentrations. Freons 11 and 12 have strong infrared absorption bands (Ramanathan, 1975; Reck et al. 1978) in the region of 8 to 13 μm, wavelengths at which the atmosphere is relatively transparent, and the sensitivity to absorbing pollutants is strongest. CFM's absorb IR from the surface and re-emit it at lower atmospheric temperatures, thus effectively trapping energy in the atmosphere and causing a heating effect at the surface and in the atmosphere. Calculations show that a 5 ppb tropospheric mixing ratio of Freon 12 could increase the earth's average surface temperature by 1K, which could have an important climatic effect on variables such as rain and ice cover. Heating of the stratosphere will result in an increase in the rate of the O_3 loss mechanisms, while the reaction

$$O + O_2 + M \longrightarrow O_3 + M \qquad \text{(A-30)}$$

the major source of O_3, decreases in rate with increasing temperature.

The opposite effect occurs when CO_2 is introduced into the stratosphere (Groves et al., 1978). In the upper stratosphere CO_2 emits more IR than it absorbs, therefore creating a cooling effect. This tends to increase O_3 production and reduce the rate cf loss mechanisms, thereby increasing the concentration of the ozone column. A feedback

mechanism is involved, in that as the concentration of O_3 increases, it absorbs more DUV, which heats the stratosphere.

These more recent reports, along with numerous others, were considered by a second N.A.S. panel, which reported updated findings in 1979 (NAS Report, 1979). The best estimate of the steady state ozone column reduction due to CFM release, more than doubled the 1976 prediciton, to a value of 16.5%, with a 95% probability that the true value lies between 5 and 28%, a factor of six. It was reported that the ozone column reduction is expected to reach half its steady state value in 30 years, that a 2.1% reduction has already occurred, and that it is not accurately measurable due to natural concentration fluctuations. Furthermore, it was noted that high reliance cannot be placed on steady state values of high ozone column reduction, since such large changes would alter the dynamics and temperature structure of the stratosphere, thereby invalidating most model predictions. Calculations show that if all CFM releases were to be immediately terminated, there would still be a 5% reduction in the ozone column in 15 years, followed by a gradual recovery. It was also reported that any possible ozone column reduction due to increased amounts of NO_x in the stratosphere was at present too small for serious concern. Thus the outlook has worsened with regards to the CFM release problem.

This summary is intended to communicate a feeling for the complexity of the atmosphere, and how this hampers

accurate predictions. Many effects compete in influencing ozone concentrations, and inaccurate and incomplete knowledge of rates, mechanisms, transport effects, sinks and radiative effects make predictions difficult at best, and meaningless at worst. It seems obvious that no single model can be fully accepted unless it is supported by accurate measurements of ambient stratospheric concentrations, which is the impetus for the main body of this thesis.

Effects of Reduced Ozone

Most biological effects of reduced ozone result from the fact that ozone absorbs damaging ultraviolet radiation, which is in the beta wavelength range from 290-320nm.

There are many possible human and nonhuman biological effects that can arise upon increased exposure to DUV. DNA is affected by short wavelength radiation (NAS Report, 1979), and repair mechanisms for such damage can become overloaded if the dosage is too high. Plant hormones also exhibit sensitivity to this wavelength band, and could affect total growth and development of agricultural staples. It is believed that life evolved in the sea, where absorption of DUV by water provided a protective cover, and that living organisms emerged onto land only when the ozone shield developed sufficiently to protect them from lethal doses. This is supported by the fact that many sea creatures, in their natural habitat exist near their DUV tolerance level (e.g., anchovies, crabs, shrimp) and that an increased dosage would either force them to change their habitat (i.e. live in deeper waters)or be destroyed. This has serious

implications in that the food chain on earth could be altered in ways too complex to predict. When the multiplicative effect associated with ozone loss and increases in DUV dosage (i.e., a 7.5% ozone decrease will increase the DUV flux by 19%) is taken into account, and that natural ozone concentrations vary approximately 5% seasonally, it becomes evident that not only can nonhuman biological effects become important, but that they will be at least partially masked by natural variations which render long term trends more difficult to identify.

Recent evidence has shown (NAS Report, 1979) that increased dosages of DUV are a contributing cause in the occurrence of non-melonoma skin cancer in humans, with suspected contributions to melonoma (malignant) skin cancer. This conclusion is supported by the following facts:

A) There are higher incidences of this disease in latitudes which receive higher DUV exposure;

B) There are statistically more occurrences on parts of the body heavily exposed to sunlight;

C) The rate of incidence correlates well with the amount and type of exposure as a result of different occupations;

D) There is experimental evidence that increased DUV exposure increases the risk of skin cancer in laboratory animals.

Since the change in DUV flux with change in ozone concentration has a slope of approximately -2, and the rate of skin cancer increases by a factor of 2 relative to the percent increase in DUV, the overall amplification factor,

which describes the slope of the skin cancer incidence versus percent change in ozone concentration is -4, not -2 as previously reported. Thus each 1% reduction in the ozone column will cause a 4% increase in skin cancer incidences, if they are truly DUV-related. This points out the very immediate dangers that this problem can introduce.

DNA damage due to DUV also applies to humans, and could affect life in its embryonic stages. Eye damage due to increased DUV flux is also possible.

In summary, a brief review of some of the problems and potential effects of ozone column chemistry are presented. In view of this situation, amongst other requisite research needs, a well understood stratospheric composition sampling technique is clearly an invaluable tool. It is to the understanding of one such technique that this thesis is directed.

REFERENCES

Chapman S., Mem. Roy. Meteor. Soc., 103-125, 1930.

Crutzen P.J., Quart. J. Roy. Meteor. Soc. 96, 320-325, 1970.

Glasgow L.C., Gumerman P.S., Meakin P., Jesson J.P., Atmos. Env. 12, 2159-2172, 1978.

Grobecker A.J., Coroniti, S.C., Cannon R.H., Doc. No. DOT-TST-75-50 Nat. Tech. Info. Serv., Springfield VA, 1974.

Groves K.S., Mattingly S.R., Tuck A.F., Nature 273, 711-715, 1978

Halocarbons: Effects On Stratospheric Ozone, National Academy of Sciences, Washington D.C., 1976.

Hoffert M.I., Stewart R.W., Astro. and Aero. 42-55, Oct. 1975.

Jesson J.P., Meakin P., Glasgow L.C., Atmos. Env. 11, 499-508, 1977.

Johnston H.S., Science 173, 517-522, 1971.

Johnston H.S., J. Geophy. Res. 82, 1767-1772, 1977.

McCarthy R.L., Bower F.A., Jesson J.P., Atmos. Env. 11, 491-497, 1977.

Meakin P., Gumerman P.S., Glasgow L.C., Jesson J.P., Atmos. Env. 12, 1271-1285, 1978.

Molina M.J., Rowland F.S., Nature 249, 810-812, 1974.

Protection Against Depletion of Stratospheric Ozone, National Academy of Sciences, Washington D.C., 1979.

Ramanathan V., Science 190, 50-52, 1975.

Reck R.A., Fry D.L., Atmos. Env. 12, 2501-2503, 1978.

Rowland F.S., Molina M.J., J. Phys. Chem. 80, 2049-2056, 1976.

Rowland F.S., Spencer, J.E., Molina M.J., J. Phys. Chem. 80, 2711-2713, 1976(a).

Rowland F.S., Spencer, J.E., Molina M.J., J. Phys. Chem. 80, 2713-2715, 1976(b).

Stolarski R.S., Cicerone R., Can. J. Chem. 52, 1610-1615, 1974

Sze N.D., Wu M.F., Atmos. Env. 10, 1117-1125, 1976.

Turco R.P., Whitten R.C., Poppoff I.G., Capone L.A., Nature 276, 805-807, 1978.

Wofsy, S.C., McElroy M.B., Sze N.D., Science 187, 535-537, 1975.

APPENDIX B - THE SCATTERING MODEL

As described in section 3.3, a cell model was devised to calculate densities and changes in beam flux due to molecular collisions just in front of the cryosurface. Beer's law type attenuation (eq. (3.3-3)), collisions between incident and reflected beams (eq. (3.3-4)) and changes in cell density due to effusion (eq. (3.4-5)) are all accounted for. The model itself, as well as parameter values, are described in section 3.3, and therefore will not be repeated here.

In the program that follows, the Fortran line numbers listed below correspond to the following calculation sequences.

Line	Description
3-11	Input-output of parameter values
12-17	Initialize the background density and beam intensity in each cell.
19-26	Loop counting of cells and iterations
27-32	Calculate the change in cell densities due to collision.
33-44	Calculate the change in cell densities due to effusion, including boundary effects.
45-55	Calculate the new incident or reflected intensities, depending on the iteration pass, and a new background density.
56-62	Calculate the final intensity values at the end of the iteration.

The following is an incomplete listing of program variable names and their meaning.

AREA = cell cross sectional area

S = collision cross section, Beer's law

SIGMA = collision cross section, beam-beam

XLEN = cell length

NCELLS = number of cells

VEL = beam velocity

VELB = background molecule velocity

ITER = number of iterations desired

N DATA = number of data points desired

BOUNC = percent of beam which reflects off of the cryosurface

BBNC = percent of background flux which reflects off of the cryosurface

DB = original background density

DDA = change in density due to incident beam-background scattering

DDR = change in density due to reflected beam-background scattering

DDRA = change in density due to incident-reflected beam collisions

A = incident beam intensity

R = reflected beam intensity

```
OBTRAN IV G1  RELEASE 2.0            MAIN              DATE = 81081          17/21/32

0001                  DIMENSION A(105),B(105),D(105)
0002                  DATA AREA,S, SIGMA,XLEN/ .3848, 5E-14,5E-14,.5/
0003                  READ(5,*) NCELLS
0004                  READ(5,*) VEL,VELB
0005                  READ(5,*) A1
0006                  READ(5,*) DTME
0007                  READ(5,*) ITER
0008                  READ(5,*) NDATA
0009                  READ(5,*) BOUNC
0010                  READ(5,*) DB,EBNC
0011                  WRITE(6,*) NCELLS,VEL,VELB,A1,DTME,ITER,NDATA,BOUNC,DB,BBNC
0012                  A(1)=A1
0013                  PI=3.14159
0014                  KK=NCELLS+1
0015                  DO 105 J=1,KK
0016                  B(J)=0.
0017                  D(J)=DB
0018            105   CONTINUE
0019                  X=XLEN/NCELLS
0020                  VOL=AREA*X
0021                  I=1
0022                  DO 108 JK=1,ITER
0023                  JJJ=2*NCELLS
0024                  DO 107 K=1,JJJ
0025                  IF(K.LE.NCELLS)J=K
0026                  IF(K.GT.NCELLS)J=(2*NCELLS+1)-K
0027                  C=EXP(-D(J)*S*X)
0028                  DDA=A(J)*(1-C)*AREA*DTME/VOL
0029                  DDB=B(J)*(1-C)*AREA*DTME/VOL
0030                  Z=A(J)*B(J)*SIGMA*2/VEL
0031                  DDBA=2.*Z*DTME
0032                  DD=D(J)+DDA+DDB+DDBA
0033                  G=2
0034                  B=1
0035                  AL=1
0036                  IF(J.EQ.1)B=0
0037                  IF(J.EQ.NCELLS)AL=0
0038                  IF(J.EQ.NCELLS)G=1
0039                  CON=2*PI*SQRT(AREA/PI)
0040                  T=(-G*P(J))+(B*D(J-1))+(AL*D(J+1))+(DB-D(J))*(CON*X/AREA)
0041                  IF(J.EQ.1)T=T+EB
0042                  IF(J.EQ.NCELLS)T=T-D(J)*(1-BBNC)
0043                  DDB=VELB*DTME*T*AREA/(4*VOL)
0044                  D(J)=DD+DDB
0045                  IF(K.LE.NCELLS)A(J+1)=A(J)*C-Z*VOL/AREA
0046                  IF(K.EQ.NCELLS)B(J)=A(J+1)*BOUNC
0047                  IF(K.GT.NCELLS)B(J-1)=P(J)*C-Z*VOL/AREA
0048                  IF((K.GT.NCELLS).AND.(I.EQ.NDATA)) WRITE(6,*)J,A(J),B(J),D(J),JK
0049            107   CONTINUE
0050                  VFR=14.3
0051                  STICK=(A(NCELLS+1)-B(NCELLS))*AREA
0052                  STICK=STICK+D(NCELLS)*(1-BBNC)*VELB*AREA/4.
0053                  DB=(A(1)*AREA-STICK)/(VFR*1000+(20.27-AREA)*(1-BBNC)*VELB/4)
0054                  I=I+1
0055                  IF(I.GT.NDATA)I=1
0056            108   CONTINUE
```

```
CRTRAN TV G1  RELEASE 2.0              MAIN                DATE = 81081          17

0057                    RFINAL=R(1)*C-Z*VOL/AREA
0058                    RATIO=RFINAL/A1
0059                    WRITE(6,*) RATIO
0060                    WRITE(6,*) RFINAL,DB
0061                    STOP
0062                    END
```

APPENDIX C - THE NUCLEATION MODEL

This program solves the system of nucleation kinetics model equations developed in section 3.2. The main program functions for the most part as a vehicle for input-output and loop counting, while most of the calculations are done in subroutines. The IMSL7 subroutine DGEAR, designed to solve stiff ordinary differential equations, is employed for the solution of the main model equations, (3.2-28) and (3.2-29). Documentation for this subroutine is readily available, and will not be discussed further here.

The subroutine DEN returns the values of $\overset{*}{N}$ (DN(1)) and $\overset{*}{T}$ (DN(2)) by calculating their values from equations (3.2-28) and (3.2-39) with input values of N (N(1)) and T (N(2)), as well as the necessary parameter values. The calculation is straightforward.

The subroutine SIGMA calculates the value of parameters σ_x (eq. (3.2-11)) and σ_k (eq. by first solving equation (3.2-13) for L_k by Newton-Ralphson iteration, and then substituting.

FUNJ is a dummy function necessary for DGEAR. It serves no purpose.

The subroutine BIND calculates binding energies for various size clusters. It considers several configurations (i.e., 1, 1, 2, 2, 3, 2 for i = 2, 3, 4, 6, 8, 10, respectively) possible for a given critical cluster size, and calculator which is most stable, which depends on the values of E_a and E_b. This is discussed in more detail in section 3.4.

The initial value of the cluster density, defined by equation (3.2-46), is calculated by DORIG. It values this equation to the form

$$DX = \gamma [AB^i \; V^{i+1}]^{2/3} \tag{C-1}$$

and then rearranges to solve explicitly for i, that is

$$i = \frac{\ln \; (CAC)^{-1} \; (\frac{DX}{\gamma})^{3/2})}{\ln \; (BC)} \tag{C-2}$$

If DX is then assumed to be an appropriately low value (i.e., in the region of extreme incomplete condensation), then one can reduce the initial temperature until $i_{calculated} = i$, which thereby gives the initial conditions for cluster density and temperature.

The following is an incomplete list of variable names used in the MAIN program, and then corresponding names in section 3.2.

AX = a_x

XLK = L_k

TPO = initial temperature

EA = E_a

ED = E_d

EI = E_i

UN = ν, frequency

DO = N_o, surface site density

AV = Ω, atomic volume

B = dT/dt

R = beam intensity

I = i, critical cluster size

TA = τ

DF = D, diffusion coefficient

EB = E_b, binding energy

TP = temperature

H = integration step size

ZF = final Z value

EDMLT = multiplicative factor i.e., $E_d = (EDMLT)_x E_a$

SI = σ_i

N(1) = n_x/N_o

```
0001                    IMPLICIT REAL*8(A-H,O-Z)
0002                    REAL*8 K,N
0003                    DIMENSION K(4,2),N(2),DN(2),TN(2),IWK(2),WK(26)
0004                    COMMON XLK,TPO,EA,ED,EI,UN,DO,AV,R,R,I
0005                    DATA H,ZP/.001,1.0/
0006                    EXTERNAL DEN,FUNJ
0007                    TA(TP)=1./(UN*DEXP(-EA/(1.987*TP)))
0008                    DP(TP)=(0.25*UN/DO)*DEXP(-ED/(1.987*TP))
0009                    READ(4,*)EA,EB
0010                    READ(4,*)AV,LO
0011                    READ(4,*)TPO
0012                    TPOO=TPO
0013                    HO=H
0014                    READ(4,*)IA,IB,IC
0015                    READ(4,*)EDMLT
0016                    READ(4,*)ERA,ERB,ERC
0017                    DO 102 I=IA,IB,IC
0018                    DO 101 ICNT=1,3
0019                    WRITE(7,77)
0020                77  FORMAT(1X,'* * * * * * * * * * * * * * * * * * * * * * *')
0021                    TPO=TPOO
0022                    H=HO
0023                    IF(ICNT.EQ.1)R=ERA
0024                    IF(ICNT.EQ.2)R=ERB
0025                    IF(ICNT.EQ.3)R=ERC
0026                    CALL BIND(EI,CODE,EA,EB,I)
0027                    ED=EDMLT*EA
0028                    UN=1.013
0029                    R=-.0792
0030                    INDEX=1
0031                    PI=3.14159
0032                    SI=3.
0033                    CALL DCBIG(DX)
0034                    N(1)=DX/DO
0035                    AX=(I+1)*AV**(2./3.)
0036                    Z=DX*AX
0037                    XLK=(1./(PI*DX))**.5
0038                    N(2)=0.0
0039                    WRITE(7,41)
0040                41  FORMAT(1X,'EB, AV, DO, AND CODE')
0041                    WRITE(7,*)EB,AV,DO,CODE
0042                    WRITE(7,42)
0043                42  FORMAT(1X,'TPO, EA, ED, EI, I, R')
0044                    WRITE(7,39) TPO,EA,ED,EI,I,R
0045                39  FORMAT(1X,D13.6,3F8.3,I4,D13.1)
0046                    WRITE(7,20) N(1),Z,DX
0047                20  FORMAT(1X,'N1=',D13.6,5X,'Z=',D13.6,5X,'DX=',D13.6)
0048                    H1=H
0049                    J=(ZP-Z)/(200.*H)
0050                    XEND=J*H1/10.
0051                11  CONTINUE
0052                    CALL DGEAR (2,DEN,FUNJ,Z,H,N,XEND,.0001,2,2,INDEX,IWK,WK,IER)
0053                    T=N(2)*DO/R
0054                    TP=TPO+8*T
0055                    SX=4.*PI*(1.-Z)/(DLOG(1./Z)-(3.-Z)*(1.-Z)/2.)
0056                    A=DP(TP)*TA(TP)*DO
```

```
*FORTRAN IV G1  RELEASE 2.0            MAIN                DATE = 81081        17/25/22

0057                    AMP=1.-(1.-Z)/(1.+SX*A*N(1))
0058                    XEND=XEND +J*H1
0059                    I*(AMP-0.1)45,43,43
0060              43    CONTINUE
0061                    WRITE(*,44)
0062              44    FORMAT(1X,'AMP, TP, T, Z, N(1)')
0063                    WRITE(*,21) AMP,TP,T,Z,N(1)
0064              21    FORMAT(1X,5D13.6)
0065                    WRITE(8,*) I,R,IP
0066                    GO TO 100
0067              45    CONTINUE
0068                    IF(IER.GT.128) GO TO 99
0069                    IF(Z.LT.ZP) GO TO 11
0070                    GO TO 100
0071              99    CONTINUE
0072                    WRITE(*,98) IER
0073              98    FORMAT(1X,'THE ERROR MESSAGE IS',I5)
0074             100    CONTINUE
0075             101    CONTINUE
0076             102    CONTINUE
0077                    STOP
0078                    END
```

```
FORTRAN IV G1  RELEASE 2.0            DEN                DATE = 81081          17/25/-

0001                  SUBROUTINE DEN(J,Z,N,DN)
0002                  IMPLICIT REAL*8(A-H,O-Z)
0003                  REAL*8 N(J),DN(J)
0004                  COMMON XLK,TPO,EA,ED,EI,UN,DO,AV,B,E,I
0005                  TA(TP)=1./(UN*DEXP(-EA/(1.987*TP)))
0006                  DF(TP)=(0.25*UN/DO)*DEXP(-ED/(1.987*TP))
0007                  T=N(2)*DO/B
0008                  TP=TPO+B*T
0009                  DX=DO*N(1)
0010                  CALL SIGMA(SI,SX,Z,DX,AV,I,XLK)
0011                  A=DF(TP)*TA(TP)*DO
0012                  BB=((B/DO)/(DO*DF(TP)))**I
0013                  BB=BB*DEXP(EI/(1.987*TP))
0014                  PI=3.14159
0015                  Y=SX*A*N(1)
0016                  Q=(A/(1.+Y))**(I+1)
0017                  Q=Q*SI*BB*(1.-Z)
0018                  W=(1.+Y)/(Z+Y)
0019                  W=W*(Z/N(1))**.5
0020                  W=W/(AV*PI**.5)
0021                  W=W/DO**1.5
0022                  X=Z*W/(N(1)*3.)
0023                  DN(1)=W*O-2.*N(1)
0024                  DN(1)=DN(1)/(1.+Q*X)
0025                  DN(2)=W+2.*X*N(1)
0026                  DN(2)=DN(2)/(1.+Q*X)
0027                  RETURN
0029                  END
```

```
FORTRAN IV G1  RELEASE 2.0            SIGMA                DATE = 81081
0001                  SUBROUTINE SIGMA (SI,SX,Z,DX,AV,I,XLK)
0002                  IMPLICIT REAL*8(A-H,O-Z)
0003                  REAL*8 L
0004                  PI=3.14159
0005                  SX1=DLOG(1./Z)-((3.-Z)*(1.-Z)/2.)
0006                  SX=4.*PI*(1-Z)/SX1
0007                  RI=((I/PI)*AV**(2./3.))**.5
0008                  ZI=PI*DX*RI**2.
0009                  L=(1./(PI*DX))**.5
0010               10 CONTINUE
0011                  FP1=DLOG((XLK/RI)**2.)-(1.-(RI/XLK)**2.)
0012                  FP=FP1*(XLK/L)**2.-DLOG(1./Z)+(1.-Z)
0013                  FP=(2.*XLK/L**2.)*FP1
0014                  FPP1=2./XLK-2*(RI**2./XLK**3.)
0015                  FPP=FPP+FPP1*(XLK/L)**2.
0016                  XLK1=XLK
0017                  XLK=XLK1-FP/FPP
0018                  TEST=DABS((XLK-XLK1)/XLK)
0019                  IF (TEST.GT.(1.E-6)) GO TO 10
0020                  SI=4.*PI*(1.-ZI)*(XLK/L)**2.
0021                  RETURN
0022                  END
```

```
FORTRAN IV G1  RELEASE 2.0                    FUNJ                    DATE = 81321      17/25/22

0001                  SUBROUTINE FUNJ(N,X,Y,PD)
0002                  INTEGER N
0003                  REAL Y(N),PD(N,N),X
0004                  RETURN
0005                  END
```

```
FORTRAN IV G1  RELEASE 2.0              BIND                    DATE = 81091      17/25/2_

0001                  SUBROUTINE BIND(EI,CODE,EA,EB,I)
0002                  IF(I.EQ.2)GO TO 10
0003                  IF(I.EQ.3)GO TO 24
0004                  IF(I.EQ.4)GO TO 11
0005                  IF(I.EQ.6)GO TO 14
0006                  IF(I.EQ.8.AND.EB.LE.EA)GO TO 17
0007                  IF(I.EQ.9.AND.EB.GT.EA)GO TO 20
0008                  IF(I.EQ.9)EI=12.*EB
0009                  IF(I.EQ.5)GO TO 99
0010                  IF(I.EQ.10)GO TO 21
0011            10    EI=EB
0012                  CODE=21
0013                  GO TO 99
0014            11    IF(EB-(.5*EA)) 12,12,13
0015            12    EI=4.*EB
0016                  CODE=42
0017                  GO TO 99
0018            13    EI=6.*EB-EA
0019                   CODE=41
0020                  GO TO 99
0021            14    IF(EB-(.75*EA))15,15,16
0022            15    EI=8.*EB
0023                  CODE=62
0024                  GO TO 99
0025            16    EI=12.*EB-3.*EA
0026                  CODE=61
0027                  GO TO 99
0028            17    IF(EB-(.5*EA)) 18,18,19
0029            18    EI=13.*EB
0030                  CODE=82
0031                  GO TO 99
0032            19    EI=16.*EB-3.*EA
0033                  CODE=81
0034                  GO TO 99
0035            20    EI=15.*EB-2.*EA
0036                  CODE=83
0037                  GO TO 99
0038            21    IF(EB-(.75*EA))22,22,23
0039            22    EI=18.*EB
0040                  CODE=102
0041                  GO TO 99
0042            23    EI=22.*EB-3.*EA
0043                  CODE=101
0044                  GO TO 99
0045            24    EI=3.*EB
0046                  CODE=31
0047                  GO TO 99
0048            99    CONTINUE
0049                  RETURN
0050                  END
```

```
FORTRAN IV G1  RELEASE 2.0            DORIG              DATE = 81081        17/25/22

0001                  SUBROUTINE DORIG(DX)
0002                  IMPLICIT REAL*8(A-H,C-Z)
0003                  DIMENSION TT(3),TI(3)
0004                  COMMON XLK,TP0,EA,ED,EI,UN,D0,AV,B,R,I
0005                  TA(TP)=1./(UN*DEXP(-EA/(1.987*TP)))
0006                  DP(TP)=(0.25*UN/D0)*DEXP(-ED/(1.987*TP))
0007                  TT(3)=TP0
0008                  TT(1)=TP0-2.
0009            66    CONTINUE
0010                  SI=3.
0011                  DX=3.D+9
0012                  TT(2)=(TT(1)+TT(3))/2.
0013                  DO 99 K=1,20
0014                  DO 98 J=1,3
0015                  A=SI*DEXP(EI/(1.987*TT(J)))
0016                  BT=(B/D0)/(D0*DP(TT(J)))
0017                  C=DP(TT(J))*TA(TT(J))*D0
0018                  G=D0*0.5
0019                  TI(J)=((DX/G)**1.5)/(A*C)
0020                  TI(J)=DLOG(TI(J))/DLOG((BT*C))
0021                  TI(J)=TT(J)-I
0022            98    CONTINUE
0023                  W=TI(2)/TI(1)
0024                  X=TI(2)/TI(3)
0025                  TEST=W/X
0026                  IF(TT(1).LE.5.0)GO TO 100
0027                  IF(TEST)55,55,56
0028            56    TT(1)=TT(1)-1.
0029                  TT(3)=TT(3)-1.
0030                  GO TO 66
0031            55    CONTINUE
0032                  IF(TEST.GE.0.0)GO TO 100
0033                  IF(W)  11,11,12
0034            11    TT(3)=TT(2)
0035                  TI(2)=(TT(1)+TT(3))/2.
0036                  GO TO 14
0037            12    TT(1)=TT(2)
0038                  TT(2)=(TT(1)+TT(3))/2.
0039            14    CONTINUE
0040            99    CONTINUE
0041                  TP0=TT(2)
0042                  GO TO 101
0043           100    CONTINUE
0044                  WRITE(7,102)
0045           102    FORMAT(1X,'ERROR IN DORIG')
0046           101    CONTINUE
0047                  RETURN
0048                  END
```

END

DATE
FILMED

1-82

DTIC